

**A Study on the Feasibility of a Silica-on-Silicon
Blue Upconversion Laser Fabricated by
Flame Hydrolysis Deposition**

Thesis submitted for the degree of
Doctor of Philosophy from the Faculty of Engineering,
University of Glasgow

© **Marcos Vinícius Dias Vermelho**

September 1999

ProQuest Number: 13833921

All rights reserved

INFORMATION TO ALL USERS

The quality of this reproduction is dependent upon the quality of the copy submitted.

In the unlikely event that the author did not send a complete manuscript and there are missing pages, these will be noted. Also, if material had to be removed, a note will indicate the deletion.



ProQuest 13833921

Published by ProQuest LLC (2019). Copyright of the Dissertation is held by the Author.

All rights reserved.

This work is protected against unauthorized copying under Title 17, United States Code
Microform Edition © ProQuest LLC.

ProQuest LLC.
789 East Eisenhower Parkway
P.O. Box 1346
Ann Arbor, MI 48106 – 1346

GLASGOW
UNIVERSITY
LIBRARY

11725 (copy 1)

Abstract

The use of compact blue laser light source is showing a remarkable technological improvement in certain applications, which include devices such as optical data storage, laser printers, and colour displays, to mention a few. Therefore, these applications are requiring more reliable laser sources. Factors such as compactness, robustness, long-term stability, suitability for large-scale integration and possibility of mass-production can be decisive for the choice of the kind of blue laser source as part of a practical tool. Planar lightwave circuits provide practical solutions for such optical devices. A combination of the Flame Hydrolysis Deposition (FHD) and Reactive Ion Etching (RIE) is by now a mature technology, and it has produced planar lightwave circuits for telecommunications applications. In using these analogous technologies, the aim of this work is to study the feasibility of fabrication of compact blue upconversion laser sources.

Before proceeding to the study of the blue upconversion process, the research concentrates on the optimisation of the glass host, investigating an alternative approach to reduce the ion-ion interaction in a heavily rare earth doped matrix using sodium ions. The characteristics of the waveguides employed as cavity lasers for the devices fabricated in this planar form also demand accurate numerical modelling for optimisation. Thus, a numerical procedure is developed to complete this general optimisation. The laboratory facilities and availability of experimental data were decisive in the choice of the erbium ion as active material for this first part of the research.

The blue upconversion process investigation is initiated by considering two rare earth doping composition for the $\text{SiO}_2\text{-P}_2\text{O}_5$ glass: a single thulium and a thulium doped sensitised with ytterbium ions. Blue upconversion is examined in both glasses considering future diode lasers pump wavelength. The wavelengths at 800 nm and 980 nm demonstrated to be the potential choices for pumping the Tm/Yb glass. The inclusion of ytterbium ions in the glass composition enhanced the blue upconversion process using the pump wavelength at 800 nm, however the population inversion for laser threshold was not predicted by the modelling. The pump wavelength at 980 nm

is applied to the numerical model to study the feasibility of the fabrication of this blue upconversion laser. The preliminary results, which do not correspond to the optimised laser structure design, predicted performance comparable to the results of the employment of optical fibre based devices which have been reported so far.

Resumo

O uso de fontes de radiação laser operando na região de comprimentos de onda correspondente ao da luz azul tem proporcionado uma notável melhoria tecnológica em certas aplicações, incluindo dispositivos tais como os usados para armazenamento óptico de informações, impressoras a laser, e mostradores ópticos, para citar apenas alguns. Estes dispositivos necessitam de lasers que sejam confiáveis em termos de funcionamento. Além disso, fatores como compactidade, robustez, estabilidade em uso prolongado, alta capacidade de integração e possibilidade de produção em massa podem ser decisivos na escolha do tipo de fonte de luz azul a ser empregado no dispositivo prático. Circuitos ópticos planares (“Planar Lightwave Circuits” – PLC) apresentam soluções práticas para estes dispositivos ópticos. A combinação do método de fabricação de vidro por chama hidrolisada (“Flame hydrolysis Deposition”) e de fabricação de guias de ondas denominada “Reactive Ion Etching” é no momento uma tecnologia estabelecida que produz circuitos ópticos para aplicações em telecomunicações. Esta pesquisa tem por objetivo estudar a viabilidade de aplicar tecnologia análoga para fabricação de fontes laser de luz azul produzida por conversão ascendente de frequência em guias de ondas dopados com íons terras raras.

Anteriormente ao estudo da conversão ascendente de frequência, a pesquisa dedicase a buscar uma forma alternativa de reduzir o efeito prejudicial da interação entre os íons terras raras em amostras com alta dopagem, estudando a influência da inclusão de íons de Sódio na composição do vidro. Tendo em vista as características dos guias de ondas a serem utilizados como as cavidades laser, foi desenvolvido também um modelo visando otimizá-las através de simulações numéricas. Desta forma, a alternativa para melhoria do vidro hospedeiro e o modelo matemático para simulação formam um conjunto instrumental para a otimização dos dispositivos. Fatores concernentes à estrutura laboratorial disponível e a disponibilidade de resultados experimentais para futuras comparações foram decisivos na escolha de vidros dopados com íons de Érbio nesta primeira etapa.

A conversão ascendente de frequência em vidros $\text{SiO}_2\text{-P}_2\text{O}_5$ é feita considerando

duas composições com íons terras raras: amostras dopadas somente com íons de Túlio e amostras com íons de Túlio e Itérbio. A conversão ascendente de frequência é investigada levando-se em consideração futuras aplicações com comprimentos de ondas de bombeamento disponíveis em laser de diodo. Os comprimentos de ondas em 800 nm e 980 nm demonstraram ser os de maior potencial para bombeamentos em amostras em vidros dopados com Tm/Yb. A inclusão de íons de itérbio aumentou a eficiência da conversão ascendente de frequência nos vidros com dopagem composta para comprimento de onda em 800 nm, todavia a simulação não previu a inversão de população necessária para geração de luz coerente (laser). O comprimento de onda em 980 nm é então definido para o estudo da viabilidade de fabricação dos lasers por conversão ascendente de frequência. Os resultados preliminares, que não correspondem ao de uma estrutura laser otimizada, prevêem performance comparável aos resultados reportados até então utilizando dispositivos com fibras ópticas.

Acknowledgements

I would like to thank my academic supervisor Professor J. S. Aitchison for his constant support and advice during the development of this work, and in particular at the important initial stage of this project, prior to my scholarship award. The members of the staff of the Department of Electronics and Electrical Engineering are acknowledged for the use of its facilities. My thanks are due to the colleagues of the optoelectronic group, specially to Paulo Marques for his preliminary assistance on the use of the Flame Hydrolysis Deposition laboratory; Dr. Amr Saher for his friendship and generous help by handing over the lab space at a crucial period in the finalisation of this work. I wish to express my thanks to my office-mates during this time at the department. Among them, Dr. Ulf Peschel must be thanked for assisting me in numerous occasions, and Dr. Eugene Avrutin for, among other “helps”, his critical reading in this work. The Cleaning Room staff are also thanked, in particular Joan and Margaret. Thanks also go to the whole “team” of the mechanical workshop, for their receptive warmth and professionalism.

I wish to express my to thank to Professor Artur da S. Gouveia Neto, from the Department of Physics – UFAL/BR, for his continuous support and encouragement during part of my academic life. Professor Jandir M. Hickmann from the same Department is also acknowledged for introducing me to the Department of E&E Eng., University of Glasgow.

I would like to thank my friends in Glasgow for their care in the bleak moments of homesickness, for supporting our national football team in the last World Cup, for having pints over enjoyable conversations, and much more: Alexandra Müller, Mário Gonçalves, Flávio and Vânia Marques, Luis and Margarete Avanci, Hemerson Gama, Hélio and Waleska Lira, José Figueiredo, Sofia Figueiredo, Marcelo Vieira. I would like to include in this list my friend and brother-in-law Ilbert Cavalcanti (who followed us to Glasgow by heart) for his “Friday Family Report” e-mails which kept us up-to-date with the hottest news and sustained our good mood.

I would like to say a very special ‘thank you’ to Ildney Cavalcanti: companion, wife, and friend.

I would like to thank my parents Américo and Maria Vermelho, and sisters and brother Maria, Américo, Juares and Cristina, and their families, for understanding my long absence.

My financial support was provided by the Brazilian Agency - Conselho Nacional de Desenvolvimento Científico e Tecnológico – CNPq, which is gratefully acknowledged

Contents

CHAPTER 1 - INTRODUCTION

1.1 The Blue Laser Technology	1
1.2 Different Approaches to Obtain Blue Laser	4
1.2.1 The Diode Lasers	4
1.2.2 Nonlinear Waveguides for Second Harmonic Generation	5
1.2.3 The Frequency upconversion Laser	7
1.3 Performance Requirements for Blue Lasers	9
1.4 Motivation and Aim of the Research	13
1.5 Presentation of the Contents of the Thesis	15
1.6 References	17

CHAPTER 2 - OVERVIEW OF RARE-EARTH DOPED GLASS

2.1 Introduction	19
2.2 The Glass Fabrication Process: The Flame Hydrolysis Deposition	21
2.3 General Characteristics of Rare Earth Ions in Glasses	24
2.4 Electronic Structure: The Ions and the Static Lattice Interaction	27
2.5 Radiative Transition: The Ions and the Electromagnetic Field Interaction	29
2.5.1 The McCumber's Theory	30
2.5.2 The Judd-Ofelt Theory	34
2.6 Nonradiative Transition: The Ions and the Dynamic Lattice Interaction	38
2.6.1 Energy Transfer Processes: The Ion-Ion Interaction	40
2.7 Rare Earth Doped Glass: Al³⁺ Co-Doping Influence	45
2.8 Summary	48
2.9 References	49

CHAPTER 3 - RARE EARTH HOST GLASS OPTIMISATION: THE INFLUENCE OF SODIUM

3.1 Introduction: Rare Earth Glass Host Fabrication	53
3.2 The Erbium $^4I_{13/2} \rightarrow ^4I_{15/2}$ Transition Lifetime Measurement	62
3.2.1 Absorption and Fluorescence Measurement Results	67
3.2.2 Judd-Ofelt Parameters Measurement	72
3.3 Conclusions	80
3.4 Reference	82

CHAPTER 4 - MODELLING CW RARE EARTH HIGHLY DOPED WAVEGUIDE LASER AND AMPLIFIER

4.1 Introduction	85
4.2 Modelling CW erbium doped waveguide laser and amplifier	88
4.3 Modelling CW erbium doped waveguide laser and amplifier at low concentration	90
4.3.1 Erbium doped waveguide amplifier - Modelling amplified spontaneous emission (ASE)	96
4.4 Modelling a CW erbium doped waveguide laser and amplifier at high concentration	99
4.5 The approach to model high concentrated rare earth doped waveguide laser and amplifiers	102
4.5.1 Validation of the model	107
4.6 Conclusion	112
4.7 References	113

CHAPTER 5 - BLUE UPCONVERSION GENERATION IN Tm^{3+} - AND Tm^{3+}/Yb^{3+} -DOPED $SiO_2-P_2O_5$ GLASSES

5.1 Introduction	117
5.2 The upconversion process	119
5.3 Single Thulium doped Phosphosilicate glass	121
5.3.1 Single Tm^{3+} - $SiO_2-P_2O_5$ doped sample pumped at 1064 nm	122
5.3.2 Single Tm^{3+} - $SiO_2-P_2O_5$ doped sample pumped at 800 nm	127
5.3.3 Single Tm^{3+} - $SiO_2-P_2O_5$ doped sample pumped at 678 nm	129
5.4 Thulium doped phosphosilicate glass sensitised by Ytterbium ions	134
5.4.1 $Tm^{3+}/Yb^{3+}/Na^+$ doped samples pumped at 678 nm	135

5.4.2 Tm ³⁺ /Yb ³⁺ /Na ⁺ doped samples pumped at 800 nm	139
5.4.3 Tm ³⁺ /Yb ³⁺ /Na ⁺ doped samples pumped at 980 nm	145
5.5 Conclusion	155
5.6 References	158
CHAPTER 6 - MODELLING BLUE UPCONVERSION WAVEGUIDE LASER	
6.1 Introduction	162
6.2 Determination of the Spectroscopic Parameters of the Model	164
6.2.1 Radiative Transitions	164
6.2.2 Nonradiative Transitions - Multiphonon Relaxation	169
6.2.3 Nonradiative Transitions - Cross Relaxations	171
6.2.4 Fluorescence Contributions to the Rate Equations	174
6.3 Laser Modelling	177
6.3.1 Rate Equations for Pump Wavelength at 980 nm	177
6.3.2 Laser Design Considerations - $\lambda_p = 980$ nm	180
6.3.3 Rate Equations for Pump Wavelength at 800 nm	188
6.3.4 Laser Design Considerations - $\lambda_p = 800$ nm	191
6.4 Conclusion	195
6.5 Reference	197
CHAPTER 7 - CONCLUSION AND SUGGESTION FOR FURTHER WORKS	
7.1 Conclusions	201
7.2 Reference	208
APPENDIX A	

Chapter 1 - Introduction

1.1 The Blue Laser Technology

The increasing number of scientific publications in the past few years concerning compact blue laser sources is a demonstration of the great scientific and technological interest in this field. Besides the studies of the physical effects involved to generate these visible laser lights, their possible commercial applications are also extensive. The totality of the applications for devices delivering blue laser light is hard to be computed, but certainly among them, the optical storage is publicized to be one of the major focuses. Appliances using blue lasers, due to the shorter wavelength of the light, can raise the storage density by a factor of about two or four if compared to the commercially red or infrared laser diodes, respectively (High Density CD-ROMs, holographic storage devices) [1]. In home-entertainment, systems will be possible to store a movie in high-resolution high density TV (HDTV) quality together with several audio-channels in HiFi-stereo surround sound on a

small high-density compact disc. Multimedia applications such as interactive database or video animated computer games would also be greatly enhanced. In addition, the volume of visual data being transferred between computers via the Internet is growing exponentially.

Another well-known application for a compact blue laser source is for use as part of laser printing devices. The blue laser light can be focused better than the red light, allowing laser-assisted printing machines to be operated at higher resolutions. The processing of laser printing can also be accelerated using blue laser because the high energy of the light [2].

In a broader sense, visible lasers have a large number of practical applications as well. In medicine for instance, the use of visible laser light as a compact tool for guidance during an operation with infrared cutting lasers can be very practical and helpful. Red light is almost invisible in front of open human tissue while blue, and mainly green, is much easier to see. In the increasingly important area of environmental analysis and protection, blue and green laser light are useful in compact yet sensitive analysis systems for air pollution. Blue, as well as green, lasers are needed to complete the set of basic colours (red-green-blue) and therefore, make full colour display technologies possible (laser-TV).

Blue laser is also a potential application for undersea communications, because the seawater absorbs less blue light than longer wavelengths. An important requirement for this commercial application of blue lasers is the long device lifetime. Typically, the expected lifetime for these devices is above 10,000 hours continuously.

Undoubtedly this limited list did not include all the possible practical applications for a compact visible laser source, and others will appear whenever new robust and inexpensive devices are fabricated. Considering this, the next section will offer a survey of methods to generate blue laser light which have been the object of most intense investigation in the field. It is worth to mention that, this thesis does not intend to develop a comparative study on methods of blue laser light generation. Thus, the choice of the methods was based on the availability of the data on the subject. This information concerning different approaches to generate blue light will

be given in this chapter only in the hope of contextualising the subject.

1.2 Different Approaches to Obtain Blue Laser

The large number of industrial and educational laboratories worldwide involved in the research field to obtain blue laser sources, makes prohibitive compiling a complete review in the subject. Nevertheless, information illustrating different methods used to generate blue laser light is helpful for future comparisons. Diode lasers operating as a primary source of blue light, the nonlinear waveguide second harmonic generation, and the frequency upconversion in optical fibres are amongst the most efficient methods to obtain compact blue laser light sources. This section will be dedicated to a general presentation concerning the most commonly used approaches to obtain blue laser light generation.

The topics under discussion will consist of short considerations on its fabrication procedure, followed by some typical experimental results obtained from these devices. The values did not express the cutting-edge of research fields, however they were gathered from the most recent experimental results.

1.2.1 The Diode Lasers

For direct sources of blue light, many different materials have been used to fabricate diode lasers operating in this spectral region. Initially, the II-VI-based material¹ was used to demonstrate the first blue diode laser [3]. These diode lasers consist of a sequence of semi conducting layers from elements Zn, Mg, Se, and S or Be respectively. III-V semiconductor² GaAs crystals are used as substrate materials. During photo lithographical processes, a stripe-like contact structure is fabricated, a contact metal cladding is evaporated onto the diode and then it is cleaved into small cubes with approximately 1.0 mm edges [4]. However, according to reference [3], the degradation of the first II-VI-based blue diode lasers was so large that disable their commercialisation success. In addition, they had a short lifetime under continuous wave (CW) operation at room temperature and the central wavelength have a

¹ These semiconductors consist of elements taken from the groups II and VI of the periodical table. They are: Group II (Transition Metals) Zn, Cd, and Hg. Group VI (Oxygen Family) O, S, Se, Te, and Po.

² Group III (Aluminium Family) B, Al, Ga, In, Tl. Group V (Nitrogen Family) N, P, As, Sb, and Bi.

tendency to green, instead the blue light.

More recently, the III-V semiconductor nitride compound, mainly GaN, has been used to generate blue laser light. These diode lasers, undergoing a fabrication similar to that of its II-VI-based competitor, consist of a gallium nitride (GaN) layer grown on top of a crystal wafer. The critical goal in this blue-laser diode development is to reduce the number of defects in fabrication materials that cause degradation and a lower output power [5,6]. The main source of defects came from the crystal lattice mismatch between the semiconductor layer and the wafer's material used to support. Several substrates have been used to grow the semiconductor layers, such as sapphire (Al_2O_3), silicon carbide (SiC), and more recently aluminium nitride crystal (AlN)[7].

Generally, the diode lasers continuous wave (CW) operation, as required in most of its practical applications, is considered much more difficult than that pulsed operation because of the heating that can occur with the high currents needed to achieve lasing. To reduce these problems, lower the operating current, extracting the heat better, or make more robust devices are pointed as possible solutions. Despite the better quality of the lasers fabricated with GaN compounds, as compared with the previous solution, they are still in process of optimisation for commercial applications. Lasers operating pulsed with 300 ns and threshold current of 800 mA have already been reported. These lasers delivered a maximum output power of 20 mW with wavelength at 414 nm, although the lifetime of 5 hours was obtained only for output power at 5 mW [8]. Usually CW operation has shorter lifetime. However, recently S. Nakamura has reported an InGaN-based diode laser emitting 5 mW of blue light at 400 nm operating at 40 mA and 5V. The lifetime was estimated at 10,000 hours at room temperature [9,10].

1.2.2 Nonlinear Waveguides for Second Harmonic Generation

An important requirement for efficient conversion in any nonlinear material is that the local (blue) second harmonic polarization can drive a propagating blue wave and stay in phase along the direction of propagation of the light. This problem is usually referred to as phase matching. Normally, dispersion causes a refractive index difference between the fundamental and second harmonic wavelengths which

prevents phase matching [11]. The most common method to cancel the phase mismatch in nonlinear crystal involves matching the different polarizations in a birefringent crystal [12].

Quasi-phase matching (QPM) is a condition based on accepting the local phase mismatch caused by dispersion and inverting the crystal orientation of the region where the local blue polarization and the fundamental propagating wave are 180° out of phase. This crystal inversion gives a 180° phase shift of the local blue oscillation, bringing the regions (domains) back into constructive interference. The main advantage of the QPM second harmonic generation is that it can be achieved at any wavelength within the transparency range of the nonlinear material simply by the correct choice of period of the domain inversion [13].

Among the various nonlinear materials, the most successful so far have been the two lithium-based, lithium niobate and lithium tantalite, and the family of the potassium titanyl phosphate (KTP) and its isomorphs. The ability to form waveguides narrows down the list of nonlinear crystals, the further requirement that the material should lend itself to periodical domain inversion narrow down the list of possible nonlinear material even more. The materials that are used are so-called ferroelectrics, which have a permanent electric polarization. The electric polarization can be switched between at least two different directions [13].

The two processes used to obtain the inversion of domain in the nonlinear crystals are based in the ion exchange and the electric field poling. In the ion exchange method, the waveguide is patterned in a mask layer on the surface of the crystal substrate, which is then immersed in a melt containing the ion to be exchanged. An ion in the crystal structure diffuses out to the melt and an ion from the melt diffuses in to take its position in the crystal, resulting in an increase in the index of refraction [14]. In the electric field poling, the diffusion processes are based on the phenomenon that a concentration gradient will cause a corresponding electric field, so that when the substrate is cooled down after a quick treatment in a diffusion furnace, domain inversion will appear in regions where a dopant has been introduced. Electric field poling uses a strong external field ($\sim 20\text{kV/mm}$) to shift the ions in the crystal. The periodicity is achieved either using periodic electrodes or by periodically inhibiting

poling with chemical patterning of the surface of the crystal.

The main laser requirement for efficient doubling in nonlinear waveguides are a diffraction-limited output beam for efficient coupling to single-mode nonlinear waveguides and a narrow spectral output, less than 0.1-0.2 nm, matching the phase-matching bandwidth of the nonlinear waveguide. In addition to these laser requirements, it is convenient to have the wavelength of the laser diode adjustable to match the wavelength to the phase matching condition of the nonlinear waveguide and to have stable wavelength operation insensitive of feedback [13].

Finally, some values giving the order of magnitude or the efficiency of this visible light generation processes. A 1.0 cm long LiNbO₃ waveguides fabricated by Ti-diffusion-based poling has reported output power of 25 mW in the blue region at 421.5 nm when pumped with 120 mW of infrared light at 843 nm from a Ti:Sapphire laser. Green frequency doubled light, in a 1.0 cm long electric field poled LiNbO₃ waveguide, have generated a peak normalized efficiency³ of nearly 300 %/Wcm² of 1100 nm fundamental radiation. Frequency doubling in KTP waveguides reported 800 μW of blue power in an 8.0 mm long guide pumped at 850 nm. The typical waveguide length around 0.5-1.0 cm is a consequence of the high losses in the proton-exchange LiNbO₃ and ion exchange KTP waveguides. The typical loss numbers are 0.5-1.0 dB/cm, which set an upper limit for useful waveguide length to ~3.0 cm [13].

1.2.3 The Frequency upconversion Laser

Researchers have been chasing the idea of blue lasers for a long time, using frequency upconversion or frequency doubling from infrared radiations. One promising approach to obtain CW visible laser light has been making use of frequency upconversion in insulating solids [15]. This topic will be briefly introduced in this section because it is the subject of investigation of the present work. Thus, further information about the process will be given when necessary along the work. Frequency upconversion is a process by which the energy resident in two or more

³ Normalised efficiency is defined by: $\eta_{norm} = \eta / P_{\omega} \cdot L^2$. Where η is the efficiency of the process,

infrared photons is used to populate a high-lying energy level of a laser active ion. The resulting population inversion relaxes via one-photon transitions to low lying levels, yielding visible light. Many upconversion lasers based on doped optical fibres have produced output wavelengths ranging from the near infrared to the ultraviolet [16-19], but the greatest advantage offered by the high confinement of the waveguide geometry is that the room temperature operation is easier to obtain than in the bulk gain medium more conventionally employed. High optical confinement and long interaction length makes the optical fibre geometry an attractive laser gain medium, qualities which should be achieved in the planar form as well.

The number of experimental reports of Tm^{3+} -based blue lasers is enormous. For this reason, only the experimental results of the two well known very efficient processes are shown here. Considering single wavelength pumping scheme, Sanders and co-workers [20] have reported optical-to-optical conversion efficiency of up to 30% pumping a 2.5 m long optical fibre at 1137 nm with 550 mW obtaining 72 mW of blue light at 482 nm. The same fibre laser configuration reached 106 mW of blue light with 890 mW of incident infrared radiation, which is a 12% overall optical-to-optical conversion efficiency of infrared to blue. A maximum output power of 230 mW in a similar fibre laser was obtained pumping with up to 1.6 W of infrared radiation at 1123 nm [21].

Despite the high efficiency of the fibre laser devices, at the time of preparation of this manuscript, no report of laser device using waveguides in the planar form was found. Nevertheless, a combination of an infrared diode laser pump butting a rare earth doped planar waveguide points towards the possibility of compact packages suitable for a diversity of real-world applications.

As shown in the section 1.1, the number of practical applications for a compact blue laser is significant, so, different performance requirements, when these lasers are part of tools, are also expected. Thus, the next section will give some considerations on this issue.

P_0 is the pump power, and L is the waveguide length.

1.3 Performance Requirements for Blue Lasers

This section concentrates on presenting some realistic numbers on the minimum requirements for blue lasers, from the industrial point of view, for three practical apparatus: colour printing, data storage, and optical displays. The choice of these devices was based on their large applicability and, consequently the availability of such data. It is not the goal of this section to provide a complete technical review related to each device. It will only consist of a brief description in terms of device functionality followed by a minimum requirement for a laser as component of a practical appliance.

Future printer technologies will be driven by the need for speed, colour, resolution, power consumption and multi-functionality, e.g. scan/fax/print functions in a single unit. The major motivation for short wavelength laser development for printers is improving the beam spot size while maintaining an adequate depth of field¹ and the optical aperture. A diode laser at 780 nm in a typical optical system needs 6 mm aperture optics to achieve 35 μm full width at half maximum (FWHM) spot size required in the scanning direction. For true 1200 dpi (17 μm spot size), 780 nm lasers would require more expensive and bulky 12.0 mm aperture optics and laser polygon scanners, while producing a depth of field of only 0.5 mm. A submillimeter depth of field requires a more costly mechanical system capable of maintaining the photoreceptor surface within the laser focus. Alternatively, a 390 nm pump laser could operate at 1200 dpi with a 1.0 mm depth of field using 6.0 mm optics [22].

The performance requirements for lasers to operate in laser printers are modest, not far from what has been demonstrated in the laboratories. To discharge the photoreceptor at the speed necessary for 60 ppm printing, a laser producing 6.0 mW of continuous wave (CW) output power would be required. Higher power would enable increased printing speeds. Rise/fall times of about 1.0 ns are desired to enable image enhancement. Finally, lasers operating at wavelengths longer than 430 nm are preferred to avoid decomposition of commonly used organic photoconductor materials [23].

The recent advances towards developing compact solid-state blue light source mean high capacity data storage. This accelerated progress can be viewed by the improvement in the compact disc storage capacity (CD-ROM²) in the past few years due to shorter laser wavelengths used. The new generation of compact discs, the digital versatile discs (DVD), increased the data store capacity from 0.6 GB, for the conventional CD-ROM's, to 4.7 GB capacity for the DVD altering the pump laser wavelength. The conventional CD-ROM employs the infrared laser at 780 nm while the digital versatile disc works with the shorter red wavelengths between 635 nm and 650 nm. The DVD also increases the focus by using a more powerful focusing lens. Physically, the main difference between DVDs and CDs deals with the minimum area for store information – the pits. The DVD's pits are only 0.40 μm in diameter; in contrast, the CD's pits are 0.83 μm in diameter. The DVD data tracks are 0.74 μm apart, while the CD's are 1.60 μm apart. These two factors combined to make the DVDs data spiral 11 km long, over twice the size of CDs without altering its physical size. Although the shift of the pump wavelength from 780 nm to \sim 650 nm has had a moderate effect on the recording density, shifts to the blue spectral region predicts 15 GB DVD-ROM drives [24]. The further improvements expected if the laser wavelength is reduced is show Table 1.I. The capacity enhancement on data storage with the reduction in the laser pump wavelength is followed by the possibility of optimisation in other factors such as compression and improved tracks. The recordable DVD-RAM³ versions are also considered [25], despite the harder minimum performance demanded of the pump lasers [26]. The ideal laser for DVD-RAM should produce a single mode CW 30-40 mW beam with an aspect ratio smaller than 4. The DVD-ROM has reduced beam power requirements of 3.0-5.0 mW, but otherwise similar specifications. Ultraviolet absorption in the glass substrate becomes an issue with this pump wavelength, resulting in an optimal wavelength of 400-430 nm. Shorter wavelengths would have an optical transmission of less than 80%.

¹ Depth of field is the area within which objects are acceptably sharp behind and in front of the point of focus.

² ROM – read only memory

³ RAM – Randomly Access Memory

**Table 1.1: blue laser capacity improvement of data storage
(after ref. [28]).**

Laser Wavelength	Number of Music Albums on CD-ROM	
	Change in the Laser Wavelength	Improvement in the CD Tracks
860 nm (Near Infrared)	1	7
635 nm (Red)	2	14
430 nm (Blue)	4	28
350 nm (Ultraviolet)	9	63

In the present system for projection displays, the white light is divided into primary colours using dichroic mirrors. Because liquid crystal spatial light modulators (SLM) are used, the beams must be polarized. This results in additional losses and system complexity. After reflecting off the SLMs, the three images are recombined in a prism element and projected onto the viewing screen. Although the result is an industry leading 2048×2048 pixel projected colour image, the optics of collimating, splitting, polarizing and recombining three broadband primary colour beams is elaborated and costly.

If the lamp could be replaced by three visible lasers, the packaging would immediately benefit from a simplified power supply and cooling system, since laser diodes used as primary sources or pumping other systems, require only a few volts (vs. kilovolts for halide lamps) to operate. Polarized, monochromatic laser light eliminates the need for polarizing optics, eases the specification on the other optical elements and SLMs, and makes it easier to filter out ambient light [27]. If the laser light is pulsed in rapid succession, a single, simplified optical system could replace the three beam approach of the current system and a more saturated image spanning a broader colour range could be built up from overlaid red, green, and blue images using a scheme known as sequential colour.

For an estimate of the minimum laser requirement in a display, one may consider a hypothetical projection TV, based on lasers operating at the wavelengths at 656 nm,

532 nm and 457 nm for the red, green and blue basic colour, and operating at 6500 K white point colour balance. To achieve an expected screen brightness of 500 Cd/m² over 55" diagonal 16:9 aspect ratio screen, and assuming 33% optical efficiency and a 3× screen gain, the lasers must produce 6.6 W, 1.8 W, and 1.2 W in the red, green, and blue, respectively [27].

This section has shown how broad is the laser specification to be applied as part of a practical tool. Based on these considerations, the next section will then concentrate on the motivations and the aim of the present research.

1.4 Motivation and Aim of the Research

The rapid and global spread of the Internet and multimedia communications has accelerated the growth in optical communications network. Planar lightwave circuits (PLCs), in which fibre-matched silica based waveguides are integrated, has been providing key practical devices for such optical networks. This is because they are suitable for large-scale integration, offer long-term stability, and can be mass-produced. Some PLCs, including optical power splitters, wavelength insensitive couplers, arrayed-waveguide gratings, and thermo-optics switches are already available on the market.

Fabrication of silica-based optical waveguides on silicon substrates by a combination of the Flame Hydrolysis Deposition (FHD) and Reactive Ion Etching (RIE) is a mature technology to produce such planar lightwave circuits [29]. Low propagation loss and good uniformity of both the waveguide geometry and the refractive index difference between the core and cladding (Δn) are basic parameters to determine the performance of practical waveguide circuits. Propagation loss of 0.1 dB/cm has already been obtained in a 2.0 m long waveguide with 2% of refractive index difference; and loss of 0.035 dB/cm was obtained in a 1.0 m waveguide with $\Delta n = 0.75\%$. A further loss reduction to 0.017 dB/cm has been achieved in a 10.0 m long waveguide ($\Delta n = 0.45\%$) [29].

Thus, a combination of the technological importance in the development of low-cost compact blue laser light as described in the sections 1.1 and 1.2, added to the established Flame Hydrolysis Deposition fabrication method encouraged us to study the feasibility of the development of a rare earth doped blue upconversion laser in the PLC configuration. This expectation is supported by research into the FHD to fabricated devices as active components in the PLCs. Optical amplification in erbium-doped waveguide that has been carried out with a view to application in optical communication systems has shown promising results. Diode laser pumped waveguide amplifiers, which employ simple straight and curved erbium-doped silica-based waveguides, have already demonstrated net gains of up to 27 dB [30].

In addition, reports of upconversion blue laser in Tm^{3+} -doped fluoro-based optical

fibres suggested this rare earth as active ions to the phosphosilicate glass produced by FHD. Comparison in performance between the optical fibres and planar waveguide geometries is almost inevitable, as both undergo similar processes of fabrication and the blue light is generated by the same physical principle, the frequency upconversion. However, the planar configuration proves competitive when the definitions of complex optical circuits are needed. The prospective for straightforward photolithographic variation of waveguide parameters in the plane, and for mass production of robust devices, show the potential of these devices.

1.5 Presentation of the Contents of the Thesis

The presentation of the work developed in this research will be divided into two parts. The first part will contain the preliminary studies concerning an optimisation of glass host and a laser modelling procedure. It will be followed by the investigation of blue upconversion generation in FHD fabricated waveguides, and a study of the feasibility fabrication of lasers with similar waveguides.

Initially, chapter 2 will outline background information supporting the following chapters. It will start with a brief overview on the FHD method, followed by a short review on some spectroscopic characteristics of rare-earth doped glasses which are relevant to clear understanding of the further chapters.

Chapter 3 and chapter 4 will give attention to the basic requirements for efficient waveguide lasers: the rare earth doped glass host, and the waveguide design optimisations. Thus, before proceeding to study the blue upconversion, chapter 3 will look at the analysis of the glass optimisation. Although the ultimate goal of this thesis is to use glass doped with thulium ions, for this investigation, the choice of erbium ions as active material was made due to the large amount of published data we can compare our results with, as well as the laboratory facilities available. As will be discussed in the chapter 4, when heavily doped waveguides or composite glasses, i.e. glasses doped with at least two different rare earths exchanging their energy are used, the rate equations describing the laser system become nonlinear and the laser modelling becomes rather cumbersome. Thus, in this chapter, a new and intuitive procedure to the modelling of lasers in this situation will be presented. The availability of experimental data to serve as a base of comparison to the modelling procedure, and the similarity between their fabrication processes, pointed out to the erbium doped waveguides as an appropriate rare earth to test the model.

In chapter 5, the blue light generation by upconversion will be analysed. This investigation deals with FHD glass composition and pump wavelength in the generation of blue upconversion light. The definition of the appropriate rare-earth doped phosphosilicate glass host will take into account the inclusion of single thulium doped or thulium doped ytterbium sensitised glass as active ions. The

samples will be tested under different pump wavelength schemes, always considering future use of commercial diode lasers. These samples will also provide spectroscopic information to be used as input data for the modelling described in the chapter 6. This modelling will be carried out by adapting the model developed in the chapter 4 to the Tm-based waveguide lasers. Thus, the feasibility of blue upconversion lasers using this rare earth doped waveguides fabricated by FHD will be addressed.

Finally, chapter 7 will present a summary of the work carried out summing up the major conclusions. This will be followed by some considerations on future works.

1.6 References

- 1 G. Huber, T. Kellner, H.M. Kretschmann, T. Sandrock, and H. Scheife, "Compact diode pumped cw solid-state lasers in the visible spectral region", *Optical Materials* **11**, 205-216 (1999).
- 2 L. Beiser, Selected Papers on Laser Scanning and Recording, *SPIE Milestone Serie* **378** 1985.
- 3 S. Nakamura, Interview with Shuji Nakamura senior researcher at the department of R & D of Nichia Chemical Ind. Ltd. (Tokushima, Japan) on *Selected Articles from SPIE's New Publications* Aug. 1996 – SPIE Web Home
- 4 G. Landwehr, "Blue and green laser diodes", Physics Department at the University of Würzburg Web Page (1999).
- 5 A. Kuramata, K. Horino, and K. Domen, "GaN-based blue laser diodes grown on SiC substrate as light source of high-density optical data storage", *Fujitsu Scientific and Technical Journal* **34**, 191-203 (1998).
- 6 T. Yang, S. Goto, M. Kawata, A. Niwa, and J. Gotoh, "Optical properties of GaN thin films on sapphire substrates characterized by variable-angle spectroscopic ellipsometry", *Japanese Journal of Applied Physics, Part 2: Letters* **37**, L1105-L1108 (1998).
- 7 R.W. Hardin, "Crystal eases blue laser production", *Photonics Spectra* (1998). Lasing Publishing Co., Inc, <http://www.lasing.com>
- 8 *Compound Semiconductor Review* **3**, July (1997), <http://www.fujitsu.co.jp/index-e.html>
- 9 S. Nakamura, "High-power InGaN-based blue laser diodes with a long lifetime", *Journal of Crystal Growth* **195**, 242-247 (1998).
- 10 S. Nakamura, "Nichia delivers blue-violet laser", July (1999). <http://www.PhotonicsNet.com>
- 11 M.V.D. Vermelho, M.T. de Araújo, A.S. Gouveia-Neto, A.S.B. Sombra, J.A. Medeiros-Neto, "Second-harmonic Generation in Pr³⁺-doped gallium-lanthanum-sulphide glasses for optical fiber amplifiers at 1.3 μm ", *Conference on Lasers and Electro-Optics Europe – Technical Digest* p. 98 Paper CtuK18 – Hamburg, Ger, Sep 8-13 (1996).
- 12 E. Hecht, and A. Zajac, Optics, (Addison-Wesley Publishing Company, Massachusetts USA 1987).
- 13 J. Webjörn, S. Siala, D.W. Nam, R.G. Waarts, and R.J. Lang, "Visible laser sources based on frequency doubling in nonlinear waveguides", *IEEE Journal of Quantum Electronics* **33**, 1673-1686 (1997).
- 14 D.N. Lee, Electromagnetic principle of integrated optics, (John Wiley&Sons, New York USA 1896).
- 15 M.V.D. Vermelho, A.M. Reis, E.A. Gouveia, M.L. Lyra, A.S. Gouveia-Neto, "Efficient frequency upconversion of 1.319 μm radiation into intense yellow light at 580 nm in pure SiO₂- core monomode fiber", *Optics Letters* **18**, 1496-

- 1498 (1993).
- 16 C.L. Pope, B.R. Reddy, and S.K.N. Stevenson, "Efficient violet upconversion signal from a fluoride fiber doped with erbium", *Optics Letters* **22**, 295-297 (1997).
 - 17 G.S. Maciel, L.S. Menezes, and C.B. de Araújo, "Violet and blue light amplification in Nd³⁺-doped fluorindate glasses", *Journal of Applied Physics* **85**, 6782-6785 (1999).
 - 18 A. Saïssy, B. Dussardier, G. Maze, G. Monnom, and S.A. Wade, "Blue upconversion emission in Er³⁺-doped fluoride fibre", *Optical Fiber Technology* **2**, 249-252 (1996).
 - 19 Y. Zhao, and S. Fleming, "Theory of Pr³⁺-doped fluoride fiber upconversion lasers", *IEEE Journal of Quantum Electronics* **33**, 905-915 (1997).
 - 20 S. Sanders, R.G. Waarts, D.G. Mehuys, and D.F. Welch, "Laser diode pumped 106 mW blue upconversion fiber laser", *Applied Physics Letters* **67**, 1815-1817 (1995).
 - 21 R. Paschotta, N. Moore, W.A. Clarkson, A.C. Tropper, D.C. Hanna, and G. Maze, "230 mW of blue light from a thulium-doped upconversion fiber", *IEEE Journal on Selected Topics in Quantum Electronics* **3**, 1100-1102 (1997).
 - 22 R. Bringans, Xerox Palo Alto Research Center - At the Fall MRS Meeting Special Section on Industrial Applications of GaN Diode Lasers, Boston, Dec. 1-5, 1997 - USA.
 - 23 X.Y. Zhang, H.Z. Chen, and M. Wang, "Recent trends and developments of organic composite photoconductive materials and devices", *Progress In Natural Science* **9**, 241-247 (1999).
 - 24 F. Yokogawa, S. Ohsawa, T. Iida, Y. Araki, K. Yamamoto, and Y. Moriyama, "The path from a digital versatile disc (DVD) using red laser to a DVD using blue laser", *Japanese Journal of Applied Physics: Part 1* **37**, 2176-2178 (1998).
 - 25 J.M. Bruneau, B. Bechevet, and C. Germain, "Optical design for a double level rewritable phase change disc", *Japanese Journal of Applied Physics: Part 1* **37**, 2168-2175 (1998).
 - 26 A. Iwamoto, Toshiba Multimedia Laboratory - At the Fall MRS Meeting Special Section on Industrial Applications of GaN Diode Lasers, Boston, Dec. 1-5, 1997 - USA.
 - 27 R. Melcher, IBM Watson Research Laboratory At the Fall MRS Meeting Special Section on Industrial Applications of GaN Diode Lasers, Boston, Dec. 1-5, 1997 - USA.
 - 28 C. Chinnock, "Blue Laser, Bright Future", *Byte – Byte Magazine WebSite* Aug. 1995.
 - 29 A. Himeno, K. Kato, and T. Miya, "Silica-based planar lightwave circuits", *IEEE Journal of Selected Topics in Quantum Electronics* **4**, 913-924 (1998).
 - 30 K. Hattori, T. Katigawa, M. Oguma, Y. Ohmori, and M. Horigushi, "*Electronics Letters* **30**, 856-857 (1994).

Chapter 2 - Overview of Rare-Earth Doped Glass

2.1 Introduction

Glass is an excellent linear optical material, being isotropic, highly transparent over large spectral ranges at low light levels, and producible with high optical quality in bulk, fibre and planar waveguide form. Macroscopically, glasses appear homogeneous, thus every atom is a suitable reference point to any other. However, order is displayed over short ranges at the local level [1]. The glass lattice can be formed by single atoms, e.g. SiO₂ glass, however, far more important are the network former groups of atoms [2-5]. In order to obtain photoluminescent devices, such as solid state lasers and amplifiers, several glass matrices have been used as a host to incorporate rare earth ions, such as chalcogenide [6], telluride [7], fluoride [8-10], and silicate glasses [11,12], to mention a few.

Among them, fluoride and chalcogenide glasses, due to their low phonon energy, have been largely used as hosts to incorporate rare earth ions for active devices.

Although silica-based oxide glasses have been shown to be adequate to fabricate standard telecommunications optical fibre, with low loss at 1.55 μm and 1.32 μm , they have poor qualities to incorporate rare earth ion, as will be discussed later. However, these glasses have shown great flexibility for the fabrication of passive and active devices in planar lightwave circuits (PLC).

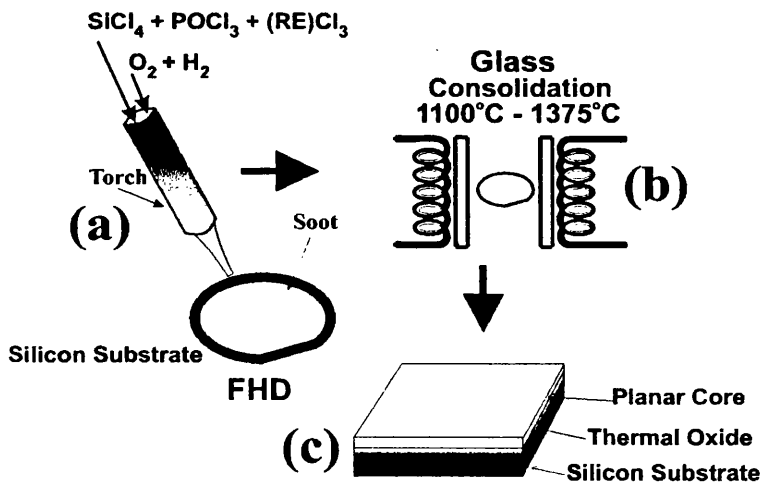
For the reasons described in the previous chapter, this thesis work will carry out investigations using oxide glasses as host material, the $\text{SiO}_2\text{-P}_2\text{O}_5$ glass system fabricated by Flame Hydrolysis Deposition (FHD), to incorporate rare earth ions to make active devices. Before presenting the results of the investigations, this chapter will outline background information supporting them. It will begin with a brief overview on the FHD method, followed by a short review on some spectroscopic characteristics information of rare-earth doped glasses which are relevant to understanding future chapters. This review does not intend to be a comprehensive survey of theoretical and experimental results on glasses and/or their spectroscopic characteristics, rather it will reflect only some applicable properties which are peculiar to glass as a laser and amplifier host.

2.2 The Glass Fabrication Process: The Flame Hydrolysis Deposition

Deposition

Planar lightwave circuits (PLCs)¹ are composed of optical waveguides collected together on a planar silicon substrate. Beside the very low propagation loss already obtained in this planar form fabricated by FHD, another noteworthy characteristic in comparison to other waveguides is the high degree of compatibility with silica fibres. Waveguides parameters, such as core dimensions and refractive index, are comparable to those of single mode fibres. Thus, the coupling losses between waveguide and fibre is extremely low, and since the refractive indices are very close, it is possible to keep the reflection effects at the connection facets down to negligible levels.

The process for manufacturing silica based PLCs can be broadly divided into: formation of a silica-based glass on the silicon wafer, this stage consists of the flame hydrolysis deposition and the soot consolidation (glass sintering) steps. For example, fine patterning, in which a waveguide pattern is formed using reactive ion etching (RIE), a cladding process in which the core is covered with a second, low index, film.

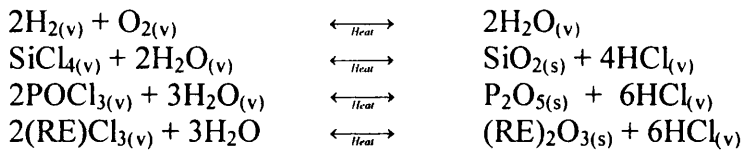


Silica-Based Film Formation

Figure 2.1: Flame Hydrolysis Deposition (FHD) process.

¹ In this work, only PLC fabricated by FHD will be considered.

Figure 2.1 depicts the first part of this silica-based film formation process. Initially, fine particles of silica-based soot are deposited on a silicon substrate by a flame hydrolysis reaction initiated by an oxyhydrogen torch, Figure 2.1(a). The basic chemical reactions involved in phosphosilicate glasses fabrications are:



The (RE) stands for the trivalent rare earth ions. The fine particles of soot of $\text{SiO}_2(\text{s}) + \text{P}_2\text{O}_5(\text{s}) + (\text{RE})_2\text{O}_3(\text{s})$ deposited on the top of the substrate are sintered at high temperature (1100°C-1375°C) in an electrical furnace to complete the transparent consolidation, Figure 2.1(b). As will be explained later in this chapter, phosphorus is added into the glass matrix to decrease the sintering temperature and to increase the core refractive index to allow optical confinement. In addition, it also increases the solubility of rare earth ions in silica-based glass avoiding clustering formation. This first stage of the fabrication process finishes with the formation of a layer of phosphosilicate glass film on the top of a thermal oxide layer on a silicon substrate, which forms the basis of a three-dimensional waveguide structure, Figure 2.1(c).

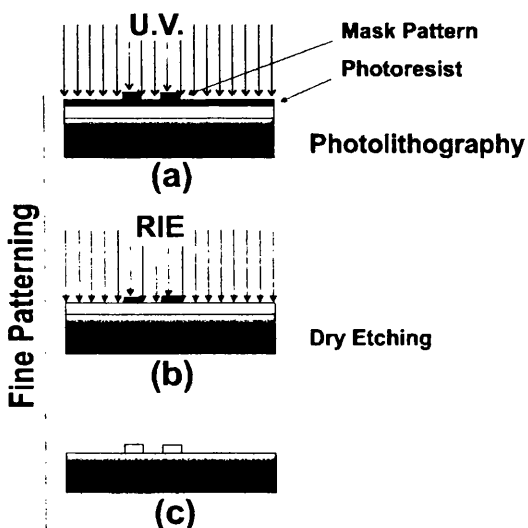


Figure 2.2: Fine patterning process

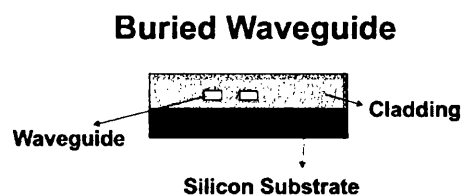


Figure 2.3: Second stage of waveguide fabrication.

The second phase of the waveguide fabrication process is related to the fine

patterning. This patterning process consists of a photolithography step, when the waveguide pattern is transferred to the planar core (Figure 2.1(c)) , and a dry etching step, in which the pattern is transferred into the glass film.

The fine patterning process can be described as follows: during the photolithography process (Figure 2.2(a)), a photosensitive polymer (photoresist) film is applied to the planar waveguide core to be patterned, and then exposed to ultraviolet light through a photomask in which the required geometrical patterns are defined. Depending on the type of photoresist used (positive or negative), exposed or non-exposed areas of photoresist are removed during the developing process. Figure 2.2(b) represents the reactive ion etching (RIE) process. It shows how the pattern transferred by photolithography is then etched into ridge waveguides. The point requiring the most attention in waveguide etching is the roughness and perpendicularity of the sides of the ridge structure. The waveguide pattern is then transferred and the core is defined, as shown in Figure 2.2(c).

Finally, the etched waveguide pattern as depicted in the Figure 2.2(c), which will form the core, is buried in the upper cladding as shown in Figure 2.3. The technique is identical to that used to produce the core film. FHD is carried out on the upper cladding to attain the same refractive index as that of the thermal oxide underneath the core, and this is followed by consolidation.

The FHD process described in this section stressed the phosphosilicate glass fabrication. However, the deposition procedure for other silica-based glasses is similar to the one presented in this section. A comprehensive description of the Flame Hydrolysis fabrication process can be found in ref. [13]. Following this overview on the $\text{SiO}_2\text{-P}_2\text{O}_5$ glass fabrication, the next section will consider some general characteristics of the rare earth ions when incorporated into a host.

2.3 General Characteristics of Rare Earth Ions in Glasses

From the perspective of the optical and electronic properties, a remarkable characteristic of the rare earth is the shrinkage of its $4f$ eigenfunctions as the atomic number increase across the series [14]. This effect is a consequence of imperfect screening by the $4f$ electrons, leading to a higher effective nuclear charge proportional to the atomic number across the lanthanide series. As a result, the $4f$ electrons become more tightly bounded with increase in the atomic number Z .

Table 2.I: The rare earth elements showing atomic number and electronic structure. [Xe] stands for the electronic configuration of xenon. M^{3+} correspond to the trivalent rare earth configuration. * Not stable. (After Ref. [15])

Element	Atomic Number (Z)	Ionic Radii (Å)	Symbol	Neutral Electronic configuration	M^{3+}
Lanthanum	57	1.060	La	[Xe]($6s^2 5d$)	f^0
Cerium	58	1.034	Ce	[Xe]($6s^2 4f 5d$)	f^1
Praseodymium	59	1.013	Pr	[Xe]($6s^2 4f^3$)	f^2
Neodymium	60	0.995	Nd	[Xe]($6s^2 4f^4$)	f^3
Promethium	61	*	Pm	[Xe]($6s^2 4f^5$)	f^4
Samarium	62	0.964	Sm	[Xe]($6s^2 4f^6$)	f^5
Europium	63	0.950	Eu	[Xe]($6s^2 4f^7$)	f^6
Gadolinium	64	0.938	Gd	[Xe]($6s^2 4f^7 5d$)	f^7
Terbium	65	0.923	Tb	[Xe]($6s^2 4f^9$)	f^8
Dysprosium	66	0.908	Dy	[Xe]($6s^2 4f^{10}$)	f^9
Holmium	67	0.894	Ho	[Xe]($6s^2 4f^{11}$)	f^{10}
Erbium	68	0.881	Er	[Xe]($6s^2 4f^{12}$)	f^{11}
Thulium	69	0.870	Tm	[Xe]($6s^2 4f^{13}$)	f^{12}
Ytterbium	70	0.930	Yb	[Xe]($6s^2 4f^{14}$)	f^{13}
Lutetium	71	0.850	Lu	[Xe]($6s^2 4f^{14} 5d$)	f^{14}

This process is better understood by analysing the electronic structure presented in Table 2.I. All the rare earths listed have the same outer electronic structure of $4d^{10} 5p^6 6s^2$, which are filled shells. The configuration including $4d^{10} 5p^6$ corresponds to

the closed shell of the noble gas xenon [Xe]¹. The rare-earth series starts with neutral lanthanum which has the xenon structure plus $6s^2 5d$, the electrons that are added for the neutral elements that follow are found in the $4f$ shell. Only cerium (Ce), gadolinium (Gd), and Lu have a $5d$ electron. In terms of their spatial extent, the $4f$ wave functions for Lu ($Z = 57$) lie outside the xenon shell, but by neodymium (Nd, $Z = 60$) the contraction is so much that the maximum lies within the $5s^2 5p^6$ closed shells of the xenon structure. This effect is even stronger for the other rare earth ions and has important implications, since the $5s$ and $5p$ electrons shield the $4f$ electrons from the effect of the environment [14]. Therefore, they also do not contribute to the electronic spectra from the infrared to the ultraviolet region, and their interaction with the electrons of the not complete-filled shells is negligible [15].

Ionisation preferentially removes two of the $6s$ electrons and one of the $4f$ electron, or - for elements which have the $5d$ shell – the $6s$ and $5d$ electron are removed. In condensed matter, the trivalent (M^{3+}) level of ionisation is the most stable for lanthanide ions [16].

In order to better visualise the interaction between the rare-earth ions and the host, the interaction energy – or Hamiltonian H – for an individual rare earth ion can approximately be decomposed as follows:

$$H = H_{FI} + V_{ISL} + V_{EM} + V_{IDL} + V_{II} \quad (2.1)$$

This energy decomposition is possible due to the weak interference on the $4f$ electrons of the rare earths and the electrons in the other ions. In the expression (2.1), H_{FI} accounts for the energy of the rare-earth ion in complete isolation (free ion), V_{ISL} contain the static interaction of ion with the lattice, and both are responsible for the electronic structure of the rare earth. V_{IDL} correspond to the dynamic energy interaction of the ion with the host via the emission of phonons. V_{EM} treats the interaction of the ion with the electromagnetic field through the absorption and/or emission of photons. Finally, V_{II} describes the energy transfer process between rare earth ions. This term become important for highly doped glass, as will be discussed further on. The subdivision of the equation (2.1) describing these interactions

¹ [Xe] = $1s^2, 2s^2, 2p^6, 3s^2, 3p^6, 4s^2, 3d^{10}, 4p^6, 5s^2, 4d^{10}, 5p^6$

separately is helpful. However, in reality, an excited ion may relax to a lower electronic level by different routes, or a combination of them. The relaxation can be due to a combination of radiative processes, including purely electronic and phonon-assisted transitions of various multipole nature, and nonradiative processes, such as phonon emission and resonant and non-resonant energy transfer arising from ion-ion coupling.

2.4 Electronic Structure: The Ions and the Static Lattice Interaction

The first two terms in equation (2.1) give rise to the observed rare earth electronic structure as depicted in Figure 2.4. H_{FI} corresponds to the free ion energy where the appropriate wave equation is solved, e.g. in the central field approximation in which each electron is assumed to move independently in a spherically symmetric potential formed by the nucleus and the averaged potential of all other electrons. The term V_{ISL} represents a perturbation to this energy by virtue of the ion interaction with the lattice. The surrounding atoms exert a small influence on the shielded ions which can, to a good approximation, be described by an electric field – referred to as the crystal field [17]. Thus, the static effects of the host on the rare earth dopant customarily are treated by replacing the host with an effective crystal field potential at the ion site.

Equation (2.1) is only approximate, and in reality, the host affects H_{FI} . The principal mechanism is covalent bonding, the sharing of electrons between the rare earth and its ligands, which partially screens the $4f$ electrons and reduces the effective nuclear charge. This manifests itself as a rescaling of the entire energy level diagram [18]. For glasses, this translates into host-to-host shifts of up to a few percent in the separations between energy levels. More covalent glasses, such as silicates, emit and absorb at longer wavelengths, while more ionic glasses, such as fluorides, emit and absorb at shorter wavelengths. As the electrons of the $4f$ shell are only weakly affected by the ligand field of the glass the splitting and shifts relative to the free-ion level positions are very small, of the order of 100 cm^{-1} , much smaller than the level separations (of the order of 1000 cm^{-1}). The spectra of the $4f$ electrons are, therefore, essentially the same in all matrices, as far as the position is concerned, and the free-ion level scheme can be used to identify all observed spectral lines.

These absorptions and fluorescence emissions are generally weak since the transitions are between levels of the same electronic configurations and are therefore parity forbidden. However, if the impurity lies away from the centre of symmetry, the crystal field violates the selection rules. The electronic transitions relevant to solid-state lasers, observed in the infrared and visible optical spectra of the trivalent

rare earth ions, are then a consequence of transitions between $4f$ states.

In Figure 2.4 the states are labelled as Russell-Saunders coupling (LS coupling). In this scheme total orbital angular momentum L , and the spin angular momentum S are vectorially added to form the total angular momentum J , and the states are labelled $2S+1L_J$ [15].

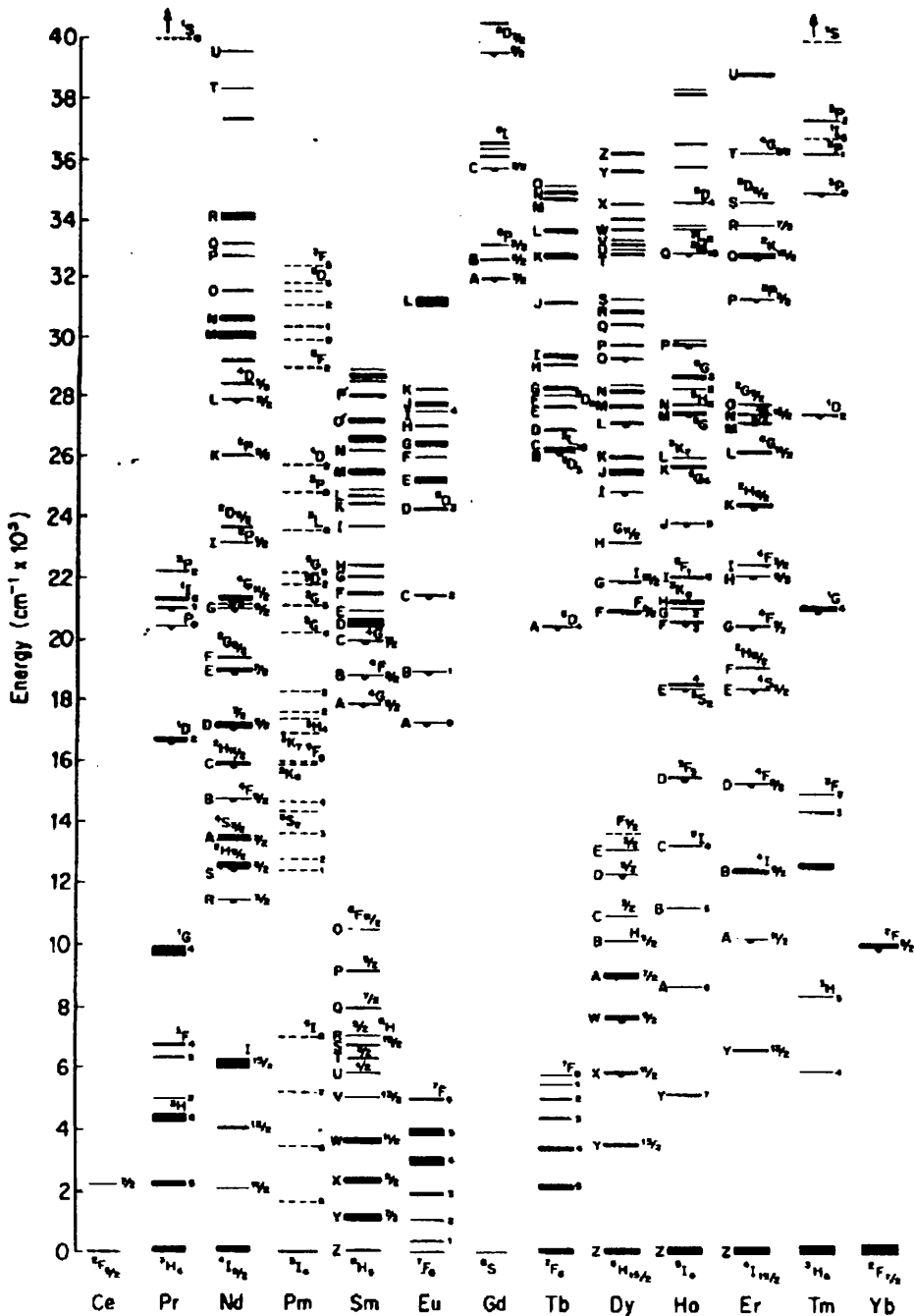


Figure 2.4: Energy levels of trivalent rare earth ions (After Ref. [18])

2.5 Radiative Transition: The Ions and the Electromagnetic Field Interaction

For luminescent devices, such as lasers and amplifiers, the most important term in equation (2.1) is V_{EM} , the interaction with the electromagnetic field, which gives rise to the emission and absorption of photons. This involves both the interaction between the electron charge and the electrical field and the interaction between the electron spin and the magnetic field. As all the transitions considered for the rare earth ions are between $4f^n$ states, and they are forbidden via electric-dipole interaction, because these transitions require change in the parity between the initial and final state [19]. However, as the ion resides in a noncentrosymmetric static or dynamic crystal field, odd harmonics in the expansion of the crystalline potential can introduce a small admixture of opposite parity states from a higher configuration, such as $4f^{n-1}5d$, into the original $4f^n$ states and thereby electric-dipole transition become allowed [20].

Theoretically the line strength $S_{a,b}$ of a transition connecting two J multiplets, a and b , is given by [21]:

$$S_{a,b} = \sum_{i,j} |\langle a, i | \hat{D} | b, j \rangle|^2 \quad (2.2)$$

where the summation is over all components of i and j of the a and b multiplets, and \hat{D} in the electric and magnetic interaction operator in the following forms:

$$\text{Electric dipole} \quad \hat{D} = \mu_{ed} = \sum_i e \hat{r}_i \quad (2.3)$$

$$\text{Magnetic dipole} \quad \hat{D} = \mu_{md} = \sum_i \frac{e}{2m} (\hat{l}_i + 2\hat{s}_i) \quad (2.4)$$

where m and e are the electron rest mass and charge, \hat{r}_i , \hat{l}_i , and \hat{s}_i are the position, orbital, and spin operator, respectively, for each electron, and the sum is over all f electrons on the ion.

In practice, the concept of oscillator strength – the number of classical oscillators equivalent to one real atom for a particular transition – is a very useful one in the context of absorption, emission, dispersion and scattering of radiation [21]. It is

defined by the relation:

$$\mathcal{N} = N_a f_{a,b} \quad (2.5)$$

where N_a is the density of atoms (or molecules) in the initial state and \mathcal{N} is the number of equivalent classical oscillator. $f_{a,b}$ is a dimensionless quantity related to the line strength $S_{a,b}$, and therefore it enters the absorption characteristic through the relation [21]:

$$\int_{line} k_\nu d\nu = \frac{\pi e^2}{mc} N_o f_{a,b} = \frac{8\pi^3 e^2}{h\lambda} \cdot \chi \cdot S_{a,b} \quad (2.6)$$

where:

k_ν is the absorption coefficient of the respective band (cm^{-1});

c is the velocity of light, and h is Planck's constants;

m and e are the rest mass and electrical charge of the electron, respectively;

the local field correction χ is assumed as $\chi_{ed} = (n^2 + 2)^2/9n$ for a electric dipole transition, and as $\chi_{md} = n$ for a magnetic dipole transitions;

N_o is the total number of active ions per unit of volume and;

$n = n(\lambda)$ is the index of refraction of the bulk isotropic dielectric medium at the mean wavelength λ of the transition;

$S_{a,b}$ and $f_{a,b}$ are the line strength and oscillator strength for a transition between initial state a and final state b , respectively.

2.5.1 The McCumber's Theory

The parameters accounting for the efficiency of these electromagnetic interactions with the rare earth ions are the absorption and emission cross-sections. Therefore, the absorption and emission spectra of the rare earth are the signatures of the energy states of the $4f$ inner electrons [22]. Glass composition has a pronounced effect on the value of the absorption and stimulated emission cross-section and the shape of

these bands, factors which play important role in determining the performance of rare earth doped lasers and amplifiers. The host has the least influence on the electronic structure and changes the relative positions of the Stark levels only slightly [23]. However, a specific rare earth transition line can have a slightly different spectrum shape due to change of hosts. This is a consequence of homogeneous broadening due to dephasing processes [24]. Furthermore, when individual dopant ions occupy very dissimilar sites in the glass, they experience different potential interactions. This disorder leads to a distribution of energies for a given Stark level component which produces inhomogeneous broadening of the emission and absorption spectra [25].

Despite the number of standard methods used to determine the rare earth cross sections [26], only McCumber's theory [27,28], or the reciprocity method, will be described in this section. The choice of this method is due to its very accurate results, as will be shown further in this section, and mainly because it provides not only absolute cross sections but also spectral information of the specific transition as well.

The high accuracy of this model can be attributed to the easily fulfilled assumptions required by this theory. It is assumed that the probability for a nonradiative transition between the two sets of levels is negligible in a spontaneous emission lifetime, and that the time required to establishing a thermal distribution within each manifold¹ is short compared to the lifetime of that manifold. As demonstrated by McCumber [28], as a generalisation of the Einstein relations, the emission and absorption cross sections can be associated by the following relation:

$$\sigma_e(\nu) = \sigma_a(\nu) \cdot \exp\left[\frac{\epsilon - h\nu}{k_B T}\right] \quad (2.7)$$

where:

$\sigma_i(\nu)$ ($i = a$ for absorption, and $i = e$ for emission) is the cross section;

k_B is Boltzman constant;

and T is the absolute temperature.

The cross sections are scaled with respect to each other by the temperature dependent

¹ Manifold corresponds to the splitting in the configurations due to the spin-orbit interaction.

excitation potential ε , which is the net free energy required to excite one ion from the lower level to a upper state maintaining the initial dielectric temperature T . If the two levels involved are in thermal equilibrium at temperature T , the parameter accounting for the free energy can be evaluated by:

$$\left(\frac{N_1}{N_2}\right)_{eq} = \exp\left(\frac{\varepsilon}{k_B T}\right) \quad (2.8)$$

where N_i is the equilibrium population of the i th level at temperature T in the absence of pumping. From the corrected emission spectra and measured lifetimes for the upper level, the experimental stimulated emission cross section is scaled by:

$$\frac{1}{\tau_e} = 8\pi n^2 c \cdot \int \frac{\sigma_e(\lambda)}{\lambda^4} d\lambda \quad (2.9)$$

where:

τ_e is the spontaneous emission lifetime of the upper level;

n is the host refractive index;

And the absorption cross section is determined using equation (2.7).

If the position of all Stark components of the specific transitions are known, ε is calculated according to [29]:

$$\frac{N_1}{N_2} = \frac{1 + \sum_{j=2}^n \exp(-E_{1j}/k_B \cdot T)}{\exp(-E_0/k_B \cdot T) \cdot \left[1 + \sum_{j=2}^m \exp(-E_{2j}/k_B \cdot T)\right]} \quad (2.10)$$

In this expression E_0 is the separation between the lowest component of each manifold, and E_{ij} is the difference in energy between the level j and the lowest component of the level i . The electronic structure required for this equation is usually obtained only due to measurement at low temperatures.

Miniscalco *et al.* [29] have developed a simple phenomenological procedure that yields a good estimate of ε for most situations. First, the electronic structure is

simplified assuming the Stark levels, for a given manifold, are equally spaced. At room temperature there is a tendency for the population in a band to congregate in the lowest Stark level, thus, the absorption cross section shifts towards shorter wavelengths and the fluorescence spectra towards longer wavelengths. Measurements have shown the peaks of the absorption and emission spectra to be usually within 5.0 cm^{-1} (1.0 nm) of each other. Then, E_0 is taken as the average of these peaks. For this specific problem, the term half-width is postulated as the separation between the peak and the energy at which the spectrum falls to 5% of the peak. As the peak emission is identified as the transitions between the lowest component of the two manifolds, $(n-1)E_{1j}$ is used as the low-energy half-width of the room temperature emission spectrum. In a similar way, the high-energy half-width of the absorption spectrum is adopted for the width of the excited state $(m-1)E_{2j}$. Figure 2.5 depicts the accuracy of the McCumber's theory [30] with the use of the previous approximation of the spectrum and electronic structure of Er^{3+} for the ${}^4I_{13/2} \rightarrow {}^4I_{15/2}$ laser transition, calculating the absorption cross section (dashed line) from the fluorescence measurement (solid line). The inset shows the agreement between the calculated and measured absorption band at 1535 nm.

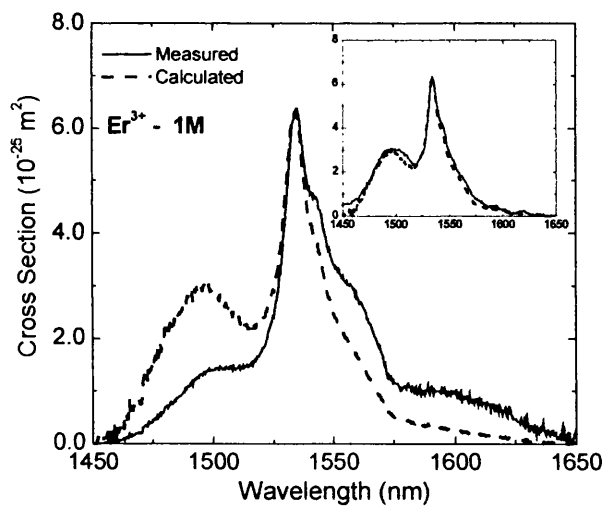


Figure 2.5: Cross section determined by McCumber theory .The inset is a comparison between the calculated absorption (dashed curve) and the experimental measurement of the absorption band.

An accurate determination of these spectrum shapes and magnitude is useful to estimate the amplified spontaneous emission (ASE) in the optical amplifier

modelling in a low signal operation regime, for instance. However, McCumber's theory does not allow one to determine, or estimate, the other important dipole-dipole interaction parameters such as the radiative transition lifetime or their branching ratios. A method to evaluate these parameters will be considered in the next section.

2.5.2 The Judd-Ofelt Theory

The Judd-Ofelt theory is widely employed to estimate non-accessible spectroscopic information relevant to rare earth doped lasers and amplifiers characterisation. This theory can be introduced considering the equation (2.2). According to the quantum mechanic theory, the line strength matrix elements $S_{a,b}$ between $4f$ states of the rare earth are identically zero since all of these states have the same parity [31]. However, as mentioned in the section 2.4, when rare earth ions are placed in crystals at sites without inversion symmetry, the odd components of the crystal field potential admix even parity states of the ion into ground configuration, and the selection rule is not obeyed anymore. Based on these considerations, Judd [32] and Ofelt [33] have demonstrated that the line strength for electric dipole transitions $S_{a,b}^{ed}$ (corresponding to the equation (2.2) with $\hat{D} = \mu_{ed}$) between an initial J manifold $|4f^n[S, L], aJ\rangle$ and a terminal J manifold $|4f^n[S', L'], bJ'\rangle$ may be written in the form²:

$$S_{a,b}^{ed} = 1/e^2 \cdot |\langle a|\hat{D}|b\rangle|^2 = \sum_{\lambda=2,4,6} \Omega_{\lambda} \cdot \left| \langle 4f^n[S, L]aJ \| U^{(\lambda)} \| 4f^n[S', L']bJ' \rangle \right|^2 \quad (2.11)$$

where the elements $\langle \| U^{(\lambda)} \| \rangle$ are the doubly reduced unit tensor operators calculated in the intermediate-coupling approximation. Since these tensor elements are virtually constant irrespective of ion environment, they can be used in the intensity computations for the ions of interest for laser applications. The spin and angular momentum quantum numbers, S and L , are used to label intermediate coupling states as described in the section 2.4. The three coefficients Ω_2 , Ω_4 , and Ω_6

² Following the literature, all physical constants and expressions shown in the section 2.5.2 are in the CGS unit system.

contain implicitly the odd crystal field terms, radial integrals, and the perturbation energy denominators. These quantities, which are independent of the state variable within the $4f^n$ configuration, may be regarded as phenomenological parameter characterising the radiative transition probabilities within the $4f^n$ configuration [34].

Due to Judd and Ofelt, the integrated absorption coefficient – equation (2.6) – for electric and magnetic dipole transitions within the shielded $4f^n$ ground electronic configuration, taking into consideration the rare earth ion embedded in a crystalline lattice, may be written as [34]:

$$\int_0^{\infty} k_{\nu} d\nu = N_0 \frac{8\pi^3 \cdot \bar{\lambda}}{3ch(2J+1)} \cdot [\chi_{ed} \cdot S_{a,b}^{ed} + \chi_{md} \cdot S_{a,b}^{md}] \quad (2.12)$$

where $\bar{\lambda}$ is the mean wavelength of the absorption band. The selection rules for the electric dipole contribution $S_{a,b}^{ed}$, defined by equation (2.11), arising from the f configuration mixing include: $\Delta l = \pm 1$, $\Delta S = 0$, $|\Delta L|$, $|\Delta J| \leq 6$. However, the magnetic dipole transitions are parity allowed between states of f^n and subject to the selection rules $\Delta S = \Delta L = 0$, $\Delta J = 0, \pm 1$ (but not $0 \rightarrow 0$ transitions) [20]. Its contribution ($S_{a,b}^{md}$ with $\hat{D} = \mu_{md}$) to the equation (2.12) is given by:

$$S_{a,b}^{md} = 1/e^2 \cdot |\langle a || \hat{D}_{md} || b \rangle|^2 = \left(\frac{h}{4\pi mc} \right)^2 \cdot |\langle 4f^n [S, L] a J || \hat{L} + 2\hat{S} || 4f^n [S', L'] b J' \rangle|^2 \quad (2.13)$$

There is some magnetic dipole character only in a few transitions among the rare earths; the induced electric dipole mechanism is dominant for the intensities of most lanthanide absorption bands [35]. Electric quadrupole transitions are also parity allowed between states of f^n with the selection rules $\Delta S = 0$, $|\Delta L|$, $|\Delta J| < 2$. However, its contribution to the oscillator strength is usually estimated to be more than three orders of magnitude smaller than the measured value, and therefore electric quadrupole transitions can be considered insignificant for the whole process [20].

There is no clear physical meaning to the phenomenological intensity parameters Ω_{λ} ($\lambda = 2, 4$, and 6). However, based on experimental observations, the parameter Ω_2 has been shown correlation with the degree of covalence between the rare earth ion

and the host: i.e. ionic materials like fluorides have very small value of Ω_2 , while covalent materials like silicates have large values. Generally, Ω_4 and Ω_6 have been shown relation with the viscosity of the medium, i.e. the most dense the material the higher the value of the parameter [20,36].

According to the theory, the best set of Judd-Ofelt intensity parameters, Ω_λ , are determined for a specific glass from a least-squares fit to the values of the measured integrated absorption coefficients. The determination of this set of parameters for a specific host, make possible the evaluation of the spectroscopic information of a specific rare earth level, as far as the reduced matrix element of the referred rare earth transition levels are known. To determine the radiative transition probabilities for emission between excited J manifold rare earth ions in glasses, using the previous Ω_λ determined parameters and the correspondent doubly reduced unit tensor operators $\langle \|U^{(\lambda)}\| \rangle$ for the specific transition, by:

$$A_{a,b} = \frac{64\pi^4 e^2}{3h(2J+1)\lambda^3} \cdot [\chi_{ed} \cdot S_{a,b}^{ed} + \chi_{md} \cdot S_{a,b}^{md}] \quad (2.14)$$

which is related to the radiative lifetime, τ_a , of the excited state by:

$$\frac{1}{\tau_a} = \sum_b A_{a,b} = A_a \quad (2.15)$$

where the summation is over the electric dipole transitions to all terminal state b , and the luminescent branching ratio is given by:

$$\beta_{a,b} = \frac{A_{a,b}}{A_a} = \tau_a \cdot A_{a,b} \quad (2.16)$$

For lasers and amplifiers analysis of rare earth materials the integrated absorption cross section, $\sigma_{a,b}(\lambda_p)$, for stimulated emission is estimated from the equation:

$$\sigma_{a,b}(\lambda_p) = \frac{\lambda_p^4}{8\pi \cdot c \cdot n^2 \cdot \Delta\lambda_{eff}} A_{a,b} \quad (2.17)$$

where λ_p is the peak fluorescence wavelength of the emission band, and $\Delta\lambda_{eff}$ is the effective fluorescence bandwidth determined by dividing the integrated fluorescence

line shape by the intensity at λ_p .

In this section, the Judd-Ofelt formulation of crystal field induced electric and magnetic dipole transition in $4f^n$ configurations was summarised. The validity of the model has received ample experimental verification with computed emission and absorption intensities generally accurate to within 10-15% [29].

2.6 Nonradiative Transition: The Ions and the Dynamic Lattice Interaction

Excited electronic states of rare-earth ions in solids can also decay nonradiatively by exciting lattice vibrations. Considering low rare-earth concentrations, in order that ion-ion energy transfer can be neglected, the nonradiative interaction is accounted by the ion-dynamic lattice energy potential (V_{IDL}). The physical process which makes phonon emission possible is a consequence of the rare earth incorporated in the glass matrix has oxygen or other ions as a nearest neighbour. The vibration of these and distant ions contribute to the fluctuating Stark field which induces nonradiative transitions. Because of the different vibrational spectra, the rate of phonon process is host dependent. When the energy gap between the excited state and the next lowest state is larger than the maximum phonon energy in the material, the emission of several phonons is required to conserve energy. For higher order processes (≥ 3 phonons), the decay rate is determined predominantly by the number of phonons required to bridge the energy gap.

Layne and co-workers [37] have derived an expression for the determination of the nonradiative relaxations accounting both for the exponential dependence of multiphonon relaxation rate on the energy gap across which the decay takes place and for the explicit temperature dependence. According to their theory, the rate for a p -order multiphonon decay is:

$$W_{a,b}^{nr} = C \cdot [n(T) + 1]^p \cdot \exp(-\alpha \cdot \Delta E) \quad (2.18)$$

In this expression

C and α are host-dependent parameters [36];

ΔE is the energy level gap;

p is the number of phonons required to bridge the gap;

and $n(T)$ is the Bose-Einstein occupation number for the effective phonon mode, given by:

$$n(T) = \frac{1}{\exp(\hbar \cdot \omega_R / k_B \cdot T) - 1} \quad (2.19)$$

Evaluation of the rate for a transition across an energy gap ΔE , accompanied by emission of p phonons, requires knowledge of the glass network vibrational frequencies (ω_R) that are excited in the decay. These frequencies can be determined from the spontaneous Raman scattering intensity measurements [38]. For each glass, the highest vibrational frequency is associated with the symmetric stretching mode of the glass network former. Oxide glasses have larger nonradiative rates, because of their strong covalent bonds which results in higher phonon frequencies. In general, glasses have much larger nonradiative rates than crystals of similar composition [39].

The process of relaxation of an excited rare earth ion can be either a radiative transition to any one to the lower lying levels, or a nonradiative transition (a cascade from one level to the next). Then the total lifetime, or the fluorescence lifetime of an excited state a is given by:

$$\frac{1}{\tau_e} = \sum_b (A_{a,b} + W_{a,b}^{nr}) \quad (2.20)$$

where $A_{a,b}$ and $W_{a,b}^{nr}$ are the radiative and nonradiative transition probabilities from level a to level b , and the summation is over all terminal levels b . Nonradiative processes include, in addition to multiphonon decay, relaxation by direct ion-ion transfer and energy migration to quenching centres when high rare-earth concentrations are present. Concentration quenching and cross relaxation due to energy transfer between ions in highly doped glass will be introduced in the next section.

The electronic states which act as upper levels for radiative transitions are called metastable levels. Metastable levels are then exclusively those that are divided by a larger gap from the nearest lower lying level reducing the probability of multiphonon relaxations. All rare earth electronic states have some finite radiative transition probability. For levels with small energy gaps to the next lower level, decay by multiphonon emission is very fast ($W_{a,b}^{nr} \gg A_{a,b}$), so fluorescence is not normally

observed. The situation can then be interpreted as a competition of both types of transitions; the nonradiative transitions have a probability that decreases strongly as the distance to the nearest level increases. When the probability of the nonradiative transition is too low, the radiative transition becomes competitive and a fluorescent emission appears. Thus, the radiative quantum efficiency of a transition $a \rightarrow b$, which correspond to the fraction of the energy of an excited state that is dissipated in the host during specific transition, is defined by:

$$\eta_{a,b} = A_{a,b} / \sum (A_{a,b} + W_{a,b}^{nr}) = \tau_a \cdot A_{a,b} \quad (2.21)$$

The contribution to be added to the nonradiative process if there is energy transfers among rare earth ions will be considered in the next section.

2.6.1 Energy Transfer Processes: The Ion-Ion Interaction

Increasing the rare earth doping level into the glass enhances the energy transfer process between ions. This effect will be responsible for an increase in the nonradiative transition probability. This process is experimentally observed by an increase in the fast decay component of the metastable levels lifetime. The interaction between rare earth ions is treated by the last term in equation (2.1) – V_{II} . From the point of view of luminescent devices, the most important manifestation of this interaction is this transfer or sharing of energy between ions. This exchange may occur among rare earth ions of the same or different species. Depending on the context, it may be either beneficial or deleterious. This section will consider all these ion-ion interaction conditions.

If there are two species of dopant ions in the matrix, one can be excited (S) and the fluorescence can be absorbed in the second (A), as depicted in the simplified energy level diagram in the Figure 2.6. As the presence of (S) makes the system sensitive to the exciting energy $h\nu_a$, this phenomenon is called *sensitisation* [15].

As depicted in Figure 2.6, the sensitiser ion system returns from the excited state S_2 to the ground state S_1 releasing its energy to bring the activator ion system from the ground state A_1 to the excited state A_2 . The transfer of energy between the sensitiser

and activator system is a purely nonradiative, i.e. no photon will appear in the system during the transfer. The radiative transition is present when the excited activator relaxed back to the ground state by an emission of a photon $h\nu_e$. This process is considered resonant transfer when the position of the energy levels of the sensitiser and activated systems has a sharp overlap.

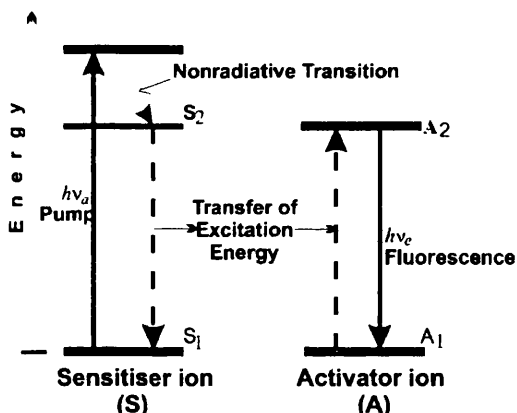


Figure 2.6: Simplified energy diagram level for resonant nonradiative energy transfer

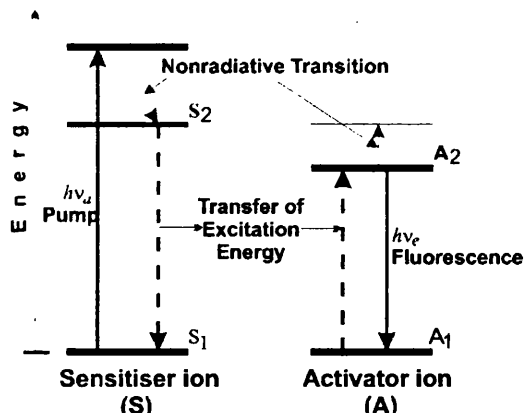


Figure 2.7: Simplified energy diagram level for non resonant nonradiative energy transfer

Energy also may be transferred as a non-resonant process. This is probably the most common to occur, because usually the energy levels which energy transfers take places does not coincide. In this situation, emission of one or more phonons is required to match the energy difference, as shown in Figure 2.7. In addition, the energy mismatch is important in driving the process in a particular direction, since energy seldom can be conserved by the electronic transition alone. Finally, the processes involving emission of phonons are much faster than the transitions requiring the absorption of photons [15].

The energy transfer processes described by Figure 2.6 and Figure 2.7 are rather general. They can be applied to analyse both situations: when activator and sensitiser ions are of the same or different species. It is also common refer to the sensitiser and activator ions as donor and acceptor ions, respectively.

Among the deleterious energy transfer processes, cooperative upconversion or cross relaxation [40] and concentration quenching [41] have been extensively studied due to the influence in the performance of the erbium doped solid state lasers and amplifiers, and neodymium solid state lasers. Cooperative upconversion, or cross

relaxation, is a process involving two excited ions, as depicted in Figure 2.8 for erbium ions. When they interact, one ion transfers energy to the other, leaving itself in the ground state and promoting the other to a higher state. The promoted ion quickly relaxes back to the previous excited state through multiphonon emission process. The net result of this process is the conversion of units of excitation into heat. Since cooperative upconversion requires two interacting ions in the excited state, it is not evident at low pumping power levels [29]. At high pumping powers, it appears as an accelerated and multi-exponential decay, the latter due to variations in the distance or interaction strength between excited ions. The pump power dependence of the upconversion mechanism has important device consequences. The process will be the most deleterious at higher population inversions, a situation usually required for amplifiers to achieve high single pass gain and good signal-to-noise ratio.

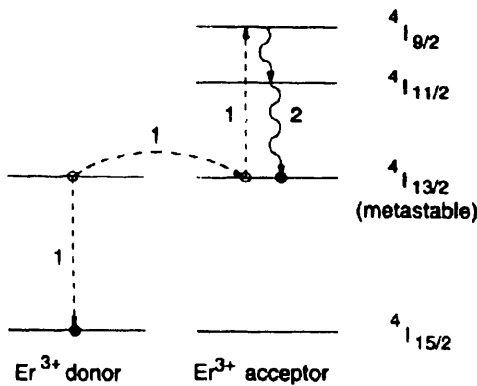


Figure 2.8: Cooperative upconversion between two erbium ions

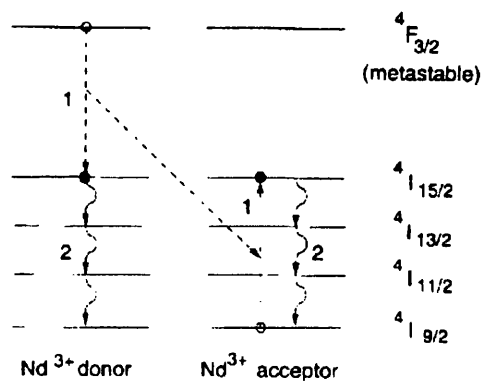


Figure 2.9: Concentration quenching for neodymium ions

Concentration quenching is shown in Figure 2.9 using Nd^{3+} as an example. This process happens if an ion excited into the metastable ${}^4F_{3/2}$ level interacts with a nearby ion in the ground state. The first ion can transfer part of its energy to the second, leaving both in the intermediate ${}^4I_{15/2}$ state. Since the energy gaps to the lower lying level are small, both ions quickly decay nonradiatively to the ground state. The net result is the conversion of the original excitation into heat in a time that is short compared to the radiative lifetime in the energy transfer rate is high. Experimentally, this quenching process manifests itself as a multi-exponential decay, which is independent of pump power, since only one excited ion is required for start

the process [41].

The beneficial use of the cooperative upconversion with two different types of ions can be used $\text{Yb}^{3+} \rightarrow \text{Er}^{3+}$ [42], or $\text{Yb}^{3+} \rightarrow \text{Tm}^{3+}$ [43] as example. In both ion systems, ytterbium ions acts as sensitiser (or donor). They are used to improve the pumping efficiency for the erbium, for the $\text{Er}^{3+}/\text{Yb}^{3+}$ pair, or creating a new possibility of pumping wavelength for the $\text{Tm}^{3+}/\text{Yb}^{3+}$ system. In addition to the large absorption band around 980 nm of the ytterbium ions; they do not undergo any deleterious energy transfer even at high concentration. It is a consequence of their simplified energy level structure. However, if the donor concentration is high enough, another mechanism that can occur is the migration of the excitation among the strongly coupled donor ions (donor-donor transfer). This transfer proceeds until the excitation reaches a donor close enough to an acceptor to complete the final step of the transfer process. This mechanism is commonly used for sensitising materials using large donor concentrations to absorb the optical excitation and transfer it to the activator or emitter when the latter has a weak or poorly placed absorption band.

A typical use for the concentration quenching as a beneficial process is the utilization of the Tb^{3+} ions to quench the $\text{Tm}^{3+} {}^3\text{H}_4$ level. The blue laser action in the thulium ions between the ${}^1\text{D}_2 \rightarrow {}^3\text{H}_4$ energy levels is rarely achieved because the lower level has a lifetime about two orders of magnitude longer than the upper. Thus, the thulium lower level is emptied faster transferring its energy to nearby Tb^{3+} [44]. There are several ions system reporting this energy transfer process with similar purpose, such as $\text{Er}^{3+} \rightarrow \text{Pr}^{3+}$, and $\text{Ho}^{3+} \rightarrow \text{Pr}^{3+}$ [45].

The comprehension of the physical effects involving energy transfer is an active research field. At large rare earth concentrations, with approximately uniformly distributed excitation of the metastable level, the pump loss is partly explained by energy transfer between two excited rare earth ions, resulting in a homogeneous upconversion process. Moreover, rare earth ions can also form pairs and large clusters, in which a rapid energy transfer leads to a fast decay and inhomogeneous upconversion [46]. For pair clusters, this effect is often called pair-induced quenching. Depending on the details of the fabrication process, clusters may be present even at low concentrations, when homogeneous upconversion is negligible.

Experimental results have shown that the energy transfer rates in the ion-ion interaction increase linearly with the doping concentration (or the inverse-distance between the ions) [47,48]. The threshold at which the upconversion process cannot be ignored can be estimated by considering the relationship between optical amplification and the microscopic structural properties of the material. The expression for the electric dipole-dipole energy transfer probability between donors and acceptor is given by the Foster-Dexter model [49]:

$$P_{da} = \frac{1}{\tau_d} \frac{3h^4 c^4}{4\pi \cdot n^4} \left(\frac{1}{R_{da}} \right)^6 \cdot \sigma_d \cdot \int \frac{f_d(E) \cdot F_a(E)}{E^4} dE \quad (2.22)$$

where:

τ_d is the radiative lifetime of the donor;

n is the host refractive index;

σ_d is the donor absorption cross section;

R_{da} is the donor-acceptor separation;

$F_a(E)$ and $f_d(E)$ are the normalised lineshape functions for the donor emission and acceptor absorption;

h and c are the Planck constant and velocity of light respectively.

The equation above can be simplified defining a critical interaction distance R_o :

$$P_{da} = \frac{1}{\tau_d} \left(\frac{R_o}{R_{da}} \right)^6 \quad (2.23)$$

where R_o incorporates all remaining parameters except τ_d and R_{da} . This implies that two ions at a distance R_o will transfer the excitations energy at a rate of one per second. To reduce the energy transfer effect, the excitation rate $P_{da} \cdot \tau_d$ must be maintained smaller than the fluorescent lifetime τ_e as expressed by equation (2.20).

2.7 Rare Earth Doped Glass: Al³⁺ Co-Doping Influence

The main glasses, or network formers, fabricated by Flame Hydrolysis Deposition are SiO₂ doped with P₂O₅ or GeO₂ to increase the refractive index and allow optical confinement. The simplest glass structure, and the base for all glasses considered in this work, the vitreous silica SiO₂, is formed by one atom of silicon in the centre of four oxygen ions in a form of a tetrahedron. Its dimensions are considered constant in most glasses, and the typical dimensions, as show in Figure 2.10, are [15]:

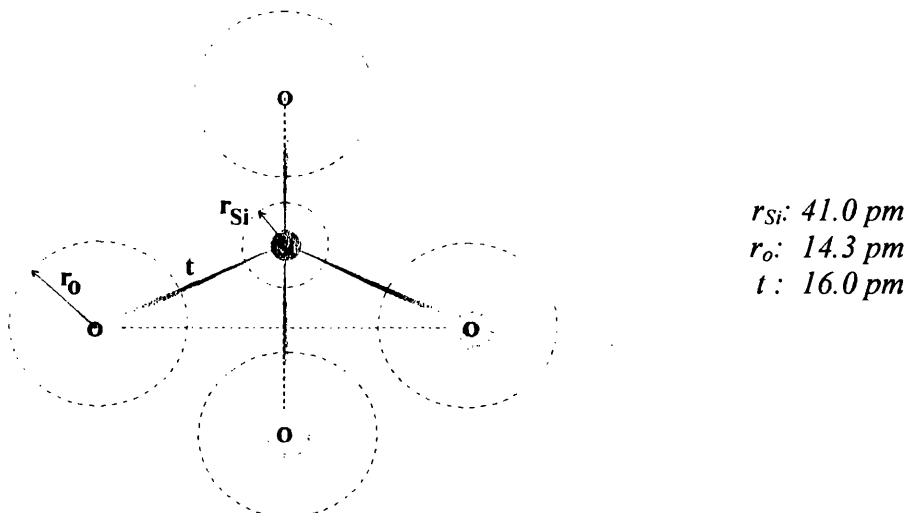


Figure 2.10: The (SiO₄)²⁻ tetrahedron and its typical dimensions.

When germanium and/or phosphorus are added to the matrix glass in order to increase the refractive index, for example, they tend to substitute the silicon ions in the matrix as network formers. As germanium has the same valence 4 as silicon, its addition to a glass does not change its characteristics very much. The glass retains its tetrahedral structure and the properties are similar to fused silica glass alone, as shown in Figure 2.11.

Pure silica or germanium-doped silica glasses can incorporate only very small amounts of rare earth ions before microscopic clustering occurs and ion-ion interaction appears [51]. Arai *et al.* have explained this phenomenon with a structural model [52]: when rare earths are incorporated into glasses, they do so as network modifiers. Due to their large ionic radii and low field strength, they tend to break up the covalently bonded glass structure. Since most of the rare earth ions are incorporated in the trivalent state, there must be charge compensation within the

network from the oxygen atoms which are now non-bridging. If the concentration of rare earth is very low, then the ions will be in an isolated site and there will be little or no effect from other rare earth ions. As concentration is increased, the absence of a sufficient number of nonbridging oxygen to co-ordinate isolated rare earth ions in the silica network causes them to cluster in order to share nonbridging oxygen.

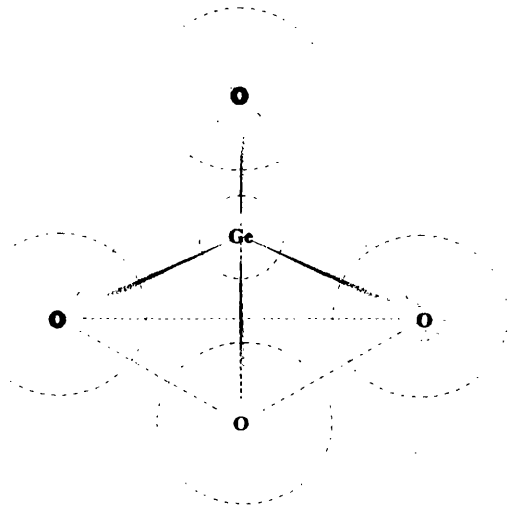


Figure 2.11: Germanium ion substituting Si ion in the tetrahedron

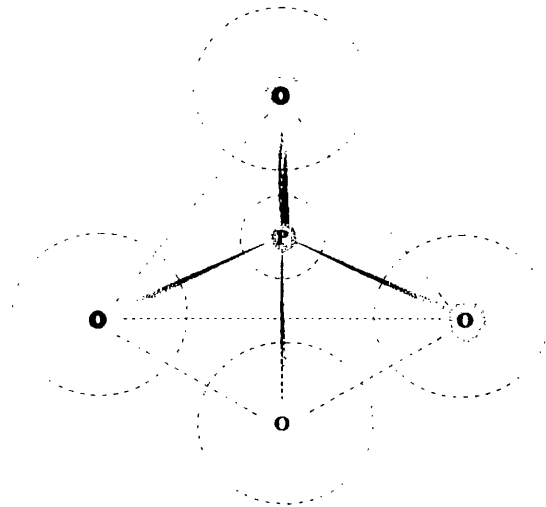


Figure 2.12: Phosphorus ion substituting Si ion in the tetrahedron

In order to incorporate higher rare earth concentration into silica-based glasses avoiding, or at least reducing, clustering formation, phosphorus or aluminium, or a combination of both, are added to the network. The phosphosilicate glass network, as SiO_2 system, is also based on tetrahedral form, with four oxygen atoms being bonded to each phosphorus atom. However, since phosphorus is pentavalent, one oxygen ion has a double bond to the phosphorus, Figure 2.12. This reduces to three the number of tetrahedra that can bond to any selected tetrahedron, leaving one oxygen ion unbounded [50]. Thus, the unbounded oxygen becomes the phosphosilicate glass system ($\text{P}_2\text{O}_5\text{-SiO}_2$) suitable to incorporate rare earth ions in a higher concentration than in pure silica without clustering formation. Furthermore, phosphosilicate glass is considered less dense than fused silica. The viscosity of silica is very effectively lowered by small additions of phosphorus to the network.

The influence of the Al_2O_3 on Nd^{3+} fluorescence in SiO_2 glass system, in the terminology of solution chemistry, was explained by Arai *et al.* as follows: in the liquid state, Al_2O_3 dissolves well in SiO_2 and Nd_2O_3 also dissolves in Al_2O_3 without

liquid immiscibility. Therefore, $\text{AlO}_{4/2}$ and/or $\text{AlO}_{6/2}$ act as solvation shells to make Nd^{3+} ions soluble in SiO_2 network. The results by Nogami *et al.* [53], based on nuclear magnetic resonance spectroscopy measurements of Al^{3+} ions in Sm_2O_3 - Al_2O_3 - SiO_2 glass system, corroborate with Arai, and they have concluded that the Al^{3+} ions preferentially form AlO_6 octahedral and the charge of the Sm^{3+} ions are compensated by the oxygen in the AlO_6 group. These results confirm the increase of the dispersion of Sm^{3+} ions in the network glass structure by the addition of Al^{3+} and explain the increasing of the fluorescence intensity observed.

The major role of P_2O_5 into SiO_2 glass in preventing rare earth clustering is not clear. Experimental evidence only shows that adding phosphorus to the SiO_2 glass system in a ratio of P-to-Nd of approximately 15, the spectroscopic changes and solubility of the rare earth are similar to those found for aluminium doping. For the GeO_2 - SiO_2 glass system, the ratio P-to-Nd is one order of magnitude larger than the than the phosphosilicate glass alone to prevent clustering. Phosphorus doping level of less than 1.0 mol% offers no improvement over the Ge doped silica glass and Er^{3+} or Nd^{3+} [16] concentration below 10^{18} cm^{-3} are still required to prevent quenching.

2.8 Summary

This chapter has concentrated on the introduction of some background information supporting the research developed.

Initially, a summary of the Flame Hydrolysis Deposition (FHD) and the rare earth doped waveguide fabrication were presented in the section 2.2.

An introduction to general characteristics of the rare earth ions in glasses was investigated considering the interaction energy between the rare earth ion and the host subdivided in several contributions. Section 2.4 concentrated on the contribution due to the ion and the static lattice, which originates in the electronic structure of the rare earth. Section 2.5 was devoted to an explanation of the interaction of ions and the electromagnetic radiation. Due to the importance of this interaction for the photoluminescent devices, two well-established theories were described for the determination of some relevant spectroscopic information for the characterisation of photoluminescent devices. The McCumber's theory has been used as a powerful tool to determine transition cross sections, and the Judd-Ofelt theory, useful to evaluate non-accessible spectroscopic information, were presented in the section 2.5.1 and 2.5.2, respectively. The choice of these two theories was based on the experimental facilities available to develop the research.

Section 2.6 was devoted to the nonradiative relaxations, attempting to focus on procedures do determine its influence in the present glass system. In this section, ion-ion interaction and its contribution to the nonradiative relaxation process was also considered.

Finally, the section 2.7 introduced some considerations on the aluminium and phosphorus co-doping influence in the solubility of rare earth ions into oxide glasses.

2.9 References

- 1 A. C. Wright, "How much do we really know about the structure of amorphous solids?", *Journal of Non-Crystalline Solids* **75**, 15-27 (1985)
- 2 A. Richter, B. Straube, and W. Pompe, "Structural changes in glasses in the context of cluster analysis", *Journal of Non-Crystalline Solids* **74**, 147-160 (1985)
- 3 J. Jäckle, "Models of the glass transition", *Report on Progress in Physics* **49**, 171-231 (1986)
- 4 C. Tarrío, and S.E. Schnatterly, "Optical properties of silicon and its oxides", *Journal of the Optical Society of America B* **10**, 952-957 (1993)
- 5 P.J. Bray, "Structural models for borate glasses", *Journal of Non-Crystalline Solids* **75**, 29-36 (1985)
- 6 C.C. Ye, M. Hempstead, D.W. Hewak, and D.N. Payne, "Proposal for an Er³⁺-doped chalcogenide glass fiber upconversion laser operating at 980 nm and pumped at 1480 nm", *IEEE Photonics Technology Letters* **9**, 1104-1106 (1997)
- 7 J.S. Wang, E.M. Vogel, and E. Snitzer, "Tellurite glass: a new candidate for fiber devices", *Optical Materials* **3**, 187-203 (1994)
- 8 J.Y. Allain, M. Monerie, H. Poignant, and T. Georges, "High-efficiency ytterbium-doped fluoride fibre laser", *Journal of Non-Crystalline Solids* **161**, 270-273 (1993)
- 9 L. Samek, J. Wasylak, and K. Marczych, "Optical properties of fluorozirconate glasses activated with rare earth elements", *Journal of Non-Crystalline Solids* **140**, 243-248 (1992)
- 10 J.Y. Allain, M. Monerie, and H. Poignant, "Blue upconversion fluorozirconate fibre laser", *Electronics Letters* **26**, 166-168 (1990)
- 11 E. Snitzer, "Glass Lasers", *Applied Optics* **5**, 1487-1499 (1966)
- 12 K. Oh, T.F. Morse, A. Kilian, L. Reinhart, and P.M. Weber, "Continuous-wave oscillation of thulium-sensitized holmium-doped silica fiber laser", *Optics Letters* **19**, 278-280 (1994)
- 13 G. Barbarossa, "Planar silica optical devices technology", Ph.D. Thesis, University of Glasgow, (1992)
- 14 M.G. Mayer, "Rare-earth transuranic elements", *Physical Review* **60**, 184-187 (1941).
- 15 K. Pátek, *Glass Lasers*, Chapter 5, London Iliffe Books (1977)
- 16 J. Wang, W.S. Brocklesby, J.R. Lincoln, J.E. Townsend, and D.N. Payne, "Local structure of rare-earth ions in glasses: the 'crystal-chemistry' approach", *Journal of Non-Crystalline Solids* **163**, 261-267 (1993).
- 17 R.J. Elliot and A.F. Gibson, An Introduction to Solid State Physics and its applications, (The Macmillan Press Ltd, London UK 1982).

- 18 G.H. Diecke and H.M. Crosswhite, "The spectra of the doubly and triply ionized rare earths" *Applied Optics* **2**, 675-686 (1963).
- 19 D. Park, The introduction to the quantum theory, (McGraw-Hill Inc. New York USA 1992).
- 20 M. J. Weber, "Probabilities for radiative and nonradiative decay of Er^{3+} in LaF_3 ", *Physical Review* **157**, 262-272 (1967).
- 21 A.P. Thorne, Spectrophysics, (Chapman and Hall, London UK 1988).
- 22 B.J. Ainslie, S.P. Craig, and S.T. Davey, "The absorption and fluorescence spectra rare earth ions in silica-based monomode fiber", *IEEE Journal of Lightwave Technology* **6**, 287-292 (1988).
- 23 R. Wyatt, "Spectroscopy of rare earth doped fibres", Ed. P.W. France, Optical fibre lasers and amplifiers, (Boca Raton, Florida USA 1991).
- 24 S. Zenon, G. Lambert, W.J. Miniscalco, and B.A. Thompson, "Homogeneous linewidth in Er^{3+} -doped glass measured by resonance fluorescence", *SPIE - Fiber Laser Sources and Amplifiers III* **1581**, 91-100 (1991).
- 25 J.T. Verdeyen, Laser Electronics, (Englewood Cliffs, New Jersey USA 1981)
- 26 W.L. Barnes, R.I. Laming, E.J. Tarbox, and P.R. Morkel, "Absorption and emission cross section of Er^{3+} doped silica fibers", *IEEE Journal of Quantum Electronics* **27**, 1004-1010 (1991).
- 27 D.E. McCumber, "Theory of phonon-terminated optical masers", *Physical Review* **134**, A299-A306 (1964).
- 28 D.E. McCumber, "Einstein relations connecting broadband emission and absorption spectra", *Physical Review* **134**, A954-A957 (1964).
- 29 W.J. Miniscalco, and R.S. Quimby, "General procedure for the analysis of Er^{3+} cross sections", *Optics Letters* **16**, 258-260 (1991).
- 30 J.R. Bonar, M.V.D. Vermelho, P.V.S. Marques, A.J. McLaughlin, and J.S. Aitchison, "Fluorescence lifetime measurements of aerosol doped erbium in phosphosilicate planar waveguides," *Optics Communications* **149**, 27-32 (1998)
- 31 W.F. Krupke, "Optical absorption and fluorescence intensities in several rare-earth-doped Y_2O_3 and LaF_3 single crystal", *Physical review* **145**, 325-337 (1966).
- 32 B.R. Judd, "Optical absorption intensities of rare-earth ions", *Physical Review* **127**, 750-761 (1962).
- 33 G.S. Ofelt, "Intensities of crystal spectra of rare earth ions", *The Journal of Chemical Physics* **37**, 511-520 (1962).
- 34 W.F. Krupke, "Induced-emission cross sections in Neodymium laser glass", *IEEE Journal of Quantum Electronics* **QE-10**, 450-457 (1974).
- 35 W.T. Carnall, "The absorption and fluorescence spectra of rare earth ions in solution", Ed. K.A. Gschneider, Jr. And L. Eyring, Handbook on the Physics and Chemistry of rare earths, Chapter 24, North-Holland Publishing Company pp. 171-208 (1979).

- 36 R. Reisfeld, "Fluorescence and nonradiative relaxations of rare earths in amorphous media and on high surface area supports: A review", *Journal of the Electrochemical Society* **131**, 1360-1364 (1984).
- 37 C.B. Layne, W.H. Lowdermilk, and M.J. Weber, "Multiphonon relaxation of rare-earth ions in oxide glasses", *Physical Review B* **16**, 10-20 (1977).
- 38 R.H. Stolen, E.P. Ippen, and A.R. Tynes, " Raman oscillation in glass optical waveguide", *Applied Physics Letters* **20**, 62-64 (1972).
- 39 F.L. Galeaner, J.C. Mikkelsen, Jr. R.H. Geils, and W.J. Mosby, " The relative raman cross sections of vitreous SiO₂, GeO₂, B₂O₃, and P₂O₅", *Applied Physics Letters* **32**, 34-36 (1978).
- 40 E. Snoeks, G.N. van den Hoven, A. Polman, B. Hendriksen, M.B.J. Diemeer, and F. Priolo, "Cooperative upconversion in erbium-implanted soda-lime silicate glass optical waveguides", *Journal of the Society of America B* **12**, 1468-1474 (1995).
- 41 B. Jacquier, A. Remillieux, M.F. Joubert, P. Christensen, and H. Poignant, " Upconversion and relaxation of high lying states in rare-earth-doped ZBLAN bulk and fibers", *Journal of Non-Crystalline Solids* **161**, 241-244 (1993).
- 42 L. Dong, W.H. Loh, J.E. Caplen, and J.D. Minelly, K Hsu, L. Reekie, "Efficient single-frequency fiber lasers with novel photosensitive Er/Yb optical fibers", *Optics Letters* **22**, 694-696 (1997).
- 43 X. Zou, and T. Izumitani, "Fluorescence mechanisms and dynamics of Tm³⁺ singly doped and Yb³⁺, Tm³⁺ doubly doped glasses", *Journal of Non-Crystalline Solids* **162**, 58-67 (1993).
- 44 T. Schweizer, B.N. Samson, J.R. Hector, W.S. Brocklesby, D.W. Hewak, and D.N. Payne, "Infrared emission and ion-ion interactions in thulium- and terbium-doped gallium lanthanum sulfide glass", *Journal of the Optical Society of America B* **16**, 308-316 (1999).
- 45 L. Wetenkamp, G.F. West, and H. Többen, "Co-doping effects in erbium³⁺- and holium³⁺-doped ZBLAN glasses", *Journal of the Non-Crystalline Solids* **140**, 25-30 (1992).
- 46 J. Nilsson, P. Blixt, B. Jaskorzynska, and J. Babonas, "Evaluation of parasitic upconversion mechanisms in Er³⁺-doped silica-glass fibers by analysis of fluorescence at 980 nm", *Journal Lightwave Technology* **13**, 341-349 (1995).
- 47 J. Nilsson, B. Jaskorzynska, "Analysis of gain improvements through a pump reflector in Er³⁺-doped optical amplifiers in the presence of concentration quenching", *IEEE Photonics Technology Letters* **8**, 346-348 (1996).
- 48 C.Y. Chen, R.R. Petrin, D.C. Yeh, W.A. Sibley, "Concentration-dependent energy-transfer processes in Er³⁺- and Tm³⁺- doped heavy-metal fluoride glass", *Optics Letters* **14**, 432-434 (1989).
- 49 D.L. Dexter, *J. Chem. Phys.* **21**, 836 (1953).
- 50 J.E. Shelby, "Rare earths as modifiers in oxide glasses", *Key Engineering Materials* **94-95**, 43-80 (1994)

- 51 V. McGahay, and M. Tomozawa, "Phase separation in rare-earth-doped SiO₂ glasses", *Journal of Non-Crystalline Solids* **159**, 246-252 (1993).
- 52 K. Arai, H. Namikawa, K. Kumata, and T. Honda, "Aluminium or phosphorus co-doping effects on the fluorescence and structural properties of neodymium-doped silica glass", *Journal of Applied Physics* **59**, 3430-3436 (1986).
- 53 M. Nogami, and Y. Abe, "Fluorescence spectroscopy of silicate glasses codoped with Sm²⁺ and Al³⁺ ions", *Journal of Applied Physics* **81**, 6351-6356 (1997).

Chapter 3 - Rare Earth Host Glass Optimisation: the influence of sodium

3.1 Introduction: Rare Earth Glass Host Fabrication

The luminescent properties of rare earth ions in glasses are a critical factor for the efficiency of lasers and amplifiers, and they are severely influenced by the rare earth environment. For example, rare earth doped crystals have narrow absorption and fluorescent bands with large cross sections, while glasses differ with small cross sections and broad bands [1]. This band broadening in the rare earth glasses is due to the multiplicity of the crystal fields that affect them in the matrix. This broadening is also dependent on the glass composition. Oxide glasses, as those used in this investigation, incorporate the rare earth ion into relatively large gaps, up to several Angstroms in diameter, located in the matrix [2]. Figure 3.1(a) is a schematic illustration of typical two dimensional example of rare earth incorporated into the glass matrix.

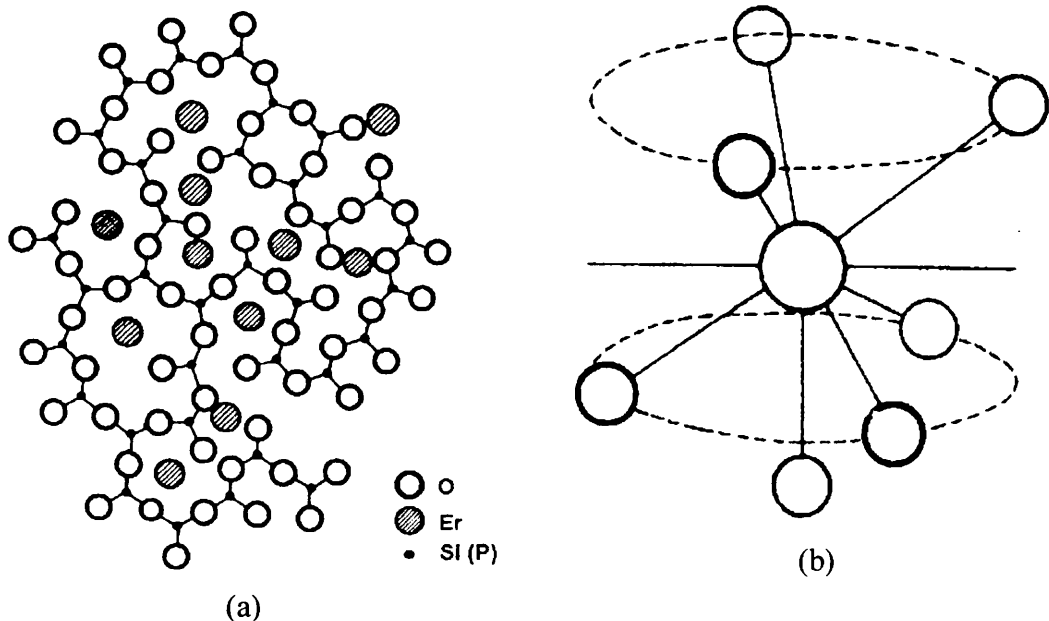


Figure 3.1: (a) - Typical two-dimensional example of rare earth ions incorporated in a phosphosilicate glass. (b) - Co-ordination number of Nd^{3+} ions in phosphosilicate glass (After Ref.[3])

Due to the large co-ordination number necessary to incorporate the rare earth ions into silica glasses [3], such as the example in the Figure 3.1(b), clustering starts to take place even at a very low doping concentration.

As described in the section 2.7, in order to increase the solubility of rare earths, while reducing clustering formation, phosphorus pentoxide (P_2O_5) has been added to the network, forming the system $\text{SiO}_2\text{-P}_2\text{O}_5$ [4,5]. Moreover, P_2O_5 doped silica glasses have also shown an increase in the refractive index, and lowering of the sintering temperature. The incorporation of phosphorus into silica-based glasses avoiding clustering is physically described as follows: phosphorus is included into the glass matrix, exchanging place with silicon ions. However, as it is a pentavalent ion, one oxygen has double covalent bounds to it, thus reducing to three the number of tetrahedra that can be bound to any tetrahedron, leaving one oxygen to bound to the rare earth. Aluminium has also been used as a glass network modifier in order to increase the uniformity of rare earth ions in phosphosilicate glasses. However, the inclusion of aluminium in our flame hydrolysis deposition (FHD) process revealed a reduction in the fluorescence efficiency, as will be shown in the next section.

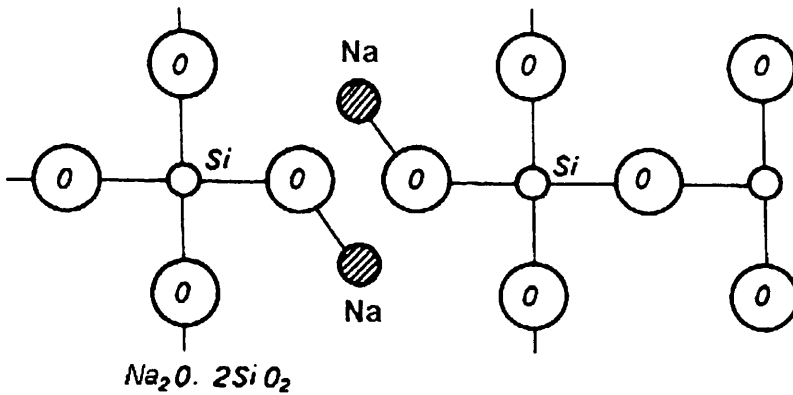


Figure 3.2: Simplified example of high sodium ions concentration in a silicate glass network, forming sodium disilicate glasses (After Ref. [6])

Besides aluminium, sodium is another option to dissolve rare earth ions into the glass matrix. Furthermore, sodium chloride is a harmless compound to be handled. Cormier *et al.* [6], employing molecular dynamics computer simulation technique, examined the optical properties of rare-earth ions in disordered system in terms of modifications of the silica-based glass. Their work revealed that, the presence of Na_2O in europium doped silica glass, the number of oxygen not coordinated to Si^{4+} , or independent from the silica network, considerably increases. The large amount of ions (Na^+) incorporated into the tetrahedral network, such as in the disilicate composition - $Na_2O \cdot 2SiO_2$, locally disrupt the silicate network and create non-bridging oxygen ions. Hence, the extra negative charge is compensated by the positive charges of the alkali ion, as depicted in Figure 3.2. According to the simulations, if rare earth ions are present in the glass system, it attracts the non-bridging oxygen into its potential field and frees it from the silicate network, while the local sodium cations are rearranged to meet the requirements of local electro-neutrality.

Based on these considerations, the proposal of this chapter is to study the influence of sodium ions on the incorporation of rare earth ions into phosphosilicate glasses fabricated by flame hydrolysis deposition. For such analysis, the use of erbium ions as active material was made due to the large amount of published data that can be used as benchmark; the laboratory facilities were also a factor which influenced this choice.

In order to measure the influence of sodium, three sets of waveguides with different

erbium doping level were fabricated. All samples underwent equivalent process of fabrication by Flame Hydrolysis Deposition, and the aerosol doping technique as described in the previous chapter, section 2.2. A combination of photolithography and reactive ion etching (RIE) was used to fabricate the channel waveguides. Cladding layers were deposited on the top of the samples to cover the waveguides. All the buried channel waveguides had the input and output facets optically polished to increase the optical coupling.

Table 3.1: Relevant characteristics of the waveguides used in the experiments. (*Estimated average thickness).

Er/Na (M)	Refractive Index (n)	Δn	Δn (%)	Er ³⁺ Ions (10^{19}cm^{-3})	Er ³⁺ Ions (wt%)	Length (cm)	Section ($\mu\text{m} \times \mu\text{m}$)
0.5/0.0	1.47363	0.015	1.05	1.58	0.20	4.40	50 × 7.0
0.5/0.1	1.47568	0.017	1.18	1.90	0.24	4.20	50 × 10.1
0.5/0.5	1.47468	0.016	1.12	1.74	0.22	4.70	50 × 9.1
0.5/1.0	1.47459	0.016	1.11	1.27	0.16	4.70	50 × 10.0
1.0/0.0	-	-	-	7.37	0.93	4.50	25 × 8.1
1.0/0.1				2.14	0.27	4.40	50 × 8.0*
1.0/0.5				2.22	0.28	4.40	50 × 8.0*
1.0/1.0	1.47454	0.016	1.11	2.40	0.30	4.40	50 × 8.0
2.0/0.0	1.47388	0.016	1.06	2.46	0.31	4.20	50 × 7.7
2.0/0.1	1.47655	0.018	1.24	2.38	0.30	4.20	50 × 10.2
2.0/0.5	1.47474	0.017	1.12	2.78	0.35	4.25	50 × 7.9
2.0/1.0	1.47428	0.016	1.09	2.85	0.36	4.50	50 × 8.1

Three different erbium aqueous solution containing 0.5 M, 1.0 M, and 2.0 M, of high purity (99.99%) REacton® erbium (III) chloride hexahydrate, respectively were prepared. Each of the three erbium doped aqueous solutions was separated in four different batches giving twelve solutions. Each of these erbium solutions received different amounts of, high purity (99.99%) REacton®, sodium chloride in the following amounts: 0.0 M (sodium free), 0.1 M, 0.5 M, and 1.0 M.

These solution concentrations enable us to observe the influence of sodium on the glass matrix and on the rare earth luminescent behaviour under three different

conditions: when the amount of the sodium solution was varied from zero up to the double of the rare earth solution concentration ($\text{Er}^{3+} = 0.5 \text{ M}$). We could also study such influence when the sodium chloride in the solution reaches the same amount of the erbium (III) chloride ($\text{Er}^{3+} = 1.0 \text{ M}$), and finally when the sodium solution is limited to half the rare earth one ($\text{Er}^{3+} = 2.0 \text{ M}$). The last solution set is useful to observe the influence of sodium in its low level concentration if compared with the amount of the rare earth ions. A summary of the main characteristics of each waveguide is illustrated in Table 3.I. It is worth to stress that the 1.0/0.0 M sample used in the experiments was produced in a different batch, and the difference for the rare earth concentration is associated to the level of phosphorus used during the deposition.

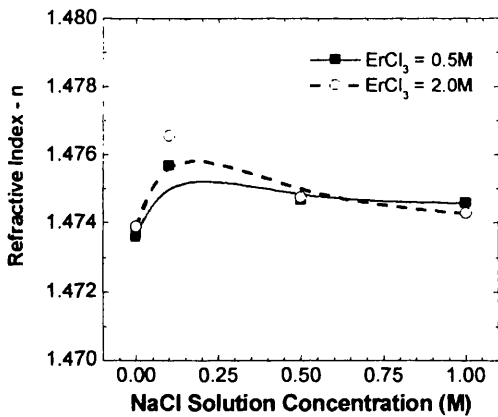


Figure 3.3: Samples refractive index variation with sodium chloride content, for two different erbium chloride solution concentrations.

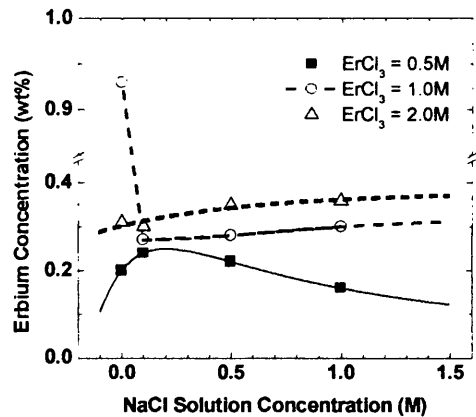


Figure 3.4: Rare earth ions concentration variations as a function of sodium chloride content, for three different erbium chloride solution concentrations.

The first difference observed in the glass matrices characteristic was in the refractive indices. Figure 3.3 summarises these results. Within experimental errors, both samples - containing erbium chloride solution concentration of 0.5 M and 2.0 M respectively - displayed similar trends. Both have shown an increase in the refractive index when low sodium chloride was used, followed by a reduction in the index when the solution become more concentrated. The refractive indices and refractive index differences shown in Table 3.I, were measured and calculated using the prism coupling method [7] at 632.8 nm (He-Ne laser line). The uncertainty of these measurements is $\sim 10^{-4}$, which is reasonable for the purpose of the current

experiments. These results can be explained based on the molecular dynamic computer simulations presented in reference [6]. Qualitatively, the explanation is as follows. A small quantity of Na^+ incorporated into the host is helpful to compensate eventual non-bridging oxygen due to the presence of rare earth ions. The immediate effect in the glass caused by the reduction of non-bridging oxygen ions is an increase in the network rigidity, resulting an increase in the refractive index. However, when the amount of Na^+ ions is superior to the unbounded oxygen, they are incorporated into the glass matrix forming $x\text{NaPO}_3 - y\text{SiO}_2$ and $x\text{Na}_2\text{O} - y\text{SiO}_2$ (where x and y represent unknown quantities). The influence of the NaPO_3 molecules on the refractive index is the opposite to that of P_2O_5 , softening the glass and reducing the refractive index. The refractive index difference Δn is defined as:

$$\Delta n = \left(\frac{n_{co}^2 - n_{cl}^2}{2n_{co}^2} \right) \cong \frac{n_{co} - n_{cl}}{n_{co}} \quad (3.1)$$

n_{co} and n_{cl} are the core and cladding refractive index respectively. However, when the difference between n_{co} and n_{cl} in the glass is small, the approximation is usually applied [9].

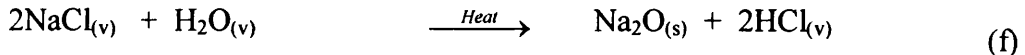
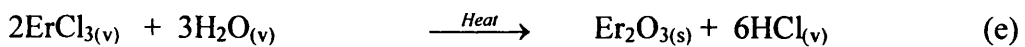
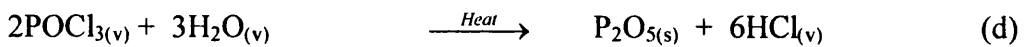
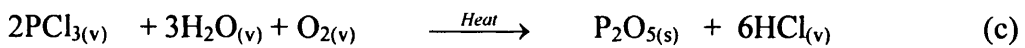
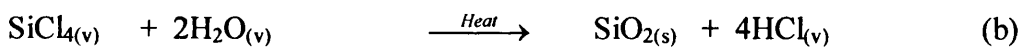
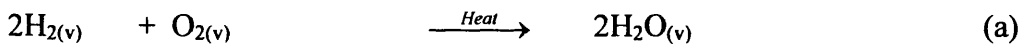
The second parameter observed in this initial analysis was the rare earth ion concentration, and the results are illustrated in Figure 3.4. The rare earth concentrations were estimated with the help of Ainslie *et al*'s [8] extinction coefficient for the ${}^4\text{I}_{13/2} \rightarrow {}^4\text{I}_{15/2}$ erbium band. For an equivalent silica-based glass, an extinction coefficient corresponding to 2.0 dB/cm·wt% was determined. Despite the inaccuracy of the method employing this extinction coefficient to determine absolute ion concentrations, it works reasonably well in estimating relative changes of rare earth levels.

As noticed from Figure 3.4, the amount of impurity ions effectively incorporated into the glass matrix did not increase proportionally to the concentration of the rare earth solution used in the deposition. It was observed during the FHD processes that high rare earth solution concentration led to some solid material being deposited at the entrance of the torch. Furthermore, the amount of this material was dependent on the rare earth solution molarity, and the same solid material was not observed when the erbium solution concentration was low. Therefore, it was attributed to the rare earth

solution becoming solid, due to the temperature gradient in the delivery process, before reaching the flame. This factor reduced the effective amount of rare earth incorporated into the glasses.

Following the lines drawn across the experimental points (Figure 3.4), it noticed that the variation in the amount of rare earth incorporated into the glass when low erbium solution concentration were delivered shows a similar behaviour to the refractive index variation, that is, initially increasing for low concentration and then falling at higher levels. However, the higher erbium concentration solutions (1.0 M and 2.0 M) show saturation in the rare earth level when the concentration of sodium in the solution was greater than 1.0 M (the maximum used in the experiment). The dashed line drawn in the 1.0 M-erbium solution indicates the high rare earth content in this sample as mentioned earlier. As this sample was fabricated with the system in a different condition, and probably due to a high phosphorus level incorporated in that deposition, the incorporation of a higher rare earth content became possible.

The changes observed in the rare earth concentration are explained with the help of the chemical reaction equations for the flame hydrolysis process:



and by the following considerations: both the erbium and the sodium cations are network modifier (NWM) ions, which are incorporated in the voids of the network as discussed in the introduction to this chapter. However, the smaller ionic radius of the erbium ions, compared to the sodium ions, provides an effective field strength¹ ~4.5 times stronger for erbium than for sodium cations. According to the equations above describing the chemical reactions, for a specific rare earth doping level, all quantities

¹ The effective field strength $E=eZ/a^2$ (eZ ionic charge, a ionic radius) is the factor determinant the classification of an ion as a network former or a network modifier (NWM).

are kept constant during the depositions except the last one, eq. (f), corresponding to the sodium chloride reaction. Thus, the effect of the addition of sodium can be analysed based only on the changes influenced by the last two equations.

However, as showed previously, depositions employing low erbium concentrations had a similar behaviour to that of the refractive index. This effect can be explained considering that small amount of sodium in the reaction means that it is favourable to include more rare earth ions into the glass soot due to its strong effective field and reduced ionic radius. Thus, the small alkali ions present in the reaction are added to the network only if there are unbound oxygen ions [6] as described in Figure 3.2. However, when the amount of sodium in the reaction becomes comparable to the erbium, the sodium starts to compete with the rare earth in number, regardless of its weaker electrostatic field, and it is more likely to incorporate in the rare earth. Moreover, the large coordination number of Er^{3+} ions in oxides (≥ 6) [10,11] is another factor to reduce its probability of incorporation under this condition. Hence, the greater the number of sodium the less the quantity of erbium in the soot, and as the result the depletion in the erbium concentration is seen.

For higher rare earth concentration (1.0 M and 2.0 M), due to the large number of these impurity ions, the sodium content has small influence on the incorporation of the rare earth, and they never reach a saturation point. The probability of incorporating rare earth ions into the network instead of an alkali is greater. The saturation-like behaviour of the high rare earth concentration curves is due to the amount of phosphorus added to the glass. This can be certified observing the rare earth concentration of the sample 1.0/0.0 M among the same rare earth sample set. The rare earth content was estimated to be close to 1.0 wt%, while the other samples have less than 50% of this value. Because the alkali ions have a coordination number smaller than the rare earth ions, they are more likely to be added to the network. Thus, when high alkali concentrations are used, it is inevitable that they occupy voids near rare earth ions, avoiding clustering of the rare earth ions.

As expected, the inclusion of sodium ions into the glass matrix has been demonstrated to be beneficial in that it increases the rare earth solubility in the network. The next section will be dedicated to the evaluation of this increase in the

rare earth doping level in terms of ion-ion interaction. This effect will be evaluated comparing the lifetime measurements of the transition ${}^4I_{13/2} \rightarrow {}^4I_{15/2}$ of erbium ions for all the samples.

3.2 The Erbium ${}^4I_{13/2} \rightarrow {}^4I_{15/2}$ Transition Lifetime Measurement

In a weakly doped medium, i.e. when the rare earth ions are sufficiently far apart from each other, the excited ions decay independently of all the other ions in the sample. However, when the concentration of the rare earth ions is increased, the probability for these ions exchange part of their energy during the relaxation process become significant. The manifestation of these interactions is noticeable through a reduction in the lifetimes of metastable levels.

In addition to the energy exchange, especially for the Er^{3+} ions, the absorption of cross relaxation or pump photons by the upper laser level (excited state absorption - ESA) is another possible loss mechanism, present even for low doping level, which must also be avoided. If ESA is present, even if there is sufficient gain on the laser medium to overcome such loss, the slope efficiency will almost certainly be degraded because of this unwanted absorption [12]. In practice, choosing a suitable pumping wavelength for the specific laser transition usually does the reduction of pump ESA.

For a heavily doped laser medium, cross relaxation is an additional factor contributing to the ESA, reducing the upper laser level population, which is reflected by an increase in the threshold pump power and consequently reducing the device efficiency [13,14]. To reduce the laser threshold and achieve gain at low pump powers, the laser medium requires a large population accumulated in the upper level (N_2), keeping the population of the lower level (N_1) as small as possible. The requirement for $\Delta N = (N_2 - N_1)$ to be large, i.e. an efficient inversion population, has two implications. Firstly, ions excited out of the ground state need to be channelled efficiently into the upper level (large absorption cross section), and, secondly, the fluorescence lifetime of this upper level should be long. Thus, the ions arriving in that level remain there for a reasonable length of time permitting an efficient population inversion [15].

This section will then study the influence of the inclusion of the sodium ions into the glass on the rare earth clustering formation using the variation in the transition laser at 1535 nm lifetime as parameter. The lifetime reduction due to the cross relaxations

is better understood if the dynamics of the process is considered. When two rare earth ions interact, the excited ion nonradiatively transfer its energy to the other also excited, leaving itself in the ground state and promoting the other to a higher state. This nonradiative relaxation, which is faster than the radiative, is responsible for the apparent reduction in the lifetime [16]. The ion-ion interaction is completed when the excited ion quickly relaxes back to the previous excited state through multiphonon emission process. The net result of this process is the conversion of one unit of excitation into heat. Since cooperative up-conversion requires two interacting ions in the excited state, it is not noticeable at low pumping power levels [1]. At high pumping powers, it appears as accelerated and multi-exponential decay.

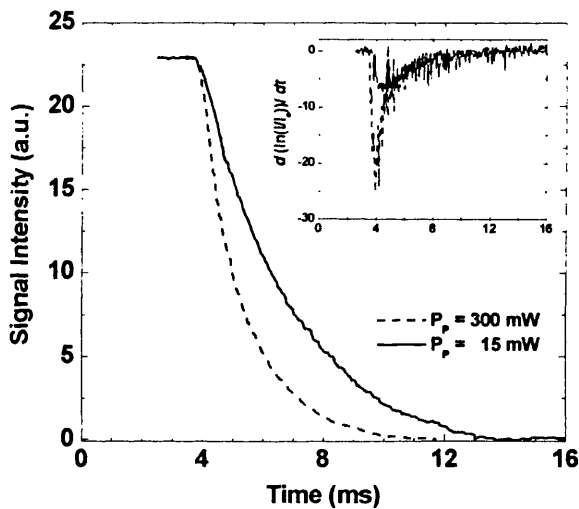


Figure 3.5: Typical fluorescence measurement under low and high pump power intensities, showing the increase in the fast decay component. The inset shows the differential of the natural logarithm of the same data.

Figure 3.5 shows a typical lifetime measurement result when using a heavily doped rare earth sample (2.0 M) for two different pump power levels at 514.5 nm. The inset of the figure, corresponding to the differential of the natural logarithm of the fluorescent decay curves, indicates the presence of fast decay components even for a low pump power - characteristic of a heavily rare earth doped medium. The use of the differential of the natural logarithm of the data is useful because it makes any small departures from the exponential behaviour easy to notice. Moreover, it shows the instantaneous decay rate at any time in the decay. A purely exponential decay, i.e. transition without the presence of nonradiative relaxations – including ion-ion

interaction, would have a constant slope of the natural logarithm against time, and a differential logarithm which is constant [18]. The result of the investigation using this technique is that all samples used in this research have a certain amount of ion-ion interaction. It was also observed that, as expected, the interaction is proportional to the rare earth doping level. All samples used in the experiments had also shown the characteristic green fluorescence from the level $^4S_{3/2}$, due to excited state absorption (ESA) when pumped at 800 nm or 980 nm.

Following this preliminary inspection on the rare earth clustering formation, the influence of the inclusion of sodium in the glass was investigated. Due to the presence of clustering in all samples, the evaluation of any departure of the lifetime of the laser transition due to the inclusion of sodium ions into the matrix can also be used as an indicative of the level of clustering formation the glass.

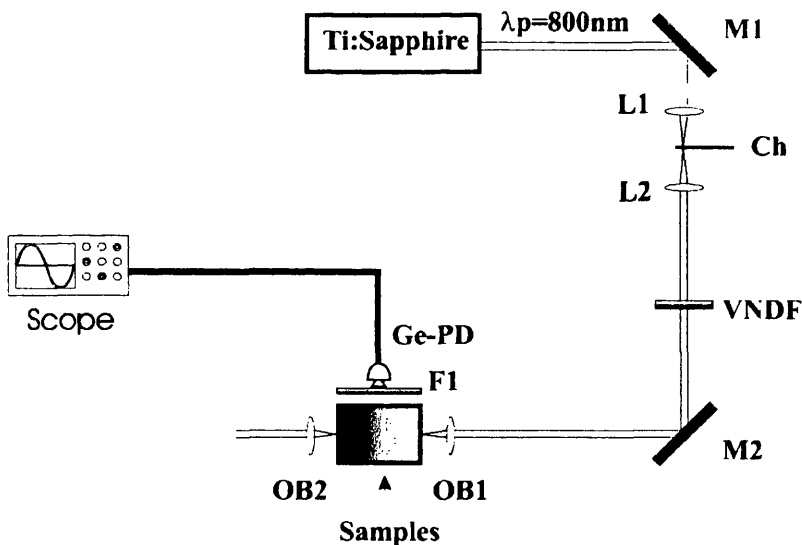


Figure 3.6: Experimental set-up for fluorescence measurements erbium doped phosphosilicate waveguides.

The experimental set-up used for the measurements of the erbium laser transition lifetime is depicted in Figure 3.6. A continuous wave (CW) Ti:Sapphire laser operating at 800 nm was used as the source of fundamental radiation. A variable neutral density filter (VNDF) was used to maintain the pumping power level constant during a series of measurements. The laser beam was pulsed through a mechanical chopper (Ch) operating with frequency near 20Hz. This frequency was chosen, considering that the lifetime to be measured is close to 5.0 ms, to ensure a complete

depopulation of the upper laser level. A pair of lenses (L1 and L2), with focal length of 10.0 cm, placed in the path length of the laser beam produced a beam waist of $\sim 50 \mu\text{m}$ were the chopper was arranged. These procedures have ensured that the lifetime to be measured is much larger than the excitation cut-off time ($\sim 0.04 \text{ ms}$) [18]. The pump signal was coupled into the waveguide via $\times 10$ objective lenses (numerical aperture $\text{NA} = 0.17$) and the signal at $1.535 \mu\text{m}$ was collected transversally to the pump propagation by a germanium photodetector (Ge-PD), with time response better than $0.1 \mu\text{s}$. The residual pump signal was removed using the colour filter F1. The lifetime signals were recorded and stored in an oscilloscope before being downloaded to a graphical plotter.

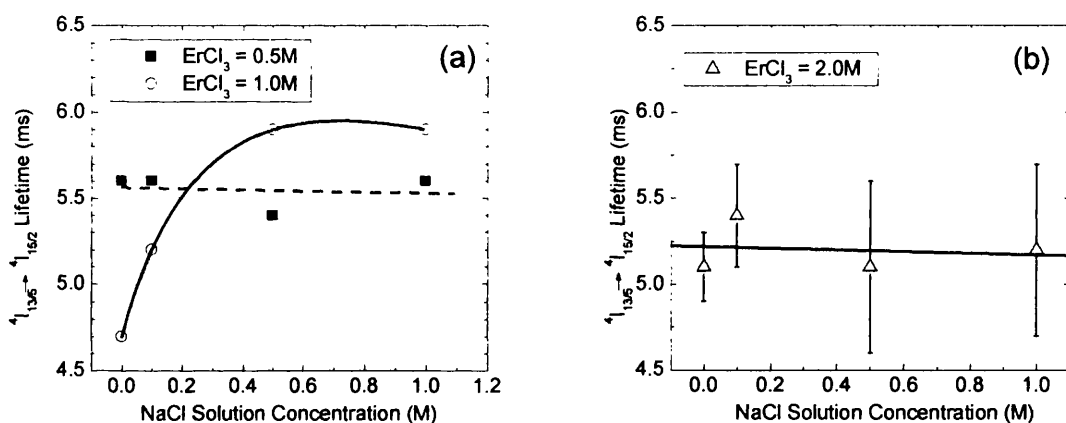


Figure 3.7: (a) Lifetime measurements as a function of the sodium solution for two erbium ions concentration 0.5 M (solid squares and dashed line) and 1.0 M open circles and straight line). (b) The same measurement in 2.0 M erbium doped sample, the figure shows the typical error in the experiments.

The results of the lifetime measurements for all samples are shown in Figure 3.7(a) and Figure 3.7(b). It was observed that the inclusion of sodium did not lead to any noticeable changes in the lifetime for samples with low and high rare earth solution concentration. The values oscillate around 5.6 ms for samples prepared with a solution containing 0.5 M of erbium chloride corresponding to the dashed lines in the Figure 3.7(a), and 5.1 ms to the 2.0 M samples, Figure 3.7(b). The small reduction observed in the best-fit lines is within the experimental errors of the measurements. However, glasses prepared with 1.0 M solution have shown an increase in the lifetime with the inclusion of sodium oxide, dashed lines in the Figure 3.7(a). The value enhanced from 4.7 ms for undoped sample to 5.9 ms when the sodium solution

was 0.5 M, showing a saturation-like behaviour for sodium beyond this level.

These results corroborate with the previous analysis of the Figure 3.3 and Figure 3.4, and they can be explained with the help of the chemical reaction equations. Based on the considerations for the rare earth concentration presented before, the minor influence in the relaxation lifetime due to the incorporation of sodium ions into the glasses containing low rare earth concentration should be expected. It is generally assumed that network modifiers, such as rare earth or alkalis ions in oxide glasses, are randomly distributed among various interstitial sites within the network-former oxygen framework [3]. Considering these ions as being homogeneously distributed into the glass due to its low concentration, the amount of ESA and the cross relaxation are expected to be weak. The further reductions of the impurity ions, as shown in the Figure 3.4 for 0.5 M, only become less favourable to the nonlinear effect. Hence, there was no appreciable change in the lifetimes due to sodium ions.

The inverse is expected to occur in the samples with a high rare earth concentration. It was observed that even the sodium-free sample have a reasonable amount of ESA, characteristic of high rare earth concentration. As depicted in the Figure 3.4, the inclusion of sodium increased the amount of the incorporated impurity ions. The solubility of the rare earth in the glass was enhanced due to sodium ions and was theoretically predicted by reference [6]. However, the experimental results depicted in the Figure 3.4 shows that the quantity of rare earth was also increased. Consequently, the balance between both, the increasing in the ion solubility and the increase in its concentration, maintained the lifetime approximately unaltered.

The trade-off between these effects can be seen in the 1.0 M erbium-doped samples. The undoped (sodium-free) sample showed the highest doping level (approximately 1.0 wt%) with the shortest lifetime. When sodium was included into the glass matrices, and as its concentration was comparable to the erbium solution during the depositions, it started to dilute the rare earth, reducing the cooperative upconversion energy transfer and the lifetime increased. Based on these observations, it is expected to be an optimum sodium and erbium concentration to maximise the lifetime. Despite the small numbers of experimental points, Figure 3.8 was done to help the visualisation of the mentioned point for this set of samples.

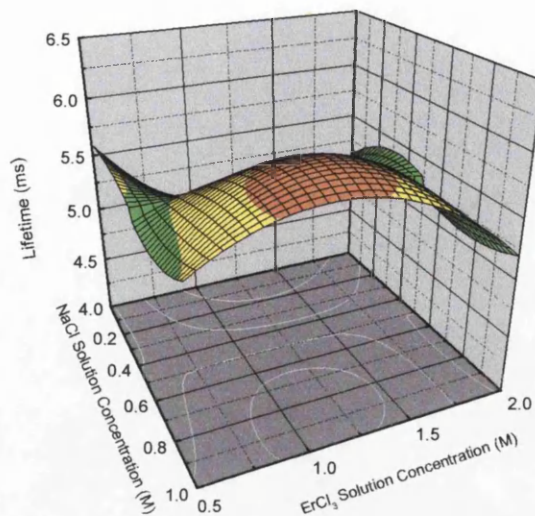


Figure 3.8: Three-dimensional picture of the laser transition lifetime as a function of the dopant levels.

In summary, the inclusion of sodium ions has shown an enhancement in the lifetime for samples with moderate rare earth doping levels. The next section will be concerned with the effect of these ions on the cross section of the laser transition.

3.2.1 Absorption and Fluorescence Measurement Results

Large stimulated emission cross-sections, and laser transitions with long lifetimes, are the most important parameters required for the design of high peak power solid-state lasers. Thus, the variation of the cross section with the glass composition has become the subject of intense study because it is necessary to optimise and achieve the best performance for amplifier or laser systems [19,20]. The glass network former composition and the codoping ions have important effects on the fluorescence and absorption of rare earth ions in glasses [21].

A common way to optimise phosphosilicate glasses to extend the solubility of the rare earth ions is the inclusion of aluminium into the network system [22]. It is known from the literature that the addition of aluminium tends to broaden the absorption and emission ${}^4I_{13/2} \rightarrow {}^4I_{15/2}$ of Er^{3+} ion reducing the cross-section peaks [23]. In the context of optimisation of practical devices, the reduction of the gain in

the fibre version of the amplifiers can be easily compensated by increasing the fibre interaction length. Furthermore, the line broadening is potentially useful to accommodate more wavelength channels. However, the inclusion of Al^{3+} ions in the FHD phosphosilicate glasses did not lead to the behaviour for fibres. The compensation in the reduction of the peak cross-sections by broadening the transition line shape was not observed in our measurements [24]. The addition of aluminium did not result in considerable changes in the metastable lifetime.

To evaluate the influence of aluminium ions in the glass system, fluorescence at 1530 nm ($^4\text{I}_{13/2} \rightarrow ^4\text{I}_{15/2}$ transition) due to erbium ions was measured and the cross section for the transition was determined by McCumber's theory [25-27]. The typical cross section result for the two different erbium concentrations studied is reproduced in the Figure 3.9.

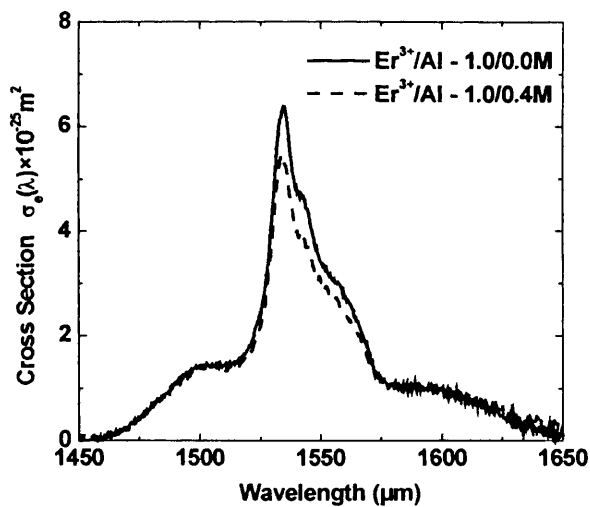


Figure 3.9: Typical cross section for Er^{3+} doped waveguide showing a reduction in the peak with the inclusion of aluminium.

These results dissuaded us from using aluminium to help the incorporation of rare earth ions into the glass matrix. Unlike the case in the optical fibres, the short interaction length and the higher scattering losses in rare earth doped planar waveguides are determinant factors for lasers and amplifiers to achieve high gain and low threshold pump power. Thus, even a minimal reduction in the fluorescence characteristic will certainly be an additional difficulty to overcome during the fabrication process. Therefore, the next investigation due to the sodium influence in

the glass was carried out measuring the fluorescence of the metastable level for different Na^+ contents.

Photoluminescence is a sensitive probe of the local environments of the active ions in the host glass. Since each rare earth ion sits in a unique site, the ligand field experienced by each ion differs. This difference leads to different Stark levels for each ion. The greater the disorder in the rare earth environment, the greater the differences in the Stark levels, leading to a photoluminescence spectrum over a larger range of wavelengths [23].

The experimental set-up for the measurement of the fluorescence efficiency and fluorescence cross sections was similar to one used to measure the lifetime presented in the previous section. The fluorescence measurements were carried out using a laser system, consisting of an Argon ion laser as a pump source to a Ti:Sapphire laser as a pumping radiation source, tuned at 980nm. This pumping radiation was free space coupled, through a $\times 10$ and $\text{NA} = 0.17$ microscopic objective, into the buried erbium doped channel waveguides. The fluorescent signals generated in the waveguides were collected transversally to the direction of the pumping radiation propagation via a multimode fibre (core diameter of $100 \mu\text{m}$) making use of noise-like characteristic of the spontaneous emission radiation; i.e. the fact that it emerges randomly in all directions, unlike the stimulated emission radiation which are expected to propagate in the same direction as the pump. Thus, the signal collected transversally consists only of spontaneous emission radiation. In order to ensure small interference of the stimulated emission, low pump powers were used. The maximum pump power without stimulated emission is obtained when the waveguide is configured as a single pass amplifier have null unit gain in the output. Under the present configuration, assuming coupling efficiency of $\sim 30\%$, the pump power has to be below 100 mW. The resulting output spectra were collected and measured with an Anritsu optical spectrum analyser in the range of the 1450-1650 nm.

The change in the fluorescence of the ${}^4\text{I}_{13/2} \rightarrow {}^4\text{I}_{15/2} \text{Er}^{3+}$ transition line as a function of sodium concentration were measured and the results are shown in Figure 3.10. Straight lines through the experimental points serve to emphasise the trends across the series. For each set of samples with a similar amount of erbium, the

measurements were acquired with the same level of pump power. As can be seen from Figure 3.10, all the three sets of samples had a similar trend, showing that there is a certain amount of sodium concentration where the fluorescence reaches a maximum near 0.1 M and then starts to decrease. The intensity of the fluorescence for the 1.0 M sodium free sample was of the same order of magnitude as that of the other samples in the same group, despite the difference in the rare earth concentration. This is because its fluorescence was measured in a 25 μm wide waveguide while the waveguide in the other samples in the same set were 50 μm wide. For all these measurements the coupling efficiency was optimised by monitoring the transversal fluorescence, and the pump power was kept constant. It is worth mentioning that the same fluorescence peak trends were observed employing higher or lower laser pump power.

The peak wavelength of the transition remained unchanged, within the accuracy of the measurements, with the addition of sodium. The lack of a shift in the fluorescence transition peak did not give a strong indication that the glass underwent structural changes with the inclusion of sodium in the matrix. All observed changes were within the experimental errors of 10%.

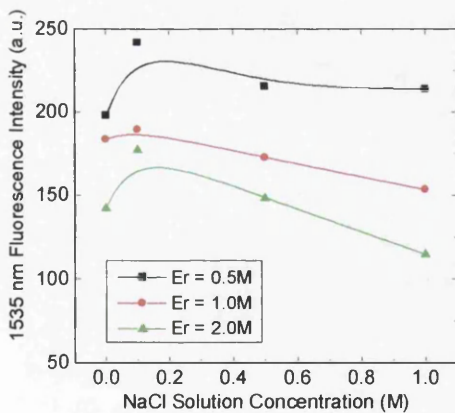


Figure 3.10: Fluorescence measurements for sodium doped waveguides with three different erbium concentrations. Lines were drawn as eye guideline.

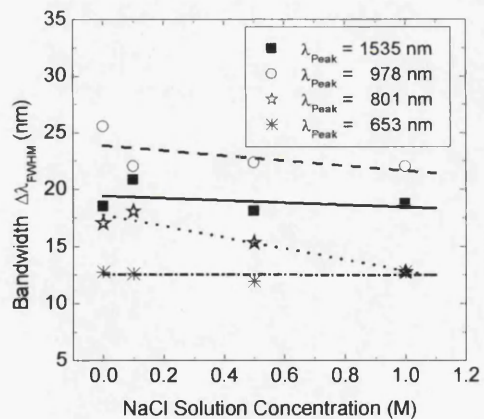


Figure 3.11: Full width at half maximum (FWHM) bandwidth variation as a function of sodium solution concentration for the four absorption bands measured.

The full widths at half maximum (FWHM) bandwidths of the four accessed absorption bands were also measured, and the results are summarised in Figure 3.11.

The trend observed in the measurements was a small reduction in the bandwidths, however, the variations noticed in the ${}^4I_{13/2} \rightarrow {}^4I_{15/2}$ transitions lines were less than 10%, if compared with the sodium-free samples, and these variations are comparable with experimental errors. Linear fittings to the experimental results are for the visualisation of those points. As the more pronounced variation occurred in the weaker band, and considering the inaccuracy in the measurements of these bands, no physical interpretation could be inferred from them.

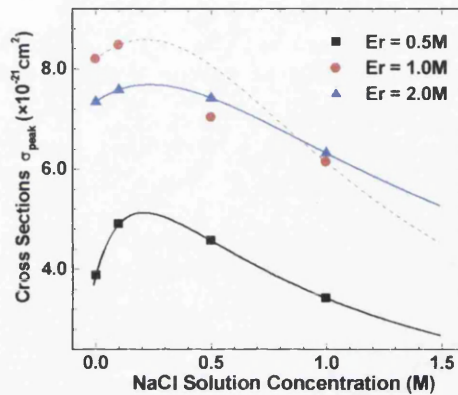


Figure 3.12: Absorption cross sections calculated applying McCumber's theory for erbium doped waveguides with three different erbium concentration increasing the amount of sodium content.

To analyse the change in the fluorescence reported in Figure 3.10, absorption measurements were also carried out and the absorption cross sections for the transition at 1535 nm were estimated. A white light source was used as the excitation radiation for the absorption measurements. Light was coupled into, and collected from, the 50 μm wide waveguides by two pieces of multimode fibres, with core diameters of 100 μm. An Optical Spectrum Analyser tuned over the wavelength range of 1450-1650 nm recorded the spectra. Prior to all waveguide measurements, the fibre-to-fibre absorption spectrum across the same wavelength region was recorded. This spectrum was then subtracted from each waveguide spectrum in order to exclude the spectral response of the entire measuring system such as white light source, optical fibres, and detection systems. The absorption cross sections were calculated applying McCumber's theory as described in the second chapter. Figure 3.12 depicts absorption cross-section peaks, for three different erbium concentrations, when the sodium content was increased. The smooth curves through

the experimental points are to emphasise the trends across the series. A possible reason for one experimental result of the 1.0/0.5 M sample did not follow the general trend in the results shown in the Figure 3.12 will be discussed later.

The peaks of the cross-sections at 1535 nm (see Figure 2.5) of all samples show a similar behaviour to the corresponding measured peak fluorescence. Small amounts of sodium enhanced the peak cross section, and this enhancement is larger for the lower rare earth solution concentrations. Further increasing in the alkali content considerably reduces the cross section peaks. The trend observed in the peak cross-sections of the Figure 3.12 and the refractive index in Figure 3.3 point towards the existence of change in the glass structure.

The general trends observed in the cross-sections results were also obtained via the measured spectroscopic parameters, such as the transition lifetime, its bandwidth, and the peak wavelength, through the relation [28]:

$$\sigma \approx \frac{1}{4\pi^2 c} \left(\frac{\lambda^4}{\Delta\lambda \cdot \tau_R} \right) \quad (3.2)$$

The final results do not corresponded to the absolute cross section values since the fluorescence lifetime and the transition bandwidth were used instead of the radiative lifetime and the lorentzian bandwidth respectively, as required by the mathematical relation. However, the reduction in the peak cross-section due to the addition of alkali ions was observed.

The change observed in the fluorescence and absorption cross section peaks points towards the existence of beneficial changes in glass characteristics due to the addition of sodium ions. However, a second confirmation will be performed using a different method of evaluation. It will be detailed in the next section.

3.2.2 Judd-Ofelt Parameters Measurement

The Judd-Ofelt theory has been established as a tool for studying laser spectroscopic parameters [20], or for predicting the strength of laser transitions in rare earth solid-state material. It has also proved to be an effective instrument to study rare earth

doped glasses [21,29]. In this section, the Judd-Ofelt theory will be adopted to investigate the influence of sodium ions in the erbium doped phosphosilicate glass, produced by flame hydrolysis deposition. Our aim is to see if the observed variation in the emission fluorescence and the absorption-cross section was accompanied by the variation in the glass composition.

A description of the Judd-Ofelt theory was given in the section 2.5.2 and can be summarised as follows: the theory relates the measured integrated absorption of a particular transition line to a theoretical integrated absorption expressed in terms of three phenomenological parameters, Ω_λ , characterising radiative transition probabilities within the ground state configuration. These parameters are determined from a least-square fit to the experimental data.

These phenomenological fitting parameters are related to the interactions between ligand field and electronic levels expressed by [21,30]:

$$\Omega_\lambda = (2\lambda + 1) \sum_{s,p} |A_{sp}|^2 \Xi^2(s, \lambda) (2s + 1)^{-1} \quad \begin{array}{l} \lambda = 2, 4, 6 \\ s = 1, 3, 5 \end{array} \quad (3.3)$$

In (3.3) A_{sp} is the crystal field parameter which relates to the structural change near the rare earth ion, e.g. symmetry and distortion. The factor $\Xi(s, \lambda)$ is related to the radial integral of the wave functions between $4f$ and admixing levels, e.g. $5d$, $5g$, and the energy dominator between these two levels, i.e., the covalence between the rare earth ion and the oxygen ion for oxide glasses. The reason for expressing this parameter more explicitly is to emphasize their positive values.

The physical meaning of these parameters will now be discussed. Reisfeld *et al* [31] attempted to give some physical interpretation to them. Ω_2 was related to the partly covalent bonding and local polarisation, or the degree of asymmetry in the vicinity of the rare ions; and Ω_6 , after comparison with several rare earth hosts, suggested a dependence on the mean vibrational amplitudes. This was inferred from the increase in measured value as the rigidity of the surrounding medium decreased. The values of Ω_6 increased as the medium hardness changed as follows: crystalline mixed oxides, glasses, viscous solvents, and aqua ions. Oomen *et al.* [29] have shown that

the parameters Ω_4 , and Ω_6 , depend mainly on factors which are related to bulk properties (long range effects). Therefore, they are possible indicators of the viscosity in vitreous material.

For convenience in presenting the data and the results of the fitting, intensities are reported in terms of oscillator strength, or f -number, which is a dimensionless quantity as shown in the section 2.5. The oscillator strength of a transition can be calculated from the absorption spectrum using [32]:

$$f = \frac{mc}{\pi e^2 N_0} \int k_\nu d\nu \quad (3.4)$$

where:

m is the electron mass;

e is the electron charge;

c is the velocity of light;

N_0 is the number of rare earth ions per cm^{-3} ;

k_ν correspond to the absorption coefficient. The theoretical oscillator strength can be calculated by equations (2.12) and (3.4).

Magnetic dipole transitions are allowed between states of the same parity and can be of sufficient strength in certain cases to contribute to the observed intensities. In the terms of LS coupling, transitions from the ground state to the first excited state (${}^4I_{15/2} \rightarrow {}^4I_{13/2}$) will be the only allowed magnetic dipole transitions considered in this experiment.

Measurements of the absorption bands to calculate the Judd-Ofelt parameters were carried out with a method similar to that described above to calculate the absorption cross sections. As the parameters are computed from the measured absorption line, the greater the number of transition lines measured the more accurate the parameter determination. For a reasonable precision at least six distinct bands have to be measured. However, with the acquisition equipment used, only four bands could be determined in our measurements. They are the following ground state ${}^4I_{15/2}$ to ${}^4I_{13/2}$,

$^4I_{11/2}$, $^4I_{9/2}$, and $^4F_{9/2}$ absorption bands. This reduced number of lines is certainly a source of uncertainty in our results.

Samples were kept at room temperature during the measurements, and at this temperature, the observed linewidth were always considerably larger than the instrumental resolution.

Figure 3.13 shows typical measured spectra, and the inset of this figure shows a probable source of errors to our results due to the measurement system. As can be observed in the inset, part of the absorption bands at 980 nm, which usually extends up to 1040 nm, match with an absorption peak from the fibre-to-fibre measurement. In this figure, the upper curve corresponds to the fibre-to-fibre measured loss and the lower is the normalised absorption loss. When the rare earth concentration is not high enough to produce an intense absorption band, the fibre-to-fibre loss can affect the correct result, adding a valley in that region of the spectrum. For a heavily doped rare earth glass, this effect is not so pronounced, or sometimes imperceptible, as observed in the spectra of samples fabricated with 2.0 M erbium solution.

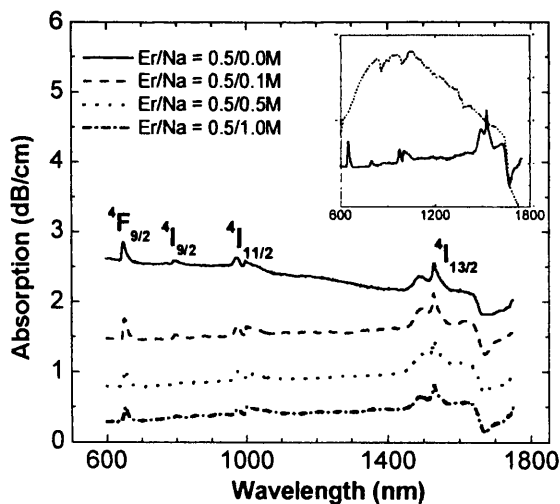


Figure 3.13: A typical absorption measurement spectrum. The inset depicts an error introduced in the measured band at 980 nm due to system interference.

According to the equation (3.3), the Ω_λ parameters must have positive values, but some of the Ω_2 found to describe each rare earth system in our experiment were negative, although the Ω_4 and Ω_6 are positive with an order of magnitude agreement

with values reported in the literature. Krupke [33] pointed out that the Judd-Ofelt parameters Ω_λ depend somewhat on the method used to establish them. However, for the minimisation of the sum of the squares of the deviation in line strength adopted here, very weak transitions will play no role in determining the minimum condition, while very strong transitions will dominate the selection of the minimising parameters.

Thus, it is not expected that the method used to determine the parameters should have such a strong effect. A possible reason for the negative values calculated is the presence of a hypersensitive band. In Judd's original treatment of rare-earth intensities in solutions [30], it was observed that transitions for which $\Delta J = \pm 2$ are peculiarly sensitive to changes in the ligands. According to reference [33], this J selection rule for hypersensitive transitions, which is the condition for the matrix elements of $\langle \|U^{(2)}\| \rangle$ to be nonzero, is a mechanism affecting Ω_2 . It has also been observed experimentally that bands corresponding to the transitions ${}^4I_{15/2} \rightarrow {}^2H_{11/2}$, ${}^4G_{11/2}$ in erbium-doped glass show great variation (by order of magnitude in some cases) in changing environments [34], while the intensity of the remaining transitions in the spectrum is not drastically increased. In the case of Er^{3+} , with ground manifold ${}^4I_{15/2}$, the hypersensitive transitions should essentially lead to ${}^4G_{11/2}$ level. However, because the large value of the spin-orbit constant for Er^{3+} , there is considerable mixing of the states in the intermediate coupling scheme and the $J = 11/2$ levels which contain component of 4G , such as the ${}^4I_{11/2}$ at 980 nm.

Table 3.II shows the result of the calculated Judd-Ofelt parameters Ω_λ . Due to the hypersensitivity of the 980 nm band and the interference in their determination, the same calculations were carried out in two different situations. The first was done considering the 950-1040 nm wavelength interval, which corresponds to the complete band. In the second case, all bands were kept in the same span except the 980 nm which was reduced to the wavelength range of 950-990 nm. This was done as an attempt to reduce the influence of the interference of the normalisation procedure. The main conclusion from these results is: Ω_2 is the most affected parameter due to the change in the referred band. The narrowest band produced the most imprecise results increasing the number of negative Ω_2 parameters, which have

no physical meaning.

Table 3.II: Judd-Ofelt parameters obtained through least-square fitting to the experimental oscillator strength.

	$\Omega_2 (\times 10^{-20} \text{ cm}^2)$	$\Omega_4 (\times 10^{-20} \text{ cm}^2)$	$\Omega_6 (\times 10^{-20} \text{ cm}^2)$
0.5/0.0M	13.04	1.72	1.64
0.5/0.1M	24.50	1.81	1.42
0.5/0.5M	14.00	1.76	1.80
0.5/1.0M	24.44	1.42	1.54
1.0/0.0M	-1.78	1.69	1.75
1.0/0.1M	7.77	2.01	1.60
1.0/0.5M	-9.35	1.32	1.66
1.0/1.0M	-4.78	2.03	1.73
2.0/0.0M	11.65	1.37	1.58
2.0/0.1M	-0.69	1.99	1.77
2.0/0.5M	-0.63	1.81	2.00
2.0/1.0M	-15.33	1.48	2.18

The other two parameters, Ω_4 and Ω_6 , are less sensitive to the measurement interference in the same band, as the results show small variation in both calculations. Similar results were obtained when all four bands were measured separately, a procedure which increases the accuracy of the absorption bands integral calculation. The behaviour observed in the parameters can also be explained by inspecting the unit tensor matrix elements for all bands included in the calculations [35]. Among them, the ${}^4I_{15/2} \rightarrow {}^4I_{11/2}$ (980 nm)¹ transition line shows the strongest influence on the Ω_2 parameter. They correspond to the highest value used to calculate Ω_2 , and the smallest to calculate Ω_4 , being three orders of magnitude smaller than the other unit elements. The three remaining parameters correspond to the most relevant, among the twelve tabulated, to determine Ω_4 . Thus, it can be concluded that, despite the inaccuracy in the determination of the Ω_2 using these four absorption bands, the remaining parameters may be expected to be precise enough to

¹ The respective unit tensor matrix elements are 0.0259, 0.0001, and 0.3994 to calculate the parameters Ω_2 , Ω_4 , and Ω_6 respectively.

estimate changes in the glass characteristics.

Figure 3.14 shows the results of the calculated Ω_6 Judd-Ofelt parameters. As pointed out by Oomen *et al.* [29], this parameter could be related to ‘long range effects’ such as the viscosity in vitreous material. The trends observed in the parameters Ω_6 agree with observed results where it has a tendency to increase with decreasing the rigidity of the medium surrounding the rare earth ions. As shown in the introductory part of this chapter, the inclusion of sodium oxide into silica-based glass has the effect of softening the glass and producing a lower sintering temperature. These corroborate the results of the lifetime measurements. According the main conclusion in the section 3.1, different reasons are presented for the low and high rare earth concentration samples to include more sodium ions in the glass matrix than to the unbounded rare earth avoiding clustering. This effect is observed in the Figure 3.14 by the more pronounced variation of the parameter Ω_6 in both Er = 0.5 and Er = 2.0 samples. While the samples Er = 1.0 M incorporate most of the sodium ions in the unbounded rare earth avoiding clustering and consequently the influence in the glass matrix is smaller than the previous one.

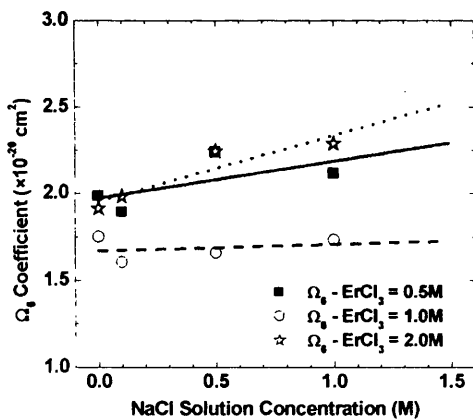


Figure 3.14: Ω_6 coefficients a function of sodium solution concentration.

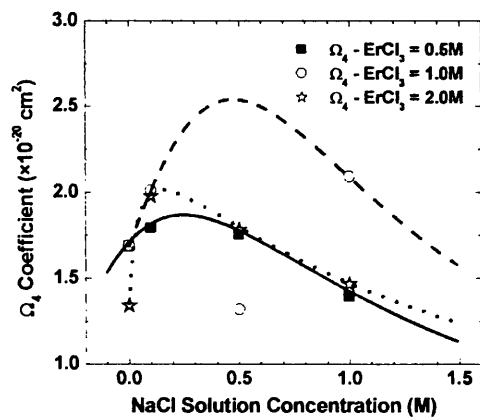


Figure 3.15: Ω_4 coefficients as a function of sodium solution concentration.

However, the characteristic observed in the Ω_4 results, as depicted in the Figure 3.15, are the similar to the trends observed in the absorption cross section and fluorescence measurements. As previously, a smooth curve has been drawn through the experimental points to show the trends across the series. The similarity of these measurements, particularly considering the curves corresponding to the 0.5 M and

2.0 M erbium concentrations. The results related to the sample 1.0/0.5 M did not follow the same trends as those obtained with the other erbium doping levels, and therefore was not considered in the fitting which determined its respective curve. Measurements in different samples fabricated from the same deposition have shown similar results. Despite the deposition record did not reveal any abnormality during the fabrication of the samples, the difference in the measurement is attributed to their characteristics. In terms of general behaviour observed, Krupke [20] reported a linear variation in the Ω_4 parameter while the neodymium cross section did not show the same behaviour with the rare earth concentration. Zou *et al* [36] also reported a linear variation on the same parameter, while the rare earth concentration was maintained constant, but the thulium cross section did not show the similar trend.

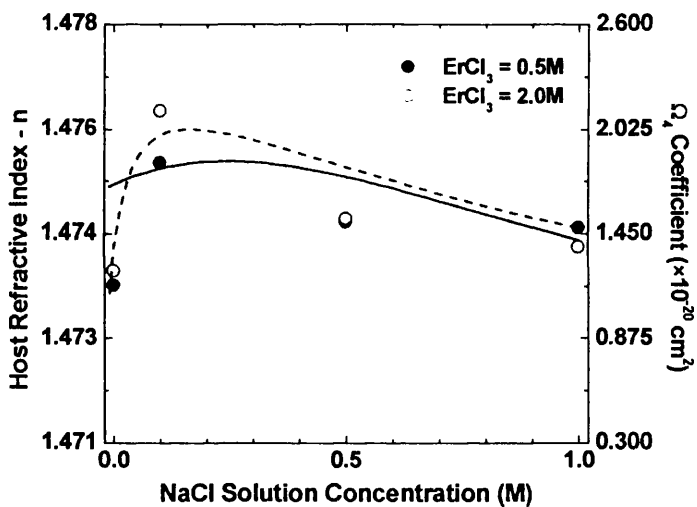


Figure 3.16: Comparison between host refractive indices and Ω_4 Judd-Ofelt parameters.

The final examination supporting our conclusions on the changes underwent by the glasses due to the inclusion of sodium is seen in Figure 3.16. It depicts the similarity between the host refractive indices, open and solid circles, and the Ω_4 coefficients represented in this graphic by its respective dashed and solid curves drawn across the experimental points imported from Figure 3.15. The agreement between the respective curves is remarkable. However, no physical interpretation for the observed behaviour of these results has been found.

3.3 Conclusions

This chapter was concerned with the estimation of the influence of sodium chloride on the chemical reaction of the flame hydrolysis deposition. This method is based on the fact, first demonstrated theoretically in [6], that the inclusion of sodium oxide (Na_2O) considerably increases the number of unbounded oxygen ions and thus makes it possible to extend the rare earth concentration in glasses avoiding cluster formation.

Three sets of samples with different erbium solution concentration (0.5 M, 1.0 M, and 2.0 M respectively) were prepared with three different sodium chloride concentration (0.1 M, 0.5 M, and 1.0 M respectively); one set was maintained sodium free to be used as a benchmark.

The first effects in the glasses were observed in the refractive indices and the rare earth concentration of the samples. The former have shown similar behaviour for all rare earth solution concentrations. It was observed that small quantities of Na^+ ions during the deposition make the matrix more rigid increasing the refractive index. As the amount of sodium increases, NaPO_4 is formed softening the glass and consequently reducing the refractive index. The rare earth concentration does not show a general trend with the inclusion of the sodium into the glass. A possible chemical reaction in the flame during the flame hydrolysis deposition was applied to explain the variation in the rare earth content when the alkali solutions were altered. According to results reported by Yamashita [37], within the Na^+ doping level of the present samples, no measurable change in the Raman spectra of the samples used is expected.

Running the deposition and maintaining the system unchanged revealed sodium and rare earth content to optimise the fluorescence lifetime for the 1.535 μm transition of erbium. In the situation analysed, an erbium solution close to 1.0 M and sodium solution between 0.1-0.5 M showed the longest lifetime. The increase in this parameter was understood because of the sodium diluting the rare earth avoiding clustering formation.

Absorption cross sections of the laser transition were also measured and the variation of the peak values with the sodium content brought to light behaviour similar to that of the refractive indices. In our measurements, a small reduction was observed in the linewidth of all measured lines, although the variations observed were smaller than the usual experimental errors of 10%. However, in terms of practical devices optimisation, an increase in the cross section was also found, with a maximum value with the sodium solution between 0.1-0.5 M, which is the same range that the lifetime of the 1.0 M erbium doped samples that have shown the most pronounced increasing.

A final verification was carried out applying the Judd-Ofelt theory to certify the evidence of change in the glass. The measurements have shown a softening in the glass viscosity due to the inclusion of sodium, results which followed the conclusions described to explain the increase in the fluorescence lifetime measurements.

3.4 Reference

- 1 W.J. Miniscalco, "Optical and electronic properties of rare earth ion in glasses", Ed. M.J.F. Digonnet, Rare earth doped fiber lasers and amplifiers, Chapter 2, 19 (1993).
- 2 C. Brecher, and L.A. Riseberg, "Laser-induced fluorescence line narrowing in Eu glass: A spectroscopic analysis of coordination structure", *Physical Review* **13**, 81-93 (1976).
- 3 S. Mockovciak, J. Pantoflicek, and K. Pátek, "Crystal field calculations of transition probabilities in Nd³⁺ in glass", *Physica Statu Solidi* **11**, 401-405 (1965).
- 4 T.Y. Tien, and F.A. Hummel, "The system SiO₂-P₂O₅", *Journal of the American Ceramic Society* **45**, 422-424 (1962).
- 5 C.R. Hummel, "Fusion temperature of SiO₂-P₂O₅ binary glasses", *Physics and Chemistry of Glasses* **19**, 41-42 (1978).
- 6 G. Cormier, J.A. Capobianco, and A. Montiel, "Molecular dynamics simulation of the trivalent europium ion doped in silica and sodium disilicate glasses", *Journal of Non-Crystalline Solids* **152**, 225-236 (1993).
- 7 R. Ulrich, and R. Torge, "Measurement of thin film parameters with a prism coupler", *Applied Optics* **12**, 2901-2908 (1973).
- 8 B.J. Ainslei, S.P. Craig, S.T. Davey, and B. Wakefield, "The fabrication, assessment and optical processing of high-concentration Nd³⁺- and Er³⁺-doped silica fibre", *Optical Materials* **6**, 139-144 (1988).
- 9 J.A. Buck, *Fundamentals of Optical Fibers*, (John Wiley & Sons, Inc. New York USA 1995).
- 10 C.C. Robinson, "Multiple sites for Er³⁺ in alkali silicate glasses (I). The principal sixfold coordinated site of Er³⁺ in silicate glass", *Journal of Non-Crystalline Solids* **15**, 1-10 (1974).
- 11 T.F. Belliveau, and D.J. Simkin, "On the coordination environment of rare earth ions in oxide glasses: Calcium titanosilicate and sodium aluminosilicate glasses", *Journal of Non-Crystalline Solids* **110**, 127-141 (1989).
- 12 A. Kellou, H. Ladjouze, F. Sanches, and G. Stephan, "Stability analysis of erbium-doped fibre laser dynamics with spontaneous emission", *Optical and Quantum Electronics* **27**, 741-746 (1995).
- 13 Y. Kimura, M. Nakazawa, "Gain characteristics of erbium-doped fiber amplifiers with high erbium concentration", *Japanese Journal of Applied Physics: Part 1* **32**, 1120-1125 (1993).
- 14 M. Federighi, I. Massarek, P.F. Trwoga, "Optical amplification in thin optical waveguide with high erbium concentration", *IEEE Photonics Technology Letters* **5**, 227-229 (1993).
- 15 J.R. Armitage, "Introduction to glass fibre lasers and amplifiers", Ed. P. W. France, Optical fibre lasers and amplifiers, (Boca Raton Florida USA 1991).

- 16 J. Thogersen, N. Bjerre, J. Mark, "Multiphonon absorption and cooperative upconversion excitation in Er^{3+} -doped fibers", *Optics Letters* **18**, 197-199 (1993).
- 17 H. Masuda, A. Tanaka, K. Aida, "Modeling the gain degeneration of high concentration erbium-doped fiber amplifiers by introducing inhomogeneous cooperative up-conversion", *Journal of Lightwave Technology* **10**, 1789-1799 (1992).
- 18 R.E. Imhof, and F.H. Read, "The measurement of lifetimes in atoms, molecules and ions", *Report on Progress in Physics*, **40**, 1-104 (1977).
- 19 M.B. Saisudha, K.S.R. Koteswara Rao, H.L. Bhat, and J. Ramakrishna, "The fluorescence of Nd^{3+} in lead borate and bismuth borate glasses with large stimulated cross section", *Journal of Applied Physics* **80**, 4845-4853 (1996).
- 20 W.F. Krupke, "Induced-emission cross sections in neodymium laser glasses", *IEEE Journal of Quantum Electronics* **QE-10**, 450-457 (1974).
- 21 Y. Nageno, H. Takebe, K. Morinaga, T. Izumitani, "Effect of modifier ions on fluorescence and absorption of Eu^{3+} in alkali and alkaline earth silicate glasses", *Journal of Non-Crystalline Solids* **169**, 288-294 (1994).
- 22 K. Arai, H. Namikawa, K. Kumata, and T. Honda, "Aluminium or phosphorus co-doping effects on the fluorescence and structural properties of neodymium-doped silica glass", *Journal of Applied Physics* **59**, 3430-3436 (1986).
- 23 W.J. Miniscalco, "Erbium-doped glasses for fiber amplifiers at 1500 nm", *Journal of Lightwave Technology* **9**, 234-250 (1991).
- 24 J.R. Bonar, M.V.D. Vermelho, P.V.S. Marques, A.J. McLaughlin, J.S. Aitchison, "Fluorescence lifetime measurements of aerosol doped erbium in phosphosilicate planar waveguides", *Optics Communications* **149**, 27-32 (1998).
- 25 D.E. McCumber, "Theory of phonon-terminated optical masers", *Physical Review* **134**, A299-A306 (1964).
- 26 D.E. McCumber, "Einstein relations connecting broadband emission and absorption spectra", *Physical Review* **134**, A954-A957 (1964).
- 27 W.J. Miniscalco, and R.S. Quimby, "General procedure for the analysis of Er^{3+} cross sections", *Optics Letters* **16**, 258-260 (1991).
- 28 E.A. Siegman, *Lasers*, (University Science Books California USA 1986).
- 29 E.W.J.L. Oomen, and A.M.A. van Dongen, "Europium (III) in oxide glasses", *Journal of Non-Crystalline Solids* **111**, 205-213 (1989).
- 30 B.R. Judd, "Optical absorption intensities of rare-earth ions", *Physical Review* **127**, 750-761 (1962).
- 31 R. Reisfeld, E. Greenberg, R.N. Brown, M.G. Drexhage, C.K. Jorgensen, "Fluorescence of europium (III) in fluoride glass containing zirconium", *Chemical Physics Letters* **95**, 91-94 (1983).
- 32 E.W.J.L. Oomen, "Up-conversion of red light into blue light in thulium doped fluorozirconate glasses", *Journal of Luminescence* **50**, 317-332 (1992).

- 33 W.F. Krupke, "Optical absorption and fluorescence intensities in several rare-earth-doped Y_2O_3 and LaF_3 single crystals", *Physical Review* **145**, 325-337 (1966).
- 34 H.U. Rahman, "Optical intensities of trivalent erbium in various host lattices", *Journal of Physics C: Solid State Physics* **5**, 306-315 (1972).
- 35 M.J. Weber, "Probabilities for radiative and nonradiative decay of Er^{3+} in LaF_3 ", *Physical Review* **157**, 262-272 (1967).
- 36 X. Zou, and Z. Izumitani, "Fluorescence mechanisms and dynamics of Tm^{3+} single doped and Yb^{3+} and Tm^{3+} doubly doped glasses", *Journal of Non-Crystalline Solids* **162**, 58-67 (1993).
- 37 H. Yamashita, H. Yoshino, K. Nagata, I. Yamaguchi, M. Ookawa, and T. Maekawa, "NMR and Raman studies of $\text{Na}_2\text{O-P}_2\text{O}_5\text{-SiO}_2$ glasses – six-coordinated Si and basicity", *Journal of the Ceramic Society of Japan* **106**, 539-544 (1998).

Chapter 4 - Modelling CW rare earth highly doped waveguide laser and amplifier

4.1 Introduction

The previous chapter analysed one aspect of optimisation of rare earth doped waveguide amplifiers and lasers: the glass host and the rare earth incorporation. Likewise the glass quality, the waveguide geometry are also important factors to determine high gain in optical amplifiers and lasers. Design and analysis tools enable a rapid optimisation of a technology before resources in manufacturing and personnel are invested. Simulation tools ultimately reduce manufacturing costs and streamline development. In addition, it is important to discover and understand the measurements issues associated with the waveguide devices so that limited metrology resources can be applied in the most effective way.

Modelling is not a difficult issue for devices developed in optical fibres geometry [1]. Usually the rare earth doping levels in optical fibres are low due to long

interaction lengths; consequently, the equations describing the population density of the system contain only linear terms, permitting the modelling procedures to be easily implemented. Generally, the main effect considered in rare earth doped fibre amplifiers is excited state absorption (ESA) for appropriate pump wavelength [2,3]. Despite the relative simplicity of this modelling, some effort has also been spent to provide closed relations to solve the propagation equations, although there is some loss of accuracy when compared with numerical methods [4-7].

Unlike optical fibre components, the integrated optical device as part of planar lightwave circuit (PLC) has a fixed length which cannot be altered after fabrication, thus reducing the number of adjustment parameters to compensate for minor deviations. The short interaction length also requires the use of high rare earth doping levels to overcome intrinsic losses. Both of these limitations mean that the optimisation of an integrated device is much more complicated.

To optimise the waveguide geometry of rare earth doped integrated components, accurate numerical models, particularly at high concentration levels, are required [8-10]. Moreover, the modelling of these active devices starts to become cumbersome at high doping levels. As will be shown further in this chapter, at high doping levels the dynamic population equations become nonlinear, due to the cross-relaxation terms, and for CW operation the populations cannot be treated in the same manner as for the low concentration problem. Thus, the numerical integration cannot be performed as previously. To overcome this problem, different numerical methods have been applied [11-13], including the accurate, but time consuming, finite element method [14,15]. Despite the high accuracy of this method, Zoboli *et al* have shown that its main disadvantage is the necessity of careful code preparation to allow it to run on workstations. In addition, the possibility of using Personal Computers can only be considered if computational time is not a constraint [16].

This chapter aims at developing a simple, fast and accurate model for the optimisation of rare earth doped waveguide lasers and amplifiers, which should be appropriate to rectangular waveguide geometry. The modelling procedure will be developed considering erbium-doped waveguides due to the availability of experimental data to verify the accuracy of the model. The subject will be presented

as follows: the introduction to the modelling procedure will start with some comments on the choice of pump wavelength in section 4.2. Section 4.3 will be devoted to a description of the principal differential equations to describe low erbium doping level lasers and amplifiers. Section 4.3.1 will include the equations to evaluate the influence of amplified spontaneous emission (ASE) on device performance. The complete system of equations describing a highly doped waveguide laser or amplifier will be given in section 4.4, based on the problem statements discussed above. Sections 4.5 and 4.5.1 will be devoted to the demonstration of the approximation procedure of the modelling followed by some comparison to reported experimental results. Finally, the conclusion to this chapter will be presented in the section 4.6.

4.2 Modelling CW erbium doped waveguide laser and amplifier

The optical absorption spectrum of erbium doped phosphosilicate glass, fabricated by flame hydrolysis deposition is shown in Figure 4.1. This spectrum reveals several possible choices for a pump wavelength for an erbium doped waveguide amplifier or lasers. However, for practical optical fibre communication systems, the lasers and amplifiers have to be pumped by semiconductor diode lasers. Therefore, the most interesting pump wavelengths are at 800 nm (${}^4I_{9/2}$), 980 nm (${}^4I_{11/2}$), and 1480 nm (${}^4I_{13/2}$).

Considering these three pumping wavelength the erbium doped waveguide devices can be described in two distinct ways. When the system is pumped at 800 nm - which correspond to the transition ${}^4I_{15/2} \rightarrow {}^4I_{9/2}$ - or at 980 nm - related to the absorption ${}^4I_{15/2} \rightarrow {}^4I_{11/2}$ - it acts as a three-level laser system. But, when the system is pumped at 1480 nm, corresponding to the ground state absorption (GSA) ${}^4I_{15/2}$ to the first excited level ${}^4I_{13/2}$, it acts as a quasi-two-level system.

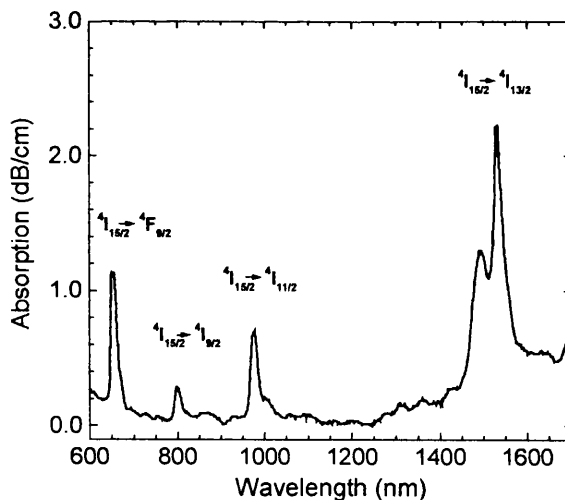


Figure 4.1: Absorption spectrum of erbium ion in phosphosilicate glass.

The presence of excited state absorption (ESA) at the 800 nm pump band implies a high pump power to achieve reasonable gain [2,3,17]. In addition to the ESA, this pump wavelength transition has a small absorption cross-section, again implying

high pump powers level to achieve high gain. The necessity of high pump power reduces the laser lifetime. Furthermore, due to the short wavelength, the probability of the pump wavelength propagating in a higher order mode is another important factor that reduces the gain.

No ESA occurs at 1480 nm pump wavelength [17]. However, at this wavelength, when the erbium ion is excited directly into the ${}^4I_{13,2}$ level (quasi-two-level laser system) the population in the upper laser level cannot increase beyond a maximum value set by the emission and absorption cross section ratio (σ_{pe}/σ_{pa}) at 1480 nm [18,19]:

$$\frac{N_2(x, y, z)}{N_o(x, y)} = \frac{\sigma_{pa}}{\sigma_{pa} + \sigma_{pe}} = \frac{1}{1 + \sigma_{pe} / \sigma_{pa}} \quad (4.1)$$

where N_o is the total erbium concentration, N_2 is the population of the ${}^4I_{13,2}$ level. According to the equation (4.1), the maximum inversion population for this pump wavelength is about 50%.

For the development of this model, the 980 nm absorption band was therefore chosen as the pump wavelength. Furthermore, this wavelength has exhibited the best performance with respect to gain and gain efficiency [2,20-22]. This is due to several positive characteristics, such as: the large absorption cross-section, the complete absence of stimulated emission and excited state absorption (ESA) at this pump wavelength.

4.3 Modelling CW erbium doped waveguide laser and amplifier at low concentration

The approach to establishing this model will initially be concerned with the establishment of the population dynamic rate equations of the rare earth ions, and subsequently with the propagation of the pump, signal, and ASE beams along the waveguide. The population dynamic equations are determined with the help of the simplified energy-level diagram of the rare earth system, as shown in Figure 4.2. In this diagram, the thick “upward arrow” represents the pump power photon transition rate R . The thin “upward” and “downward” arrows are the stimulated signal emission (W_e) and absorption (W_a) photon rates; the Einstein coefficient A_{21} accounts for the signal radiative spontaneous emission. The nonradiative decay rate, by means of multiphonon relaxations, is represented by A_{32} .

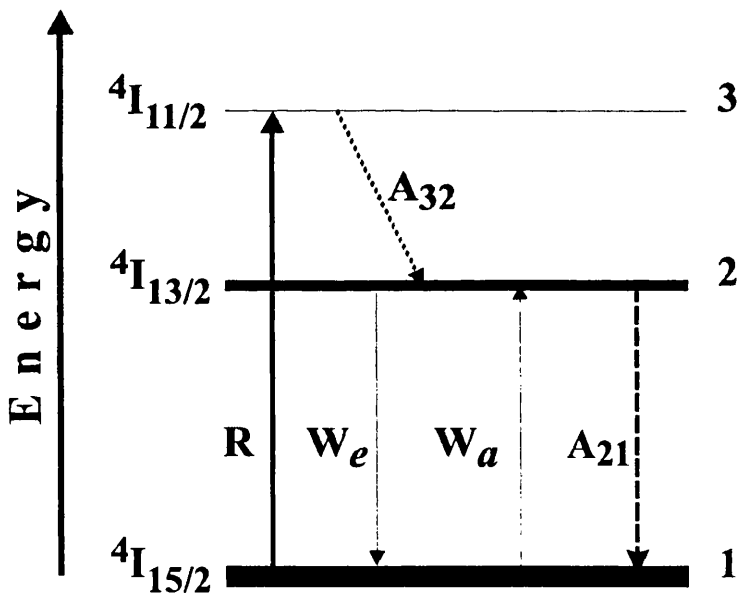


Figure 4.2: Simplified energy diagram levels of erbium

The optical gain of a laser material with an inverted population can be expressed mathematically by the rate equations describing the relationship between the pump and signal photon densities and the population densities, N_i , of the energy levels, i , as:

$$\frac{dN_1(x, y, z, t)}{dt} = -(R + W_a) \cdot N_1(x, y, z, t) + (W_e + 1/\tau_2) \cdot N_2(x, y, z, t) \quad (4.2)$$

$$\frac{dN_2(x, y, z, t)}{dt} = +(R + W_a) \cdot N_1(x, y, z, t) - (W_e + 1/\tau_2) \cdot N_2(x, y, z, t) \quad (4.3)$$

in the equations above the radiative transition rate A_{21} was substituted by $1/\tau_2$ which is the radiative lifetime of the metastable level. The photon conservation equation, where the erbium concentration, N_o , is assumed to be z -independent, and is given by:

$$N_o(x, y) \approx N_1(x, y, z) + N_2(x, y, z) \quad (4.4)$$

The description of the model of the gain medium as a two-level laser system (pumped into the 980 nm absorption band) implies that the population in the $^4I_{112}$ manifold is negligible. This depletion of the pump level is satisfied when the nonradiative decay rate, A_{32} , from the pump level is much larger than the pumping rate, R . For typical amplifiers and lasers parameters, this two-level model is valid for average pump power less than 1.0 W. This situation is satisfied in most of the reported experiments [23-26]. The transition rates shown in Figure 4.2 - R , W_a , and W_e , - are defined as:

$$W_a \equiv W_a(x, y, z) = \frac{\sigma_{sa} \cdot I_s(x, y, z)}{h \cdot \nu_s} \quad (4.5)$$

$$W_e \equiv W_e(x, y, z) = \frac{\sigma_{se} \cdot I_s(x, y, z)}{h \cdot \nu_s} \quad (4.6)$$

$$R \equiv R(x, y, z) = \frac{\sigma_{pa} \cdot I_p(x, y, z)}{h \cdot \nu_p} \quad (4.7)$$

where:

σ_{pa} is the pump ground state absorption cross-section;

σ_{sa} and σ_{se} are the signal ground state absorption and signal emission cross-sections;

$h\nu_p$ and $h\nu_s$ are the pump and signal photon energies;

$I_p(x, y, z)$ and $I_s(x, y, z)$ are the pump and signal photon intensities, respectively.

It can be shown that at the steady state condition ($d/dt = 0$), and with the help of the photon conservation law, the rate equations (4.2)-(4.3) provide explicit mathematical

relations for the distribution of the populations of the ground state levels $N_1(x,y,z)$, and the first excited state $N_2(x,y,z)$, in terms of transition rates expressions in the form:

$$N_1(x,y,z) = \frac{(W_e + 1 \tau_2) \cdot N_o(x,y)}{W_e + W_a + 1 \tau_2 + R} \quad (4.8)$$

$$N_2(x,y,z) = \frac{(W_a + R) \cdot N_o(x,y)}{W_e + W_a + 1 \tau_2 + R} \quad (4.9)$$

For clarity, the spatial dependence of the transition rates are not considered explicitly, i.e., $W_{a,e}(x,y,z) = W_{a,e}$. This dependence was introduced in the variables of the population levels to stress the dependence of the field distribution. This procedure is just to simplify the mathematical manipulation and does not describe the physical model. The intensities $I_s(x,y,z)$ and $I_p(x,y,z)$ - shown in the transition rates equations - are related to the mode densities by:

$$I_p(x,y,z) = P_p \cdot \psi_p(x,y) \cdot p(z) \quad (4.10)$$

$$I_s(x,y,z) = P_s \cdot \psi_s(x,y) \cdot s(z) \quad (4.11)$$

where P_p and P_s are the pump and signal power, respectively, which are launched into the waveguide at the input end ($z=0$). The functions $p(z)$ and $s(z)$ describe the evolution of the pump and the signal power along the waveguide, respectively, and are normalized such that $p(0)=s(0)=1$. Finally, $\psi_p(x,y)$ and $\psi_s(x,y)$ are the normalized energy densities of the pump and signal. These modes are normalized so that their surface integral over all space is unity.

$$\iint_{A \rightarrow \infty} \psi_p(x,y) \cdot dA = \iint_{A \rightarrow \infty} \psi_s(x,y) \cdot dA = 1 \quad (4.12)$$

The evolution of the pump and signal power in the waveguide, $I_p(x,y,z)$ and $I_s(x,y,z)$, along its length are described by the following propagation equations:

$$\iint_{A \rightarrow \infty} \frac{dI_p(x,y,z)}{dz} \cdot dA = - \iint_{A \rightarrow \infty} [\sigma_{pa} \cdot N_1(x,y,z) + \alpha_p] \cdot I_p(x,y,z) \cdot dA \quad (4.13)$$

$$\iint_{A \rightarrow \infty} \frac{dI_s^\pm(x,y,z)}{dz} \cdot dA = \pm \iint_{A \rightarrow \infty} [\sigma_{se} \cdot N_2(x,y,z) \mp \sigma_{sa} \cdot N_1(x,y,z) \mp \alpha_s] \cdot I_s^\pm(x,y,z) \cdot dA \quad (4.14)$$

There are two contributions to the evolution of the pump intensity along the

waveguide, both of which reduce the number of photons: the pump ground state absorption (GSA) and the background loss at the pump wavelength (α_p). The evolution of the signal intensity is described by three terms: one term contributing to the enhancement of the signal, which corresponds to the photons emitted from the upper level ${}^4I_{13,2}$ to the ground state ${}^4I_{15,2}$; and two reducing the number of photons, the GSA and the background loss at the signal wavelength (α_s). The equation accounting for the signal intensity considers the two directions of propagation: in the same direction as the pump power and in the opposite direction.

Applying the mode profiles equations (4.10)-(4.11) and the normalization condition of the energy densities, given by equation (4.12), to the pump and signal, the two propagation equations become:

$$\frac{dp(z)}{dz} = - \iint_{Core} \sigma_p \cdot N_1(x, y, z) \cdot \psi_p(x, y) \cdot p(z) \cdot dA - \alpha_p \cdot p(z) \quad (4.15)$$

$$\frac{ds^\pm(z)}{dz} = \pm \iint_{Core} [\sigma_e \cdot N_2(x, y, z) \mp \sigma_a \cdot N_1(x, y, z)] \cdot \psi_s(x, y) \cdot s^\pm(z) \cdot dA \mp \alpha_s \cdot s^\pm(z) \quad (4.16)$$

All these integrations are carried out within the rectangular waveguide core section only because the population densities N_i vanish outside the core, since the cladding is undoped.

The model can be expressed in terms of the following overlap integrals between the population densities and the electromagnetic field profiles:

$$\gamma_{pa}(z) = \iint_{Core} \sigma_{pa} \cdot N_1(x, y, z) \cdot \psi_p(x, y) \cdot dx dy \quad (4.17)$$

$$\gamma_{sa}(z) = \iint_{Core} \sigma_{sa} \cdot N_1(x, y, z) \cdot \psi_s(x, y) \cdot dx dy \quad (4.18)$$

$$\gamma_{se}(z) = \iint_{Core} \sigma_{se} \cdot N_2(x, y, z) \cdot \psi_s(x, y) \cdot dx dy \quad (4.19)$$

then the propagation equations become:

$$\frac{dp(z)}{dz} = -\gamma_{pa}(z) \cdot p(z) - \alpha_p \cdot p(z) \quad (4.20)$$

$$\frac{ds^\pm(z)}{dz} = \pm[\gamma_{se}(z) - \gamma_{sa}(z)] \cdot s^\pm(z) \mp \alpha_s \cdot s^\pm(z) \quad (4.21)$$

These two equations establish the basic mathematical tools for modelling a low-

concentration erbium doped optical waveguide laser and/or amplifier as long as the rate equations for level populations can be solved analytically in the steady state conditions (equations (4.8) and (4.9) are included in equations (4.17)-(4.19)). The propagation equations are then solved numerically.

Modelling single pass optical amplifiers consists of solving simultaneously the equations (4.20) and (4.21) with appropriate initial conditions. However, if lasers have to be modelled, the boundary conditions of the system must be included. These conditions for CW simulations are imposed on the values of $p(z)$, $s^+(z)$, and $s^-(z)$ as follows:

$$p(0) = 1$$

$$s^+(0) = R_i \cdot s^-(0), \quad s^-(L) = R_o \cdot s^+(L), \quad \text{and} \quad s^+(z) \cdot s^-(z) = \text{Constant}$$

where R_i is the reflectance of a highly reflecting mirror at the pump input end of the laser, R_o is the reflectance of the output coupler for the laser, and L is the length of the cavity.

In the following analysis of laser operation, the cavity round trip loss contributions are defined by:

$$\delta = \delta_0 + \frac{1}{L} \ln \left(\frac{1}{R_i \cdot R_o} \right) \quad (4.22)$$

the term δ_0 include contribution such as coupling loss at the waveguide-reflector interfaces, and the second factor is the amplitude condition for laser oscillation in a cavity.

The procedure implemented to solve the problem is based on the physical consideration of the device. Since at threshold the re-circulating signal intensity in the resonator is negligible, the calculated pump power threshold is such that the round trip gain provided by the laser medium equals the round trip cavity loss. Thus, the threshold condition is $2g_0(L) = \delta$, where $g_0(L)$ is the single pass small signal gain. At any operation point above the threshold, the total signal intensity travelling along

the waveguide is such that depletes the gain from its small-signal value g_0 to a value g such that the round-trip gain still equals the cavity round-trip loss. The difference in this operation condition is that now one needs to keep track of the signal saturation terms W_a and W_e , which involve two counter-propagating signals.

This is the laser system considered mainly for low rare earth doping level such as optical fibres, however, the procedure to solve numerically the problem will be adopted throughout the thesis. The next section will improve the present model including amplification of spontaneous emission. This will make it possible to model erbium doped waveguide amplifiers in the small signal operation regime.

4.3.1 Erbium doped waveguide amplifier - Modelling amplified spontaneous emission (ASE)

An important issue in optical amplifier design is the phenomenon of amplification of spontaneous emission (ASE), which occurs concurrently with noise amplification and degrades the signal-to-noise ratio (SNR). The performance of the amplifier, particularly when used as a preamplifier, depends crucially on the noise characteristics [27-29].

Figure 4.2 indicates the simplified three energy levels of interest for erbium, a high pump power level, $^4I_{11,2}$, and the two levels, $^4I_{13,2}$ and $^4I_{15,2}$, corresponding to the relevant laser transition around 1530 nm. However, the eightfold and sevenfold Stark splitting of the ground and upper levels respectively, combined with the effect of inhomogeneous broadening, make erbium doped glasses a rather complicated multilevel system. Then, a closed physical relation to account for the noise-like contribution to the amplified signal becomes impractical.

However, Desurvire *et al* [30] introduced a very useful approach to describing this laser system considering ASE. The multilevel system shown in Figure 4.3 can be modelled by considering the collective contribution of all erbium ions to the absorption and emission processes instead of that of the individual ionic system. For the computation of the ASE spectrum, the method consists of decomposing, or sampling, the absorption and fluorescence cross-section profile spectra of the laser transition in a set of N slots with an equal width $\Delta\nu$ centred at the frequency ν_i . Thus, each of the frequency slots contain the information for the amplified spontaneous emission propagating in two direction; one in the same direction as the pump (forward), and another in the opposite direction (backward). The population dynamic rate equations remains the same as shown in (4.2)-(4.3) before, the only changes are in the absorption and emission induced transition rates with the addition of the ASE contribution, thus becoming:

$$W_a \equiv W_a(x, y, z) = \frac{\sigma_{sa}(\nu_s) \cdot I_s(x, y, z)}{h \cdot \nu_s} + \sum_{i=1}^N \frac{\sigma_{sa}(\nu_i)}{h \cdot \nu_i} [I_{ASE}^+(x, y, z) + I_{ASE}^-(x, y, z)] \quad (4.23)$$

$$W_e \equiv W_e(x, y, z) = \frac{\sigma_{se}(\nu_s) \cdot I_s(x, y, z)}{h \cdot \nu_s} + \sum_{i=1}^N \frac{\sigma_{se}(\nu_i)}{h \cdot \nu_i} [I_{ASE}^+(x, y, z) + I_{ASE}^-(x, y, z)] \quad (4.24)$$

$$R \equiv R(x, y, z) = \frac{\sigma_{pa} \cdot I_p(x, y, z)}{h \cdot \nu_p} \quad (4.25)$$

The steady-state evolution of the pump, signal, and the two directions of the ASE correspond to a set of $2N+2$ differential equations, such as:

$$\frac{dp(z)}{dz} = -\gamma_{pa}(z) \cdot p(z) - \alpha_p \cdot p(z) \quad (4.26)$$

$$\frac{ds(z, \nu_s)}{dz} = [\gamma_{se}(z, \nu_s) - \gamma_{sa}(z, \nu_s)] \cdot s(z, \nu_s) - \alpha_s \cdot s(z, \nu_s) \quad (4.27)$$

$$\frac{ds_{ASE}^{\pm}(z, \nu_i)}{dz} = \pm [\gamma_{se}(z, \nu_i) - \gamma_{sa}(z, \nu_i) \mp \alpha_s] \cdot s_{ASE}^{\pm}(z, \nu_s) \pm m \cdot h \cdot \nu_i \cdot \Delta \nu_i \cdot \gamma_{se}(z, \nu_i) \quad (4.28)$$

h being the Planck constant and m the number of guided modes present at the signal wavelength. The ASE overlap integrals are now evaluated in each central frequency slot,

$$\gamma_{pa}(z) = \iint_A \sigma_{pa} \cdot N_1(x, y, z) \cdot \psi_p(x, y) \cdot dx dy \quad (4.29)$$

$$\gamma_{sa}(z, \nu_i) = \iint_A \sigma_{sa}(\nu_i) \cdot N_1(x, y, z) \cdot \psi_s(x, y) \cdot dx dy \quad (4.30)$$

$$\gamma_{se}(z, \nu_i) = \iint_A \sigma_{se}(\nu_i) \cdot N_2(x, y, z) \cdot \psi_s(x, y) \cdot dx dy \quad (4.31)$$

Considering the small difference among the ASE frequencies and the propagating signal, the same field distribution for the signal and ASE is assumed [30]. The boundary conditions for the pump, signal, and amplified spontaneous emission propagation are:

$$\begin{aligned} p(0) &= 1 & s(0) &= 1 \\ s_{ASE}^+(0, \nu_i) &= s_{ASE}^-(L, \nu_i) = 0 & \text{where } i &= 1, \dots, N \end{aligned}$$

and L is the waveguide length. The total ASE contributions at the end of each direction of propagation are computed using:

$$S_{ASE}^+ = \sum_{i=1}^N s_{ASE}^+(L, \nu_i) \quad \text{and} \quad S_{ASE}^- = \sum_{i=1}^N s_{ASE}^-(0, \nu_i)$$

and the total ASE propagating along the waveguide is:

$$S_{ASE} = S_{ASE}^+ + S_{ASE}^- \quad (4.32)$$

This sub-section restricted the mathematical problem to model low doping level erbium doped waveguides amplifiers and laser. The set of differential equations introduced previously accurately describes erbium-doped amplifiers at low doping levels, and can even account for ASE. The next section will deal with high concentrated erbium doped system and the modelling of such waveguide lasers and amplifiers.

4.4 Modelling a CW erbium doped waveguide laser and amplifier at high concentration

The fabrication of waveguides for active integrated optics devices requires, as mentioned previously, higher rare earth doping levels than that typical in fibres in order to overcome the short interaction length and enhance the gain of the amplifiers. Consequently, the deleterious upconversion process starts to take place [8,20,31]. Experimental results concerning ion-ion cross relaxation and clustering in erbium doped silicate-based glasses have pointed out these effects, reducing the efficiency of erbium doped fibre amplifiers and laser, are present even at the relatively small concentrations (below 1000ppm) [32]. As the mechanism developed in this energy transfer process was described in section 2.6.1, this section will start with the formulation of the mathematical problem itself.

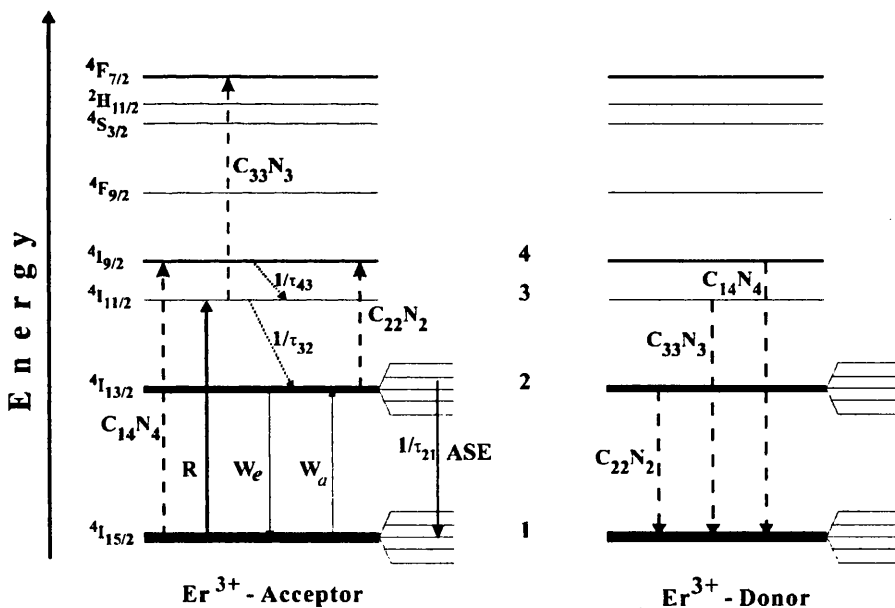


Figure 4.3: Complete energy diagram levels of erbium ion phosphosilicate glasses.

To describe ion-ion interactions, a system of dynamic differential rate equations is necessary to account for both the contribution of the neighbour ion, usually a denominated donor, which delivers the energy in the cross-relaxation process and the acceptor ion, as depicted in the Figure 4.3. For the sake of clarity, the donor ion diagram shows only the cross-relaxation contribution, represented by dashed “downward arrows”. In the acceptor level diagram, the pump transition rate R is

shown as a thick “upward arrow”. The thin “upward” and “downward” arrows represent the signal absorption, emission, and amplified spontaneous emission transition rates at the laser wavelength. Nonradiative transitions are shown as dotted “downward” arrows. The photons transferred from the donor ion (cross-relaxations) are represented in the acceptor ion diagram as dashed “upward arrows”. The Stark levels of interest in the erbium ion are numbered, from N_1 to N_4 , as shown in the diagram. The set of equations describing the dynamic evolution of photons among the Stark levels of a heavily erbium doped laser material are:

$$\frac{dN_1}{dt} = -(R + W_a) \cdot N_1 + (W_e + 1/\tau_2) \cdot N_2 + C_{22} \cdot N_2^2 - C_{14} \cdot N_1 \cdot N_4 + C_{33} \cdot N_3^2 \quad (4.33)$$

$$\frac{dN_2}{dt} = W_a \cdot N_1 - (W_e + 1/\tau_2) \cdot N_2 + \frac{N_3}{\tau_{32}} - 2C_{22} \cdot N_2^2 + 2C_{14} \cdot N_1 \cdot N_4 \quad (4.34)$$

$$\frac{dN_3}{dt} = R \cdot N_1 - \frac{N_3}{\tau_{32}} + \frac{N_4}{\tau_{43}} - 2C_{33} \cdot N_3^2 \quad (4.35)$$

$$\frac{dN_4}{dt} = -\frac{N_4}{\tau_{43}} + C_{22} \cdot N_2^2 - C_{14} \cdot N_1 \cdot N_4 + C_{33} \cdot N_3^2 \quad (4.36)$$

for clarity, the spatial and temporal dependence of the populations are not represented in the equations above, and the condition of z independence of the total number of photons is applied:

$$N_0(x, y) \approx N_1(x, y, z) + N_2(x, y, z) + N_3(x, y, z) + N_4(x, y, z) \quad (4.37)$$

The pump R , and the signal (W_a, W_e) transition rates are defined by equations (4.23)-(4.25). The new entities arising in the system of equations are C_{22} , C_{33} , and C_{14} for the heavily doped material, which represent the cross-relaxation coefficients. The procedure to obtain the propagation equations is similar to the low concentration case presented before. In connection with equations (4.17)-(4.21) or equations (4.23)-(4.31), if ASE is considered, highly doped erbium doped lasers and amplifiers can be modelled.

Thus, the set of equations which describes the evolution of the heavily and lightly, erbium doped waveguide lasers and amplifiers has been established. However, for the present rare earth doping level, a prominent difficulty arises since the differential equation system describing the population dynamics contains terms which are nonlinear with respect to the population. Consequently, the steady state population

cannot be expressed as a closed mathematical function, such as (4.8) and (4.9), and be included in the propagation equation, to be solved numerically. Different techniques have been used to deal with this problem. Usually, very fast methods are not very precise, and vice versa. The next section will be concerned with the presentation of a procedure to solve this system of equations numerically that has been demonstrated to be fast, precise and versatile.

4.5 The approach to model high concentrated rare earth doped waveguide laser and amplifiers

The approximation used in the modelling is based on the small contribution of the nonlinear terms to the population level dynamics. Evaluating the performance of the nonlinear equation system can do the estimation of the nonlinear contribution. The contribution of the nonradiative transition probabilities and their influence on the population of the main Stark levels involved are calculated and compared to the metastable level.

Considering the levels with energy below 21000 cm^{-1} , which correspond to the ${}^4F_{7,2}$ level, the largest multiphonon relaxations are due to the following energy gaps: ${}^4S_{3/2} \rightarrow {}^4F_{9/2}$, ${}^4F_{9/2} \rightarrow {}^4I_{9/2}$, and ${}^4I_{11/2} \rightarrow {}^4I_{13/2}$ corresponding to the energy gaps of $\Delta E_1 \approx 2800 \text{ cm}^{-1}$, $\Delta E_2 \approx 2600 \text{ cm}^{-1}$, and $\Delta E_3 \approx 3300 \text{ cm}^{-1}$, respective [33]. According to section 2.6, the nonradiative decay rates $W_{a,b}^{nr}$ are inversely proportional to the exponential of the energy gap separating the two levels, consequently, the larger the gap the less favourable is the material for nonradiative relaxation performance. The nonradiative decay rates can be determined by [34]:

$$W_{a,b}^{nr} = C \cdot [n(T) + 1]^p \cdot e^{-(\alpha \Delta E)} \quad (4.38)$$

In this expression C and α are host dependent parameters, assumed to be $5.4 \times 10^{12} \text{ s}^{-1}$ and $4.7 \times 10^{-3} \text{ cm}$ respectively [35], ΔE correspond to the energy gap, p is the number of phonon required to bridge the gap, and $n(T)$ is the Bose-Einstein occupation number of the effective phonon number given by $n(T) = [e^{(\hbar\omega/kT)} - 1]^{-1}$ where ω the phonon angular frequency. The phonon energy for this phosphosilicate glass is $\hbar\omega_R \cong 1200 \text{ cm}^{-1}$ [33]. Applying these experimental values, the calculated nonradiative transition rates are $W_{nr1} \approx 1.1 \times 10^7 \text{ s}^{-1}$, $W_{nr2} \approx 2.7 \times 10^7 \text{ s}^{-1}$, $W_{nr3} \approx 1.0 \times 10^6 \text{ s}^{-1}$ respectively. A first inspection in these values show us that, even the slowest transition rate, W_{nr3} , is three orders-of-magnitude faster than the metastable level lifetime of approximately 5.0 ms. This is confirmed by applying typical experimental parameters values to estimate the pump transition rate. Allowing for $\sigma_{ap} \sim 2.0 \times 10^{-25} \text{ m}^2$, $\lambda_p = 980 \text{ nm}$, and waveguide cross section of

8.0 $\mu\text{m} \times 6.0 \mu\text{m}$, the pump transition rate is given by:

$$R = \left(\frac{\sigma_{ap}}{h\nu_p} \right) \cdot I_p \approx 20 \cdot I_p \quad (4.39)$$

where I_p is given in mW, and R in s^{-1} . Considering a pump power of ~ 100 mW, R is confirmed to be about two orders of magnitude smaller than the nonradiative decay rate ($W_{nr} \sim 500R$), thus the population of the Stark level ${}^4I_{11,2}$ remains negligible as compared to the metastable level ${}^4I_{13,2}$.

Considering the small contribution of the levels 3 and 4, the population rate equation system, at the steady state condition, can be simplified to:

$$\frac{dN_1}{dt} = -(R + W_{12}) \cdot N_1 + (W_{21} + 1/\tau_{21}) \cdot N_2 - C_{22} \cdot N_2^2 + C_{14} \cdot N_1 \cdot N_4 - C_{33} \cdot N_3^2 = 0 \quad (4.40)$$

$$\frac{dN_2}{dt} = (R + W_{12}) \cdot N_1 - (W_{21} + 1/\tau_{21}) \cdot N_2 + C_{22} \cdot N_2^2 - C_{14} \cdot N_1 \cdot N_4 + C_{33} \cdot N_3^2 = 0 \quad (4.41)$$

for the populations N_1 and N_2 respectively, when they include the contribution of N_3 and N_4 levels. Therefore, the dynamic equations (4.33) and (4.34), of the levels one and two, can be used, as a first approximation, to describe the whole laser system.

The upconversion coefficient C_{22} has been measured indirectly from spectroscopic data. The measured values are of the order of $10^{-22} - 10^{-23} \text{ m}^3/\text{s}$ [36]. Unfortunately, the other coupling constants (C_{33} and C_{14}) have not been determined and only rough order-of-magnitude estimates are available. This may be a significant source of uncertainties, which have to be taken into account when high doping level and ion-ion interactions are considered. The C_{33} and C_{14} coefficients are expected to be smaller than C_{22} due to the indirect dependence on the population level [37-42]. Further simplification to the equations (4.40) and (4.41) can be made assuming all the constants equal to C_{22} ($C = C_{14} = C_{33} = C_{22}$). This represent the strongest influence of the nonlinear terms in the system of equations, and it is the least favourable situation to optimise the optical gain of an amplifier. Thus, with the above assumptions on the values of nonlinear coefficients, the rate equations for the two levels can be expressed as:

$$-(R + W_{12}) \cdot N_1 + (W_{21} + 1/\tau_{21}) \cdot N_2 - C \cdot (N_2^2 + N_3^2 - N_1 \cdot N_4) = 0 \quad (4.42)$$

$$+(R + W_{12}) \cdot N_1 - (W_{21} + 1/\tau_{21}) \cdot N_2 + C \cdot (N_2^2 + N_3^2 - N_1 \cdot N_4) = 0 \quad (4.43)$$

Applying typical experimental parameters used earlier to the equations (4.42) and (4.43) we found that, the pump transition rate gives the major contribution to the nonlinear equation terms. These terms are expected to be approximately one to three orders of magnitude smaller than the individual linear contribution.

Numerical solution of the nonlinear system of equations (4.33)-(4.36), can also be applied to estimate the influence of the nonlinear contribution to the population levels. The set of nonlinear differential rate equations were solved using the adaptive stepsize controlled Runge-Kutta method. The time stepsize varied with the simulation maintaining a fixed precision, equal to 10^{-6} , in the determination of the population levels. The simulation considered a germanosilicate optical fibre with the following characteristics:

Table 4.1: Parameters used as input data to the determination of the Figure 4.4 and Figure 4.5.

Variable	Symbol	Value – Unit
Fibre core radius	r	2.5 μm
Fibre numerical aperture	NA	0.20
Signal wavelength	λ_s	1.55 μm
Pump wavelength	λ_p	980 μm
Signal emission cross section	σ_s	$7.50 \times 10^{-21} \text{ cm}^2$
Pump absorption cross section	σ_p	$1.75 \times 10^{-21} \text{ cm}^2$
Metastable level lifetime	τ_{21}	11.0 ms
Fibre dopant concentration	N_0	0.06 and 1.00 wt%
Fibre length	L_f	0.50 m

These fibre characteristics support only single propagation mode for pump and signal. The temporal behaviour of each level is show in Figure 4.4. Two distinct doping levels were considered, a very low rare earth ions concentration (0.06 wt%) and a heavily doped (1.00 wt%), to estimate the limits of the nonlinear contribution. The first correspond to the low optical fibre doping level and the second simulation

is close to the amount of the rare earth found in the planar waveguide geometry. In both cases the simulations have run until the population equilibrium were attained. Even with a very low pump power, 5.0 ms has shown to be time sufficient to saturate the population of the metastable level. Applying the parameters listed in the Table 4.1 to the rate equations, the results show that when the equilibrium is reached, the influence in the population of the level 2 due to the nonlinear terms is about 8.5%. Moreover, as expected, the contribution of the levels 3 and 4 are negligible when compared with levels 1 and 2.

Figure 4.5 shows the result of this analysis; it corresponds to the population level of each state after 5.0 ms for different pump power. With pump power of 150 mW, the difference due to the nonlinear contribution is about 6.5%. Supported by these results, the nonlinear upconversion contribution to the system of equations is considered small and, the change suffered by the population at each Stark level due to the cross-relaxation process is expected to be proportionally small as well, compared to the respective population in the absence of the cross-relaxation.

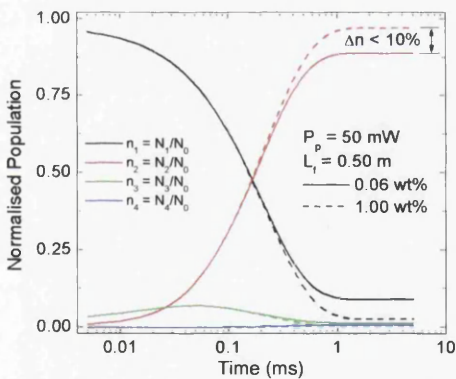


Figure 4.4: Rare earth population dynamic for two different doping levels.

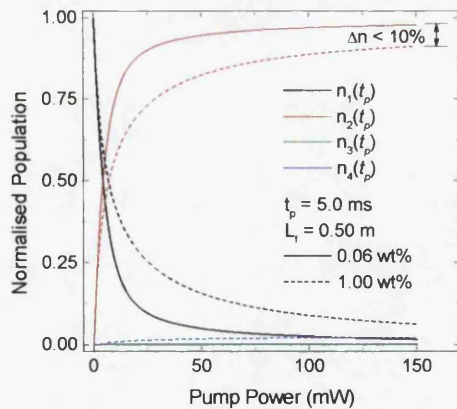


Figure 4.5: Rare earth population dynamics of two different doping level as a function of the pump power

Before proceeding with the presentation of the new modelling approach, some general considerations on modelling procedures will be addressed. As mentioned previously, the main task in the rare earth doped devices modelling consist, after the establishment of the population rate equation for the system, in the explicit determination of mathematical relations for the relevant level populations. Having

defined these expressions, the overlap integral given by equations (4.29)-(4.31) for instance, accounting for the interaction between a population level and the electromagnetic fields can be evaluated. In principle, closed-form solutions cannot be obtained if the rate equations contain nonlinear terms.

However, according to the electromagnetic theory, the characteristics of the guided-mode of the signal and pump radiations are functions of parameters related to the waveguide geometry and refractive index of the medium [43-45] which, generally speaking, do not depend in their turn on the state of rare earth ions. Even when the radiation wavelength coincides with a rare earth absorption band the contributions to the refractive index is insignificant ($\sim 10^{-8}$) [46-48]. Therefore, it is not expected that the re-distribution of the rare earth populations levels during the device operation will influence the guided mode of a radiation, even if the doping concentration increase becoming the rate equations nonlinear. Based on these considerations, a new assumption is introduced to express the rare earth population of the heavily doped medium as [49]:

$$\tilde{N}_i(x, y, z) \approx N_i^L(x, y, z) \cdot \left[1 + \Delta_{Ni}^{NL}(z) \right] \quad (4.44)$$

where $N_i^L(x, y, z)$ are the explicit expressions for the populations N_1 and N_2 defined for the low concentration devices (equations (4.33)-(4.36) setting $C_{ij} = 0$), and $\Delta_{Ni}^{NL}(z)$ are numerical factors which account for the nonlinear contribution due to the cross-relaxation process to the respective level. The nonlinear factors can be calculated as:

$$\Delta_{Ni}^{NL}(z) = N_i^L(x, y, z) \cdot \left[1 - \frac{N_i^{NL}(x, y, z)}{N_i^L(x, y, z)} \right] \quad (4.45)$$

$N_i^L(x, y, z)$ are the populations of the levels i calculated with the explicit expressions in the absence of cross-relaxation, and $N_i^{NL}(x, y, z)$ are the values of the population of the same level obtained through the numerical solutions of the system of equations; when both are calculated under the same pump conditions. To reduce the computation time required to solve the problem, a numerical routine to find the solution of a nonlinear system of equations was preferred instead to the traditional Runge-Kutta method.

Applying the approximation (4.44) to the spatial integral expressions (4.29)-(4.31),

the overlap integrals are then approximated by:

$$\begin{aligned}\gamma_{pa}(z) &= \iint_A \sigma_{pa}(v) \cdot \tilde{N}_1(x, y, z) \cdot \psi_p(x, y) \cdot dA \\ &\approx \iint_A \sigma_{pa}(v) \cdot N_1^l(x, y, z) \cdot [1 + \Delta_{N1}^{NL}(z)] \cdot \psi_p(x, y) \cdot dA\end{aligned}\quad (4.46)$$

$$\begin{aligned}\gamma_{sa}(z, v_i) &= \iint_A \sigma_{sa}(v_i) \cdot \tilde{N}_1(x, y, z) \cdot \psi_s(x, y) \cdot dA \\ &\approx \iint_A \sigma_{sa}(v_i) \cdot N_1^l(x, y, z) \cdot [1 + \Delta_{N1}^{NL}(z)] \cdot \psi_s(x, y) \cdot dA\end{aligned}\quad (4.47)$$

$$\begin{aligned}\gamma_{se}(z, v_i) &= \iint_A \sigma_{se}(v_i) \cdot \tilde{N}_2(x, y, z) \cdot \psi_s(x, y) \cdot dA \\ &\approx \iint_A \sigma_{se}(v_i) \cdot N_2^l(x, y, z) \cdot [1 + \Delta_{N1}^{NL}(z)] \cdot \psi_s(x, y) \cdot dA\end{aligned}\quad (4.48)$$

Applying this approximation, the heavily doped amplifier modelling procedure has the same approach as that for the low doping level. The contribution of the nonlinear terms appears as a corrective numerical factor. Verification of the accuracy of the approximation and the modelling itself will be made by comparison of calculations and experimental results as described next.

4.5.1 Validation of the model

Verification of the approximation and the model will be made by fitting calculations performed using the model to some experimental results of well-examined waveguide amplifiers [23-26,42]. All the input data used for modelling were obtained from the referenced papers, and are displayed in Table 4.II and Table 4.III. Table 4.II contains a list of general parameters, and Table 4.III are the parameters related to the specific waveguide. The absorption and emission cross-sections around 1530 nm are shown in Figure 2.5; they are typical values for phosphosilicate erbium-doped glasses [50].

Forward and backward amplified spontaneous emission has been spectrally resolved by using 200 frequency slots from 1450 nm to 1650 nm. The input signal considered as $P_s = 1.0 \mu\text{W}$ for all simulations.

Table 4.III is the summary of the specific parameters for each amplified analysed. The parameters listed are respectively the waveguide length, the rectangular

waveguide cross-section (width \times thickness), the measured scattering losses - when more than one value is given, they correspond to the pump and signal losses near their respective wavelengths. The next parameters correspond to the reported erbium concentration in wt%, followed by the refractive index difference between cladding and core layers. The numbers in the last column correspond to the referenced paper which has provided the experimental data.

Table 4.II: Fixed waveguide parameters used in all modelling simulations

Parameter	Symbol	Value – Unit
Pump wavelength	λ_p	980 nm
Signal wavelength	λ_s	1530 nm
Pump absorption peak cross-section	σ_{ap}	$1.95 \cdot 10^{-25} \text{ m}^2$
Signal absorption and emission peak cross section	$\sigma_{sa} = \sigma_{se}$	$5.60 \cdot 10^{-25} \text{ m}^2$
Cladding refractive index	n	1.4764
Radiative lifetime	τ_{21}	8.00 ms
Nonradiative transition rates	A_{32}, A_{43}	$5 \cdot 10^4 \text{ s}^{-1}, 4 \cdot 10^4 \text{ s}^{-1}$
Upconversion coefficients	$C_{22} = C_{33} = C_{14}$	$(-6.40 + 18.00 \cdot N_{i0}) \cdot 10^{-24} \text{ m}^3/\text{s}$

The choice of these experimental results was because all devices were fabricated by the flame hydrolysis deposition method. Moreover, the most important parameters to be used as input data to simulate should be also available. The test of the model under different pump power regimes of operations was also performed.

Table 4.III : Individual parameters for each waveguide analysed

	Length (cm)	A = x·y ([M1]μm ²)	Loss (dB/cm)	Concentration (wt%)	Δn (%)	References
Figure 4.6	23.0	8×7	0.15	0.54	1.2	25
Figure 4.7	7.0	8×7	0.08/0.09	0.46	1.2	26
Figure 4.8	7.5	8×11	0.17	0.48	1.6	24
Figure 4.10	19.4	8×7	0.07	0.54	1.2	23/41

Figure 4.6, Figure 4.7, and Figure 4.8 depict the comparison between modelling and experiment when the amplifiers were tested in the three different pump power regime

of operation mentioned above. The low pump power case is particularly interesting to estimate the influence of the amplified spontaneous emission on the final amplifier performance. As depicted in the figures, all the simulations are in very good agreement with the respective experimental results. Any small discrepancies can be attributed to the uncertainty in the experimental parameters, such as the upconversion coefficient. The best agreement between simulation and experiment were seen for medium and high pump power levels Figure 4.7 and Figure 4.8 respectively.

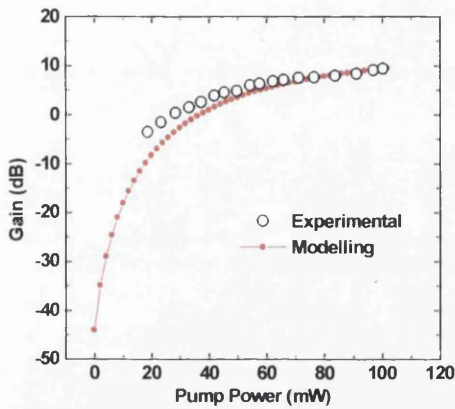


Figure 4.6: Erbium doped waveguide amplifier modelling under low pump power.

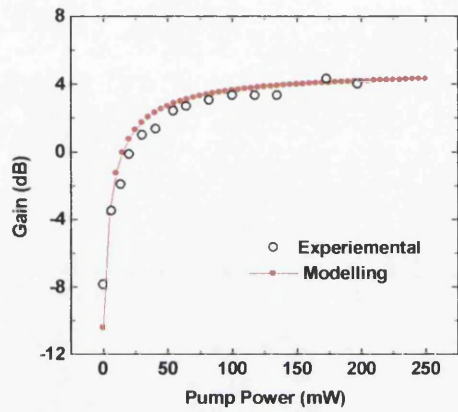


Figure 4.7: Erbium doped waveguide amplifier modelling under normal pump power.

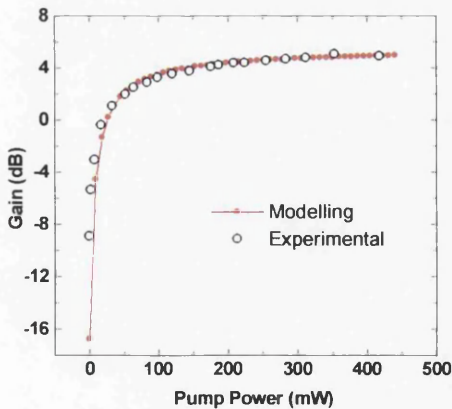


Figure 4.8: Erbium doped waveguide amplifier modelling under high pump power.

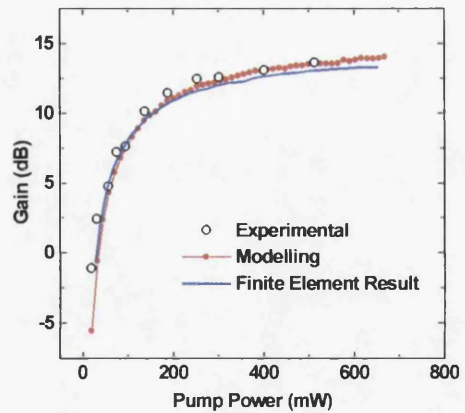


Figure 4.9: Modelling result compared with experimental data and the result obtained with finite element modelling in the same waveguide structure [42].

A final test of the validity of the model is performed through a comparison of the results of the amplifier gain reported in the Figure 4.9 to Figure 4.11 where the model was tested against others amplifier parameters, such as waveguide length and

rare earth concentration. In the Figure 4.9 was also included a reported result from the literature [42] of the same amplifier structure solved by the finite element modelling (FEM). It should be noted that there is excellent agreement between the results from this model (red solid circles) and the one from the result calculated using the FEM (solid blue line). There is no report on the time required for the FEM to compare with the new procedure. Measurements shown in Figure 4.10 were concerned with the dependence of the gain on the amplifier length. According to reference [23], the best experimental result shown a gain of 13.7 dB in a 19.4 cm long waveguide pumped at 500 mW. Under the same situation, our model calculated a 13.55 dB gain.

Di Pasquale *et al.* [42], modelling the influence of uniform upconversion mechanisms in the same waveguide structure, proposed the inclusion of a linear concentration function for the nonlinear coefficients, as reported in Table 4.I. The same function was considered in the present modelling which shows a good fitting to the experimental data as reported in Figure 4.11.

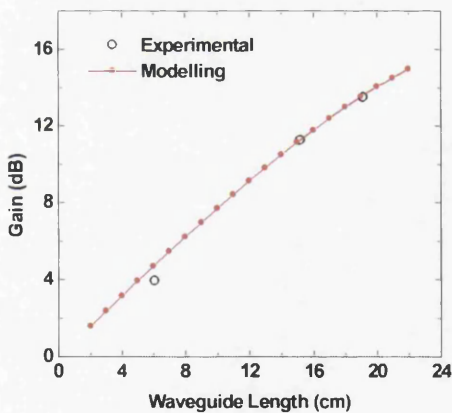


Figure 4.10: Experimental and modelling results for the variation of the amplifiers gain against waveguide length.

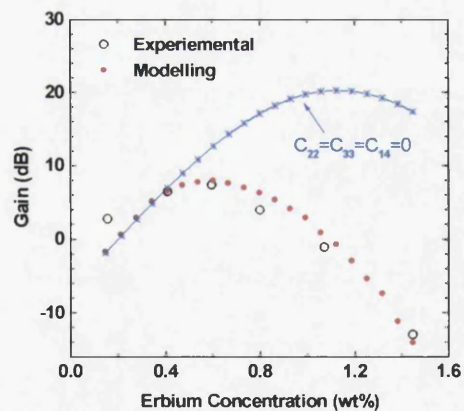


Figure 4.11: Modelling of the amplifier gain as a function of the rare earth concentration. The blue line corresponds to the modelling setting the cross relaxation coefficients to zero.

Finally, some consideration on computation time required to the simulations. All these results came from simulation programs written in FORTRAN-77 running on an IBM/PC - Pentium with 100MHz clock rate.

While maintaining a fixed precision in the propagation subroutine, we observed a linear variation between the run time simulations and the number of equations used

to evaluate the amplified spontaneous emission (ASE). Propagation considering only two differential equations, no ASE, takes approximately 12 s, whereas for 400 ASE differential equations it took about 100 s for the same propagation distance. This run time increase represented a variation of less than $\pm 2\%$ in calculated gain. This variation in the calculated gain is much less than the uncertainties in some measured experimental parameters necessary as input data, such as cross-section and lifetime.

The same calculations were also performed for the saturated regime to minimise the influence of the ASE on the net gain. As the precision in the adjustable-step size subroutine is a crucial factor determining the run time, its effect was also measured. An increase of the precision from 10^{-5} to 10^{-9} resulted in an increase in the run time from 12 s to 110 s, whereas the calculated gain was not altered by more than 0.01%. This small influence of the precision on the calculated gain is true for relatively low rare earth concentrations (~ 0.50 wt%), when the gain varies smoothly along the waveguide. For a heavily doped material (~ 1.50 wt%) a similar variation of precision can result in a difference of up to 7% in the gain. However, smaller step sizes and accuracy do not have a linear relation. Less than 1.5% of improvement in the gain, against the 12 minutes run time, is obtained if the precision is altered from 10^{-9} to 10^{-11} .

Forward and backward amplified spontaneous emissions were sampled in 100 frequency slots each. Pump, signal, and ASE, as a set of 202 coupled differential equation, are solved by numerical integration through the waveguide in approximately 115 s, showing the validity of this tool to design erbium doped waveguide amplifiers.

4.6 Conclusion

In conclusion, following the comparisons between experimental and theoretical results, the approximation proposed and introduced in the present chapter, has been shown to be suitable to analyse and optimise heavily rare earth doped waveguide amplifier. The modelling procedure was tested against experimental results obtained from erbium-doped phosphosilicate glass amplifiers in a planar form, fabricated by flame hydrolysis deposition.

The amplifier model was tested against four different well-known waveguide amplifiers. Within the accuracy of the input data, all calculations have shown very good agreement with the respective experimental results. The model was compared with reported results, for the same waveguide structure, modelled by finite element and has shown excellent agreement between both set of data. Besides, very simple and fast computer programs can be generated using this new approach. Therefore it becomes a simple task to deal with hundreds of differential equations at the same time, and the degradation of noise figure can be estimated through the amplified spontaneous emission prediction.

The important achievement of these calculations is the possibility of predicting and optimising CW operation of high concentration erbium doped waveguide laser. This is not easily done by finite element modelling because the time needed for simulation can become prohibitive for small computers. This high accuracy observed in all results are not only attributed to the small contribution of the nonlinear terms to the population equations, but also to the unique approximation used to solve the problem. The origin of the assumption to obtain the approximations indicates that similar procedure can be used as a tool to model other rare earth ion, including system with more than one ion such as $\text{Er}^{3+}/\text{Yb}^{3+}$ and $\text{Tm}^{3+}/\text{Yb}^{3+}$ waveguide laser system.

4.7 References

- 1 C.R. Giles, E. Desurvire, "Modeling erbium-doped fiber amplifiers", *Journal of Lightwave Technology* **9**, 271-283 (1991).
- 2 P. Petersen, M.P. Sharma, A. Gravielides, "Modelling of excited state absorption and upconversion in erbium germanosilicate continuous wave fibre lasers", *Optical and Quantum Electronics* **28**, 1089-1103 (1996).
- 3 P.R. Morkel, R.I. Laming, "Theoretical modeling of erbium-doped fiber amplifiers with excited-state absorption", *Optics Letters* **14**, 1062-1064 (1989).
- 4 M.J.F. Digonnet, "Closed-form expressions for the gain in the three- and four-level laser fibers", *IEEE Journal of Quantum Electronics* **26**, 1788-1796 (1990).
- 5 C. Barnard, P. Myslinski, J. Chrostowski, M. Kavehrad, "Analytical model for rare-earth-doped amplifiers and lasers", *IEEE Journal of Quantum Electronics* **30**, 1817-1830 (1994).
- 6 S. Jarabo, M.A. Rebolledo, "Analytic modeling of erbium-doped fiber amplifiers on the basis of intensity-dependent overlapping factors", *Applied Optics* **34**, 6158-6163 (1995).
- 7 I.M.I. Habbab, A.A.M. Saleh, P.K. Runge, "Erbium-doped fiber amplifiers: Linear approximations", *Journal of Lightwave Technology* **13**, 33-36 (1995).
- 8 M. Federighi, I. Massarek, P.F. Trwoga, "Optical amplification in thin optical waveguide with high erbium concentration", *IEEE Photonics Technology Letters* **5**, 227-229 (1993).
- 9 J. Thogersen, N. Bjerre, J. Mark, "Multiphonon absorption and cooperative upconversion excitation in Er^{3+} -doped fibers", *Optics Letters* **18**, 197-199 (1993).
- 10 J.L. Wagener, P.F. Wysocki, M.J.F. Digonnet, H.J. Shaw, "Effects of concentration and clusters in erbium-doped fiber lasers", *Optics Letters* **18**, 2014-2016 (1993).
- 11 T. Rasmussen, A. Bjarklev, J.H. Povlsen, O. Lumholt, K. Rottwitt, "Numerical modeling of an integrated erbium-doped glass laser", *Fiber and Integrated Optics* **10**, 239-243 (1991).
- 12 O. Lumholt, A. Bjarklev, T. Rasmussen, C. Lester, "Rare earth-doped integrated glass components: modeling and optimization", *Journal of Lightwave Technology* **13**, 275-282 (1995).
- 13 P. Torres, A.M. Guzman, "Complex finite-element method applied to the analysis of optical waveguide amplifiers", *Journal of Lightwave Technology* **15**, 546-550 (1997).
- 14 F. Di Pasquale, M. Zoboli, "Analysis of erbium-doped waveguide amplifiers by a full-vectorial finite-element method", *Journal of Lightwave Technology* **11**, 1565-1574 (1993).
- 15 F. Di Pasquale, M. Zoboli, M. Federighi, I. Massarek, "Finite-element modeling of silica waveguide amplifiers with high erbium concentration", *IEEE Journal of Quantum Electronics* **30**, 1277-1282 (1994).

- 16 M. Zoboli, and P. Bassi, "The finite element method for anisotropic optical waveguides", C.G. Someda and G. Stegeman (ed.), Anisotropic and Nonlinear Optical Waveguides (Elsevier Science Publishers pp.77-116 (1992))
- 17 C.G. Atkins, J.R. Armitage, R. Wyatt, B.J. Ainslie, S.P. Craig-Ryan, "Pump excited state absorption in Er³⁺-doped optical fibres", *Optics Communications* **73**, 217-222 (1989).
- 18 C.G. Atkins, J.F. Massicot, J.R. Armitage, R. Wyatt, B.J. Ainslie, S.P. Craig-Ryan, "High-gain, broad spectral bandwidth erbium-doped fibre amplifier pumped near 1.5 μ m", *Electronic Letters* **25**, 910-911 (1989).
- 19 F. Horst, T.H. Hoekstra, P.V. Lambeck, Th.J.A. Popma, "Design of 1480-nm diode-pumped Er³⁺-doped integrated optical amplifiers", *Optical and Quantum Electronics* **26**, S285-S299 (1994).
- 20 Y. Kimura, M. Nakazawa, "Gain characteristics of erbium-doped fiber amplifiers with high erbium concentration", *Japanese Journal of Applied Physics: Part 1* **32**, 1120-1125 (1993).
- 21 M. Artiglia, P. Di Vita, M. Potenza, "Optical fibre amplifiers: physical model and design issues", *Optical and Quantum Electronics* **26**, 585-608 (1994).
- 22 B. Pedersen, "Small-signal erbium-doped amplifiers pumped at 980 nm: a design study", *Optical and Quantum Electronics* **26**, S273-S284 (1994).
- 23 T. Katigawa, K. Hattori, K. Shuto, M. Yasu, M. Kobayashi, M. Horiguchi, "Amplification in erbium-doped silica-based planar lightwave circuit", *Electronics Letters* **28**, 1818-1819 (1992).
- 24 K. Shuto, K. Hattori, T. Katigawa, Y. Ohmori, M. Horiguchi, "Erbium-doped phosphosilicate glass amplifier fabricated by PECVD", *Electronics Letters* **29**, 139-141 (1993).
- 25 K. Hattori, T. Katigawa, M. Oguma, M. Wada, J. Temmyo, M. Horiguchi, "Erbium-doped silica-based amplifier pumped by 0.98 μ m laser diodes", *Electronics Letters* **29**, 357-359 (1993).
- 26 K. Hattori, T. Katigawa, M. Oguma, H. Okazaki, Y. Ohmori, "Optical amplification in Er³⁺-doped P₂O₅-SiO₂ planar waveguides", *Journal of Applied Physics* **80**, 5301-5308 (1996).
- 27 R.J. Mears, L. Reekie, I.M. Jauncey, D.N. Payne, "Low-noise erbium-doped fibre amplifier operating at 1.54 μ m", *Electronics Letters* **23**, 1026-1028 (1987).
- 28 S. Wen, S. Chi "Characteristics of gain and signal-to-noise ratio of a distributed erbium-doped fiber amplifier", *Journal of Lightwave Technology* **10**, 1869-1878 (1992).
- 29 I. Jacobs, "Dependence of optical amplifier noise figure on relative-intense-noise", *Journal of Lightwave Technology* **13**, 1461-1465 (1995).
- 30 M. Desurvire, J.R. Simpson, "Amplification of spontaneous emission in erbium-doped single-mode fibers", *Journal of Lightwave Technology* **7**, 835-845 (1989).
- 31 H. Masuda, A. Tanaka, K. Aida, "Modeling the gain degeneration of high concentration erbium-doped fiber amplifiers by introducing inhomogeneous

at these wavelengths is rather low, leading to an insufficient population in the 3H_4 state. In contrast, the ground state absorption (GSA) grows significantly at wavelengths between 1160 and 1240 nm. Thus, a combination of the first and second Stokes components at 1113 and 1167 nm respectively results in this efficient blue upconversion [24,28]. Sanders *et al.* have also demonstrated the most efficient single wavelength pumped blue upconversion lasing, in Tm^{3+} fluoro-based optical fibre is 1120 nm [5].

The dependence of the blue light intensity on the pump power is plotted in Figure 5.4. The inset of the figure shows the same dependence in the log units, revealing a slope equal to three, corresponding to a three-photon process. The blue light was the strongest, with the measured power of 141 nW at the output of the 5.9 cm long device for an average pump power of ~ 70 mW.

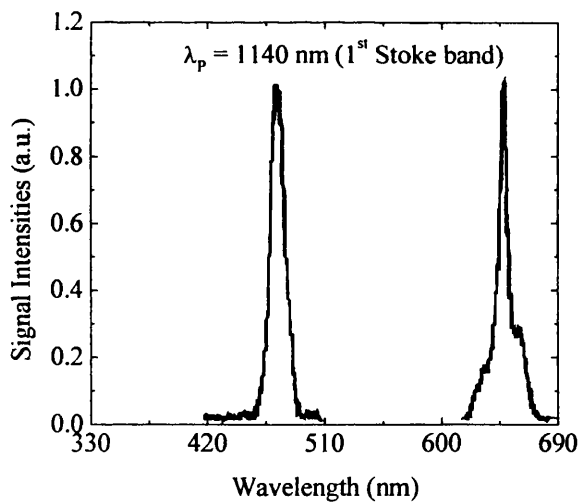
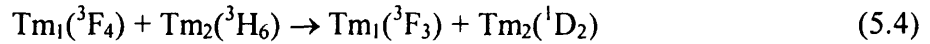
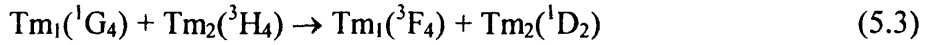
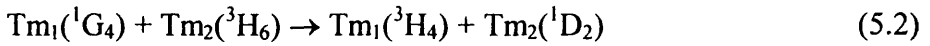


Figure 5.5: Fluorescent upconversion signals generated in a single Tm^{3+} (0.2 M) sample pumped at 1113 nm (correspond to the first Stoke band of the SRS).

Additional weaker lines were also observed. The ultraviolet band at 366 nm (marked as “a” in figure) is due to the transition $^1D_2 \rightarrow ^3H_6$ ($\beta = 0.43$), and the weak blue signal at 451 nm (“b”) corresponding to the transition $^1D_2 \rightarrow ^3H_4$ ($\beta = 0.41$). The near infrared signal at 648 nm - marked as “e” and corresponding to the $^1D_2 \rightarrow ^3F_4$ transition with the branching ratio smaller than $\beta = 0.08$ - is present as a small contribution to the broad base of the red transition at 648 nm (this transition is not represented in the energy level diagram). Finally, the bands marked with a “star”

were identified as the contribution from the third-order diffraction grating of the first and second SRS Stokes, respectively.

Different possibilities exist for the excitation mechanism of the 1D_2 level: three-photon absorption from the ground state to the 1D_2 level is one of them. An alternative route involving the fundamental laser radiation at 1064 nm is due to photons stored in the 3H_5 level after the first resonant absorption step. These photons would be excited to 1D_2 level through two-photon absorption. It is also feasible, especially as the Tm^{3+} doping level is high, that cross relaxation between neighbouring ions takes place. There are three possible paths:



In order to isolate the various excitation processes involved, the experiment was modified to separate the fundamental signal and individual Stokes lines incident at the waveguide using a prism and aperture. Exciting with the first Stokes line (1113 nm) only, both the blue light (482 nm) and the red light (648 nm) were easily detectable. Of particular note when using this pump wavelength was the absence of the 366 nm and 451 nm lines from the 1D_2 level. The emptying of the 1D_2 upper level when the fundamental laser radiation at 1064 nm is not present, is an evidence that the three photon and(or) two photon absorption are(is) important mechanism(s) to populate this level. The generated spectrum measured when pumping with the first Stoke band is shown in Figure 5.5.

Due to the lower efficiency conversion to the second Stoke line, both the red and blue fluorescence were reduced in intensity but still detectable.

The lifetime of the 1G_4 level was measured with the laser operated in the QSML regime. A monochromator tuned to the blue emission wavelength and a fast photodetector were used to separate and collect the signal. The fluorescence lifetime of the $^1G_4 \rightarrow ^3H_6$ transition (482 nm) was measured to be 280 μs , indicating that the Tm^{3+} ions were incorporated into the glass matrix in a rather homogeneous manner. It is widely known that high rare earth concentration form clusters which are responsible for reducing the fluorescence lifetime. For instance, Zou *et al.* [29]

reported a reduction from 288 μs to 22 μs when the concentration of thulium ions was increased from 0.1 to 2.0 cat% in germanate glasses.

In summary, blue light upconversion generation was demonstrated in single Tm^{3+} -doped phosphosilicate waveguides pumped by Nd:YAG laser operation in both ML and QSML regimes. It was possible to obtain efficient blue upconversion only when the waveguide was pumped by wavelength in the range 1113-1167 nm, generated in a commercial optical fibre due to SRS. This pumping scheme has shown the maximum conversion efficiency when a combination of the first (1113 nm) and second (1167 nm) Stokes lines due to the stimulated Raman scattering, along with the fundamental laser radiation at 1064 nm were launched into the waveguide. The next section of this work will be devoted to demonstrating the viability of this upconversion process at wavelengths available from commercial diode lasers.

5.3.2 Single Tm^{3+} - SiO_2 - P_2O_5 doped sample pumped at 800 nm

The experimental set-up described here will be used for all the following measurements. The schematic arrangement is depicted in Figure 5.6. It consists of an argon ion laser, pumping a tuneable, CW Ti:Sapphire laser which was used as a source of fundamental radiation. The visible or infrared radiation (at 678 nm, 798 nm, or 977 nm) was coupled into, and collected from, a 50.0 μm wide waveguide through a pair of $\times 10$ (numerical aperture $\text{NA} = 0.17$) objective lenses. For the lifetime measurements, a pair of quartz lenses (L1 and L2, with focal length of 10.0 cm), and a mechanical chopper placed in the beam waist, will also be included in the laser beam path.

The pump wavelength of 798 nm in single Tm^{3+} -doped samples is not appropriate for blue upconverted light generation. The reason can be explained with the help of the energy level diagram in Figure 5.7. The only possible mechanism to match the energy of two photons at the pump wavelength, and excite them from the ground state $^3\text{H}_6$ to the upper $^1\text{G}_4$ level is show as thick up arrows in the figure. The first pump photon is used to excite the thulium ions from the ground state ($^3\text{H}_6$) to the intermediate level ($^3\text{F}_4$). A high efficiency for populating the $^1\text{G}_4$ level depends on a high population in the level $^3\text{H}_5$, from where a second pump photon experiment ESA

to the upper level. However, according to the branching ratios of the 3F_4 level, only approximately 4% of those photons relax to the lower 3H_5 energy level, making this pumping scheme very inefficient. Blue light was only just seen by naked eye, in a dark room, under very high pump power, usually above 500 mW.

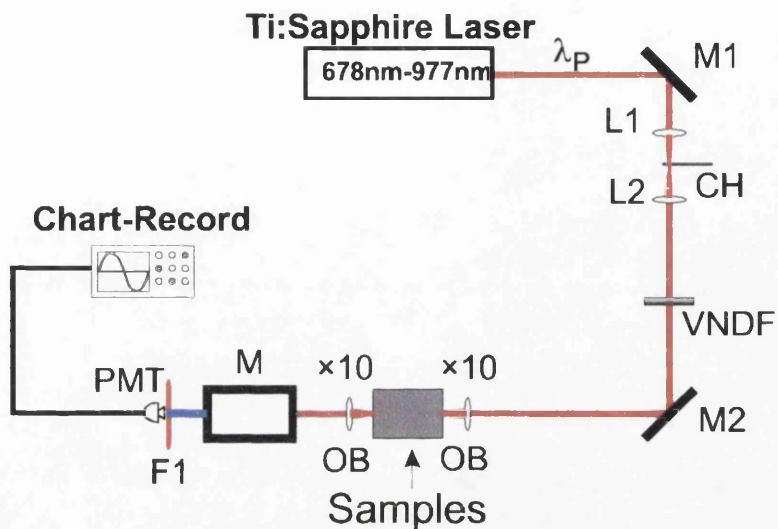


Figure 5.6: Experimental set-up arrangement for the measurements at 678 nm, 798 nm, and 977 nm. L1 and L2 are lenses with focal length of 10.0 cm, CH is a mechanical chopper. VNDF is a variable neutral density filter. M1 and M2 are mirrors. OB is two objective lenses ($\times 10$ NA=0.17). PMT, F1, M are photomultiplier tube with maximum response in the blue region, filter cutting the laser pump wavelength and a monochromator, respectively.

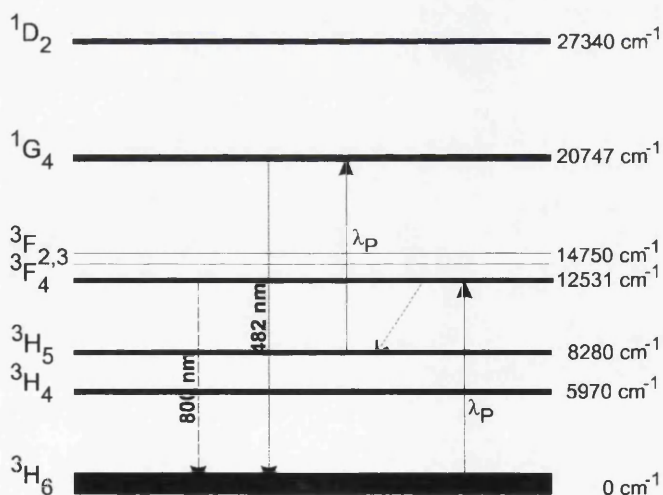


Figure 5.7: Energy level diagram of Tm^{3+} ion in $SiO_2-P_2O_5$ glass system pumped at 798 nm. The solid up “arrows” correspond to the pump wavelength and the thick dashed down “arrow” is the measured signal. The thin dotted “arrow” shows the transition to generate blue light at 482 nm

5.3.3 Single Tm^{3+} - SiO_2 - P_2O_5 doped sample pumped at 678 nm

In the early 90's a new pumping scheme to generate blue upconversion in Tm^{3+} -doped fluoride glasses via two-photons was reported [1,34]. In those experiments, red light at 647 nm and/or 676 nm, from a Kr laser, was used to excite Tm^{3+} -doped fluoride glasses and generated blue light at 450 nm and 480 nm. Providing that red diode lasers with sufficient power become available, blue emission as a result of a two-step upconversion process, should be generated with one diode laser in the red spectral range. Several groups have been doing research in optimisation of new single Tm^{3+} ions doped hosts at this wavelength, usually fluoro-based glasses [4,14,31,35,36].

In this section, the availability of the single thulium doped phosphosilicate glass to generate blue upconversion light is analysed. Figure 5.8 depicts a typical measured spectrum from a 0.2 M single thulium doped waveguide sample pumped at 678 nm, and Figure 5.9 shows a possible excitation mechanism to obtain these signals. The measured signals are ascribed due to the following upconversion transitions:

$^1\text{D}_2 \rightarrow ^3\text{H}_6$	corresponding to 361 nm;
$^1\text{D}_2 \rightarrow ^3\text{H}_4$	corresponding to 451 nm;
$^1\text{D}_2 \rightarrow ^3\text{H}_5$	corresponding to 545 nm;
$^3\text{F}_3 \rightarrow ^3\text{H}_6$	corresponding to 721 nm.

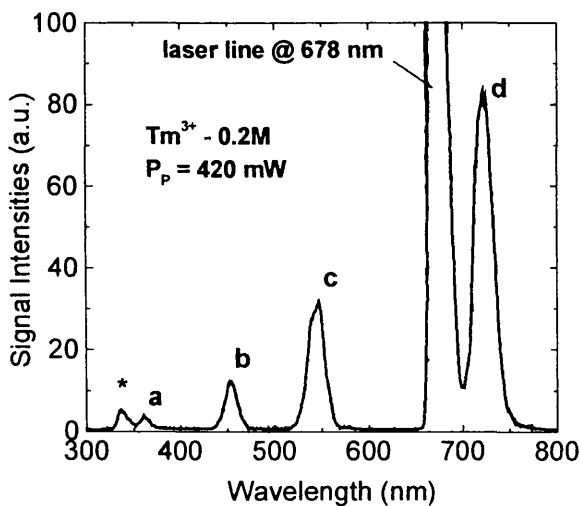


Figure 5.8: Upconversion signals in the UV, visible, and near infrared spectral region recorded using 420 mW of red light from a CW Ti:Sapphire laser at 678 nm, coupled into a 0.2 M single Tm^{3+} waveguide.

The spectral band marked with a star in the Figure 5.8 corresponds to the second order diffraction grating of the pump wavelength ($\lambda_p/2$). Due to the proximity of the signals and pump wavelengths, a filter was used to minimise the intensity of the laser line and avoid saturation of the photomultiplier tube (PMT). A major new feature in this result, compared with the published literature [35], is the absence of measurable blue light at 482 nm (corresponding to the thulium transition $^1G_4 \rightarrow ^3H_6$). The reported upconversion mechanism for fluoride glasses [14,31] indicates the absorption of one pump photon from the metastable level 3H_4 to the level 1G_4 as the route responsible for exciting Tm^{3+} ions and generating visible signals. This process is represented as dashed arrows in the energy diagram level of Figure 5.9. However, as observed in the previous pumping mechanism at 800 nm, most of the relaxation from level 3F_4 ($\beta \sim 0.78$) is to the ground state 3H_6 , leaving the 3H_4 , and 3H_5 levels almost empty. This also shows that the 1G_4 level is not efficiently populated by relaxation or any other process from the 1D_2 level.

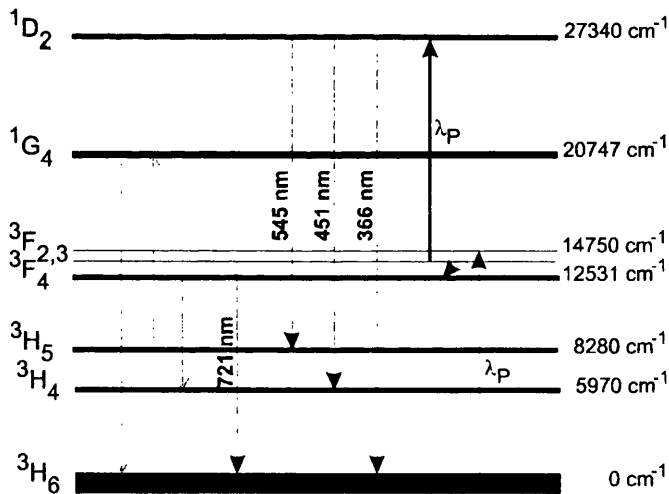


Figure 5.9: Energy level diagram of Tm^{3+} ion in $SiO_2-P_2O_5$ glass system pumped at 678 nm. The solid up “arrows” correspond to the pump wavelength and the thick dashed down “arrows” represent the measured signals. The three thin dashed “arrows” at the left hand side of the diagram, show the expected transitions to generate blue light at 482 nm.

Attempting to follow the upconversion process path, two signals were measured as a function of the pump power. As previously shown, the number of photons involved in each step is evaluated by the power dependence of the measured curve. The quadratic dependence of the blue signal at 451 nm and the linear dependence of the signal at 721 nm with the laser pump power for the same sample is shown in Figure

5.11, and Figure 5.10, respectively. These are indication of the two and one photon processes respectively. The near infrared signal at 721 nm has shown indication of saturation when the pump power exceed 300 mW, while the generated blue light has not. This different behaviour for both signals is caused by the efficient depopulation of the 3F_3 level, responsible for the ESA of the second photon to 1D_2 level.

Besides the high pumping rate to the $^3F_{2,3}$, there are effective nonradiative and radiative transitions to the 3F_4 and 3H_6 levels respectively, reducing the population and the possibility of saturating the population of 1D_2 upper level.

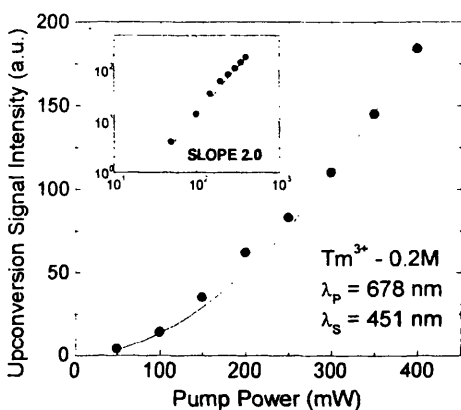


Figure 5.10: Pump power dependence of the upconverted signal at 451 nm. The inset corresponds to the linear Log-Log plot of the same experimental data with slope 2.

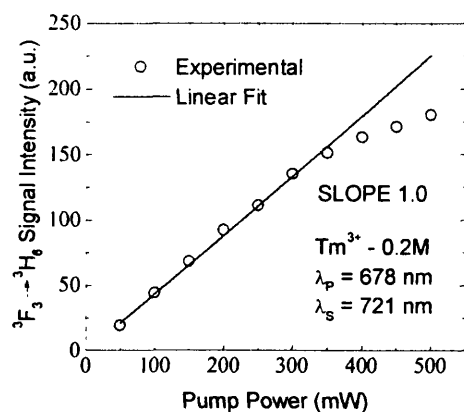


Figure 5.11: The linear pump power dependence of the intermediate signal at 721 nm.

The lifetime of $^1D_2 \rightarrow ^3H_4$ transition was also measured. The experimental set-up used for the measurements of the blue light lifetime is depicted Figure 5.6. A continuous wave (CW) Ti:Sapphire laser operating at 678 nm, delivering 70 mW of red light, was used as radiation source. A variable neutral density filter (VNDf) was used to maintain the pumping power level constant during a series of measurements. The laser beam was pulsed through a mechanical chopper (Ch) operating with frequency near 20Hz. Although this frequency is not critical, considering the reported lifetime for this transition is close to 100 μs , this period ensures a complete depopulation of the upper level. A pair of lenses (L1 and L2), with focal length of 10.0 cm, placed in the path length of the laser beam, produced a beam waist of $\sim 20 \mu m$ at the chopper. These procedures have ensured that the lifetime to be measured is much longer than the excitation cut-off time ($\sim 17 \mu s$) [37]. The pump

signal was coupled into the waveguide via $\times 10$ objective lenses (numerical aperture $NA = 0.17$) and the signal at 451 nm was collected in the same direction as the pump by a photomultiplier (PMT). The residual pump signal was removed via the colour filter F1. The lifetime signals were recorded and stored in an oscilloscope before being downloaded to a graphical plotter.

The lifetime measured corresponds to (259 ± 34) μs . This value is rather long compared with the values reported for the same energy level in other glass hosts. For fluoride glasses, which usually have longer lifetime than silica-based glasses, the reported lifetime values are usually close to 200 μs [14]. This difference can be attributed to the noisy characteristic of the measurement, due to the low pump power. This reduced pump power was a precaution to avoid stimulated emission which reduces the fluorescent lifetime. A second factor which probably increases the measured lifetime is the probability of the low time response of the photomultiplier. A fast photodetector was used but it did not have enough gain to detect the low signal intensity.

This section analysed the possibility of pumping thulium-doped phosphosilicate oxide glasses with one wavelength to generate blue light at 450 nm and/or 480 nm. The first scheme was based on Nd:YAG laser operating in ML or QSML regimes. The fundamental radiation at 1064 nm from the laser coupled into the waveguide did not generate blue upconversion light, probably due to the low absorption cross section of this wavelength. The upconversion process was markedly enhanced when stimulated Raman radiation (SRS) generated in an external fibre was used. The first and second Raman Stokes bands were generated in either 1.0 km long fibre for the laser operating in the mode-locked regime, or 10.0 m long fibre in the QSML regime. In both regimes, several Watts (5.0 W) of laser radiation at 1064 nm was necessary in order to generate ~ 140 nW of blue light. Despite the report of Nd-doped fibre laser delivering more than 9.0 W at 1064 nm (CW), in that configuration it would be necessary to deploy nine powerful diode lasers operating at 810 nm (delivering approximately 9.0 W each) as pump source [38]. This pumping scheme is therefore not suitable for a compact solid-state laser pumped at 1064 nm.

Pumping the same sample with a CW Ti:Sapphire laser in the near infrared, around

800 nm, shows a poor conversion efficiency. Due to the low intensity of the blue upconverted signal generated, it was not possible to record it.

The final pumping configuration, tuning the CW Ti:Sapphire laser to 678 nm, was based on the reports of blue upconversion in thulium fluoride fibres. This pumping wavelength has shown a better efficiency than at 798 nm. However, we had to apply hundreds of mW's (~300 mW) to have a detectable amount of blue light. The main problem of operating at this wavelength is that powerful diode lasers are so far not available. Another disadvantage for this pumping wavelength arises if one aims at CW blue laser operation at room temperature. Despite the four level laser of this configuration, the lower level 3H_4 has the lifetime approximately 2 orders of magnitude longer than the upper level 1D_2 . Thus, in order to achieve CW laser operation and high efficiency at 451 nm, there is the requirement that the 3H_4 final metastable level be emptied. This problem can be addressed using two different approaches: codoping with terbium which induces cross relaxation effects to relieve the 3H_4 population efficiently [39], or pumping near 1.06 μm in resonance with $^3H_4 \rightarrow ^3F_{2,3}$ excited-state absorption transition [4]. However, the latter scheme does not allow single pump wavelength operation.

5.4 Thulium doped phosphosilicate glass sensitised by Ytterbium ions

The previous section reported upconversion based on ESA of the pump wavelength to excite a Tm^{3+} -doped $\text{SiO}_2\text{-P}_2\text{O}_5$ glass system. However, energy transfer mechanism between ions of the same, or different, species has been demonstrated to be more efficient than the ESA [29]. It has also been recognised that thulium doped glass sensitised with ytterbium ions is another useful composition to generate upconversion blue light pumping when pumping in the Yb^{3+} ground state absorption (GSA) peak cross section at 977 nm, excitation is transferred to the neighbour Tm^{3+} ion. Under this configuration, Yb^{3+} ions act as donor or sensitiser ions and the Tm^{3+} are the acceptors. This glass system also offers another possibility of using a pumping source based on commercial diode lasers at 980 nm. In addition to the large ytterbium absorption cross section, these ions are widely employed as donors because they do not undergo concentration quenching, even in highly doped glasses, due to their simplified electronic configuration. Thus, Yb^{3+} can be incorporated into the glass matrix in high concentrations, ensuring a good pump wavelength absorption and efficient energy transfer to the acceptor ions.

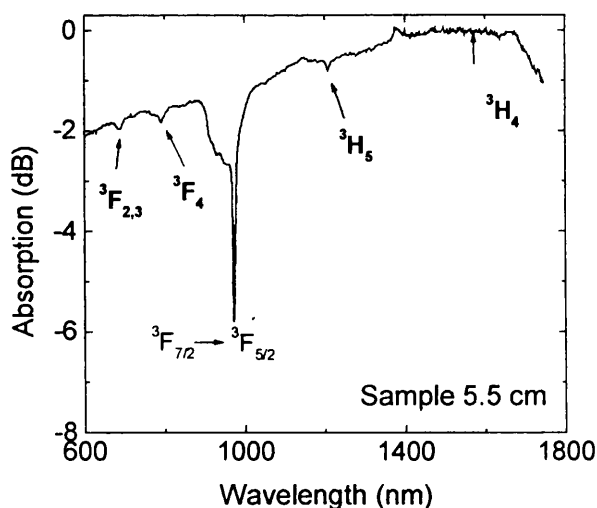


Figure 5.12: Absorption spectrum of a 0.1/1.0/0.1 M ($\text{Tm}^{3+}/\text{Yb}^{3+}/\text{Na}^+$) doped waveguide in the region 600-1750 nm. The ${}^2\text{F}_{7/2} \rightarrow {}^2\text{F}_{5/2}$ transition corresponds to the Yb^{3+} GSA, the remaining are due to Tm^{3+} ions.

Samples were prepared using the same procedure described in the section 5.3. Two

aqueous solutions containing $\text{Tm}^{3+}/\text{Yb}^{3+}/\text{Na}^+$ chloride in two different concentrations were employed to fabricate the samples. They are 0.1/1.0/0.1 M, and 0.05/0.5/0.05 M of thulium chloride, ytterbium chloride, and sodium chloride, respectively. All aqueous solution were prepared with high purity (99.99%) *REacton*® thulium (III), ytterbium (III) chloride hexahydrate, and sodium chloride. As the upconversion efficiency coming from those samples will be compared with the previous Tm^{3+} -doped glass results, it is worth emphasising the change in the waveguide cross section for the new samples. The only difference between the geometry of the thulium doped and the ytterbium-sensitised waveguides came from the reactive ion etching (RIE). For the Tm/Yb/Na samples, the RIE reached less than 50% of the total thickness of the core deposition ($\sim 10.0 \mu\text{m}$). Consequently, the waveguides were not completely buried, being close to a rib waveguide configuration. This geometry reduces the optical confinement of the radiation and the efficiency of the upconversion process as well. This is easily noticed in photo 2 on page 150, with the blue light underneath the cladding. During the experiments, it was observed that the blue upconversion light consisted of a bright spot in the centre of a thin blue horizontal line. The ratio $\text{Yb}^{3+}/\text{Tm}^{3+}$ was chosen close to 10 to ensure an efficient energy transfer process between the donor (Yb^{3+}) and acceptor (Tm^{3+}) ions.

Figure 5.12 shows a typical absorption measurement of a $\text{Tm}^{3+}/\text{Yb}^{3+}/\text{Na}^+$ (0.1/1.0/0.1 M) doped sample. The measurements were carried out as described previously for the Tm^{3+} -doped sample. This figure depicts the ground state absorption to $^3\text{H}_4$ (1675 nm), $^3\text{H}_5$ (1210 nm), $^3\text{F}_4$ (798 nm), and $^3\text{F}_3$ (678 nm) Stark levels corresponding to the thulium absorption, and the strong $^3\text{F}_{7/2} \rightarrow ^3\text{F}_{5/2}$ absorption band at 977 nm ascribed to the ytterbium ions. From this figure, the difference in the absorption coefficient is easily noticed. The ytterbium ion absorption coefficient (0.86 dB/cm) is more than 14 times that of thulium at 798 nm (0.06 dB/cm).

5.4.1 $\text{Tm}^{3+}/\text{Yb}^{3+}/\text{Na}^+$ doped samples pumped at 678 nm

The first pumping scheme for this multi-component glass employed the CW Ti:Sapphire laser tuned at 678 nm, which correspond to the absorption line

$^3H_6 \rightarrow ^3F_{2,3}$. A typical fluorescence spectrum for sample doped with thulium 0.1 M is shown in Figure 5.13.

Remarkable differences appear when the result shown in Figure 5.13 is compared to Figure 5.8 showing the 0.2 M single thulium doped sample. Firstly, one notices a reduction of the upconversion processes efficiency and consequently the intensity of the blue upconversion light at 451 nm. Due to the low intensity of these transition lines, it was not possible to use colour filter to reduce the interference of the pump power in the measurements. Therefore, the second order diffraction grating of the pump wavelength, as well as an unidentified UV band extending from 350 to 450 nm, were present. This relatively intense UV band overlapped the upconverted signal at 360 nm ($^1D_2 \rightarrow ^3H_6$) and 451 nm ($^1D_2 \rightarrow ^3H_4$). The second difference is the presence of the 482 nm and 740 nm bands, ascribed on the spectrum to the transitions $^1G_4 \rightarrow ^3H_6$ and $^1D_2 \rightarrow ^3F_3$ respectively. This new infrared line overlapped with the 721 nm ($^3F_3 \rightarrow ^3H_6$) transition, which due to the broadband characteristics, it was not possible to resolve with our measurement setup. Finally, due to the lower solution concentration used during the fabrication of this $Tm^{3+}/Yb^{3+}/Na^+$ sample, the amount of incorporated thulium ions was smaller than for the Tm^{3+} -doped (0.2 M). This caused a decrease in the upconversion light generation efficiency.

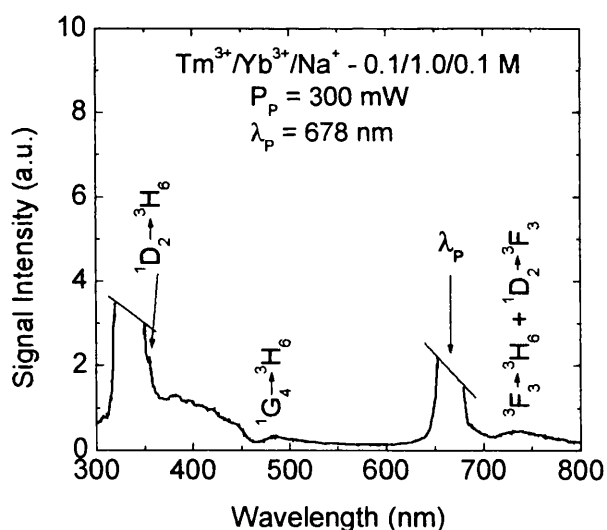
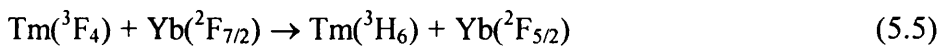


Figure 5.13: Fluorescent upconversion spectrum for the $Tm^{3+}/Yb^{3+}/Na^+$ doped $SiO_2-P_2O_5$ glass system pumped at 678 nm.

The observed change in the fluorescence spectrum due to the glass composition is better understood by analysing the energy level diagram of the Tm/Yb/Na glass system, Figure 5.14. Unlike the case of single thulium doped glass, the upconverted signal at 482 nm is possible, following the mechanism proposed by Oomen [31], when the upper level 1G_4 is populated as a consequence of the absorption of one pump photon from the metastable 3H_4 level. This metastable level is supposed to be populated because ytterbium offers the possibility of draining the population of the 3F_4 level to the 3H_5 level through two very efficient cross relaxation mechanisms and nonradiative transition, described by the equations:



These mechanisms also explain the low efficiency of populating the 1D_2 upper level. The up conversion process populating the 1D_2 excited state of Tm^{3+} is explained as follow: the first pump photon absorption populates the $^3F_{2,3}$ excited state, which is followed by a fast nonradiative transition to the 3F_4 state. Then a second pump photon is absorbed, bringing the Tm^{3+} ion to the 1D_2 excited state from where 450 nm ($^1D_2 \rightarrow ^3H_4$) and 366 nm ($^1D_2 \rightarrow ^3H_6$) emissions take place. Due to the cross relaxation expressed by the first equation, the 3F_4 level is very efficiently depopulated thus exciting Yb^{3+} ions.

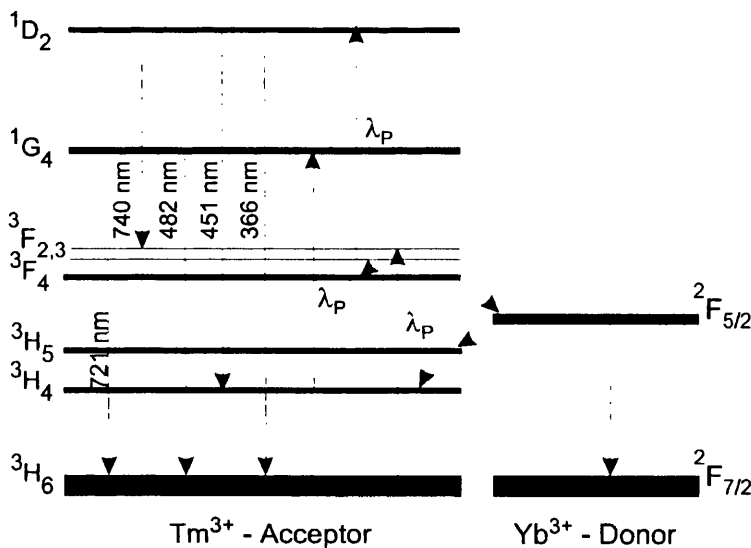


Figure 5.14: Simplified energy level diagram due to $\text{Tm}^{3+}/\text{Yb}^{3+}$ ions in $\text{SiO}_2\text{-P}_2\text{O}_5$ glass matrix. The solid lines correspond to the absorption of pump wavelength, the dashed represent the fluorescence, and the dotted arrows are nonradiative transitions.

The dependence of the 482 nm and 740 nm upconverted signals are shown in Figure 5.15 and Figure 5.16, respectively. Both signals show a quadratic dependence on the input pump power with a certain degree of saturation. Despite the uncertainty in the measurements due to the low signal powers, it was observed that the saturation in the blue transition line is less pronounced than the near infrared (721nm + 740 nm) band. This tendency to the quadratic dependence also indicates that the major contribution to this band should come from the 740 nm transition line. The low intensity of the blue light at this pumping wavelength scheme and the impossibility of adequately filtering the pump radiation were the limiting factors in measuring the lifetime.

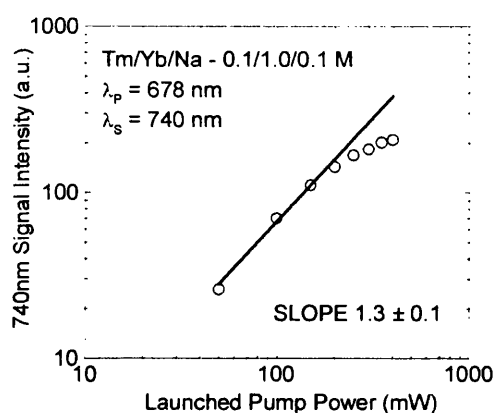
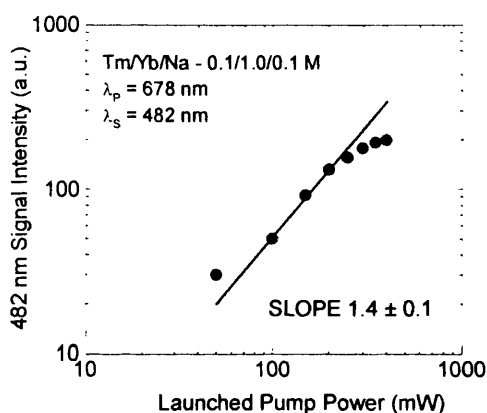


Figure 5.15: Blue upconversion generation as a function of the pump power radiation.

Figure 5.16: Near infrared radiation (721nm + 740 nm) as a function of the pump power.

Unlike the 451 nm blue light generated by the Tm^{3+} doped samples, the blue signal at 482 due to the $\text{Tm}^{3+}/\text{Yb}^{3+}$ sample has shown a high degree of saturation in the power dependence with the pump intensity. This is an additional indication of the efficiency of the cross relaxation given by equations (5.5)-(5.7) leaving the $^3\text{H}_4$ energy level saturated.

Pumping the $\text{Tm}^{3+}/\text{Yb}^{3+}/\text{Na}^+$ -doped sample at 678 nm, the ytterbium ions show no contribution, or maybe a deleterious effect, on the generation of blue light at 451 nm and UV at 360 nm. The actual effect on those fluorescent bands could not be evaluated due to the close spectral distance between the signals and the second order diffraction grating of the pump wavelength. The presence of a broad UV band in the range 350-450 nm overlapping with those fluorescent signals was also a second factor which reduced the precision of the results. However, after rare earth doping

level optimisation this glass composition could be applied as a new possibility of generating blue light at 482 nm via a two-photon process, as shown in the Figure 5.14.

5.4.2 Tm³⁺/Yb³⁺/Na⁺ doped samples pumped at 800 nm

Pumping the Tm³⁺/Yb³⁺/Na⁺ samples at the ³F₃ absorption line (678 nm) has shown a measurable blue light at 482 nm. Comparing the experimental results obtained in the sections 5.3.3 and 5.4.1 it was deduced that this signal was generated in the rare earth composed sample only due to the presence of population in the ³H₅ level. As described previously, the large population in the Tm³⁺ ³F₄ metastable level relaxes to the ³H₄ due to the efficient cross relaxation between the thulium and ytterbium ions. Due to nonradiative relaxation, this energy is transferred to the lower level ³H₅. Consequently, this Tm³⁺/Yb³⁺/Na⁺ glass will open a new prospect for efficient upconversion mechanism pumping at 800 nm.

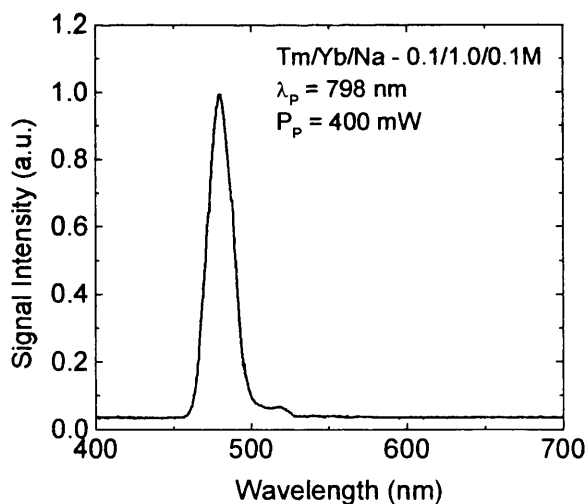


Figure 5.17: Intense blue upconversion generation at 482 nm in a Tm³⁺/Yb³⁺/Na⁺ doped SiO₂-P₂O₅ glass system, pumped at 798 nm.

To evaluate the efficiency of this mechanism, the CW Ti:Sapphire laser was tuned at the peak absorption line corresponding to the ³F₄ level. This wavelength corresponds to 798 nm and the typical fluorescence spectrum, due to a 0.1 M thulium-doped sample sensitised with ytterbium ions, is shown in Figure 5.17. Under this pumping configuration, a very strong blue light, visible by eye even in a light room, was

generated. A unique strong signal ascribed to the thulium ions transition $^1G_4 \rightarrow ^3H_6$ (corresponding to 482 nm), was detected in the spectral range of 400-700 nm. An infrared filter was used to attenuate radiation with wavelengths above 700 nm. However, spectrum in the same region was also recorded without filtering revealing only weak bands due to other transitions from 1G_4 level.

Figure 5.18 shows evidence of the high efficiency of this pumping scheme. As depicted in the figure, there is a pronounced saturation of the upconverted signal for pump power above 400 mW. Beyond 750 mW, the blue signal shows a complete saturation. The blue curve drawn across the experimental data is a mathematical function with quadratic dependence with the pump power. It is useful to emphasise the blue light saturation. The quadratic dependence of the blue light at 482 nm with the launched pump power depicted in the low pump power portion of Figure 5.18 is evidence of a two-photon process. The insert is a Log-Log plot of the same experimental data, and the straight line correspond to the best fitting to the signal generated by pump power inferior to 400 mW. At this situation, the blue upconverted signal had shown an increase with the launched pump power with slope of 1.84 ± 0.02 , indicating some sort of saturation in the process.

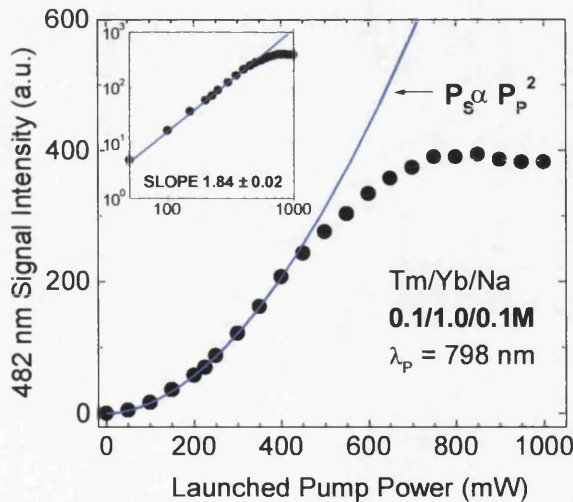


Figure 5.18: Blue light generation at 482 nm as a function of the pump power at 798 nm in a $Tm^{3+}/Yb^{3+}/Na^+$ $SiO_2-P_2O_5$ doped glass. The curve drawn across the experimental data is a quadratic mathematical function. The insert is the Log-Log representation of the same experimental data

The expected upconversion mechanism is depicted in Figure 5.19. The CW Ti:Sapphire laser is the radiation source for the first excitation of the Tm^{3+} ions to the $^3\text{F}_4$ level. This laser wavelength at 798 nm corresponds to the Tm^{3+} ground state absorption peak of the $^3\text{H}_6 \rightarrow ^3\text{F}_4$ transition. According to equation (5.5) on page 137, part of the energy is transferred, via cross relaxations, exciting the ytterbium ions to the $^2\text{F}_{5/2}$ level. These ions relax transferring back their energy to the excited Tm^{3+} in the $^3\text{F}_4$ level, which, through excited state absorption (ESA), populates level $^1\text{G}_4$. The energy mismatch (ΔE) is absorbed by the glass matrix. Thus, blue light at 482 nm is generated via radiative transition to the ground state ($^3\text{H}_6$).

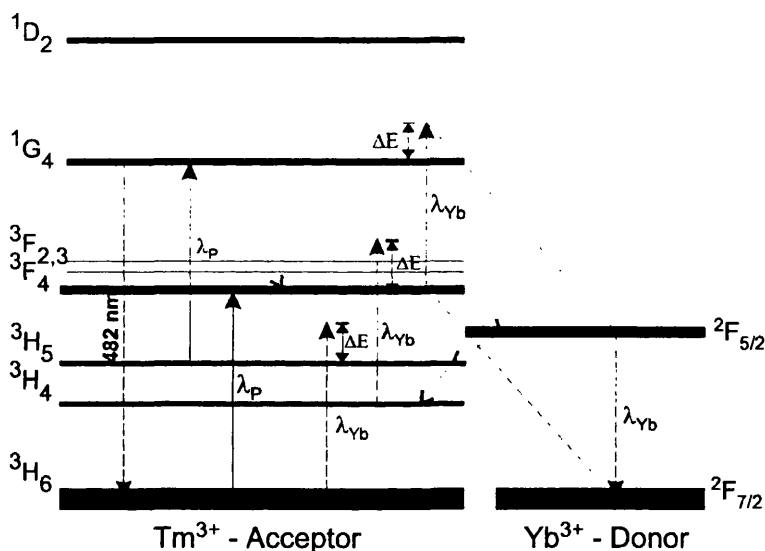


Figure 5.19: Simplified energy level diagram of $\text{Tm}^{3+}/\text{Yb}^{3+}$ ions. λ_p correspond to the pump wavelength, and λ_{yb} represent the energy donated by ytterbium ions by cross relaxation.

To analyse this mechanism, the upconverted signal at 482 nm and the ytterbium ions fluorescence at 977 nm were simultaneously monitored as a function of the laser pump wavelength, for a fixed pump power. Although, in principle, more upconversion signals should be monitored to trace the actual participation of ytterbium ions in the cross relaxation mechanism, only the blue upconversion and the Yb^{3+} fluorescence signals were observable. The $^3\text{F}_4 \rightarrow ^3\text{H}_6$ (~ 800 nm) and the $^3\text{H}_5 \rightarrow ^3\text{H}_6$ (1210 nm) transitions cannot be measured. The reason in that the former is too close to the pump wavelength, and the latter, due to the high phonon energy of the glass ($\hbar\omega_R \approx 1200 \text{ cm}^{-1}$), decays nonradiatively to the metastable $^3\text{H}_4$. In addition, the signal generated from the radiative transition $^3\text{H}_4 \rightarrow ^3\text{H}_6$ in $\text{SiO}_2\text{-P}_2\text{O}_5$ glass system is absorbed due to a broad absorption band of H_2O ($\sim 1.9 \mu\text{m}$) [40].

Furthermore, the remaining observed signals without filtering are very weak, and their origins were not determined. In the experimental set-up, the blue light was collected at the output end of the waveguide, after an infrared filter removed the pump radiation. The visible signal was selected by a monochromator and measured by a photomultiplier with a maximum spectral response in the blue region. The infrared fluorescence from ytterbium was collected transversally to the direction of propagation of the pump, through a multimode commercial optical fibre with a core diameter of 100 μm , and recorded by a spectrum analyser. The peak intensities of both signal as a function of the pump wavelength are shown in Figure 5.20. The solid lines are only guides to the eye.

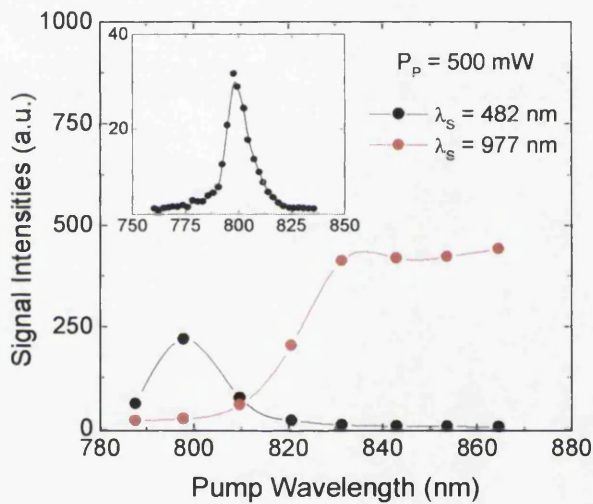


Figure 5.20: Thulium blue upconverted signal at 482 nm and ytterbium fluorescence at 977 nm as a function of the detuning of the pump wavelength relative to the peak absorption ${}^3\text{H}_6 \rightarrow {}^3\text{F}_4$. The inset corresponds to the blue signal generated as a function of the pump wavelength.

The dependence of the upconverted blue light shows an increase of 75% when the wavelength was changed from 785 nm to a value close to the peak at 798 nm, while the infrared fluorescence shows an increase of only 25%. Further detuning the pump wavelength to 805 nm was followed by a reduction of 65% of the blue light and an enhancement of 240% of the infrared signal. Beyond this wavelength, the blue light drastically reduced to $\sim 1\%$ of the peak value while the ytterbium fluorescence increased until it saturated at 830 nm. These values were measured relatively to the peak blue upconversion signal optimised to the pump wavelength. These results also agree with the pumping scheme described previously. A displacement towards longer

pumping wavelength was accompanied by a reduction in the blue upconversion process due to an *increase* in the energy mismatch required to populate 1G_4 level. Thus, the very efficient cross relaxation between the Yb^{3+} and Tm^{3+} ions is important in the relaxation to the ground state. Detuning in the opposite direction, towards shorter wavelengths, is beneficial to the 3F_4 absorption band which preferentially relaxes to the ground state level ($\beta \cong 0.78$).

An alternative route to populate the 1G_4 upper level could be described by the equations (5.5) to (5.7). Thus, the population in the intermediate state (3H_5) absorbing one pump photon could excite the Tm^{3+} ions to 1G_4 level. However, due to this relaxation mechanism, a “red” shift displacement in the pumping wavelength should be accompanied by an increase in the upconversion process due to the increase in the 3H_5 level population.

The result depicted in inset of Figure 5.20 is a detailed measurement of the efficiency of the upconverted signal at 482 nm as a function of the pump wavelength, for a fixed pump power. The upconversion process was maximised when the Ti:Sapphire laser was tuned at 798 nm. This measurement also reveal that there is a ~23 nm wide band, centred at the wavelength of maximum gain, available with reasonable upconversion efficiency.

Table 5.I: Branching ratios of the level 1G_4 (Tm^{3+}).

Transitions	Branching Ratios (β)
$^1G_4 \rightarrow ^3H_6$	0.59
$\rightarrow ^3H_4$	0.21
$\rightarrow ^3H_5$	0.13
$\rightarrow ^3F_4$	0.04
$\rightarrow ^3F_3$	0.02
$\rightarrow ^3F_2$	0.01

The high efficiency of this pumping mechanism can be understood by considering the possible relaxation routes from the 1G_4 level, Table 5.I and Figure 5.19. According to the branching ratio from this level, ~59% of its whole energy corresponds to the ground state relaxation and consequently the blue light at 482 nm. The remaining 41% relaxes to different energy levels obeying the following branching ratio relations: $^3H_4 \cong 21\%$, $^3H_5 \cong 13\%$, $^3F_4 \cong 4\%$. However, part of this

energy can be “recycled”, returning to the 1G_4 excited state, and the 3F_4 intermediate state. Photons in the 3H_5 energy level are excited to the 1G_4 metastable level absorbing one pumping photon at 798 nm and the 3H_4 level transfers part of its energy to the 1F_4 level, whenever the Yb^{3+} ions transfer its energy it due to cross relaxation. This second process involving cross relaxation between Yb/Tm ions will be investigated in the next section.

Around ~ 10 nW of blue light was measured with 200 mW of launched pump power in a waveguide 50.0 μm wide. Several factors can be optimised to increase this conversion efficiency:

- a) Waveguide cross section area to ensure monomode regime operation, mainly at the pump wavelength, to increase the optical confinement to provide high pump intensities for modest pump power;
- b) The waveguide length: increasing the interaction length is one possibility to reduce the dopant concentration. However, long waveguides in the planar form suffer higher scattering losses;
- c) The active ion doping level to ensure a high thulium doping without deleterious cross relaxation taking place. If a high Yb^{3+} concentration is desired for efficient blue upconversion promoting ions from the 3F_4 to the 1G_4 , it also acts as loss to the 1G_4 level due to the cross relaxation depopulation of the 3F_4 level. Further analysis of this pump wavelength will be carried out in the next chapter.

In summary, in this section it was shown that a considerable improvement in the efficiency of blue upconversion in thulium doped phosphosilicate glasses was achieved when ytterbium ions were included in the glass system. The efficiency of this process is expected to be further increased with the optimisation of the waveguide geometry and the dopant levels. Thus, the addition of ytterbium ions was an improvement in this glass system, and the mature technology of commercial powerful diode lasers operating around 800 nm should offer a new possibility for compact solid state lasers in phosphosilicate glass as host to incorporate the rare earths.

The next section is concerned with the same glass system pumped at 977 nm, which corresponds to the absorption peak of ytterbium ions.

5.4.3 Tm³⁺/Yb³⁺/Na⁺ doped samples pumped at 980 nm

The development of powerful diode lasers operating in the 800 nm and 980 nm regions offers new prospect for the blue and green (Tm³⁺ and Ho³⁺) [27] solid state laser using frequency upconversion process. Because of the blue or UV emission from ¹D₂, ¹G₄ levels of thulium ions, and its relative simple energy structure, the upconversion process using this ion has been shown to be very efficient in some glass hosts, such as the fluoro-based glass. As shown in the previous section, at the longer wavelengths, such as 800 nm, it is almost impossible for Tm ions to emit strong enough upconversion luminescence in single doped oxide glass. The absence of absorption band at 980 nm is also a limiting factor to the use of these ions as dopants in solid-state lasers when pumped at a wavelength provided by commercial diode lasers. However, it has been demonstrated in many different glass hosts that ytterbium is a very useful source offering a strong absorption at 980 nm [18,19,22,29]. Furthermore, ytterbium has shown efficient energy transfer to many other ions when used as co-dopant [43,44]. No report was found of efficient blue upconversion in oxide glasses doped with thulium and sensitised with ytterbium ions pumped at 980 nm. This section is devoted to investigating this upconversion mechanism in FHD fabricated SiO₂-P₂O₅ glass hosts.

The thulium/ytterbium-doped samples used in these experiments are the same as described previously when pumped at 678 nm and 798 nm. As depicted in Figure 5.12, ytterbium ions (Yb³⁺) have an absorption peak at 977 nm (~0.820 dB/cm) which is approximately 15 times the strength of thulium absorption at 798 nm (~0.057 dB/cm) (measured for a ratio Yb³⁺/Tm³⁺ concentrations of 10 times). This high pump absorption was responsible for the fluorescent upconversion processes shown in Figure 5.21. This typical fluorescence spectrum in the range of 400-800 nm is due to the Tm³⁺/Yb³⁺/Na⁺ (0.05/0.5/0.05 M) doped sample pumped 470 mW at 977 nm. The experimental set-up for this measurement was similar to those introduced in the Figure 5.6, with the Ti:Sapphire laser now tuned at the absorption

peak of Yb^{3+} ions. The two observed lines across the spectral region from 400 nm to 800 nm were blue at 482 nm and the near infrared at 710/721 nm. These signals are ascribed to the ${}^1\text{G}_4 \rightarrow {}^3\text{H}_6$, and ${}^3\text{F}_{2,3} \rightarrow {}^3\text{H}_6$ Tm^{3+} Stark level transitions, respectively. The signal originating at ${}^3\text{F}_4$ level was not recorded due to the infrared filter attenuating wavelengths above 750 nm. The filter was used to avoid saturation in the photomultiplier due to pump wavelength. Similar measurements were carried out with the $\text{Tm}^{3+}/\text{Yb}^{3+}/\text{Na}^+$ (0.1/1.0/0.1 M) doped sample with equivalent results. No signal was originated from ${}^1\text{D}_2$ level, e.g. 366 nm (${}^1\text{D}_2 \rightarrow {}^3\text{H}_6$) or 450 nm (${}^1\text{D}_2 \rightarrow {}^3\text{H}_4$). These signals are usually reported in other low phonon energy glass host [19], with the similar doping levels. As reported, the ${}^1\text{D}_2$ level is populated via the absorption of a fourth pump photon from level ${}^1\text{G}_4$. The short measured lifetime of the ${}^1\text{G}_4$ level in the phosphosilicate glass is probably a factor responsible for the low population in the ${}^1\text{D}_2$ level. It corresponds to 1/3 of the reported value of the fluorophosphates [42].

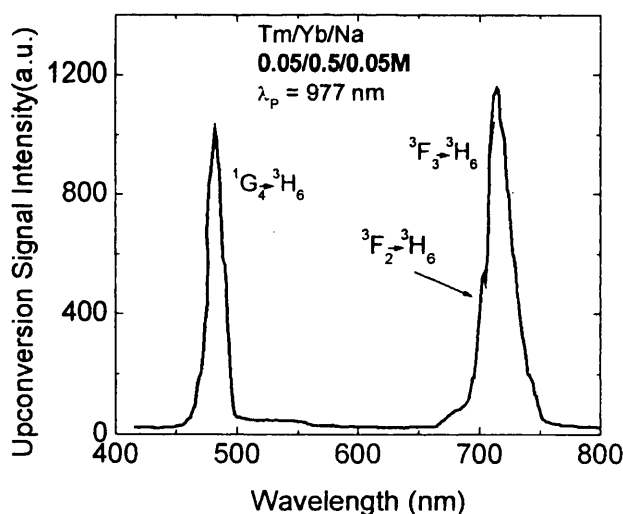
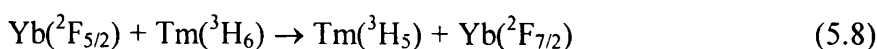
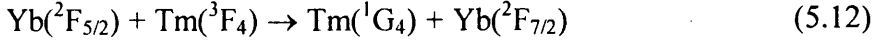
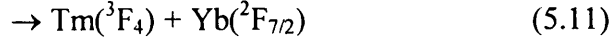
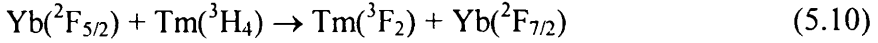
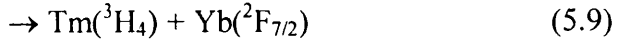


Figure 5.21: Blue upconversion signal at 482 nm and near infrared upconversion in a $\text{Tm}^{3+}/\text{Yb}^{3+}$ doped $\text{SiO}_2\text{-P}_2\text{O}_5$ glass, pumped at 977 nm.

The upconversion pumping mechanism for this wavelength is a well-known process [43], although most of the reported experimental results are concerned with fluoride glasses. The three steps of this upconversion mechanism shown in Figure 5.22 are described by the following equations:





In other words, an excited Yb^{3+} ion relaxes nonresonantly transferring the energy to a neighbouring Tm^{3+} ion, exciting it to its first level $^3\text{H}_5$. This transition requires the matrix to absorb 1992 cm^{-1} of the excess energy. The energy in the $^3\text{H}_5$ state relaxes nonradiatively by multiphonon relaxation to the metastate level $^3\text{H}_4$. From this level, a second photon released by an Yb^{3+} promotes the thulium photon one step up to the $^3\text{F}_2$ level, transferring 1477 cm^{-1} of its energy to the host. The $^3\text{F}_2$ state also relaxes by multiphonon relaxation to the $^3\text{F}_4$ state. The signature of this step of the upconversion is the $^3\text{F}_{2,3}$ levels emitting fluorescence at 710/721 nm. A third Yb^{3+} ion nonresonantly transfers its energy to a neighbouring excited Tm^{3+} ion populating the $^1\text{G}_4$ state with 2041 cm^{-1} of energy released. The $^1\text{G}_4$ level then emits the fluorescent upconversion signal at 482 nm.

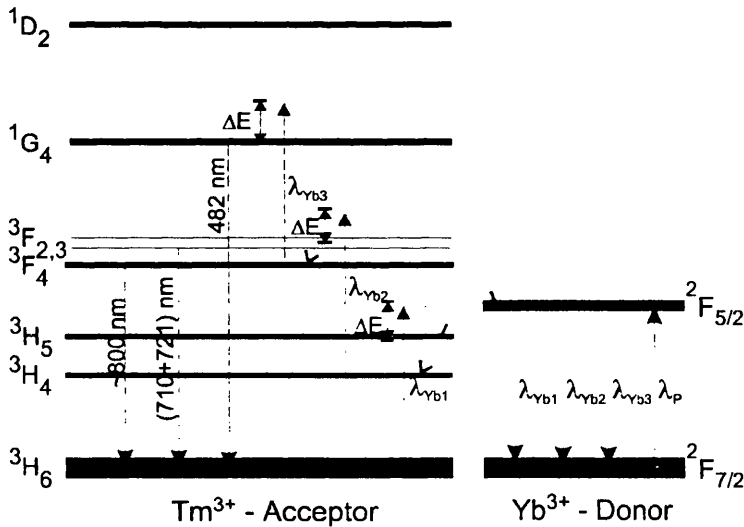


Figure 5.22: Simplified energy level diagram for $\text{Tm}^{3+}/\text{Yb}^{3+}$ ions in $\text{SiO}_2\text{-P}_2\text{O}_5$ glass system pumped at 977 nm.

The remarkable difference in the present measurements is the quadratic dependence of the blue light at 482 nm with the launched pump power at 977 nm, as shown in Figure 5.23. The decrease in this exponent of the pump power dependence has been already reported in [43] and references there in.

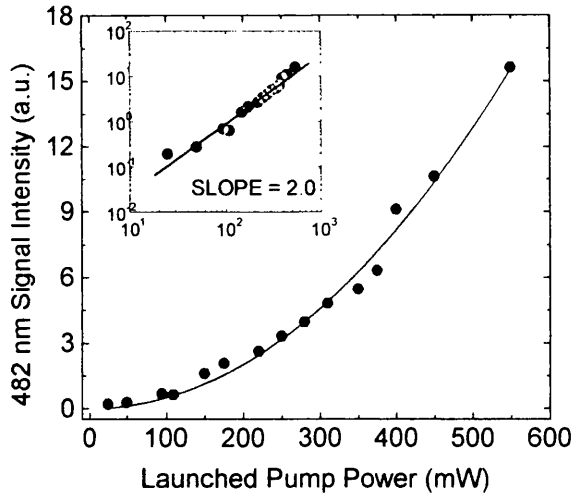


Figure 5.23: Pump power dependence of the blue signal at 482 nm. The saturation of intermediate level is enhanced in the quadratic dependence show in the inset.

This is attributed to a possible saturation of one, or more, energy level involved in the process. This is better illustrated if the theoretical rate equation model is applied to the system of Figure 5.22. The derivation of these and following equations, as well as the physical meaning of each term is described in Appendix A. The dependence of upconversion intensity signal on the low pumping intensity can be described by:

$$I_{60} = \left[\frac{h\nu_{60} W_{60} C_{82} C_{85} C_{86} \tau_{60}}{\tau_{43} \left(\frac{1}{\tau_{30}} + C_{38} N_7 + C_{86} N_8 \right) \left(\frac{1}{\tau_{40}} + \frac{1}{\tau_{43}} \right) \tau_{21} \left(\frac{1}{\tau_{10}} + C_{85} N_8 \right) \left(\frac{1}{\tau_{20}} + \frac{1}{\tau_{21}} \right)} \right] \cdot N_0 N_8^3 \quad (5.13)$$

where N_0 and N_8 are the ground state and excited state populations of thulium and ytterbium ions, respectively. Equation (5.13) shows that, considering low pump power levels and consequently low excitation of the Yb^{3+} ions, it is expected a small contribution of the terms containing N_8 in the denominator, thus, they can be neglected. Therefore, the ground state of donor and acceptor can be considered not depleted and they are treated as constants. Hence, the dependence of the blue upconverted signal is cubic with respect to the pump photons, through the number of photons donated by ytterbium ions. However, when the pump power is high enough to depopulate thulium ground state (N_0) the depletion of this level has to be considered. Thus, the ground state is expressed as:

$$N_{0D} \approx \frac{N_{Tm}}{1 + \alpha N_8} \quad (5.14)$$

Applying equation (5.14) into equation (5.13), the dependence of the upconverted signal on the donor concentration becomes explicit. The parameter α is defined in Appendix A. As the excited state population of the donor increases, due to the efficient energy transfer, these photons are transferred to thulium ions depleting their ground state. At higher pump power the term αN_8 becomes greater than 1 and consequently the dependence of the upconverted signal with the pump power decreases. For a very efficient upconversion process, a quadratic dependence could be expected.

In order to confirm this effect, measurement of the blue upconverted emission were carried out in different ranges of pump power. Figure 5.24 shows the result. For an intermediate pump power range the dependence is seen to be weaker than the expected cubic one but stronger than the quadratic one seen for high pump power. The inset of this figure shows the dependence of the same signal at a very low pump power showing the expected cubic dependence.

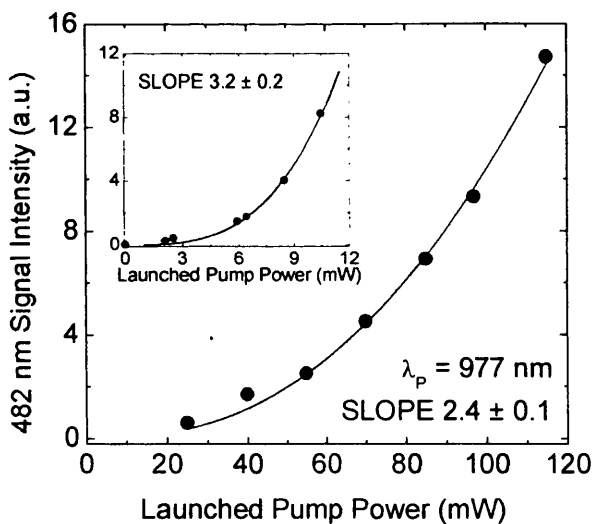


Figure 5.24: Blue upconverted signal dependence with the pump power for two distinct situation showing saturation in intermediate levels. The inset shows the cubic dependence in the low pump power regime and in the main graphic the intermediate pump power intensities with reduced exponent.

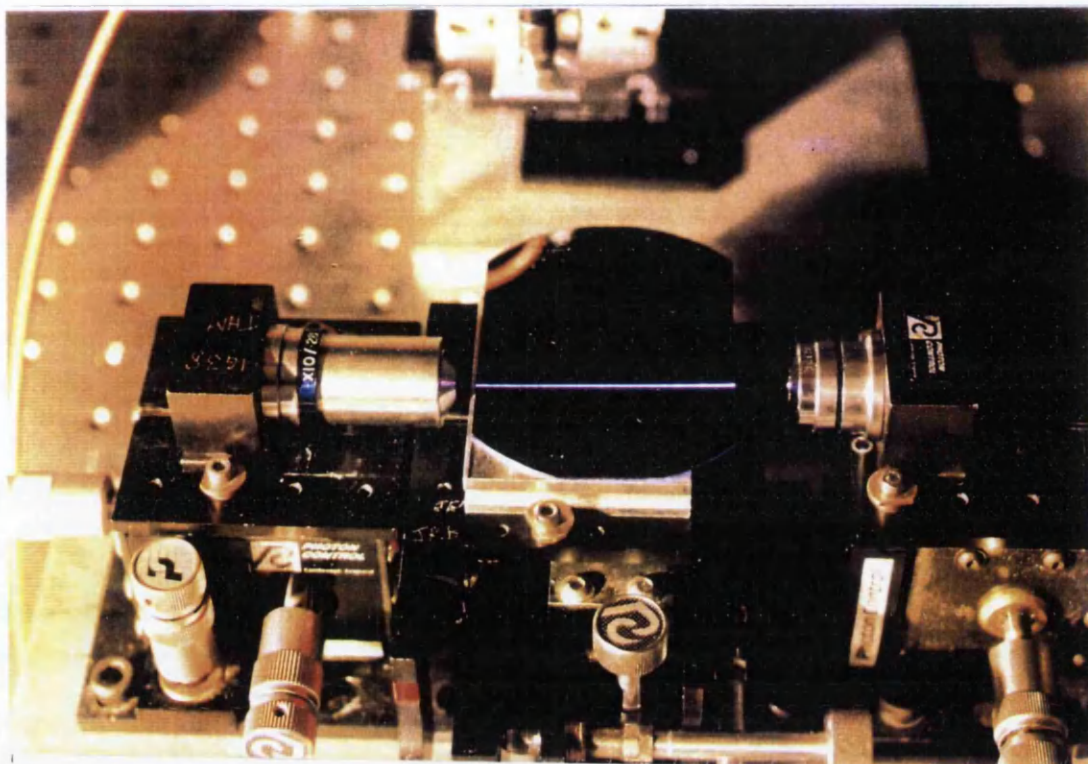


Photo 1: Blue Upconversion generation in a 50 μm wide $\text{Tm}^{3+}/\text{Yb}^{3+}/\text{Na}^{+}$ phosphosilicate waveguide fabricated by FHD and RIE. Signal generated at 482 nm due to 500 mW of infrared radiation at 977 nm

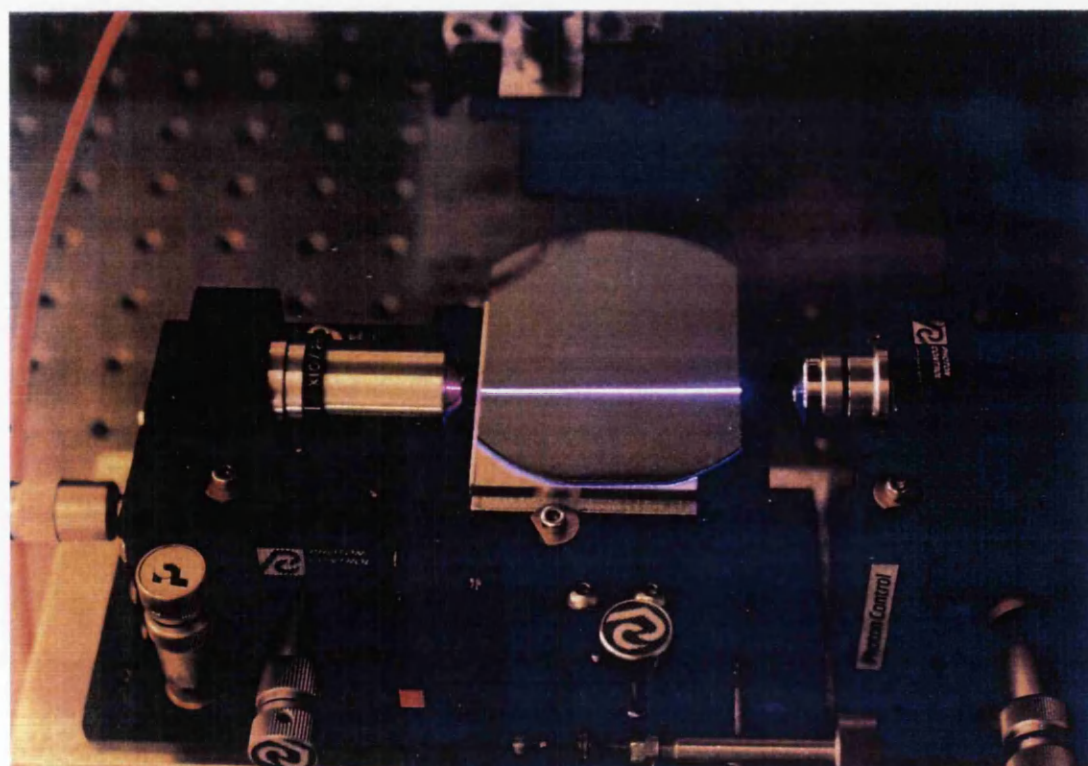


Photo 2: Long exposure photo of the same experiment to evidence the blue light underneath the cladding.

The fluorescence lifetime for transitions from level 1G_4 , measured with the experimental set-up described previously, was measured as $(472 \pm 146) \mu\text{s}$. To avoid stimulated emission taking place, reducing the measured lifetime, the pump power at 977 nm was adjusted to 80 mW. However, the actual input power into the waveguide is expected to be smaller than this value, when the reductions in the average pump power after the mechanical chopper and coupling loss were considered. Despite the large variation in the result, the value measured is within the limits reported in the literature. For comparison, a list of lifetime predictions for the same transition for different glass hosts reported in the literature is presented: Aluminate 440 μs , Fluoride 885 μs , Gallate 385 μs , Fluorophosphate 728 μs , Germanate 666 μs , Silicate 811 μs [29]. The divergence between this result and the previous one using Nd:YAG laser can be attributed to two factors. The first one is the low pump power from the CW Ti:Sapphire laser. This reduces the possibility of stimulated emission from the upper level, as well as possible cross-relaxation process. A second possible reason for the reduction in the lifetime of the Nd:YAG laser measurement could be the fact that measurement coupled light into the $6.0 \times 6.0 \mu\text{m}$ waveguide, whereas using the Ti:Sapphire laser, light was coupled into the $50.0 \mu\text{m}$ waveguide, reducing the density of energy inside and consequently the possibility of stimulated emission at wavelength of interest.

The fluorescence lifetime due to the transition from ${}^3F_{2,3}$ band at 710/721 nm was measured as $(1.46 \pm 0.28) \text{ms}$. Due to the high intensity and stability of the signals during the measurements the lifetime was determined more precisely when compared with the blue light. The measured value at this wavelength was comparable to values in fluoride glasses [29].

An important parameter for a diode laser pumped device is the flexibility in wavelength. Figure 5.25 shows the intensity of the blue light signal at 482 nm versus the pump wavelength varying in the range 930-990 nm, while the pump power was kept constant at 200 mW. The result has shown the maximum conversion efficiency whit pump wavelength at 977 nm, corresponding to the absorption peak of ytterbium ions. However, the signal shows conversion efficiency close to 40% of the peak in the range of 950-960 nm. Efficient pump absorption at these wavelengths offers a prospect of using a Nd:YAG laser as a pump source [45].

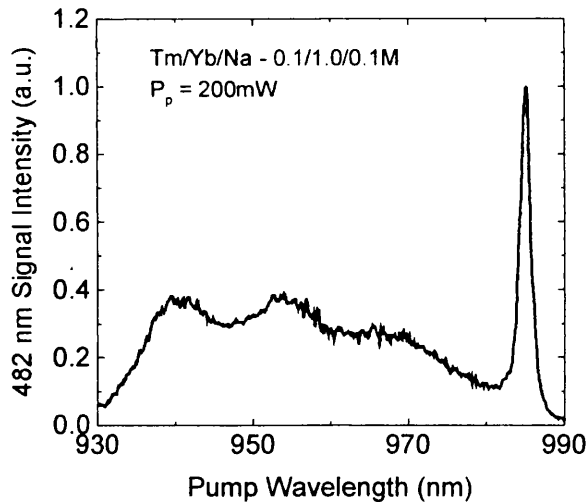


Figure 5.25: Blue upconversion generation as a function of the pump wavelength, maintaining the input power constant.

As mentioned in the Chapter 1, ability to work in an environment with high temperatures should be a requirement for a compact blue laser, as part of a practical tool, such as a laser printer, for instance. Thus, the measurement of the behaviour of the intensity of the blue upconverted signal at 482 nm was monitored against the sample temperature. For this measurement, a heating element consisting of a block of aluminium with a surface of 25.0×7.0 mm was placed in the central region of the waveguide. The aluminium block was maintained with the long side in the same direction of the light propagation, with a constant separation to the sample surface of ~ 1.0 mm. The physical contact between the heating element and the waveguide surface was avoided. This was a precaution in order to minimise the pump light coupling misalignment due to the waveguide bending during the heating up process. The pump power was kept constant at 200 mW during the measurement, and the intensity of the blue light was optimised before heating up the aluminium block. Figure 5.26 depicts the behaviour of the blue signal during the measurement. The heating element variation temperature was measured with a thermocouple type “N” attached to it, and the signal recorded in a chart record. The result is shown as the blue line with open circles and the scale corresponds to the right hand side axis. Simultaneously, a photomultiplier tube measured the blue light with maximum wavelength gain in the blue region, and the signal recorded by the second channel of the same chart recorder. The result corresponds to the black noise-like curve and the

scale is at the left hand side axis. The pump signal coupling was corrected in order to get the maximum upconversion efficiency, whenever the blue signal disappeared. This procedure was interrupted when the blue upconversion signal was maintained constant for more than 5.0 minutes. We observed a reduction of approximately 50% in blue upconversion efficiency with an increase of 165°C, and small departure from the room temperature operation for temperature below 100°C. This result is consistent with the report in the literature with the same rare earth in glass host [43].

In this section an efficient upconversion blue light generation in a $\text{Tm}^{3+}/\text{Yb}^{3+}/\text{Na}^+$ phosphosilicate doped sample pumped at 977 nm was demonstrated. A signal power of 130 nW was generated from 150 mW of infrared pump power at 977 nm. Considering that the injected power into the waveguide corresponds to 30% of the delivered power, the calculated process efficiency is $2.0 \times 10^{-4}\%$. Optimisation of this upconversion process can be achieved by reducing the waveguide cross-section ensuring monomode operation at the pump power. This will increase the pumping density energy. Further optimisation of the system can be implemented in the Tm^{3+} doping level to avoid cross relaxation. Yb^{3+} does not undergo concentration quenching due to high doping levels, but the ratio of $\text{Yb}^{3+}/\text{Tm}^{3+}$ concentrations must be optimised in order to avoid the $^3\text{F}_4$ level depopulated in excess. As can be inferred from the energy level diagram of these ions pumped at 977 nm, Figure 5.22, the intermediate $^3\text{F}_4$ level, responsible for the third step in the upconversion process, is depopulated by the efficient cross relaxation with the ytterbium ions. The emptying of the level in a laser configuration is an additional loss to be overcome. Paschotta *et al.* [9] have pointed out that the transition $^3\text{F}_4 \rightarrow ^3\text{H}_6$ have a gain coefficient 2.5 times greater than the $^1\text{G}_4 \rightarrow ^3\text{H}_6$, usually lasing first than the blue. The same behaviour was observed by Mejía and co-works [24] in a ZBLAN fibre laser. The inclusion of ytterbium in the glass system can act as an option to depopulate the intermediate $^3\text{F}_4$ level, transferring its population to the $^3\text{H}_4$ via cross relaxation with Yb^{3+} ions, increasing the threshold of the laser action. Finally, the highest efficiency of this upconversion process can be evaluated for the photo 1. This digital photo was taken for an upconversion pumped with 500 mW at 977 nm.

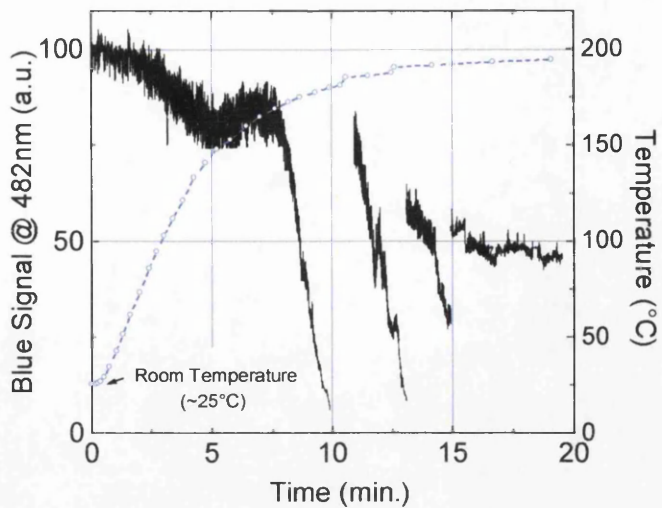


Figure 5.26: Peak intensity of the blue light as a function of the temperature. The signal have shown great stability for temperature up to 100 °C.

5.5 Conclusion

This chapter was devoted to the study of the viability of using Thulium and $\text{Tm}^{3+}/\text{Yb}^{3+}$ doped $\text{SiO}_2\text{-P}_2\text{O}_5$ glass matrix to generate blue upconversion light. The aim of this investigation was to demonstrate the potential of using rare earth doped glass produced by the FHD method to fabricate compact solid-state blue light devices for converting infrared radiation from commercial diode lasers into blue light. Two different rare earth compositions were analysed: a Tm^{3+} doped glass, and a Tm^{3+} doped sensitised by Yb^{3+} ions. In this glass system, sodium ions were also incorporated as an additional component to decrease the glass sintering temperature, as well as to increase the solubility of ytterbium ions as described for erbium in Chapter 3.

A Nd:YAG laser operating at 1064 nm was the first pump wavelength considered. Due to the small absorption cross-sections, blue light upconversion was not demonstrated in single Tm^{3+} -doped phosphosilicate waveguides when pumped at the fundamental wavelength of 1064 nm. It was possible to obtain efficient blue upconversion only when the waveguide was pumped by wavelengths in the range of 1113-1167 nm, generated in a commercial optical fibre due to SRS. This pumping scheme has shown the maximum conversion efficiency when a combination of the first (1113 nm) and second (1167 nm) Stokes lines due to the stimulated Raman scattering, along with the fundamental laser radiation at 1064 nm were launched into the waveguide. Due to relying on an external optical fibre to generate the Stimulate Raman Scattering, this pumping scheme at 1064 nm is not suitable for compact devices. In this configuration it was possible to generate ~130 nW of blue light with ~70 mW of ML infrared radiation. Thus, this pump configuration will become interesting for compact devices when powerful and inexpensive diode lasers operating in the 1130 nm region become available.

To explore a commercial diode laser wavelength as a pump source, ytterbium ions were incorporated into the glass matrix. Then, another three-photon process was analysed in a $\text{Tm}^{3+}/\text{Yb}^{3+}$ doped phosphosilicate glass pumped at 977 nm. From the absorption coefficient measurement it was inferred that ytterbium ions have a cross

section at 977 nm ~15 times the thulium at 798 nm (which corresponds to the other pump option via diode lasers). Besides the large cross section of ytterbium ions, this upconversion process is governed by energy transfer between ions, which was already demonstrated to be more efficient than the excited state absorption (ESA) of the previous experiment. In spite of the unfavourable waveguide geometry, this pumping scheme was shown to be promising. Infrared to blue upconversion at 482 nm with 25 mW of CW pump power in $\text{Tm}^{3+}/\text{Yb}^{3+}$ co-doped waveguides was observed. Optimisation of this glass system and waveguide geometry may allow an improvement in the measured conversion efficiency of $2 \times 10^{-4}\%$, and this value is very close to the 10^{-6} reported in glass ceramic with similar doping level [19]. The optimisation of the $\text{Tm}^{3+}/\text{Yb}^{3+}$ co-doped glass also consists of the determination of the best doping level ratio between these two ions.

Comparing these two phosphosilicate glasses with pumping upconversion scheme involving three photons, the $\text{Tm}^{3+}/\text{Yb}^{3+}$ doped glass system was shown to be more advantageous than Tm^{3+} . The first benefit of the co-doped glass is the choice of the pump wavelength. Diode lasers operating in the spectral region of 980 nm have a more developed technology than the diode lasers operating at 1130 nm. The second is higher efficiency in order to obtain laser operation at 482 nm.

The upconversion efficiency not only depends strongly on the rare earth concentration and on the host material in which the rare earth ions are incorporated. The number of photons required to generate the signal is limiting as well. As is known, the relative upconversion efficiency decreases rapidly for increasing numbers of photons involved. Thus, the two photons pumping scheme was analysed.

The first pump wavelength employed was at 678 nm, exciting the thulium ions from the ground state to the $^3\text{F}_{2,3}$ energy level. Unlike the three-photon process, this pumping wavelength was shown to be more efficient for thulium-doped waveguides than the composed doping glass ($\text{Tm}^{3+}/\text{Yb}^{3+}$). However, it does not show similar efficiency as fluoro-based glasses, and upconversion of red light into blue at 451 nm (single thulium) or 451 nm and 482 nm ($\text{Tm}^{3+}/\text{Yb}^{3+}$) were obtained only with hundreds of milliwatts of pump power. Thus, this pumping configuration does not appear to be reliable as a compact solid-state blue laser, because diode lasers

operating at this pump wavelength are not commercially available in this range of power.

A new promising result was obtained with the $\text{Tm}^{3+}/\text{Yb}^{3+}$ doped sample pumped at 798 nm. At the same pump wavelength, thulium doped sample did not generate blue upconverted emission. The conversion efficiency showed a good stability with the temperature. The upconverted signal reduced in ~50% of the peak power when temperature increased from room temperature to 180 °C. The process has also shown flexibility with the pump wavelength. Conversion efficiency of ~50% of the peak blue upconverted light was obtained detuning the pump wavelength within 23 nm, centred at 798 nm. As the diode lasers operating at this range of pump wavelength are a mature technology, this becomes a very encouraging result to obtain a compact source of blue upconversion light.

This chapter has shown that two pump wavelengths, which are available from commercial diode lasers, can be used to generate blue upconversion light in $\text{Tm}^{3+}/\text{Yb}^{3+}/\text{Na}^+$ doped $\text{SiO}_2\text{-P}_2\text{O}_5$ samples. The next chapter will concentrate on the development of a laser model and the study of the feasibility of laser action with this glass using these pumping wavelengths.

5.6 References

- 1 J.Y. Allain, M. Monerie, and H. Poignant, "Blue upconversion fluorozirconate fibre laser", *Electronics Letters* **26**, 166-168 (1990).
- 2 R. Paschotta, P.R. barber, A.C. Tropper, and D.C. Hanna, "Characterization and modeling of thulium:ZBLAN blue upconversion fiber lasers", *Journal of the Optical Society of America B* **14**, 1213-1218 (1997).
- 3 S.G. Grubb, K.W. Bennett, R.S. Cannon, and W.F. Humer, "CW room-temperature blue upconversion fibre laser", *Electronics Letters* **28**, 1243-1244 (1992).
- 4 M.P.Le Flohic, J.Y. Allain, G.M. Stéphan, and G. Mazé, "Room-temperature continuous-wave upconversion laser at 455 nm in a Tm^{3+} fluorozirconate fiber", *Optics Letters* **19**, 1982-1984 (1994).
- 5 S. Sanders, R.G. Waarts, D.G. Mehuys, and D.F. Welsh, "Laser diode pumped 106 mW blue upconversion fiber laser", *Applied Physics Letters* **67**, 1815-1817 (1995).
- 6 F. Duclos, P. Urquhart, "Thulium-doped ZBLAN blue upconversion fiber laser: theory", *Journal of the Optical Society of America B* **12**, 709-717 (1995).
- 7 G. Tohmon, J. Ohya, H. Sato, and T. Uno, "Increased efficiency and decreased threshold in $Tm:ZBLAN$ blue fiber laser co-pumped by 1.1 μm and 0.68 μm light", *IEEE Photonics Technology Letters* **7**, 742-744 (1995).
- 8 I.J. Booth, C.J. Mackechnie, and B.F. Ventruco, "Operation of diode laser pumped Tm^{3+} ZBLAN upconversion fiber laser at 482 nm", *IEEE Journal of the Quantum Electronics* **32**, 118-123 (1996).
- 9 R. Paschotta, P.R. barber, A.C. Tropper, and D.C. Hanna, "Characterization and modeling of thulium:ZBLAN blue upconversion fiber lasers", *Journal of the Optical Society of America B* **14**, 1213-1218 (1997).
- 10 G. Tohmon, H. Sato, J. Ohya, and T. Uno, "Thulium:ZBLAN blue fiber laser pumped by two wavelengths", *Applied Optics* **36**, 3381-3386 (1997).
- 11 J. Sanz, R. Cases, and R. Alcalá, "Optical properties of Tm^{3+} in fluorozirconate glass", *Journal of Non-Crystalline Solids* **93**, 377-386 (1987).
- 12 J.R. Lincoln, W.S. Brocklesby, F. Cusso, J.E. Townsend, A.C. Tropper, and A. Pearson, "Time resolved and site selective spectroscopy of thulium doped into germano- and alumino-silicate optical fibres and preforms", *Journal of Luminescence* **50**, 297-308 (1991).
- 13 B.C. Joshi, and M.C. Joshi, "Sensitizing Pr^{3+} ions by Tm^{3+} ions in phosphate glass", *Journal of Non-Crystalline Solids* **142**, 171-174 (1992).
- 14 E.W.J.L. Oomen, "Upconversion in Tm^{3+} -doped ZBLAN glasses", *Journal of Non-Crystalline Solids* **140**, 150-152 (1992).
- 15 A. Kermaoui, J.P. Denis, G. Özen, Ph. Goldner, F. Pellé, b. Blanzat, "Effect of Yb^{3+} on red to blue conversion fluorescence of Tm^{3+} in fluorozirconate

- glass”, *Optics Communications* **110**, 581-584 (1994).
- 16 K. Hirao, K. Tamai, S. Tanabe, and N. Soga, “Frequency upconversion and its new mechanism in Tm^{3+} -doped fluoroaluminate glasses”, *Journal of Non-Crystalline Solids* **160**, 261-267 (1993).
 - 17 I.R. Martin, V.D. Rodriguez, R. Alcalá, R. Cases, “Cross-relaxation for Tm^{3+} ions in indium-based glasses”, *Journal of Non-Crystalline Solids* **161**, 294-296 (1993).
 - 18 G. Özen, X. Wu, J.P.Denis, A. Kermaoui, F. Pellé, and B. Blanzat, “Optical properties and upconversion emissions of Tm^{3+} in Yb^{3+} doped fluorophosphate glasses”, *Journal of Physical and Chemistry of Solids* **54**, 1533-1542 (1993).
 - 19 X. Wu, J.P.Denis, G. Özen, A. Kermaoui, and F. Pellé, “The up-conversion luminescence of Tm^{3+} in glass ceramic doped with Yb^{3+} under infrared excitation”, *Physics of Status Solid (a)* **141**, 445-455 (1994).
 - 20 B. Dussardier, J. Wang, D.C. Hanna, D.N. Payne, “Spectroscopy and CW 2-photon upconversion in Tm^{3+} -doped ZnCl_2 -based glass”, *Optical Materials* **4**, 565-573 (1995).
 - 21 X.X. Zhang, P. Hong, M. Bass, and B.H.T. Chai, “Blue upconversion with excitation into Tm ions at 780 nm in Yb- and Tm-codoped fluoride crystals”, *Physical Review B* **51**, 9298-9301 (1995).
 - 22 Z. Hao, X. Chen, G. Zhang, F. Song, and Y-bing Hou, “Blue upconversion with excitation at 970 nm in $\text{Yb}_{0.18}$ -doped $\text{Tm}_{0.03}\text{LaP}_5\text{O}_{14}/\text{Tm}_{0.1}\text{LaP}_5\text{O}_{14}$ ”, *Proceeding SPIE* **2897**, 275-278 (1996).
 - 23 T. Schweizer, B.N. Samson, J.R. Hector, W.S. Brocklesby, D.W. Hewak, and D.N. Payne, “Infrared emission and ion-ion interactions in thulium- and terbium-doped gallium lanthanum sulphide glass”, *Journal of the Optical Society of America B* **16**, 308-316 (1999).
 - 24 E.B. Mejia, A.N. Starodumov, and Yu. O. Barmenkov, “Blue and infrared up-conversion in Tm^{3+} -doped fluorozirconate fiber pumped at 1.06, 1.117, and 1.18 μm ”, *Applied Physics Letters* **74**, 1540-1542 (1999).
 - 25 J. Webjörn, S. Siala, D.W. Nam, R.G. Waarts, and R.J. Lang, “Visible laser sources based on frequency doubling in nonlinear waveguides”, *IEEE Journal of Quantum Electronics* **33**, 1673-1686 (1997).
 - 26 L. Wetenkamp, G.F. West, and H. Többen, “Co-doping effects in erbium³⁺- and holmium³⁺-doped ZBLAN glasses”, *Journal of Non-Crystalline Solids* **140**, 25-30 (1992).
 - 27 B. Peng, and T. Izumitani, “Blue, green and 0.8 μm Tm^{3+} , Ho^{3+} doped upconversion laser glasses, sensitized by Yb^{3+} ”, *Optical Materials* **4**, 701-711 (1995).
 - 28 J.R. Bonar, M.V.D. Vermelho, A.J. McLaughlin, P.V.S. Marques, J.S. Aitchison, J.F. MartinsFilho, A.G. Bezerra Jr, A.S.L. Gomes, C.B. deAraujo, “Blue light emission in thulium doped silica-on-silicon waveguides”, *Optics Communications*, **141**, 137-140 (1997).

- 29 X. Zou, and T. Izumitani, "Fluorescence mechanisms and dynamics of Tm^{3+} single doped and Yb^{3+} , Tm^{3+} doubly doped glasses", *Journal of Non-Crystalline Solids* **162**, 58-67 (1993).
- 30 A. Yariv, *Optical Electronics*, (Saunders College Publishing, Philadelphia USA, 1991)
- 31 E.W.J.L. Oomen, "Up-conversion of red light into blue light in thulium doped fluorozirconate glasses", *Journal of Luminescence* **50**, 317-332 (1992).
- 32 F.L. Galeaner, J.C. Mikkelsen, Jr. R.H. Geils, and W.J. Mosby, "The relative raman cross sections of vitreous SiO_2 , GeO_2 , B_2O_3 , and P_2O_5 ", *Applied Physics Letters* **32**, 34-36 (1978).
- 33 G.P. Agrawal, *Nonlinear Fiber Optics*, (Academic Press, INC Boston USA 1989).
- 34 M. Monerie, T. Georges, P.L. Francois, J.Y. Allain, and D. Neveux, *Electronics Letters* **26**, 320 (1990).
- 35 K. Hirao, S. Tanabe, S. Kishimoto, K. Tamai, and N. Soga, "UV and blue upconversion in Tm^{3+} -doped fluoroaluminate glass by 0.655 μm excitation", *Journal of Non-Crystalline Solids* **135**, 90-93 (1991).
- 36 K. Hirao, K. Tamai, S. Tanabe, and N. Soga, "Frequency upconversion and its new mechanism in Tm^{3+} -doped fluoroaluminate glasses", *Journal of Non-Crystalline Solids* **160**, 261-267 (1993).
- 37 R.E. Imhof and F.H. Read, "The measurement of lifetimes in atoms, molecules and ions", *Report on Progress in Physics*, **40**, 1-104 (1977).
- 38 H. Zellmer, U. Willamowski, A. Tunnermann, and H. Welling, "High-power cw neodymium-doped fiber laser operating at 9.2 W with high beam quality", *Optics Letters* **20**, 578-580 (1995).
- 39 T. Sakamoto, M. Shimizu, M. Yamada, T. Kanamori, Y. Ohishi, Y. Terunuma, and S. Sudo, "35-dB gain Tm -doped ZBLAN fiber amplifier operating at 1.65 μm ", *IEEE Photonic Technology Letters* **8**, 349-351 (1996).
- 40 K. Oh, A. Kilian, L. Reinhart, Q. Zhang, T.F. Morse, and P.M. Weber, "Broadband superfluorescence emission of the $^3\text{H}_4 \rightarrow ^3\text{H}_6$ transition in Tm -doped multicomponent silicate fiber", *Optics Letters* **19**, 1131-1133 (1994).
- 41 Z. [Hao 1], X. Chen, G. Zhang, F. Song, and Y-bing Hou, "Blue upconversion with excitation at 970 nm in $\text{Yb}_{0.18}$ -doped $\text{Tm}_{0.03}\text{LaP}_5\text{O}_{14}/\text{Tm}_{0.1}\text{LaP}_5\text{O}_{14}$ ", *Proceeding SPIE* **2897**, 275-278 (1996).
- 42 G. Özen, X. Wu, J.P.Denis, A. Kermaoui, F. Pellé, and B. Blanzat, "Optical properties and upconversion emissions of Tm^{3+} in Yb^{3+} doped fluorophosphate glasses", *Journal of Physical and Chemistry of Solids* **54**, 1533-1542 (1993).
- 43 R.A Hewes, and J.F. Sarver, "Infrared excitation processes for the visible luminescence of Er^{3+} , Ho^{3+} , and Tm^{3+} in Yb^{3+} -sensitized rare-earth trifluorides", *Physical Review* **182**, 427-436 (1969).
- 44 M.A. Chamarro, and R. Cases, "Energy transfer between (Yb,Pr), (Yb,Sm)

and (Yb,Dy) in fluorohafnate glasses”, *Journal of Non-Crystalline Solids* **107**, 178-186 (1989).

45 A.A. Kaminskii, Laser Crystal: Their Physics and Properties, (Springer-Verlag Berlin 1989).

Chapter 6 - Modelling Blue Upconversion Waveguide Laser

6.1 Introduction

The previous chapter demonstrated several pump schemes to generate blue light in thulium-doped and ytterbium sensitised thulium doped phosphosilicate waveguides. Those results pointed towards the possibility of obtaining efficient upconversion in the $\text{Tm}^{3+}/\text{Yb}^{3+}/\text{Na}^{+}$ doped samples, especially when pumped at 980 nm and 800 nm, which correspond to wavelengths available from commercial diode lasers.

In the past few years, great efforts have been made in the development of hosts for thulium doped upconversion lasers [1-6]. To date, all reported thulium-doped lasers were developed using fluoride-based optical fibres [7,8]. In this host, practical blue upconversion lasers efficiencies from 10% to up to 30% have been reported. Output powers of a few milliwatts of blue light using a single wavelength diode laser, or more than 100 mW of blue light employing two powerful tunable lasers have been

reported. An upconversion laser based on two-photon process in Tm^{3+} has also been reported in the same type of fibre, but pumped by two different wavelengths [9].

Fibre geometry is preferred for these lasers, due to the low scattering loss, and long interaction length. The possibility of optimisation of the cavity length during the experiments is also an attractive feature. Fibre lasers with long interaction lengths and low rare earth doping concentration make it possible to obtain laser action while avoiding the cross relaxation process. However, shorter and higher-doped laser cavity may have an advantage if a commercial single mode laser system is required as a component of practical devices [10]. Nevertheless, accurate modelling has to be developed to achieve this target.

This chapter aims to fulfil these considerations and develop a model for a thulium-ytterbium doped waveguide laser, and establish the potentiality of the Flame Hydrolysis Deposition (FHD) method for fabricating such an integrated laser. The FHD technology has been used for the realisation of monolithically integrated erbium doped lasers and amplifiers for the 1.55 μm optical communication wavelength [12-17]. The advantage of an integrated version compared to the fibres is in terms of size. One widely known application for blue laser light sources is for use in optical data storage. Consequently, a compact blue light source is a fundamental requirement [18].

To study the feasibility of a $\text{Tm}^{3+}/\text{Yb}^{3+}$ -doped phosphosilicate waveguide glass laser, initially the modelling procedure will be presented with the determination of the rate and propagation equations for the laser system. In order to define a simple and precise model, only the major contributions to the laser upconversion process have to be considered. Thus, the first part of the chapter is concerned with the determination of these contributions, as well as the estimation of the relevant spectroscopic parameters that will be used as input data to model. The modelling procedure developed in chapter four, for erbium-doped lasers, will be adapted to the thulium ions. After the definition of the rate equation systems, the latter part of this chapter will discuss the predicted characteristics of the observed ${}^1\text{G}_4 \rightarrow {}^3\text{H}_6$ laser emission, such as threshold, and the dependence on the doping level, along with the prospect for improved performance and continuous wave (CW) laser operation.

6.2 Determination of the Spectroscopic Parameters of the Model

The essential parameters required to model the CW upconversion Tm^{3+} -doped waveguide laser will be derived in three phases. Firstly, applying the Judd-Ofelt theory, parameters related to the radiative transitions, such as radiative lifetime and branching ratios, will be determined. Secondly, nonradiative transitions and the radiative quantum efficiency of all transitions will be evaluated. Finally, some considerations will be devoted in order to estimate the $\text{Tm} \leftrightarrow \text{Yb}$ cross relaxation coefficients.

6.2.1 Radiative Transitions

According to the Judd-Ofelt theory, the line strength of an electric-dipole transition between an initial J manifold and a terminal J' may be written in the form [19,20]:

$$S = \sum_{\lambda=2,4,6} \Omega_{\lambda} \left\langle \left\| f^N \alpha(S, L) J \left\| U^{(\lambda)} \right\| f^N \alpha'(S', L') J' \right\rangle \right|^2 \quad (6.1)$$

As described in the model, the Ω_{λ} may be regarded as phenomenological parameters characterising the radiative transition probabilities within the ground state configuration. The $\langle \left\| U^{(\lambda)} \right\| \rangle$ elements are the doubly reduced unit tensor operators calculated in the intermediate-coupling approximation. Thus, from the expression for the line strength, the value of the corresponding Einstein B -coefficient can be derived, and consequently, by means of the universal relation between A and B coefficients, the expressions for the spontaneous emission rate determined. A summary of the Judd-Ofelt theory is presented in section 2.5.2, where the relation between radiative transition, radiative lifetime, branching ratio, and peak cross-section are presented.

The doubly reduced unit tensors, which are independent of the host, are tabulated for several rare earth ions and are available in the literature. Unfortunately, not all the relevant parameters for the present modelling were found, and it was necessary to calculate them.

Using the technique described by Weber for erbium ions [21], the matrix elements of $U^{(\lambda)}$ for thulium were evaluated from the formula:

$$\begin{aligned} \langle f^{12} \alpha(S, L) J \| U^{(\lambda)} \| f^{12} \alpha'(S', L') J' \rangle &= (-1)^{S+L'+J+\lambda} \delta(S, S') [(2J+1)(2J'+1)]^{1/2} \\ &\times \begin{Bmatrix} J & J' & \lambda \\ L' & L & S \end{Bmatrix} \langle f^{12} \alpha(S, L) J \| U^{(\lambda)} \| f^{12} \alpha'(S', L') J' \rangle \end{aligned} \quad (6.2)$$

All parameters in the expression above, except the Kronecker delta symbol δ , and the Klebsh-Gordon coefficients (6-j) [24] are explained in the Russell-Saunders coupling described in the section 2.4. Initially, the wave functions for Tm^{3+} derived by Krupke and Gruber [22] were used to compute the unit tensor operator matrix elements between low-lying energy levels. Then, the Russell-Saunders values of the $U^{(\lambda)}$ were readily calculated using the tables of Nielsen and Koster [23], and the tabulated 6-j symbols of Rotenberg *et al.* [24]. The matrix elements of equation (6.2) are then transformed from the LS basis state to the intermediate coupling scheme before being squared. The results of these calculations are listed in the Table 6.1

Experimental fluorescence results measured in these samples at the 980 and 800 nm pumping wavelengths did not reveal signals generated by transitions above the 1G_4 level. Hence, this was assumed to be the upper level in the present upconversion process. The definition of the reduced matrix elements for thulium ions made possible the determination of the Judd-Ofelt parameters Ω_λ . The procedure to perform this measurement was described in section 3.2.2 for erbium ions. Only the main information for the thulium-doped samples will be repeated in this section.

Two samples with different thulium concentration were analysed. These included a single thulium doped glass, prepared with a 0.2 M solution, and a $Tm^{3+}/Yb^{3+}/Na^+$ doped sample prepared with a solution containing 0.1/1.0/0.1 M of thulium, ytterbium, and sodium chlorides, respectively. The Judd-Ofelt parameters of the Tm^{3+} -doped samples will be used as a benchmark to the $Tm^{3+}/Yb^{3+}/Na^+$, in order to observe any change in the glass due to the inclusion of Na^+ ions. Using a white light source to generate a broad spectral band radiation, four ground state absorption bands were individually measured along the spectral region between 600-1750 nm, namely

the ${}^3\text{H}_4$, ${}^3\text{H}_5$, ${}^3\text{F}_4$, and ${}^3\text{F}_{2,3}$; the typical results are depicted in Figure 5.1 and Figure 5.12, respectively.

Table 6.I
Reduced Matrix Elements for Tm^{3+}

Transition $[SL]J \rightarrow [S'L']J'$	$\langle J \ U^{(2)} \ J' \rangle^2$	$\langle J \ U^{(4)} \ J' \rangle^2$	$\langle J \ U^{(6)} \ J' \rangle^2$
${}^3\text{H}_4 \rightarrow {}^3\text{H}_6$	0.5274178	0.7182038	0.2276400
${}^3\text{H}_5 \rightarrow {}^3\text{H}_6$	0.1073174	0.2312564	0.6379007
$\rightarrow {}^3\text{H}_4$	0.0890630	0.1247453	0.9048682
${}^3\text{F}_4 \rightarrow {}^3\text{H}_6$	0.2488663	0.1179329	0.6081923
$\rightarrow {}^3\text{H}_4$	0.1292449	0.1323697	0.2125416
$\rightarrow {}^3\text{H}_5$	0.0107788	0.4795059	0.0043699
${}^3\text{F}_3 \rightarrow {}^3\text{H}_6$	0.0000000	0.3161708	0.8405278
$\rightarrow {}^3\text{H}_4$	0.0047857	0.0004463	0.1665701
$\rightarrow {}^3\text{H}_5$	0.6285713	0.3467813	0.0000000
$\rightarrow {}^3\text{F}_4$	0.0805146	0.3440599	0.2637414
${}^3\text{F}_2 \rightarrow {}^3\text{H}_6$	0.0000000	0.0000000	0.2574232
$\rightarrow {}^3\text{H}_4$	0.3103726	0.0562653	0.0441798
$\rightarrow {}^3\text{H}_5$	0.0000000	0.2899824	0.5825276
$\rightarrow {}^3\text{F}_4$	0.2868174	0.1624475	0.0740635
$\rightarrow {}^3\text{F}_3$	0.0035485	0.0745279	0.0000000
${}^1\text{G}_4 \rightarrow {}^3\text{H}_6$	0.0463722	0.0746921	0.0099585
$\rightarrow {}^3\text{H}_4$	0.0028373	0.0181418	0.0691259
$\rightarrow {}^3\text{H}_5$	0.0772811	0.0078059	0.5633094
$\rightarrow {}^3\text{F}_4$	0.1645116	0.0036333	0.4114455
$\rightarrow {}^3\text{F}_3$	0.0117345	0.0808467	0.3253330
$\rightarrow {}^3\text{F}_2$	0.0094892	0.0784151	0.0431720

To calculate the three phenomenological Judd-Ofelt parameters Ω_λ for each glass system, the integrated absorption bands and the respective reduced matrix elements in the equation 2.12, a least-square fitting procedure were applied and the parameters determined. The results are listed in Table 6.II. From a first inspection of these parameters, it can be inferred that the inclusion of sodium ions into the matrix of the thulium-doped glass has only a small effect on the parameters Ω_2 and Ω_4 . According

to interpretations for the Judd-Ofelt parameters, explained in chapter three, the small change in the Ω_2 indicates minor alteration in the ligand field of the glass components [25,26]. However, the parameter Ω_6 for the sample containing sodium has shown an increase of ~550% if compared with the single thulium doped. This suggests a reduction in the viscosity of the glass system [27]. The result also agrees with the influence of co-doping studied in the chapter three for erbium-doped samples containing different amounts of sodium ions.

Table 6.II
Judd-Ofelt parameters Ω_λ for the Tm^{3+} and $Tm^{3+}/Yb^{3+}/Na^+$ doped $SiO_2-P_2O_5$ samples

Sample	$\Omega_2 (\times 10^{-20} \text{ cm}^2)$	$\Omega_4 (\times 10^{-20} \text{ cm}^2)$	$\Omega_6 (\times 10^{-20} \text{ cm}^2)$
Tm^{3+}	8.23	3.73	0.25
$Tm^{3+}/Yb^{3+}/Na^+$	7.52	4.39	1.86

The radiative transition probabilities for emission between excited J manifold to the lower level J' of the Tm^{3+} ions in phosphosilicate glasses were calculated, using the Ω_λ values of Table 6.II, and the corresponding doubly reduced unit tensor operators $\langle \|U^{(\lambda)}\| \rangle$ (Table 6.I) for specific transitions, in the form [27]:

$$A_{a,b} = \frac{64\pi^4 e^2}{3h(2J+1)\lambda^3} \cdot [\chi_{ed} \cdot S_{a,b}^{ed} + \chi_{md} \cdot S_{a,b}^{md}] \quad (6.3)$$

The terms $S_{a,b}^{ed}$ and $S_{a,b}^{md}$ correspond to the electric and magnetic dipole line strength, respectively. The other parameters have the usual meaning as explained in section 2.5.2. Observing the magnetic dipole and electric dipole selection rules, the probabilities for the respective radiative transitions were calculated. They are listed in the third and fourth column of Table 6.III.

The calculation of the radiative transition probabilities for all energy levels of interest makes possible the determination of the respective radiative lifetimes and the branching ratios. The results are listed in the final two columns of Table 6.III, respectively. The accuracy of these parameters can be tested by comparing the calculated radiative lifetime of the $^3F_4 \rightarrow ^3H_6$ transition and the measured fluorescence lifetime. The determined value of 1.26 ms is close to the 1.40 ms

measured in the previous chapter.

Table 6.III
Calculated Spontaneous emission probabilities of Tm³⁺/Yb³⁺/Na⁺ in phosphosilicate glass prepared with solution 0.1/1.0/0.1 M.

Transition	Average Frequency (cm ⁻¹)	A _{ed} (s ⁻¹)	A _{md} (s ⁻¹)	Radiative Lifetime (ms)	Branching Ratio (β _{ij})	σ _{ij} (×10 ⁻²⁵ m ²)
³ H ₄ → ³ H ₆	5945.2	149.6		6.69	1.00	
³ H ₅ → ³ H ₆	8334.3	162.0	15.2	5.53	0.98	4.3
→ ³ H ₄	2389.2	3.6			0.02	
³ F ₄ → ³ H ₆	12615.2	672.2		1.26	0.84	4.2
→ ³ H ₄	6670.0	98.7			0.12	
→ ³ H ₅	4280.8	25.9			0.04	
³ F ₃ → ³ H ₆	14520.5	1106.8		0.70	0.78	
→ ³ H ₄	8575.6	226.8			0.16	3.8
→ ³ H ₅	6186.0	84.8			0.06	
→ ³ F ₄	1905.3	2.3	0.10		0.00	
³ F ₂ → ³ H ₆	14836.8	268.4		2.86	0.77	
→ ³ H ₄	8891.6	57.5			0.16	
→ ³ H ₅	6502.4	22.4			0.06	
→ ³ F ₄	2221.6	0.8			0.00	
→ ³ F ₃	316.3	0.0	0.01		0.00	
¹ G ₄ → ³ H ₆	20746.9	595.0		1.00	0.59	1.0
→ ³ H ₄	14801.1	214.9			0.21	1.0
→ ³ H ₅	12412.5	126.5			0.13	0.9
→ ³ F ₄	8131.7	35.4			0.04	1.9
→ ³ F ₃	6226.4	15.8			0.02	
→ ³ F ₂	5910.1	13.5			0.01	

Finally the stimulated emission cross section σ_{a,b} for the relevant thulium transitions for the lasers modelling has been calculated and are listed in the last column of Table 6.III. The stimulated emissions were estimated from the equation [28]:

$$\sigma_{a,b}(\lambda_p) = \frac{\lambda_p^4}{8\pi \cdot c \cdot n^2 \cdot \Delta\lambda_{eff}} A_{a,b} \quad (6.4)$$

where λ_p is the peak fluorescence wavelength of the emission band and Δλ_{eff} is the effective fluorescence bandwidth. This parameter is used because of the asymmetry of the emission bands, and is determined by dividing the integrated fluorescence line

shape by its peak intensity at λ_p . When it was impossible to measure the fluorescence lineshape, e.g. for transitions between two excited states, it was assumed to equal the lifetime broadening, i.e. the final linewidth was assumed to correspond to the sum of the individual ground state widths ($\Delta\nu_{21} = \Delta\nu_1 + \Delta\nu_2$) [29]. Finally, the emission cross sections were converted into absorption cross sections using the relation [29]:

$$\sigma_{h,a} = \frac{(2J_a + 1)}{(2J_h + 1)} \sigma_{a,h} \quad (6.5)$$

The ytterbium absorption cross section was determined from the absorption spectrum applying McCumber's theory [30,31], and the fluorescence lifetime was measured in a similar procedure as used for measuring the lifetime of erbium ions described in the third chapter of this thesis. The peak cross section was estimated to be $6.0 \times 10^{-25} \text{ m}^2$, and the lifetime of the ${}^2F_{5/2} \rightarrow {}^2F_{7/2}$ transition was measured $\sim 1.50 \text{ ms}$.

Thus, the spectroscopic parameters relating to radiative dipole-dipole interactions were evaluated. The next two sections will be concerned with estimations of nonradiative parameters.

6.2.2 Nonradiative Transitions - Multiphonon Relaxation

Rare earth ions in solids can undergo transitions because of their interaction with the lattice vibrations of the host material. This process occurs predominantly in the downward direction, i.e., the ion makes a nonradiative transition to a lower electronic state through the emission of multiple phonons to conserve energy [32]. Thus, if the nonradiative relaxation rate of a level is comparable to its radiative transition rate, the efficiency of the luminescent processes originating on that level is degraded. However, as discussed in the section 2.6, nonradiative transitions are not always a deleterious process in upconversion. Phonon energies are also required for efficient upconversion processes because the subsequent energy gaps usually do not match exactly the excitation energy steps. This energy difference (mismatch) has to be overcome by multiphonon transitions.

The expression from Layne and co-workers [33] was employed to evaluate the nonradiative transition rate for a p - order multiphonon decay:

$$W_{nr} = C \cdot [n(T) + 1]^p \cdot \exp(-\alpha \cdot \Delta E) \quad (6.6)$$

in this expression C and α are host-dependent parameters; ΔE is the energy level gap; p is the number of phonons required to bridge the gap; and $n(T)$ is the Bose-Einstein occupation number for the effective phonon mode, as expressed in equation 2.19 (section 2.6). In practice, C and α are regarded as empirical parameters that are host dependent, but insensitive to the rare earth ion and energy level involved [32]. Table 6.IV summarises these parameters for two glass hosts [32,34]. As the thulium-doped samples fabricated by FHD belong to a $\text{SiO}_2\text{-P}_2\text{O}_5$ glass system, the parameters for phosphate glasses, which are the worst-case parameters for laser action, were chosen.

Table 6.IV
Parameters describing the Nonradiative relaxation of rare earth ions in glass
[34].

Host	C (s^{-1})	α ($\times 10^{-3}$ cm)	$h\nu$ (cm^{-1})
Phosphate	5.4×10^{12}	4.7	1200
Silicate	1.4×10^{12}	4.7	1100

Substituting these parameters into equation (6.6), the nonradiative transition rates and the radiative quantum efficiency were calculated, and the results are listed in Table 6.V. The determination of the radiative and nonradiative transitions made it possible to calculate the radiative quantum efficiencies for each level. Their respective values are listed in the last column in the same table.

To complete the estimate of spectroscopic parameters to model the upconversion thulium doped waveguide laser, the cross relaxation contribution to the nonradiative transition have to be estimated. This will be carried out in the next section.

Table 6.V
Calculated non-radiative transition probabilities and the radiative quantum efficiency

Transition	Average Frequency (cm ⁻¹)	Nonradiative Transition (s ⁻¹)	Radiative Quantum Efficiency (η _i)
³ H ₄ → ³ H ₆	5945.2	0.86	0.99
³ H ₅ → ³ H ₆	8334.3	~ 10 ⁻⁵	~ 10 ⁻⁵
→ ³ H ₄	2389.2	1.60 × 10 ⁷	
³ F ₄ → ³ H ₆	12615.2	~ 0	0.27
→ ³ H ₄	6670.0	3.00	
→ ³ H ₅	4280.8	2.21 × 10 ³	
³ F ₃ → ³ H ₆	14520.5	~ 0	~ 10 ⁻⁵
→ ³ H ₄	8575.6	~ 10 ⁻⁶	
→ ³ H ₅	6186.0	0.29	
→ ³ F ₄	1905.3	1.55 × 10 ⁸	
³ F ₂ → ³ H ₆	14836.8	~ 0	0.00
→ ³ H ₄	8891.6	~ 10 ⁻⁵	
→ ³ H ₅	6502.4	6.47	
→ ³ F ₄	2221.6	3.51 × 10 ⁷	
→ ³ F ₃	316.3	2.71 × 10 ¹¹	
¹ G ₄ → ³ H ₆	20746.9	~ 0	0.99
→ ³ H ₄	14801.1	~ 0	
→ ³ H ₅	12412.5	~ 0	
→ ³ F ₄	8131.7	~ 10 ⁻³	
→ ³ F ₃	6226.4	0.24	
→ ³ F ₂	5910.1	1.04	

6.2.3 Nonradiative Transitions - Cross Relaxations

Part of the nonradiative relaxations in certain rare earth doped materials are attributed to the cross relaxations, which involve an exchange of energy between active ions [35]. Thus, a precise determination of the parameters governing these interactions is crucial for rare earth doped devices. A precise definition of these parameters is particularly important in the present modelling because the efficiency of the upconversion process involving Tm³⁺/Yb³⁺ depends on the energy transfer

between these two ions. Thus, to improve the accuracy of modelling of a laser based on two rare earths, it is essential to determine the precise relation between these cross relaxation parameters. The purpose of this study is to provide data on the energy transfer between Tm^{3+} and Yb^{3+} ions. As demonstrated by several research groups, the Forster-Dexter energy-transfer model for dipole-dipole interactions is a suitable method to describe these interactions. The direct relation between the transition probability of the dipole-dipole energy transfer model and the transfer coefficients in the rate equations have already been demonstrated and widely applied [36,37]. The transition probability rate is given by [37]:

$$P_{da} = \frac{1}{\tau_d} \frac{3h^4 c^4}{4\pi \cdot n^4} \left(\frac{1}{R_{da}} \right)^6 \cdot \sigma_d \cdot \int \frac{f_d(E) \cdot F_a(E)}{E^4} dE \quad (6.7)$$

The meaning of each term was introduced in section 2.6.1. This expression can be simplified, defining in terms of a critical radius R_0 . This radius correspond to the case when $P_{da} \cdot \tau_d = 1$, i.e. the rate of the transition probability is comparable to the radiative transition of the level. In this case, the critical radius is defined as $R_{da} = R_0$. In terms of R_0 , the expression can be simplified and written as:

$$P_{da} = \frac{1}{\tau_d} \left(\frac{R_0}{R_{da}} \right)^6 \quad (6.8)$$

The main task in determining the critical radius is the evaluation of the overlap integral in equation (6.7), because usually the lineshape of the emission and absorption lines are not known. The following procedures were adopted in order to determine and normalise the line shapes of the donor emissions and the acceptor absorptions involved. The absorption line shape of the ytterbium ions was measured using a white light source. The fluorescence line shape was evaluated by means of McCumber's theory [30,31] (section 2.5.1). The accuracy of the prediction was verified using the transversal fluorescence measurement of the same transition of the ytterbium ions, and the spectral profiles were in a very good agreement.

To estimate the Tm^{3+} transitions, only the ${}^3\text{H}_6 \rightarrow {}^3\text{H}_5$ and the ${}^3\text{H}_6 \rightarrow {}^3\text{F}_4$ absorption measurements were available. Using a procedure similar to that used for ytterbium,

the respective fluorescence line shapes were calculated from the absorption measurements. The shapes of the remaining absorption lines, ${}^3\text{H}_4 \rightarrow {}^3\text{F}_{2,3}$ and ${}^3\text{F}_4 \rightarrow {}^1\text{G}_4$, are not accessible for direct measurement and were estimated using the following considerations: due to the low concentration of the thulium ions in the present samples, they were considered homogeneously distributed. Thus, the line broadenings could be considered due to only homogeneously broadening and Lorentzian profiles were assumed. Due to the lack of information concerning the actual bandwidths, the same value as the ${}^3\text{H}_6 \rightarrow {}^3\text{F}_4$ transition ($\sim 30\text{nm}$) was assumed for each level. The required absorption cross sections were calculated before and shown in the Table 6.III. The critical radii R_0 were calculated for each transition and the result are listed in Table 6.VI. These results are in the range found for other rare earths in other matrices.

Table 6.VI
Calculated critical radii for the dipole-dipole energy transfer model.

Donor Level	Acceptor Level	Critical Radius (nm)	Cross relaxation coefficients ($\times 10^{-24} \text{ m}^3/\text{s}$)
$\text{Tm}^{3+}({}^3\text{F}_4)$	$\text{Yb}^{3+}({}^2\text{F}_{5/2})$	1.03	1.24
$\text{Yb}^{3+}({}^2\text{F}_{5/2})$	$\text{Tm}^{3+}({}^3\text{H}_5)$	1.96	60.18
$\text{Yb}^{3+}({}^2\text{F}_{5/2})$	$\text{Tm}^{3+}({}^3\text{F}_{2,3})$	1.53	13.62
$\text{Yb}^{3+}({}^2\text{F}_{5/2})$	$\text{Tm}^{3+}({}^1\text{G}_4)$	1.34	6.15

The next step in calculating the energy transfer rate is the determination of the donor-acceptor distance as a function of the rare earth concentration. For the current model, a simple case of the nearest-neighbour interaction was used, i.e. only those excited donors that had an acceptor as its neighbour were considered. Therefore, only the fraction $N_a/(N_a + N_d)$ of all donors is in the situation. In the expression, N_a and N_d are the acceptor and donor concentrations, respectively.

An accurate determination of the nearest neighbour distance R_{da} in a glass is difficult. However, Quimby *et al.* [38] have shown using elementary statistic arguments that the fraction p of ions having a neighbouring ion within a distance R is given by:

$$p = 1 - e^{-N_T (4\pi/3)R_{da}^3} \quad (6.9)$$

where N_T is the sum of the donor and acceptor ion concentrations. Thus, the radius R_{da} was chosen as the distance within which there is a $(1-1/e)$ probability of finding a neighbour. For a random distribution, the donor acceptor ions distance can be estimated by:

$$R_{da} \cong \frac{0.62}{\sqrt[3]{N_a + N_d}} \quad (6.10)$$

Combining the preceding results, the energy transfer coefficients when the two species of ions are incorporated into the matrix can be expressed by:

$$C_{ij} \cong 17.6 \cdot \left(\frac{R_0^6}{\tau_d} \right) \cdot (N_a + N_d) \quad (6.11)$$

The last column in Table 6.VI contain typical values of the cross relaxation coefficients for a 0.11 wt% thulium doped sample with a $\text{Yb}^{3+}/\text{Tm}^{3+}$ ratio of 10. The order of magnitude of the calculated results is in good agreement with the values reported in the literature [36,37].

This section completes the introductory part of this chapter describing the evaluation of the spectroscopic parameters necessary to model a Tm/Yb doped upconversion laser. The following part of the chapter will be concerned with the development of the model as well as some initial simulations.

6.2.4 Fluorescence Contributions to the Rate Equations

The estimates for the spectroscopic parameters defined in the previous section will allow a more realistic waveguide laser model to be attempted, by making as few assumptions as possible, and maintaining practical computer run times. Initially the fluorescence contributions to the rate equations were estimated assuming each level can undergo both radiative and nonradiative transitions, making their contribution proportional to the radiative quantum efficiency of the level. The results of this calculation are shown in Table 6.VII. Thus, an excellent approximation to the

fluorescent process in a Tm^{3+} phosphosilicate glass system is expected if only the dominant transition rates are considered. These contributions are written in boldface, blue characters in Table 6.VII

The values in Table 6.VII allow the definition of more realistic spontaneous emission and nonradiative transitions for thulium ions incorporated in a phosphosilicate glass system. The overestimated values of the nonradiative transitions can be observed in the calculated fluorescence lifetime of the transition ${}^3\text{F}_4 \rightarrow {}^3\text{H}_6$. The measured value was ~ 1.40 ms, while the calculated value is only ~ 0.32 ms. According to equation (2.20), this difference is a consequence of the overestimated contribution of the nonradiative transition to the lifetime. It was pointed out in the section concerning the calculation of the nonradiative transition due to multiphonon relaxation that, as a result of the lack of information about the necessary constant to calculate the problem, we adopted the values which presented the worst-case estimate for laser operation.

The next step consists of determining the rate equations for the Tm/Yb doped glass system. Based on the experimental observation of the efficiency of the upconversion processes of the $\text{Tm}^{3+}/\text{Yb}^{3+}/\text{Na}^+$ -doped samples reported in the previous chapter, only the pump wavelengths at 980 nm and 800 nm will be considered. This choice of pump wavelengths is also supported by the great technological interest in the development of blue upconversion laser light pumped by one of these infrared wavelengths, since production of commercial diode lasers at these wavelengths is an established technology.

Table 6.VII
Determination of the relevant fluorescence contribution to the upconversion
process in thulium doped SiO₂-P₂O₅ glass.

Transition	Average Wavelength (nm)	$(1 - \eta_i) \cdot W_{i,j}^{nr}$ (s ⁻¹)	$\eta_i \cdot \beta_{i,j} \cdot (A_{ed} + A_{md})$ (s ⁻¹)
³ H ₄ → ³ H ₆	1682	5.21 × 10 ⁻³	148.70
³ H ₅ → ³ H ₆	1200	~ 10 ⁻⁵	1.97 × 10 ⁻²
→ ³ H ₄	4185	1.60 × 10⁷	~ 10 ⁻⁵
³ F ₄ → ³ H ₆	793	~ 0	1504.20
→ ³ H ₄	1499	2.16 × 10 ⁻²	3.24
→ ³ H ₅	2336	1621.70	0.22
³ F ₃ → ³ H ₆	689	~ 0	7.9 × 10 ⁻²
→ ³ H ₄	1166	~ 10 ⁻⁶	3.31 × 10 ⁻³
→ ³ H ₅	1617	0.29	~ 10 ⁻⁵
→ ³ F ₄	5249	1.55 × 10⁸	< 10 ⁻⁶
³ F ₂ → ³ H ₆	674	~ 0	< 10 ⁻⁶
→ ³ H ₄	1125	< 10 ⁻⁶	< 10 ⁻⁶
→ ³ H ₅	1538	6.47 × 10 ⁻²	< 10 ⁻⁸
→ ³ F ₄	4501	3.51 × 10⁷	~ 0
→ ³ F ₃	31612	2.71 × 10¹¹	~ 0
¹ G ₄ → ³ H ₆	482	~ 0	353.15
→ ³ H ₄	676	~ 0	46.06
→ ³ H ₅	806	~ 0	15.95
→ ³ F ₄	1230	< 10 ⁻⁸	1.25
→ ³ F ₃	1606	3.02 × 10 ⁻⁴	0.25
→ ³ F ₂	1692	1.33 × 10 ⁻³	0.18

6.3 Laser Modelling

The models will be applied to two different pump wavelengths, namely 980 nm, corresponding to the ytterbium ions absorption band, and 800 nm resonant with the thulium ions $^3H_6 \rightarrow ^3F_4$ absorption band. The main fluorescence contributions to the rate equation systems of both models are analogous. The differences are only in the terms involving the pump wavelengths. A similar and more detailed derivation of all equations describing a laser model was developed in the chapter four. Here, only an outline will be presented.

Both models are grouped by the two types of equations used. These are the time dependent laser rate equations and the space dependent scalar wave propagation equations. The wave equations describe mathematically the forward and backward propagation of the optical fields in the laser cavity. For simplicity, two optical frequencies have been used to generate the results of the simulations. These are the laser signal frequency at 482 nm and the pump signal.

The next section will be devoted to the determination and modelling of the system pumped at 980 nm.

6.3.1 Rate Equations for Pump Wavelength at 980 nm

The simplified diagram of energy levels for a thulium/ytterbium doped phosphosilicate glass is shown in Figure 6.1. This diagram was elaborated by considering the pump wavelength at 980 nm, related to the ytterbium absorption band and the relevant contributions defined in the Table 6.VII. Based on the experimental evidence of the absence of fluorescence from levels above 1G_4 , the thulium ions diagram energy levels was considered up to this limit. Ytterbium ions were represented by a two-level system. The energy levels are labelled so that numbers from zero to six correspond to the ground state to the upper level of the thulium ions and the numbers 7 and 8 represent the ytterbium ground state and excited state, respectively.

The convention adopted for the diagram uses dotted lines for the nonradiative

transitions, and dashed lines for the energy transfer between donors and acceptor ions by cross relaxation. Dot-dashed lines represent spontaneous radiative transitions, and solid lines are stimulated emission and absorption transitions.

The cross relaxation parameters C_{ij} are labelled in such a way that the index 'i' is related to the donor level and 'j' is to the acceptor level.

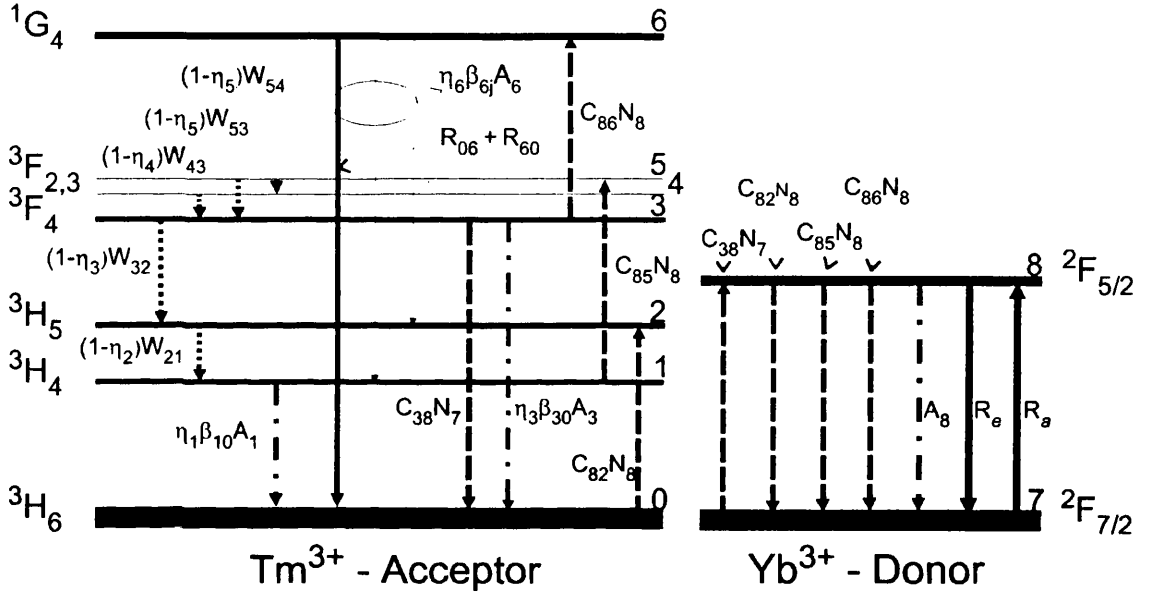


Figure 6.1: Energy level diagram showing radiative, nonradiative, and stimulated transitions of the Tm^{3+} ions.

The rate equations defined for pumping at a wavelength of 980 nm based on the diagram of Figure 6.1 are:

$$\frac{dN_0}{dt} = -R_{06}N_0 + \eta_1\beta_{10}A_1N_1 + \eta_3\beta_{30}A_3N_3 + (R_{60} + \eta_6\beta_{60}A_6)N_6 - C_{82}N_0N_8 + C_{38}N_3N_7 \quad (6.12)$$

$$\frac{dN_1}{dt} = -\eta_1\beta_{10}A_1N_1 + (1-\eta_2) \cdot W_{21}^{nr}N_2 + \eta_6\beta_{61}A_6N_6 - C_{85}N_1N_8 \quad (6.13)$$

$$\frac{dN_2}{dt} = -(1-\eta_2) \cdot W_{21}^{nr}N_2 + (1-\eta_3) \cdot W_{32}^{nr}N_3 + \eta_6\beta_{62}A_6N_6 + C_{82}N_0N_8 \quad (6.14)$$

$$\frac{dN_3}{dt} = -[(1-\eta_3) \cdot W_{32}^{nr} + \eta_3\beta_{30}A_3]N_3 + (1-\eta_4) \cdot W_{43}^{nr}N_4 + (1-\eta_5) \cdot W_{53}^{nr}N_5 - C_{38}N_3N_7 - C_{86}N_3N_8 \quad (6.15)$$

$$\frac{dN_4}{dt} = -(1-\eta_4) \cdot W_{43}^{nr}N_4 + (1-\eta_5) \cdot W_{54}^{nr}N_5 \quad (6.16)$$

$$\frac{dN_5}{dt} = -(1 - \eta_5)[W_{53}^{nr} + W_{54}^{nr}]N_5 + C_{85}N_1N_8 \quad (6.17)$$

$$\frac{dN_6}{dt} = R_{06}N_0 + C_{86}N_3N_8 - [R_{60} + \eta_6(\beta_{60} + \beta_{61} + \beta_{62})A_6]N_6 \quad (6.18)$$

$$\begin{aligned} \frac{dN_7}{dt} = -\frac{dN_8}{dt} = & -R_aN_7 + (R_e + A_8)N_8 - C_{38}N_3N_7 + \\ & + (C_{82}N_0 + C_{85}N_1 + C_{86}N_3)N_8 \end{aligned} \quad (6.19)$$

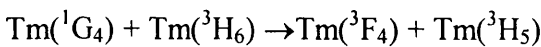
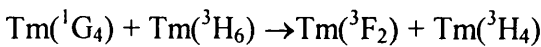
This set of differential equations describes the rate at which each energy level in the material is populated and depleted by absorption, stimulated emission, spontaneous emission, and cross relaxation processes as a function of the longitudinal and transverse dimensions. The N_i 's are the population densities of thulium ($0 \leq i \leq 6$) and ytterbium ($i = 7$ and 8) ions, they are functions of time and position $N_i = N_i(t, x, y, z)$. The conservation of the number of photons dictates that $N_{Yb} = N_7 + N_8$, and, $N_{Tm} = \sum_{i=0}^6 N_i$ where N_{Yb} and N_{Tm} are the total ytterbium and thulium ions concentrations, respectively. R_a and R_e are the pump and, R_{ij} are the signal stimulated transition rates, respectively. They are represented by:

$$R_{a,e} = \frac{\sigma_{a,e} I_p(t, x, y, z)}{h\nu_p} \quad R_{i,j} = \frac{\sigma_{i,j} I_s(t, x, y, z)}{h\nu_{i,j}}$$

where η_i and β_{ij} are the radiative quantum efficiency of level i and the branching ration of the transition $i \rightarrow j$. A_i correspond to the total radiative lifetime of level i . The intensities $I_p(t, x, y, z)$ and $I_s(t, x, y, z)$ are the pump and signal intensities and are related to the mode densities according to equation (4.10) and (4.11), respectively.

The cross relaxation among thulium ions was not considered in the model at this stage. According to the reported Tm^{3+}/Tm^{3+} cross relaxation processes in fluoride glasses, the possible routes are [18]:

from the 1G_4 level



$\text{Tm}(^1\text{G}_4) + \text{Tm}(^3\text{H}_6) \rightarrow \text{Tm}(^3\text{H}_5) + \text{Tm}(^3\text{F}_4)$, and

and from the $^3\text{F}_4$ level:

$\text{Tm}(^3\text{F}_4) + \text{Tm}(^3\text{H}_6) \rightarrow \text{Tm}(^3\text{H}_4) + \text{Tm}(^3\text{H}_4)$.

However, according to Table 6.VII, only the $^1\text{G}_4 \rightarrow ^3\text{H}_5$ fluorescence transition is likely to happen in the phosphosilicate glass host, because the other transitions are dominated by nonradiative relaxations. In addition, applying the Forster-Dexter energy-transfer model, it was estimated that thulium concentration below 0.31 wt% is unlikely to undergo cross relaxation energy transfer. A small contribution of this factor in the population levels is also expected because the $^1\text{G}_4 \rightarrow ^3\text{H}_5$ radiative transition represents only a small fraction ($\sim 4.0\%$) of the relaxations from $^1\text{G}_4$ level. Based on these considerations, the laser model did not include energy exchange between Tm^{3+} ions.

The wave equations coupled with the set of laser rate equations governing the evolution of the pump and signal along the waveguide are:

$$\frac{dI_p(t, x, y, z)}{dz} = -\sigma_a \left[N_7 - \left(\frac{\sigma_e}{\sigma_a} \right) \cdot N_8 \right] \cdot I_p(t, x, y, z) - \alpha_p \cdot I_p(t, x, y, z) \quad (6.20)$$

$$\frac{dI_s^\pm(t, x, y, z)}{dz} = \pm \sigma_{60} \left[N_6 - \left(\frac{\sigma_{06}}{\sigma_{60}} \right) \cdot N_0 \right] \cdot I_s^\pm(t, x, y, z) \mp \alpha_s \cdot I_s^\pm(t, x, y, z) \quad (6.21)$$

where σ_a and σ_e are the peak absorption and emission cross sections at the pump wavelength of the ytterbium ions, while σ_{06} and σ_{60} correspond to analogous cross sections at the signal wavelength. α_p and α_s represent the scattering losses at the pump and signal wavelength, respectively.

6.3.2 Laser Design Considerations - $\lambda_p = 980 \text{ nm}$

To limit the huge flexibility of waveguide designs fabricated by the FHD method, only straight waveguide configurations will be considered in the following simulations. From the practical point of view, this reduces the possibility of bending

losses being added to the system. Thus, the maximum laser cavity length analysed was a 10.0 cm long, assuming fabrication on a 4.0-inch wafer. Unless specified, the laser cavities in all simulations will be assumed 6.0 cm long, the typical value for a 3.0-inch wafer.

In order to give single transversal mode operation, a $5.0 \mu\text{m} \times 5.0 \mu\text{m}$ waveguide cross section was chosen. This waveguide ensures monomode operation only for the pump wavelength. However, experimental results reveal that fundamental operation can usually dominates, even when the waveguides support higher modes [8]. For the present simulations single mode operation for both the signal and pump wavelengths were assumed.

A Fabry-Perot laser cavity was composed of two mirrors with signal wavelength reflectivity R_i (0.99) and R_o (0.90), for the input and output mirrors, respectively, mounted against a thulium-ytterbium-doped waveguide. The mirrors were assumed transparent to the pump wavelength.

The accuracy of the parameters defined by the Judd-Ofelt theory is already known, and has been successfully used by several research groups [39-45]. The nonradiative relaxations influence in the laser performance is important, but is not vital. Thus, their overestimated values will not invalidate the prediction of the laser modelling. However, among the spectroscopic parameters defined earlier, the cross relaxation coefficients are those with greater influence on the laser performance. At the same time, they were defined with a number of assumptions and approximations. For this reason, prior to modelling the laser performance itself, the model was used to predict the sensitivity of the laser performance on these coefficients variation. A variation of $\pm 25\%$ of the calculated value was assumed.

Typical reported scattering loss in phosphosilicate glass waveguides fabricated by FHD are ~ 0.15 dB/cm at $1.30 \mu\text{m}$ [12-14]. The present simulations were carried out assuming two values of loss: 0.10 and 0.25 dB/cm. In the remaining calculations, the backscattering losses at the pump and signal wavelengths were assumed fixed at 0.25 dB/cm. Figure 6.2 depicts the results of the simulation. In both conditions analysed, even a deviation of 25% in the cross relaxation evaluation, did not invalidate the

analysis. The saturation in the blue output power when the pump power exceeds 50 mW will be discussed later.

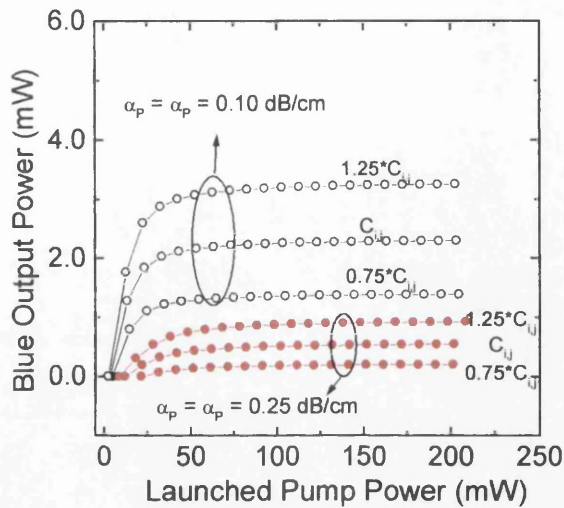


Figure 6.2: Predicted output power as a function of the launched pump power for the cross relaxation parameters varying in $\pm 25\%$ of the calculated value. The backscattering loss was considered as parameter. The design considered the following waveguide parameters: squared cross section of $5.0 \mu\text{m} \times 5.0 \mu\text{m}$, and straight 6.0 cm long.

The first parameter whose effect on laser operation investigated was the rare earth doping level. Low threshold pump power is a general requirement for all laser systems. However, for active integrated optic devices pumped by semiconductor lasers operating at 980 nm , due to the diode lasers relatively low output power, the threshold pump power is a limiting factor. Generally, parameters such as low cavity loss and long gain medium contribute to reducing the required threshold pump power. Increasing the rare earth doping level can compensate the limited length of the fabrication process. However, it has been experimentally observed during FHD that high doping concentrations usually tend to solidify in the torch at some point during glass deposition, thus causing severe damage to the surface. Thus, the rare earth concentration was analysed to evaluate the feasibility of realising the upconversion laser.

The simulations assumed thulium-doping levels from $0.05 \text{ wt}\%$ to $0.5 \text{ wt}\%$ with ytterbium/thulium ions ratio as adjustable parameter. Four ratios were considered as shown in Figure 6.3. For the phosphosilicate glass system under consideration,

one wt% approximately corresponds to $8.0 \times 10^{25} \text{ m}^{-3}$.

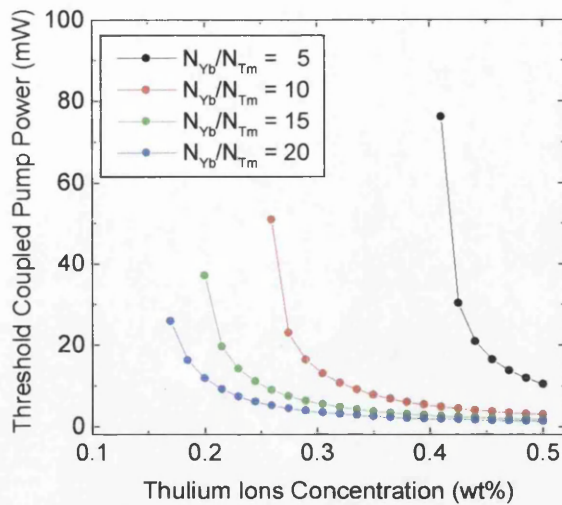


Figure 6.3: Laser threshold pump power as a function of the Tm ions concentration. The ratio of ytterbium / thulium doping level was the parameter. Waveguide cross-section was $5.0 \times 5.0 \mu\text{m}$ and cavity length of 6.0 cm.

From a practical device fabrication point of view, the rare earth concentration ratios Yb/Tm of 10 and 15 are preferable. In order to test this suggestion, an extended simulation was for the concentration ratio of 10. It took into account other modes propagating for the pump and signal wavelengths, for this the waveguide cross section was increased to $8.0 \mu\text{m} \times 7.0 \mu\text{m}$. This made possible two and four propagation modes for pump and signal, respectively. The propagation loss was also increased to 0.40 dB/cm for both signal and pump wavelengths. Under this situation, the threshold was 120 mW for a 0.30-wt% concentration of thulium ions. In terms of rare earth doping concentrations, these waveguide parameters are still feasible for FHD devices. Returning to the previous waveguide parameters, the next simulations will analyse the cavity length for a given doping level.

The importance of obtaining an understanding of the influence of the waveguide length is due to two main reasons. Firstly, if a long interaction length is necessary for laser action to take place, it will become a serious obstacle to be overcome. To obtain long waveguides it is necessary to design them in the form of a spiral and it will considerably increase the background loss due to bending. The second reason for prior determination of the optimum cavity length is that, unlike optical fibres, the

waveguide lengths cannot be easily changed after fabrication.

The modelling above, guided by practical considerations, assumed the thulium concentration of 0.30 wt% and a rare earth doping ratio of 10 to study the influence of cavity length. This doping level results in a predicted threshold power of 13 mW in a 6.0 cm long cavity as depicted in Figure 6.3. This condition indicates a good starting point for optimisation. Thus, the laser cavity characteristic was analysed under four pump power regimes, from 25 mW to 100 mW of coupled power, and the results are in Figure 6.4.

The simulated results agree with known experimental result. As is well known from rare earth doped single pass fibres optical amplifiers, a net positive gain can exist in a medium as long as the population inversion is maintained [46]. Thus, optimal cavity lengths are expected for different pump power regime. According to Figure 6.4, for higher pump power the positive gain can be maintained with a signal propagating along a 6.0 cm cavity. Under this waveguide laser configuration, shorter cavities have been shown to be preferable for low pump power regime. However, gain was observed only for cavity lengths longer than 2.5 mm for all pump power regime investigated in this configuration.

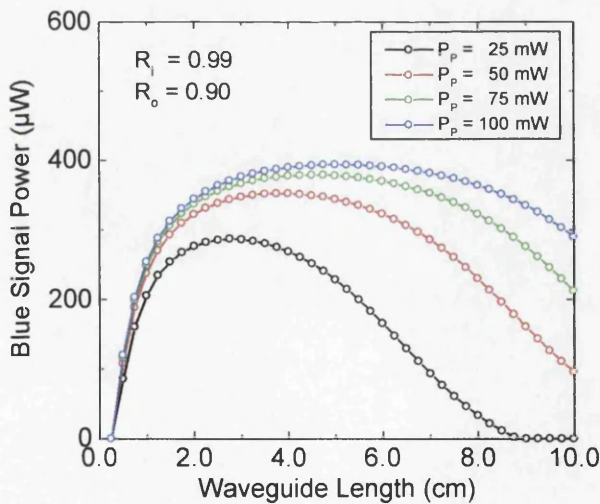


Figure 6.4: Predicted blue laser output power as a function of the laser cavity length. The pump power regime was the parameter. Backscattering loss $\alpha_p = \alpha_s = 0.25$ dB/cm. Waveguide cross-section was $5.0 \times 5.0 \mu\text{m}$.

A change in the output mirror reflectivity, at the signal wavelength, from 0.90 to 0.80 increases the optimum cavity length from 2.75 cm to 3.50 cm, for a pump power of 25 mW. At the same time, the blue signal output power at 482 nm increased from 286 μW to 424 μW at the optimum cavity length. This result suggests the choice of output mirror reflectivity at the signal wavelength is important for optimisation of the waveguide laser, and it is examined next.

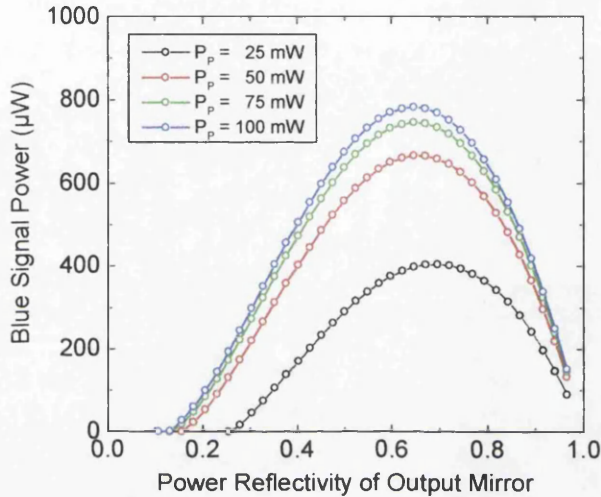


Figure 6.5: Blue laser output power as a function of the output mirror reflectivity. The pump power regime was the parameter. Backscattering loss $\alpha_p = \alpha_s = 0.25$ dB/cm, input mirror reflectivity equal 0.99.

Setting the cavity length to 5.0 cm and maintaining the parameters used above, the influence of the output reflectivity mirror was analysed in the same laser structure. The result of the modelling is depicted in Figure 6.5. All curves of Figure 6.5 should cut the horizontal axis in two places, corresponding to the extreme situation of $R_0 \approx 0$ (single-pass amplifier) and for $R_0 \approx 1$ (blocked cavity). The high reflectivity should intersect the zero value at $R_0 = 0.99$ because of the 1% of loss considered in this mirror. This loss could be due to an imperfect waveguide end mirror interface, for example. The simulations did not reach this limit because of the large steps used in the simulations. The low reflectivity intersections are not all in the same position because they are the points that satisfy the laser threshold condition. When the reflectivity is below these cut-off values, the gain generated by the pump is insufficient to compensate for the total internal plus output loss.

It can be seen from Figure 6.5 that the optimum reflectivity shifts to lower values of R_o as the launched pump power is increased. Although it is not particularly sensitive for heavily pumped devices, the optimum value of R_o has to be chosen according to the pump power to be used.

Finally, plots of the generated laser output power variation with the launched pump power are considered. According to the Rigrod's analysis, it reflects the influence of the laser-saturated gain on the extracted signal power [29]. This analysis is important because it provides the slope efficiency and the threshold pump power, and is useful for comparison with experiment. For this final simulation, the waveguide parameters which show the best results, in terms of blue light generation for the two characteristics analysed previously, were chosen. Therefore, the next simulation considered a 5.0 cm long waveguide, with a $5.0 \mu\text{m} \times 5.0 \mu\text{m}$ cross section, and 0.25 dB/cm of scattering losses at the pump and signal wavelengths. The cavity laser was formed by two mirrors with 99.0% and 64.7% of reflectivity at the signal wavelength for the input and output mirrors, respectively. The same set of mirrors has transmission of 100.0% at the pump wavelength. The thulium doping level was 0.30 wt%, and the ytterbium content was varied, and it was plotted as a parameter.

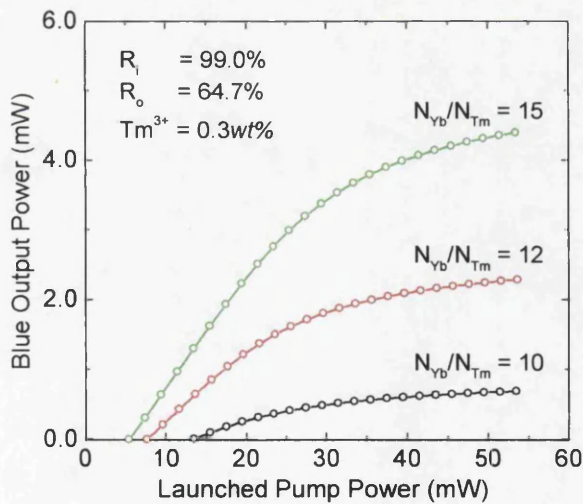


Figure 6.6: Blue output power as a function of the launched pump power. The mirrors reflective were $R_i = 99.0\%$ and $R_o = 64.7\%$. The Tm^{3+} concentration was maintained constant at 0.3 wt%, and Yb^{3+} varied with the 10, 12, and 15 ratios.

The waveguide specifications adopted for this last simulation are probably not

optimal in terms of optimisation of the blue output power. However, as the goal of this chapter was only to demonstrate the viability of this waveguide configuration for the development of Tm³⁺/Yb³⁺-doped lasers, these results can be used as a guide. In the present modelling, thulium ions concentrations below 0.30 wt% were considered. Laser action was predicted if the backscattering losses were kept below 0.5 dB/cm. Although experimental evidence of losses of 0.09 dB/cm at 1.3 μm has been reported, for devices operating at shorter wavelengths these values tend to increase. The increase of the Yb³⁺ ions content has led to a considerable enhancement in the laser efficiency with a reduction in the threshold pump power. According to Figure 6.6, the threshold power reduced from 13.5 mW to 5.5 mW, while the efficiency increased from 3.9 to 15.7%. This efficiency was calculated for the linear output regime of operation. The ratio of the maximum signal output power and the respective pump power per unit of waveguide length is an appropriate guiding parameter to compare the efficiency of this short waveguide configuration with the reported long optical fibres, $\xi = P_{MAX}^S / (P_P \cdot L)$. Here, P_{MAX}^S is the maximum output signal obtained with the pump power P_P in a waveguide with L meters long. The efficient Tm-doped ZBLAN optical fibre laser consisted of a 2.5 m long fibre (3.0 μm core diameter) reported by Sanders [8] will be used for comparison. The cavity was formed by a set of mirrors with 99% and 80% reflectivity for the input and output mirrors, respectively. Pumped by a single tunable powerful diode laser, tuned at 1130 nm, 72 mW of blue light was generated from 550 mW of laser output power (coupling efficiency of ~60%). This corresponds to ~26% of optical-to-optical conversion efficiency, with the threshold value at 48 mW of launched power. The ratio defined above was determined for the fibre laser as $\xi \approx 0.1 \text{ m}^{-1}$, while the waveguide simulations have predicted $\xi \approx 0.3, 0.9$ and 1.8 m^{-1} for the three Yb/Tm ratios.

The conversion efficiency is higher for the fluoro-based optical fibre lasers, however, the threshold pump power was predicted to be better for the SiO₂-P₂O₅ glass waveguide laser in the 980 nm pumping scheme. The reduced pump threshold when compared with Tm-ZBLAN fibres can be expected due to several reasons.

Firstly, the fast nonradiative decay from ³H₅ to ³H₄, due to the high phonon energy of

the phosphosilicate glass, makes it possible to maintain a large population in the metastable level 3H_4 . Thus, the ground state level is easily depopulated and the first excited state absorption from this level is increased. In addition, stimulated emission from 3H_5 can be considered as negligible in this glass. A decrease in the threshold power was experimentally observed in a Tm^{3+} -doped laser when a second pump wavelength was employed to depopulate the ground state [11].

A second factor that increases the pump threshold for thulium doped ZBLAN lasers is due to the transition $^3F_4 \rightarrow ^3H_6$. Mejía *et al.* [48] has reported in a 2.4 m long fibre that the blue fluorescence was suppressed by the amplified spontaneous emission from 3F_4 level. In fact, they reported laser action at 790 nm due to a cavity formed by the ends of the fibre. Reference [47] has shown that this transition produces 2.5 more gain than at 480 nm. Thus, the threshold for ~ 800 nm is much lower than at 480 nm. Lasing at ~ 800 nm depopulates the 1G_4 level, resulting in a suppressed fluorescence at 480 nm. This effect is minimised in the Tm/Yb-doped waveguide laser configuration because the cross relaxation between Tm and Yb is faster than the fluorescence of the Tm. Thus, when this energy returns to the Tm ions through cross relaxation, it will depopulate the ground state.

In conclusion, the Tm/Yb-doped $SiO_2-P_2O_5$ glass system fabricated by FHD method appears to be a suitable configuration for an integrated blue upconversion laser. The process is expected to be efficient due to the high phonon energy of the glass, so that nonradiative relaxations enhance the efficiency of the process. Conversion efficiency of $\sim 15\%$ have been predicted in the present modelling. This value is lower than that reported in the optical fibre version ($\sim 30\%$). However, complete modelling, considering higher thulium doping level, can be performed to optimise this efficiency.

6.3.3 Rate Equations for Pump Wavelength at 800 nm

Data from Table 6.VII, used in the previous section (Figure 6.1), was also used to establish the simplified energy level diagram shown in Figure 6.7. This diagram is analogous to the one defined for the pumping at 980 nm, and the same convention as in Figure 6.1 was adopted. The only difference is that at 800 nm, the pump

wavelength is now applied in the ${}^3\text{H}_6 \rightarrow {}^3\text{F}_4$ transition of the thulium ions instead of the ${}^2\text{F}_{7/2} \rightarrow {}^2\text{F}_{5/2}$ of ytterbium ions. Consequently, under this pump scheme the Yb^{3+} ions are not participating in the upconversion process as previously. Rather, they have been used as a route to more efficiently transfer energy from the metastable ${}^3\text{F}_4$ to the lower states ${}^3\text{H}_5$ and ${}^3\text{H}_4$.

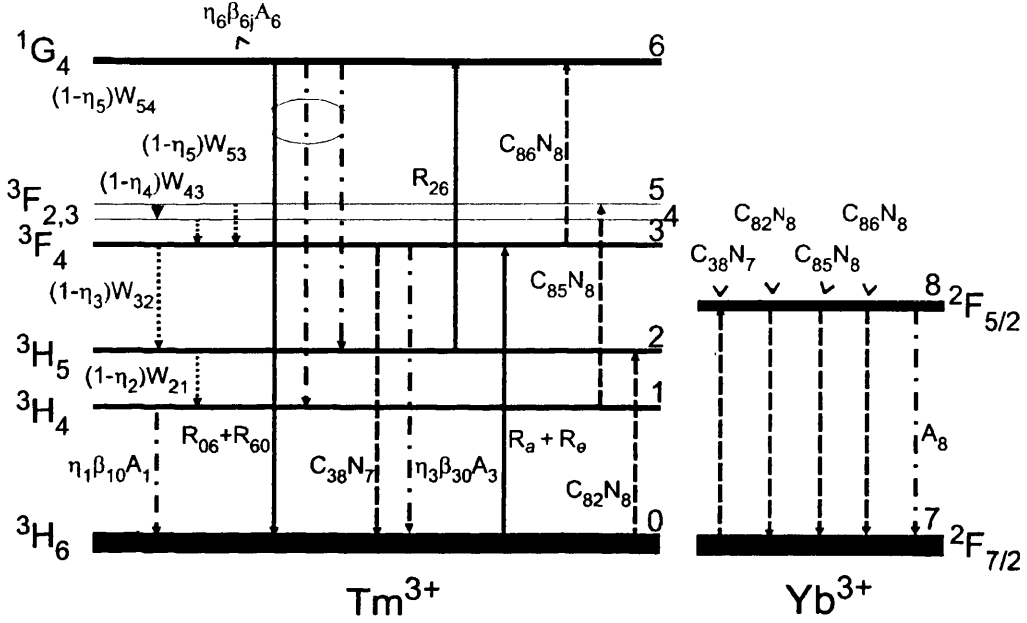


Figure 6.7: Energy level diagram showing radiative, nonradiative, and stimulated transitions of the Tm^{3+} ions. Pumping scheme ~ 800 nm.

Based on the energy level diagram of Figure 6.7, the rate equations for pumping at 800 nm are defined:

$$\begin{aligned} \frac{dN_0}{dt} = & -(R_a + R_{06} + C_{82}N_8 + C_{63}N_6)N_0 + \eta_1\beta_{10}A_1N_1 \\ & + (R_{30} + \eta_3\eta_{30}A_3 + C_{38}N_7)N_3 + (R_{60} + \eta_6\beta_{60}A_6)N_6 \end{aligned} \quad (6.22)$$

$$\begin{aligned} \frac{dN_1}{dt} = & -(\eta_1\beta_{10}A_1 + C_{85}N_8)N_1 + (1 - \eta_2) \cdot W_{21}^{nr} N_2 \\ & + \eta_6\beta_{61}A_6N_6 \end{aligned} \quad (6.23)$$

$$\begin{aligned} \frac{dN_2}{dt} = & (C_{63}N_6 + C_{82}N_8)N_0 - [(1 - \eta_2) \cdot W_{21}^{nr} + R_{26}] \cdot N_2 \\ & + (1 - \eta_3) \cdot W_{32}^{nr} N_3 + (R_{62} + \eta_6\beta_{62}A_6)N_6 \end{aligned} \quad (6.24)$$

$$\begin{aligned} \frac{dN_3}{dt} = & (R_a + C_{63}N_6)N_0 + (1 - \eta_4) \cdot W_{43}^{nr} N_4 + (1 - \eta_5) \cdot W_{53}^{nr} N_5 \\ & - \left[(1 - \eta_3) \cdot W_{32}^{nr} + R_{30} + \eta_3 \beta_{30} A_3 + C_{38} N_7 + C_{86} N_8 \right] \cdot N_3 \end{aligned} \quad (6.25)$$

$$\frac{dN_4}{dt} = -(1 - \eta_4) \cdot W_{43}^{nr} N_4 + (1 - \eta_5) \cdot W_{54}^{nr} N_5 \quad (6.26)$$

$$\frac{dN_5}{dt} = -(1 - \eta_5) \cdot [W_{53}^{nr} + W_{54}^{nr}] \cdot N_5 + C_{85} N_1 N_8 \quad (6.27)$$

$$\begin{aligned} \frac{dN_6}{dt} = & (R_{06} - C_{63}N_6)N_0 + R_{26}N_2 + C_{86}N_3N_8 \\ & - [R_{60} + R_{62} + \eta_6(\beta_{60} + \beta_{61} + \beta_{62})A_6] \cdot N_6 \end{aligned} \quad (6.28)$$

$$\begin{aligned} \frac{dN_7}{dt} = -\frac{dN_8}{dt} = & -C_{38}N_3N_7 + (C_{82}N_0 + C_{85}N_1 + C_{86}N_3)N_8 \\ & + A_8N_8 \end{aligned} \quad (6.29)$$

As defined in the equations (6.12)-(6.19), the N_i 's are the population densities of the thulium ($0 \leq i \leq 6$) and ytterbium ($i = 7$ and 8), they are functions of time and position $N_i = N_i(t, x, y, z)$. The conservation of the number of photons dictates that

$$N_{Yb} = N_7 + N_8, \text{ and } N_{Tm} = \sum_{i=0}^6 N_i, \text{ where } N_{Yb} \text{ and } N_{Tm} \text{ are the total ytterbium and thulium ions concentrations, respectively.}$$

R_a and R_e are the pump and, R_{ij} are the signal stimulated transition rates defined previously. In the rate equations, the factor C_{36} was also included to account for the cross relaxation $\text{Tm}(^1\text{G}_4) + \text{Tm}(^3\text{H}_6) \rightarrow \text{Tm}(^3\text{H}_5) + \text{Tm}(^3\text{F}_4)$ between thulium ions allowing high thulium doping level simulations. These transitions were not included in the diagram of Figure 6.7.

Similarly to the previous derivation for the 980 nm pumping scheme, the wave equations coupled with the set of laser rate equations governing the evolution of the pump and signal along the waveguide are:

$$\frac{dI_p(t, x, y, z)}{dz} = -\sigma_a \left[N_3 - \left(\frac{\sigma_e}{\sigma_a} \right) \cdot N_0 \right] \cdot I_p(t, x, y, z) - \alpha_p \cdot I_p(t, x, y, z) \quad (6.30)$$

$$\frac{dI_s^\pm(t, x, y, z)}{dz} = \pm \sigma_{60} \left[N_6 - \left(\frac{\sigma_{06}}{\sigma_{60}} \right) \cdot N_0 \right] \cdot I_s^\pm(t, x, y, z) \mp \alpha_s \cdot I_s^\pm(t, x, y, z) \quad (6.31)$$

where σ_a and σ_e are the peak absorption and emission cross sections at the pump

wavelength of the ytterbium ions, while σ_{06} and σ_{60} correspond to analogous cross sections at the signal wavelength. α_P and α_S represent the scattering losses at the pump and signal wavelength, respectively.

6.3.4 Laser Design Considerations - $\lambda_p = 800$ nm

The computer program used for modelling the $\text{Tm}^{3+}/\text{Yb}^{3+}$ -doped waveguide laser pumped at 980 nm was adapted to the 800 nm pumping condition. The same waveguide configuration that generated the results shown in Figure 6.6 was used at this pumping wavelength. However, the modelling does not predict laser generation. In order to understand this behaviour, the rate equations were used to analyse the population dynamic of the thulium ions.

The model was used to study the steady-state thulium ions population distribution as a function of the pump power P_P coupled into the waveguide. It was assumed that each level i is split into g_i sublevels where g_i is the degeneracy factor ($g_i = 2J_i + 1$ with J_i the total angular momentum) [18]. For the modelling, it was assumed that by thermal equilibrium the population of each sublevel i are equally distributed, namely (N_i/g_i) . Laser action may be expected if inversion occurs between the ground state (N_0) and the excited state (N_6), i.e. when $(N_6/g_6)/(N_0/g_0) > 1$.

Focusing the pump in a $5.0 \mu\text{m} \times 5.0 \mu\text{m}$ cross section, the pump power was varied from 0-500 mW, and several calculations were performed with different Tm^{3+} concentrations, and a fixed $\text{Yb}^{3+}/\text{Tm}^{3+}$ ratio equal to 10. The typical results of the simulations shown in Figure 6.8, which can be used to explain the laser modelling behaviour above. In this figure, the result corresponding to the population of the levels $^3\text{H}_5$ and $^1\text{G}_4$ were magnified 10^4 and 25 times, respectively.

Initially, a population inversion between the levels 0 and 6 was not observed. Even in the high pump power regime, the ground state saturates in its minimum population level, and the excited state level N_6 is at least one order of magnitude smaller than the N_0 state. This result can be followed from the black line and the open circles in the Figure 6.8, corresponding to N_0 and N_6 respectively. Depletion in the population level N_6 for pump power above 240 mW was also observed. This population is

to the pump power to the level 3F_4 , and its long radiative lifetime, make the contribution of the cross relaxation to the process of populating the 1G_4 level more pronounced than the pump ESA. Thus, for the high pump power regime, stimulated emission becomes more effective in depopulating this level. This is corroborated by the magnified curve corresponding to the population of the 3H_5 level in the high pump power regime, while this level shows a small increase in the population the blue signal has shown a reduction.

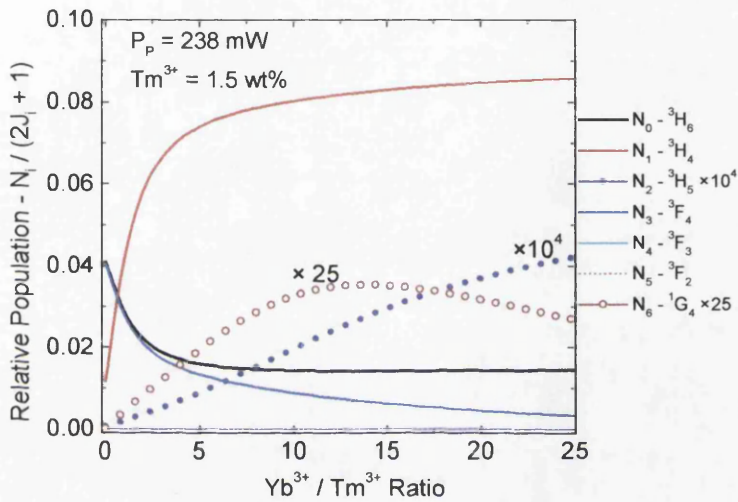


Figure 6.9: The sublevel occupation of the seven energy levels of the Tm^{3+} model as a function of the Yb^{3+}/Tm^{3+} ratio. The fixed $P_p = 238$ mW was focused in a $5.0 \mu m \times 5.0 \mu m$ waveguide cross section.

Maintaining the previous waveguide characteristics and fixing the pump power intensity at 238 mW (this correspond to the condition of the maximum N_6 population obtained in the Figure 6.8) the ytterbium content was varied and the result is shown in Figure 6.9. This result shows evidence of the major contribution of the ytterbium ions to the population level from where the blue upconversion light is generated (N_6). Without ytterbium ions, there is neither population inversion between N_0 and N_6 (black solid line and open circles, respectively) nor a significant population in the 3H_5 level (solid circles), despite the high population of the 3F_4 level (blue line). Increasing the rare earth doping level, a maximum population in the level N_6 occurs at Yb/Tm ratio of 13.9 followed by a reduction. This is expected if, above a certain limit, the ytterbium ions are more efficient in depopulating the metastable level than

in transferring part of their energy to the upconversion process. This is observed by the continuous reduction in the 3F_4 population level and the increasing in that of the 3H_5 and 3H_4 (red line) level. Thus, the two energy transfer routes $Tm(^3F_4) + Yb(^2F_{7/5}) \rightarrow Tm(^3H_6) + Yb(^2F_{5/2})$ and $Tm(^3H_6) + Yb(^2F_{5/2}) \rightarrow Tm(^3H_5) + Yb(^2F_{7/5})$ are more efficient than the $Tm(^3F_4) + Yb(^2F_{5/5}) \rightarrow Tm(^1G_4) + Yb(^2F_{7/2})$ route.

In summary, simulations of the thulium ytterbium doped phosphosilicate glass system using the pumping scheme at 800 nm did not predict laser operation.

6.4 Conclusion

This chapter was devoted to the study of the viability of the use of the thulium/ytterbium ions as active material, and SiO₂-P₂O₅ glass system as host, to generate blue laser light. The study was based on the experimental evidence of the blue light generation reported in the previous chapter.

Initially, relevant spectroscopic information for laser modelling was determined. The technique of the Judd-Ofelt theory was applied to experimental data. The cross relaxation coefficients were evaluated and approximate mathematical relations as a function of the rare earth doping level determined. Considering the calculated radiative and nonradiative transition parameters, the contributions to the expected fluorescence spectrum were determined. These results were used as a guideline to reduce the assumptions simplifying the laser model.

Two pumping wavelength at 980 nm and 800 nm, which are available from commercial diode lasers, were considered in modelling the laser. Simulations of the 980 nm pumping wavelength, the modelling predicted blue light generation under different conditions. Conversion efficiency above 15% was obtained with relatively low thulium doping level, i.e. with Tm³⁺ ions doping level of approximately 0.30 wt% and 5.0 cm long. This result indicates a promising starting point for optimisation if compared with the best result found in the literature, in a single thulium doped fluoride-based optical fibre, with 26% of conversion efficiency in a 2.4 m long fibre [48]. The waveguide laser results were not optimised. This should be done when more samples are available. This will also ensure the possibility of the spectroscopic determination of several different fabrication parameters.

The simulations of operation with the pumping wavelength at 800 nm did not predict blue laser light generation. The modelling was then used to study the level populations behaviour. The calculations were carried out with the same parameters used for the laser pumped at 980 nm, and the results predicted by the modelling qualitatively agree with the experimental results obtained in the previous chapter.

Thus, Tm³⁺/Yb³⁺/Na⁺ incorporated into SiO₂-P₂O₅ glass system fabricated by Flame

Hydrolysis Deposition method have shown to be an option to produce a compact solid-state blue light laser source. The laser modelling did not consider high thulium doping level, however, heavily doped waveguide lasers could allow one to use a shorter cavity, ideal for single cavity mode laser operation.

6.5 Reference

- 1 G. Özen, X. Wu, J.P.Denis, A. Kermaoui, F. Pellé, and B. Blanzat, "Optical properties and upconversion emissions of Tm^{3+} in Yb^{3+} doped fluorophosphate glasses", *Journal of Physical and Chemistry of Solids* **54**, 1533-1542 (1993).
- 2 X. Wu, J.P.Denis, G. Özen, A. Kermaoui, and F. Pellé, "The up-conversion luminescence of Tm^{3+} in glass ceramic doped with Yb^{3+} under infrared excitation", *Physics of Status Solid (a)* **141**, 445-455 (1994).
- 3 B. Dussardier, J. Wang, D.C. Hanna, D.N. Payne, "Spectroscopy and CW 2-photon upconversion in Tm^{3+} -doped $ZnCl_2$ -based glass", *Optical Materials* **4**, 565-573 (1995).
- 4 X.X. Zhang, P. Hong, M. Bass, and B.H.T. Chai, "Blue upconversion with excitation into Tm ions at 780 nm in Yb- and Tm-codoped fluoride crystals", *Physical Review B* **51**, 9298-9301 (1995).
- 5 Z. Hao, X. Chen, G. Zhang, F. Song, and Y-bing Hou, "Blue upconversion with excitation at 970 nm in $Yb_{0.18}$ -doped $Tm_{0.03}LaP_5O_{14}/Tm_{0.1}LaP_5O_{14}$ ", *Proceeding SPIE* **2897**, 275-278 (1996).
- 6 T. Schweizer, B.N. Samson, J.R. Hector, W.S. Brocklesby, D.W. Hewak, and D.N. Payne, "Infrared emission and ion-ion interactions in thulium- and terbium-doped gallium lanthanum sulphide glass", *Journal of the Optical Society of America B* **16**, 308-316 (1999).
- 7 M.P.Le Flohic, J.Y. Allain, G.M. Stéphan, and G. Mazé, "Room-temperature continuous-wave upconversion laser at 455 nm in a Tm^{3+} fluorozirconate fiber", *Optics Letters* **19**, 1982-1984 (1994).
- 8 S. Sanders, R.G. Waarts, D.G. Mehuys, and D.F. Welsh, "Laser diode pumped 106 mW blue upconversion fiber laser", *Applied Physics Letters* **67**, 1815-1817 (1995).
- 9 G. Tohmon, J. Ohya, H. Sato, and T. Uno, "Increased efficiency and decreased threshold in Tm:ZBLAN blue fiber laser co-pumped by 1.1 μm and 0.68 μm light", *IEEE Photonics Technology Letters* **7**, 742-744 (1995).
- 10 G. Huber, T. Kellner, H.M. Kretschmann, T. Sandrock, H. Scheife, "Compact diode pumped cw solid-state lasers in the visible spectral region", *Optical Materials* **11**, 205-216 (1999).
- 11 G. Tohmon, H. Sato, J. Ohya, and T. Uno, "Thulium:ZBLAN blue fiber laser pumped by two wavelengths", *Applied Optics* **36**, 3381-3386 (1997).
- 12 T. Katigawa, K. Hattori, K. Shuto, M. Yasu, M. Kobayashi, M. Horiguchi, "Amplification in erbium-doped silica-based planar lightwave circuit", *Electronics Letters* **28**, 1818-1819 (1992).
- 13 K. Shuto, K. Hattori, T. Katigawa, Y. Ohmori, M. Horiguchi, "Erbium-doped phosphosilicate glass amplifier fabricated by PECVD", *Electronics Letters* **29**, 139-141 (1993).
- 14 K. Hattori, T. Katigawa, M. Oguma, M. Wada, J. Temmyo, M. Horiguchi,

- “Erbium-doped silica-based amplifier pumped by 0.98 μm laser diodes”, *Electronics Letters* **29**, 357-359 (1993).
- 15 K. Hattori, T. Katigawa, M. Oguma, H. Okazaki, Y. Ohmori, “Optical amplification in Er^3 -doped P_2O_5 - SiO_2 planar waveguides”, *Journal of Applied Physics* **80**, 5301-5308 (1996).
- 16 C.K. Madsen, J. Wagener, T.A. Strasser, D. Muehlner, M.A. Milbrodt, E.J. Laskowski, J. DeMarco, “Planar waveguide optical spectrum analyser using a UV-induced grating”, *IEEE Journal of Selected Topics in Quantum Electronics* **4**, 925-929 (1998).
- 17 A. Himeno, K. Kato, T. Miya, “Silica-based planar lightwave circuits”, *IEEE Journal of Selected Topics in Quantum Electronics* **4**, 913-924 (1998).
- 18 E.W.J.L. Oomen, and E.J. Lous, “A material and device study for obtaining a blue upconversion fiber laser”, *Philips Journal of Research* **46**, 157-198, (1992).
- 19 B.R. Judd, “Optical absorption intensities of rare-earth ions”, *Physical Review* **127**, 750-761 (1962).
- 20 G.S. Ofelt, “Intensities of crystal spectra of rare earth ions”, *The Journal of Chemical Physics* **37**, 511-520 (1962).
- 21 M.J. Weber, “Probabilities for radiative and nonradiative decay of Er^{3+} in LaF_3 ”, *Physical Review* **157**, 262-272 (1967).
- 22 W.F. Krupke, and J.B. Gruber, “Optical-absorption intensities of rare earth ions in crystals: the absorption spectrum of thulium ethyl sulphate”, *Physical Review* **139**, A2008-A2016 (1965).
- 23 C.W. Nielsen, and G.F. Koster, Spectroscopic coefficients for the p^n , d^n , and f^n configurations (The M.I.T. Press, Cambridge, Massachusetts, 1963).
- 24 M. Rotenberg, R. Bivens, N. Metropolis, and J.K. Wooten Jr., The 3-j and 6-j symbols, (Technology Press, M.I.T., Cambridge, Massachusetts, 1959).
- 25 W.T. Carnall, P.R. Fields, and B.G. Wybourne, “Spectral intensities of the trivalent lanthanides and Actinides in solution. I. Pr^{3+} , Nd^{3+} , Er^{3+} , Tm^{3+} , and Yb^{3+} ”, *The Journal of Chemical Physics* **42**, 3797-3806 (1965).
- 26 W.T. Carnall, P.R. Fields, and K. Rajnak, “Electron energy levels in the trivalent lanthanides aquo ions. I. Pr^{3+} , Nd^{3+} , Pm^{3+} , Sm^{3+} , Dy^{3+} , Ho^{3+} , Er^{3+} , and Tm^{3+} ”, *The Journal of Chemical Physics* **49**, 4424-4442 (1968).
- 27 W.F. Krupke, “Radiative transition probabilities within the $4f^3$ ground state configuration of Nd:YAG”, *IEEE Journal of Quantum Electronics* **QE-7**, 153-159 (1971).
- 28 J. Sanz, R. Cases, and R. Alcalá, “optical properties of Tm^{3+} in fluorozirconate glass”, *Journal of Non-Crystalline Solids* **93**, 377-386 (1987).
- 29 A. E. Siegman, Lasers, (University Science Books, Sausalito, California, 1986).
- 30 D.E. McCumber, “Theory of phonon-terminated optical masers”, *Physical Review* **134**, A299-A306 (1964).

- 31 D.E. McCumber, "Einstein relations connecting broadband emission and absorption spectra", *Physical Review* **134**, A954-A957 (1964).
- 32 R. Reisfeld, and Y. Eckstein, "radiative and non-radiative transition probabilities and quantum yields for excited states of Er^{3+} in germanate and tellurite glasses", *Journal of Non-Crystalline Solids* **15**, 125-140 (1974).
- 33 C.B. Layne, W.H. Lowdermilk, and W.J. Weber, "Multiphonon relaxation of rare-earth ions in oxide glasses", *Physical Review* **16**, 10-20 (1977).
- 34 W.J. Miniscalco, "Optical and electronic properties of rare earth ions in glasses", *Rare earth doped lasers and amplifiers*, Ed. M.J.F. Digonnet (1993).
- 35 M.A. Chamarro, and R. Cases, "Energy transfer between (Yb,Pr), (Yb,Sm) and (Yb,Dy) in fluorohafnate glasses", *Journal of Non-Crystalline Solids* **107**, 178-186 (1989).
- 36 C.Y. Chen, R.R. Petrin, D.C. Yeh, W.A. Sibley, "Concentration-dependent energy in Er^{3+} - and Tm^{3+} -doped heavy-metal fluoride glass", *Optics Letters* **14**, 432-434 (1989).
- 37 D.C. Yeh, R.R. Petrin, W.A. Sibley, V. Madigou, J.L. Adam, and M.J. Suscage, "Energy transfer between Er^{3+} and Tm^{3+} ions in a barium fluoride-thorium fluoride glass", *Physical review B* **39**, 80-90 (1989).
- 38 R.S. Quimby, W.J. Miniscalco, and B. Thompson, "Clustering in erbium-doped silica glass fibres analysed using 980 nm excited-state absorption", *Journal of Applied Physics* **76**, 4472-4478 (1994).
- 39 H.U. Rahman, "Optical intensities of trivalent erbium in various host lattices", *Journal of physics C: Solid State Physics* **5**, 306-314 (1972).
- 40 J.A. Caird, L.G. Deshazer, J. Nella, "Characteristics of room-temperature 2.3 μm laser emission from Tm^{3+} in YAG and YAlO_3 ", *IEEE Journal of Quantum Electronics* **EQ-11**, 874-881 (1975).
- 41 E.W.J.L. Oomen, "Up-conversion of red light into blue light in thulium doped fluorozirconate glasses", *Journal of Luminescence* **50**, 317-332 (1992).
- 42 Y. Subramanyam, L.R. Moorthy, and S.V.J. Lakshman, "Judd-Ofelt intensity parameters and laser analysis of Tm^{3+} in certain sulphate glasses", *Journal of Non-Crystalline Solids* **139**, 67-73 (1992).
- 43 G. Özen, X. Wu, J.P. Denis, A. Kermaoui, F. Pellé, and B. Blanzat, "Optical properties and upconversion emissions of Tm^{3+} in Yb^{3+} doped fluorophosphate glasses", *Journal of Physical and Chemistry of Solids* **54**, 1533-1542 (1993).
- 44 X. Zou, and T. Izumitani, "Fluorescence mechanisms and dynamics of Tm^{3+} single doped and Yb^{3+} , Tm^{3+} doubly doped glasses", *Journal of Non-Crystalline Solids* **162**, 58-67 (1993).
- 45 R.H. Page, K.I. Schaffers, P.A. Waide, J.B. Tassano, S.A. Payne, W. F. Krupke, and W.K. Bischel, "Upconversion-pumped luminescence efficiency of rare-earth-doped hosts sensitised with trivalent ytterbium", *Journal of the Optical Society of America B* **15**, 996-1008 (1998).
- 46 E. Desurvire, and J.R. Simpson, "Amplification of spontaneous emission in

erbium-doped single-mode fibers”, *Journal of Lightwave Technology* **7**, 835-845 (1989).

47 R. Paschotta, P.R. barber, A.C. Tropper, and D.C. Hanna, “Characterization and modeling of thulium:ZBLAN blue upconversion fiber lasers”, *Journal of the Optical Society of America B* **14**, 1213-1218 (1997).

48 E.B. Mejia, A.N. Starodumov, and Yu. O. Barmenkov, “Blue and infrared up-conversion in Tm³⁺-doped fluorozirconate fiber pumped at 1.06, 1.117, and 1.18 μm ”, *Applied Physics Letters* **74**, 1540-1542 (1999).

Chapter 7 - Conclusion and Suggestion for Further works

7.1 Conclusions

As shown in the short review contained in the beginning of this thesis, several fabrication procedures and physical effects have been employed to generate blue laser light sources usually due to the large variation in the minimum requirements for these sources concerning practical applications. Based on successful demonstration of blue upconversion laser in the optical fibre geometry, the research developed in this thesis has focused on the study of the feasibility of silica-on-silicon blue upconversion laser fabrication using FHD thulium-doped phosphosilicate glass ($\text{SiO}_2\text{-P}_2\text{O}_5$). This chapter will then concentrate in addressing the main conclusions of the work developed in this thesis to obtain a new optically integrated blue laser

light source.

Previous reports of the erbium doped waveguide lasers and amplifiers in the planar form have shown the necessity of high ion doping level to overcome the elevated losses (if compared with optical fibres) and the short interaction length. Initially this study concentrated on the glass host optimisation through the reduction of the rare earth clustering formation, avoiding the deleterious effect of ion-ion interaction. The inclusions of aluminium and sodium ions into the glass matrix were attempted to reduce this disadvantageous effect. It was demonstrated that the amount of aluminium necessary to evidence effects on the rare earth clustering formation has caused reduction in some important spectroscopic characteristics of the laser transition [1]. As a result, sodium was chosen as a possible alternative to reduce the effect of the rare earth clustering formation.

In making use of sodium ions into the glass it was observed that, for a certain amount of rare earth, they were beneficial. The two preliminary glass parameters that revealed variation with the inclusion of sodium ions were the refractive index and the rare earth concentration. The former has shown a similar behaviour for two rare earth concentrations. Both have shown an increase in the refractive index when low sodium concentration was used, followed by a reduction in the index when the sodium content was increased. The latter have shown similar trend as the refractive index only when the rare earth concentration was low. When rare earth was above 1.0 M both sets of samples have shown an increase in the doping level. These results were interpreted in terms of the chemical reactions during the glass fabrication and the theoretical molecular dynamics simulations developed by [2].

The theoretical work mentioned above predicted that when rare earth and sodium ions are present in the glass system, the former attracts the non-bridging oxygen into its potential field and frees it from the silicate network; while the latter are rearranged to meet the requirements of local electro-neutrality. According to our results, this happened when the amount of sodium was smaller than the rare earth. For the situation when both have similar concentration, the sodium ions increased the dispersion of the erbium ions bounding to them, avoiding clustering formation. As

shown in the section 2.6 and 2.6.1, the presence of ion-ion interaction in the host can be observed experimentally by a reduction in the laser lifetime. Thus, the confirmation of the evaluation of the effect of clustering formation due to the increasing of the rare earth was analysed with the fluorescence lifetime as parameter. In these series of measurements it was verified that samples with the lowest and highest rare earth concentrations (0.5 and 2.0 M, respectively) had insignificant variation in the lifetime with the inclusion of the alkali. In contrast, the sample containing a comparable amount of rare earth and alkali has shown a substantial augmentation in the parameter. This indicated that the sodium ions in these samples (1.0 M) were incorporated in the unbounded rare earth avoiding the cluster formation.

A final verification of this assumption was carried out using the Judd-Ofelt analysis of these glass systems. Following the physical interpretation reported in the literature for the variation of the parameter Ω_6 , it was verified that the viscosity of the medium had a significant decrease if a smaller or greater rare earth than the sodium contents were used. According to the molecular simulation, it was predicted that the cations that are not bounded to rare earth ions are incorporated into the glass matrix forming Na_2O . In our FHD glass, due to the presence of phosphorus in the composition, the formation of NaPO_3 is also expected. In both circumstances the inclusion of sodium ions is responsible for the rupture of the tetrahedral formation softening the glass and, consequently decreasing the viscosity. The small influence in the viscosity of the glass containing a similar amount of cations and rare earth observed in the Figure 3.14 agrees with this result.

Based on the measurements in the sets of samples, a theoretical optimum concentration for the maximum solubility of the rare earth ions was found with $\text{Na}^+ \cong 0.85 \text{ M}$ and $\text{Er}^{3+} \cong 1.05 \text{ M}$. An extended investigation on the influence of other alkali ions in the glass matrix concerning the incorporation of rare earth should be developed. Despite the small influence of the host on the rare earth luminescence characteristics, other ions should also be used to complete this analysis.

To optimise the rare earth doped integrated devices, accurate numerical models,

particularly at high concentration levels, are required. In chapter four then the modelling procedure for CW rare earth doped waveguide lasers and amplifiers in both, the low and high doping level was established. The main problem to be addressed in relation to the heavily doped devices is the presence of nonlinear terms in the dynamic rate equations. These nonlinear terms make unable the used of the straightforward numerical procedure for the low rare earth situation. The main difficulty is the impossibility of stating explicitly the relevant contributions of the population levels to solve the overlap integral between the optical fields modes. In principle, this practice is applicable only if the rate equations do not contain nonlinear terms. However, according to the electromagnetic theory, the characteristics of the guided-mode of the field radiation are governed by the waveguide geometry and refractive index of the medium. Experimental results have revealed that the presence of rare earth ions into the glass host have insignificant contributions to the refractive index, even when the radiation wavelength coincides with an absorption band. Therefore, it is expected that the rare earth population densities will not influence the guided mode of a radiation, even if the doping levels reach the condition in which the nonlinear contribution has to be considered in the rate equations. Based on these considerations, a new assumption was introduced expressing the rare earth population of the heavily doped medium as a function of the low doping level population density [3]. Applying this approximation, the heavily doped modelling procedure has the same approach as the low doping level. The contribution of the nonlinear terms appears as a corrective numerical factor. The accuracy of the approximation and the modelling itself was made by comparison of calculations and experimental results which showed very good agreement.

The first step of this research concentrated in the improvement of key factors to improve the performance of rare earth doped waveguide devices: the optimisation of the glass host, permitting an augmentation of the rare earth doping level reducing the harmful effect of ion-ion interaction, and the establishment of a simple and accurate modelling procedure to determine the optimum device parameters.

The second stage of this investigation of the Tm^{3+} -based blue upconversion waveguide laser started by determining a suitable rare earth composition for a

commercial diode laser pump wavelength. Initially, upconversion in single thulium doped samples was investigated under ML and QSML fundamental radiation at 1064 nm. This pumping scheme showed the best performance when Stimulated Raman Scattering generated in standard communication optical fibre was coupled into the waveguide. Approximately 130 nW of blue light at 482 nm was generated from ~70 mW of mode locked infrared radiation [4]. This pumping wavelength has proved to be an option for blue upconversion generation when powerful and inexpensive diode laser operating in ~1100-1250 nm was available. An alternative pump wavelength at 678 nm was also applied showing less efficiency, despite the two-photon process. The low efficiency of the unique blue upconverted signal generated at 451 nm and the spectral proximity to the pump wavelength did not allow the optical filtering of this visible light to measure the efficiency of the process.

The long lifetime of the metastate 3F_4 , added to the minor contribution of its radiative transition to the levels 3H_5 and 3H_4 , produced low efficient upconversion for the pump wavelength at 800 nm. Thus, different sets of samples were produced adding ytterbium ions into a similar Tm^{3+} -doped glass matrix in order to create an additional route to transfer energy more efficiently from the metastate level 3F_4 to the 3H_5 and 3H_4 . Following the results obtained in the spectroscopic characteristics in the glass due to the inclusion of sodium, this ion was also included forming the $Tm^{3+}/Yb^{3+}/Na^+$ doped glass system. The first wavelength analysed with this multi-component glass was at 678 nm. This wavelength has shown a reduction in the upconversion generation for the blue light at 451 nm if compared with the single thulium doped. The participation of the ytterbium ions was detected by the presence of the signal at 482 nm not seen in the single doped sample. The level 1G_4 , from where the signal at 482 nm originates due to the relaxation to the ground state, was populated by the absorption of one pump photon from the level 3H_4 .

A remarkable improvement in the pump efficiency for the wavelength at 800 nm using samples containing ytterbium ions was obtained. The undetectable blue signal of the single doped sample was enhanced to ~10 nW in the composed glass, with only 200 mW of infrared radiation. The dependence of the blue signal with the pump

power has shown saturation for power above 300 mW; and depletion of the upconverted signal for pump power above 700 mW was also observed. Despite the improvement in the upconversion process, numerical simulations with this pumping wavelength did not reveal population inversion to generate blue laser light. This behaviour qualitatively agreed with the experimental results. In the simulation it was observed that the population of the 1G_4 level was depleted for launched pump power superior to ~ 230 mW, which is a good agreement to the observed ~ 750 mW, if a typical coupling coefficient of $\sim 30\%$ is assumed.

Experimentally it was determined that there are only two possible routes to populate the upper 1G_4 level. They are when photons in the level 3F_4 are transferred to the upper level by absorbing the energy delivered from cross relaxations of the ytterbium ions, or through the pump excited state absorption (ESA) from the 3H_5 level. Simulations revealed that the ytterbium to thulium cross relaxation gives the major contribution to the upconversion process, because the population of the 3H_5 level is three orders of magnitude smaller than 3F_4 . It was observed that to populate the upper level of the ytterbium ions, photons have to be transferred from the 3F_4 thulium level, which is populated via the pump photons. The high pump power, required to enhance the energy transfer, is also responsible for the stimulated emission from the 3F_4 metastable level resulting in the depletion in the blue light.

The inclusion of ytterbium ions in the multi-component glass has opened the possibility of the pump wavelength at 980 nm. The high efficiency of the cross relaxation between Tm and Yb ions added to the high cross section of ytterbium ions at pump wavelength were the key factors for the high efficiency of the process. The modelling procedure developed previously was adapted to the Tm/Yb-doped structure for the compact blue upconversion laser in $\text{SiO}_2\text{-P}_2\text{O}_5$ FHD doped glass. The simulations were carried out using spectroscopic information from the glass system itself as input data. Considering typical physical FHD-waveguide parameters the simulation predicted threshold with 5.5 mW of launched pump power. Optical-to-optical conversion efficiency of 15% was also obtained, although the FHD doped waveguide results were not from an optimised laser structure. These values are competitive with the well-known reported results from ZBLAN optical fibres.

Further improvement in the laser performance is expected if two different pump wavelengths are considered.

For the simulations at this pump wavelength the thulium level was considered below 0.30 wt%. This maximum rare earth concentration has ensured the absence of cross relaxation among Tm ions. The 0.25 dB/cm for scattering losses was considered in the simulations, although previous experimental results had shown losses as small as 0.035 dB/cm in similar germanium doped waveguide structures.

The broad absorption band of the ytterbium ions has shown conversion efficiency of 40% of the peak at 977 nm for pump wavelength in the region between 940-960 nm. This pump region is a possible alternative for Nd:YAG diode lasers as fundamental radiation. The upconversion process at this wavelength has maintained relatively constant operation above the room temperature conditions. This characteristic can be a determinant factor for devices operating in aggressive environment, for instance.

In conclusion, this work has demonstrated the viability of fabrication of diode pumped blue upconversion waveguide laser using the FHD-doped glass as host for the rare earth. To explore the potential of this rare earth doped glass, full optimisation of the rare earth doping level and waveguide characteristics should be investigated to improve the laser features. A fully optimised FHD blue upconversion laser structures, the prospect of straightforward photolithographic variation of waveguide parameters, and the mass production of robust devices are factors which, taken together, indicate the great potentiality of these optical integrated devices.

7.2 Reference

- 1 J.R. Bonar, M.V.D. Vermelho, P.V.S. Marques, A.J. McLaughlin, and J.S. Aitchison, "Fluorescence lifetime measurements of aerosol doped erbium in phosphosilicate planar waveguides", *Optics Communications* **149**, 27-32 (1998).
- 2 G. Comier, J.A. Capobianco, and A.Montiel, "Molecular dynamics simulation of the trivalent europium ion doped in silica and sodium disilicate glasses", *Journal of Non-Crystalline Solids* **152**, 225-236 (1993).
- 3 M.V.D. Vermelho, U. Peschel, and J.S. Aitchison, "Simple and accurate procedure for modelling erbium-doped waveguide amplifiers and lasers with high erbium concentration", submitted to publication to *Journal of Lightwave Technology*
- 4 J.R. Bonar, M.V.D. Vermelho, A.J. McLaughlin, P.V.S. Marques, J.S. Aitchison, J.F. MartinsFilho, A.G. Bezerra Jr, A.S.L. Gomes, C.B. deAraujo, "Blue light emission in thulium doped silica-on-silicon waveguides", *Optics Communications* **141**, 137-140 (1997).

Appendix A

In this appendix, the theoretical rate equation model described in the section 6.3.1 is applied to study the dependence of the fluorescence ${}^1G_4 \rightarrow {}^3H_6$ emission intensity on the concentration of the acceptor ions and the pumping power intensity. Due to this analyse has been considered for qualitative evaluation, some simplifications in the previous model were done to become workable the algebraic manipulations. The diagram of the laser system is accounting only the most relevant contributions to the process. The energy transfer rate is simplified considering the fluorescence lifetime of the transitions in the absent of ion-ion interaction, $\tau_{a,b}$, instead the radiative and/or nonradiative contributions; and the levels 3F_2 and 3F_3 were merged in the ${}^3F_{2,3}$ level. In order to maintain the same nomenclature used in the previous model, the level 5 was omitted. Stimulated transitions were also neglected, from the levels 6 and 8. The parameters used the simplified energy level diagram shown in the *Figure A.1*, and they have the same meaning as described previously.

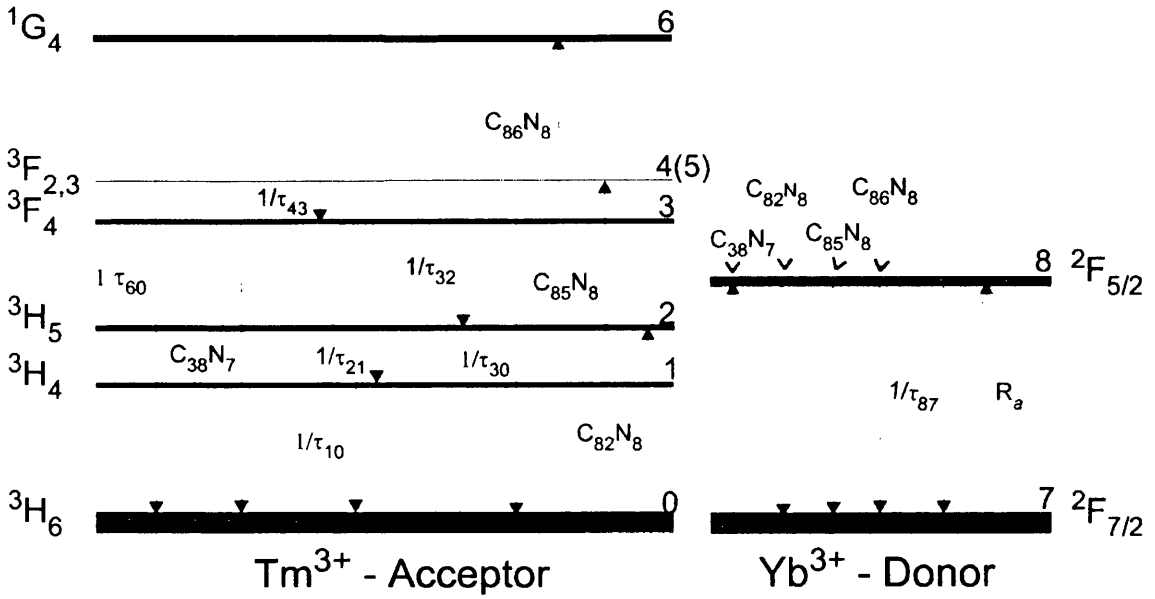


Figure A.1 - Simplified energy level diagram of the Tm/Yb laser system.

The rate equations for the $\text{Tm}^{3+}/\text{Yb}^{3+}$ laser system based in the diagram above are:

$$\frac{dN_1}{dt} = -\frac{N_1}{\tau_{10}} - C_{85}N_1N_8 + \frac{N_2}{\tau_{21}} \quad (\text{A.1})$$

$$\frac{dN_2}{dt} = -\left(\frac{1}{\tau_{20}} + \frac{1}{\tau_{21}}\right)N_2 + C_{82}N_0N_8 \quad (\text{A.2})$$

$$\frac{dN_3}{dt} = -\frac{N_3}{\tau_{30}} + \frac{N_4}{\tau_{43}} - (C_{38}N_7 + C_{86}N_8)N_3 \quad (\text{A.3})$$

$$\frac{dN_4}{dt} = -\left(\frac{1}{\tau_{40}} + \frac{1}{\tau_{43}}\right)N_4 + C_{85}N_1N_8 \quad (\text{A.4})$$

$$\frac{dN_6}{dt} = -\frac{N_6}{\tau_{60}} + C_{86}N_3N_8 \quad (\text{A.5})$$

$$\frac{dN_8}{dt} = R_aN_7 - \frac{N_8}{\tau_{87}} + C_{38}N_3N_7 - (C_{38}N_0 + C_{85}N_1 + C_{86}N_3)N_8 \quad (\text{A.6})$$

In order to determine the population of each level, the steady state condition ($d/dt = 0$) was assumed and the system of equations solved. The contributions of the Tm ions levels are:

$$N_1 = \frac{N_2}{\tau_{21} \left(\frac{1}{\tau_{10}} + C_{85}N_8 \right)} \quad (\text{A.7})$$

$$N_2 = \frac{C_{82} N_0 N_8}{\left(\frac{1}{\tau_{20}} + \frac{1}{\tau_{21}} \right)} \quad (\text{A.8})$$

$$N_3 = \frac{N_4}{\tau_{43} \left(\frac{1}{\tau_{30}} + C_{38} N_7 + C_{86} N_8 \right)} \quad (\text{A.9})$$

$$N_4 = \frac{C_{85} N_1 N_8}{\left(\frac{1}{\tau_{40}} + \frac{1}{\tau_{43}} \right)} \quad (\text{A.10})$$

$$N_6 = (C_{86} N_3 N_8) \tau_{60} \quad (\text{A.11})$$

In order to determine the relation between the intensity of the fluorescence from a specific transition, the relation $I_{a,b} = h\nu_{a,b} W_{a,b} N_a$ [1] was used. $W_{a,b}$ is the transfer rate between the levels a and b of a single ion, $\nu_{a,b}$ is the optical frequency between the transition levels, and N_a is the photon density (population) in the upper level. h is the Planck's constant. For the laser transition level 1G_4 of the Tm ions, the intensity of the fluorescence is given by:

$$I_{60} = h\nu_{60} W_{60} N_6 \quad (\text{A.12})$$

or, expressing in terms of the spectroscopic parameters described in the energy level diagram, the fluorescence intensity can be described by:

$$I_{60} = \left[\frac{h\nu_{60} W_{60} C_{82} C_{85} C_{86} \tau_{60}}{\tau_{43} \left(\frac{1}{\tau_{30}} + C_{38} N_7 + C_{86} N_8 \right) \left(\frac{1}{\tau_{40}} + \frac{1}{\tau_{43}} \right) \tau_{21} \left(\frac{1}{\tau_{10}} + C_{85} N_8 \right) \left(\frac{1}{\tau_{20}} + \frac{1}{\tau_{21}} \right)} \right] \cdot N_0 N_8^3 \quad (\text{A.13})$$

Equation (A.13) establishes the relation between the fluorescent signal intensity and the concentration of the Tm and ytterbium ions. To determine the correlation of this intensity with the pump power, two limits of operations have to be considered.

If the pump intensity I_p is sufficiently weak, the ground states of the thulium and ytterbium ions are not severely depopulated and the following approximation for the

two population densities in the equation (A.13) can be assumed as:

$$\begin{aligned} N_0 &\cong N_{Tm} \\ N_7 &\cong N_{Yb} \end{aligned} \quad (\text{A.14})$$

where N_{Tm} and N_{Yb} are the total concentration of thulium and ytterbium, respectively. Consequently, the rate equation corresponding to the excited state of the ytterbium ions, equation (A.6), can be solved in the steady state with the following approximation:

$$R_a N_7 - \frac{N_8}{\tau_{87}} - C_{82} N_0 N_8 \cong 0 \quad (\text{A.15})$$

and the population level 8 is giving by:

$$N_8 \cong \frac{R_a N_{Yb}}{\left(\frac{1}{\tau_{87}} + C_{82} N_{Tm} \right)} \quad (\text{A.16})$$

The dependence on the pump intensity in the equation (A.16) arises from the pump transition rate dependence on this parameter, given by:

$$R_a = \frac{\sigma_{78} I_p}{h\nu_p} \quad (\text{A.17})$$

Employing the typical spectroscopic values shown in the chapter six, the following approximations can be assumed:

$$\frac{1}{\tau_{30}} \gg (C_{38} N_7 + C_{86} N_8), \quad \frac{1}{\tau_{10}} \gg C_{85} N_8, \quad \text{and} \quad \frac{1}{\tau_{87}} \gg C_{82} N_{Tm}$$

introducing these approximations into equation (A.13), and applying equation (A.17) into equation (A.16), considering the low intensity of the pump power through the approximations (A.14), the intensity of the fluorescent level 1G_4 can be expressed in a simplified form as:

$$I_{60} \cong \left[\frac{h\nu_{60} W_{60} C_{82} C_{85} C_{86} \tau_{60}}{\left(\frac{\tau_{43}}{\tau_{30}} \right) \left(\frac{1}{\tau_{40}} + \frac{1}{\tau_{43}} \right) \left(\frac{\tau_{21}}{\tau_{10}} \right) \left(\frac{1}{\tau_{20}} + \frac{1}{\tau_{21}} \right)} \cdot \left(\frac{\sigma_{78} \tau_{87}}{h\nu_p} \right)^3 \right] \cdot N_{Tm} N_{Yb}^3 I_p^3 \quad (\text{A.18})$$

and the cubic dependence of the fluorescence due to the transition $^1G_4 \rightarrow ^3H_6$ of the

Ytterbium ions with the pump power becomes explicit.

However, this approximation will not be valid in the high pump power regimes. For these situations, the depletions of the thulium ground state have to be considered. The depletion of this level can be evaluated assuming the conservation of the number of photons, and the population of the level '0' can be expressed by:

$$N_0 = N_{7m} - (N_1 + N_2 + N_3 + N_4 + N_6) \quad (\text{A.19})$$

Applying equations (A.7)-(A.11) into the equation (A.19), after straightforward algebraic manipulations, it can be expressed as:

$$N_0 = N_{7m} - \alpha N_0 N_8 - \beta N_0 N_8^2 - \gamma N_0 N_8^3 \quad (\text{A.20})$$

where α , β , and γ are three parameters containing spectroscopic parameter, and are expressed by:

$$\alpha = \left\{ \frac{1 + 1/\left[\tau_{21} \left(\frac{1}{\tau_{10}} + C_{85} N_8 \right) \right]}{(1/\tau_{20} + 1/\tau_{21})} \right\} C_{82} \quad (\text{A.21})$$

$$\beta = \frac{C_{82} C_{85}}{\tau_{43} \left(\frac{1}{\tau_{30}} + C_{38} N_7 + C_{86} N_8 \right) \left(\frac{1}{\tau_{40}} + \frac{1}{\tau_{43}} \right) \tau_{21} \left(\frac{1}{\tau_{10}} + C_{85} N_8 \right) \left(\frac{1}{\tau_{20}} + \frac{1}{\tau_{21}} \right)} \quad (\text{A.22})$$

$$\gamma = \frac{C_{82} C_{85} C_{86} \tau_{60}}{\tau_{43} \left(\frac{1}{\tau_{30}} + C_{38} N_7 + C_{86} N_8 \right) \left(\frac{1}{\tau_{40}} + \frac{1}{\tau_{43}} \right) \tau_{21} \left(\frac{1}{\tau_{10}} + C_{85} N_8 \right) \left(\frac{1}{\tau_{20}} + \frac{1}{\tau_{21}} \right)} \quad (\text{A.23})$$

Thus, the depletion in the ground state can be expressed in terms of these three parameters and the excited state population of the ytterbium ions by:

$$N_{0D} = \frac{N_{7m}}{1 + \alpha N_8 + \beta N_8^2 + \gamma N_8^3} \quad (\text{A.24})$$

Assuming the previous experimental values of the spectroscopic parameter, it is expected that, the main contribution in the denominator comes from the linear term. Thus the depleted ground state population can be expressed by:

$$N_{0D} \cong \frac{N_{7m}}{1 + \alpha N_8} \quad (\text{A.25})$$

Thus, when the high pump power is applied to the medium, the depletion of the $^3\text{H}_6$ level is accounted and the fluorescence of the $^1\text{G}_4$ level can be approximated by:

$$I_{60} \cong K \cdot \left(\frac{N_{7m}}{1 + \alpha N_8} \right) \cdot N_8^3 \quad (\text{A.26})$$

where K is given by:

$$K = \left[\frac{h\nu_{60} W_{60} C_{82} C_{85} C_{86} \tau_{60}}{\tau_{43} \left(\frac{1}{\tau_{30}} + C_{38} N_7 + C_{86} N_8 \right) \left(\frac{1}{\tau_{40}} + \frac{1}{\tau_{43}} \right) \tau_{21} \left(\frac{1}{\tau_{10}} + C_{85} N_8 \right) \left(\frac{1}{\tau_{20}} + \frac{1}{\tau_{21}} \right)} \right]$$

Therefore, the dependence of the fluorescent signal with the pump power, through the population of the excited state of the donor ions, can have values smaller than the expected cubic for higher pump power.

1. M.A. Chamarro, and R. Cases, "Energy transfer between (Yb,Pr), (Yb,Sm) and (Yb,Dy) in fluorohafnate glasses". *Journal of Non-Crystalline Solids* **107**, 178-186 (1989)